Unveiling viral structures by single-molecule localization microscopy

Maria Arista Romero

Doctoral thesis

Unveiling viral structures by single-molecule localization microscopy

Author:

María Arista Romero

Barcelona 2021

UNIVERSITAT DE BARCELONA

Unveiling viral structures by single-molecule localization microscopy

Memory presented to apply for the doctorate degree by the Universitat de Barcelona

Doctorate program in nanosciences

Author:

María Arista Romero

Directors:

Dr. Lorenzo Albertazzi & Dr. Silvia Pujals Riatós

Tutor:

Dr. Josep Samitier Martí

Barcelona 2021

UNIVERSITAT DE BARCELONA

A mis padres y a Genís

“She knew she wouldn't manage it right away,

but she felt fairly confident that with a great deal of practice and effort,

she would succeed in the end”

Roald Dahl, Matilda

Table of contents

Abstract

Influenza A virus is one of the most outstanding human viruses. It produces seasonal epidemics every year, it has caused 5 pandemics between the XX and the XXI century, and it is responsible for more than 60 million deaths. The major treatments against influenza are small analogues, monoclonal antibodies and vaccines, however, due to the fast mutation of the seasonal influenza strain, these methods are easily outdated, so vaccine production and antiviral development need to be in continuous growth and study to improve immunity and fight against influenza disease. The characterization of the viral structure and the identification of the mechanisms of action of newly synthesized antivirals are crucial to develop fast and powerful treatments, nonetheless, due to the small size of viruses, conventional fluorescence techniques are lacking the resolution power to resolve individual viral structures. In this context, super-resolution microscopy has positioned in the last decade as a powerful technique to characterize viral constructs by achieving resolutions up to 10 nm.

Here, we have optimized and established a type of super-resolution microscopy technique entitled single-molecule localization microscopy (SMLM) to study viral structures at single-particle level by characterizing several viral structures, antivirals and vaccines.

Firstly, we could characterize the filament formation of influenza virus and described how monoclonal antibodies disturbed the development of those filaments, deforming them. Further, we could relate this malformation with an inhibition of the infectivity, suggesting the crucial role of filament formation in the infectivity of influenza. Moreover, we optimized and implemented a novel SMLM called DNA-PAINT in the study of the target distribution and quantification in the nanoscale, validating this method using commercial nanoparticles for its further implementation in the study of the expression of recombinant proteins of influenza and the corresponding virus-like particle produced, proving how this method could work as a characterization platform for the improvement of the production of recombinant vaccines.

In addition, we studied and identified several other viral structures and antivirals interactions using SMLM such as the distribution of Hepatitis B and Hepatitis Delta on paraffin tissues, the interaction of analogues of sialic acid on four strains of influenza and the uptake of nanovaccines from antigen-presenting cells, obtaining features on how these viruses and antivirals interact in order to produce a smart design of antivirals and vaccines, corroborating how SMLM could increase the knowledge of the mechanism of action of viruses.

Resumen en castellano

Los virus son amenazas permanentemente presentes contra todo tipo de animales, incluidos los seres humanos. Uno de los virus que más infecciones produce cada año es el virus de la gripe A (Influenza A), una enfermedad ancestral que produce infección respiratoria en mamíferos y aves domésticas y generalmente surge de reservorios zoológicos como aves y murciélagos[1]. Los efectos de la gripe en nuestra sociedad son notables, siendo la causa de al menos 5 pandemias entre el siglo XX y el siglo XXI, provocando más de 60 millones de muertes[2] y creando la necesidad de una vacunación anual para la población de riesgo.

Los antivirales y los anticuerpos monoclonales son muy útiles como tratamiento de primera línea para evitar la propagación de la gripe, pero la única forma de obtener una protección prolongada y exitosa en la población es la inmunidad obtenida por las vacunas. Sin embargo, el virus influenza muta cada año generando nuevas variantes que no son reconocidas por las vacunas previamente sintetizadas, por lo que la producción de vacunas y el desarrollo de antivirales deben estar en continuo crecimiento y estudio con el fin de mejorar la inmunidad y bloquear de manera satisfactoria el virus. Es por ello que la caracterización de la estructura viral y la identificación de los mecanismos de acción de los antivirales recién sintetizados son cruciales para desarrollar tratamientos rápidos y potentes.

Los virus se han estudiado en profundidad con técnicas bioquímicas como ELISA, Western blots, PCR y ensayos de hemaglutinación para comprender la composición de las proteínas y la afinidad por los antivirales y las células diana[3-7]. Sin embargo, estas técnicas miden un gran número de partículas virales al mismo tiempo, lo que implica una falta de comprensión de las distribución de las proteínas de manera individual[8,9]. La microscopía de fluorescencia contribuye a llenar este vacío al estudiar la estructura y función de los virus en el espacio y el tiempo[10,11]. Sin embargo, debido al pequeño tamaño de los virus, generalmente menor de 200 nm, las técnicas de fluorescencia convencionales carecen de la resolución necesaria para distinguir estructuras virales de manera individual[12].

En este contexto, la microscopía de súper-resolución se ha posicionado en la última década como una técnica muy potente para caracterizar estructuras virales logrando resoluciones de hasta 10 nm[13-17]. Una de las familias de microscopía de súper-resolución, denominada “single-molecule localization microscopy” (SMLM) o microscopía de localización de molécula única, permite realizar imágenes con múltiples colores y caracterizando la distribución espacial de dos o más

proteínas del virus a lo largo de la partícula viral[18,19]. Además permite cuantificar la cantidad de proteínas marcadas debido a su capacidad de reconstruir imágenes de súper-resolución "molécula a molécula". Esto abre la posibilidad de medir la cantidad de proteínas agrupadas en ciertas áreas de la partícula viral y la membrana celular infectada y estudiar cómo cambia con el tiempo[14]. Podemos encontrar dos tipos de SMLM: dSTORM[20] y DNA-PAINT[21,22]. Ambas son técnicas de súper-resolución SMLM que nos permitirían alcanzar la nano-escala y estudiar diferentes características de influenza a nivel de proteína y de partícula.

Por lo tanto, con el fin de obtener una mejor comprensión de las estructuras virales y el proceso de infección por influenza, con el fin de desarrollar mejores vacunas y medicamentos, hemos optimizado y aplicado los dos tipos de SMLM previamente comentados (dSTORM y DNA-PAINT) para estudiar las estructuras virales en la nano-escala.

En primer lugar, utilizando imágenes dSTORM pudimos caracterizar la morfología de los filamentos de la cepa de influenza A/Udorn/72 y sus diferentes características, como los cuerpos de Archetti y la distribución de los filamentos[23,24]. Además, pudimos estudiar cómo los anticuerpos monoclonales (MAb) específicos contra la proteína M2e mediaron la inhibición de la formación de filamentos, descubriendo que los MAbs interferían en la formación de los filamentos producidos a partir de las células infectada por el virus. Gracias a la resolución obtenida, pudimos medir detalles estructurales como el ancho, el largo y la relación de aspecto de los filamentos, confirmando que los filamentos afectados por MAbs resultaron ser más cortos y más anchos en comparación con los no tratados. En general, nuestros datos pudieron determinar que la proteína M2 juega un papel crucial en la formación de filamentos y que su bloqueo condujo a una disminución de la infectividad del virus.

También se optimizó e implementó la nanoscopía DNA-PAINT en el estudio de la distribución y cuantificación de proteínas en la nano-escala. Para ello validamos este método utilizando nanopartículas comerciales, para así poder implementar estos análisis en el estudio de la expresión de proteínas recombinantes de influenza y las correspondientes "partículas virales vacías" (virus-like particles VLP) producidas a partir de estas. Ambas estructuras constituyen el nuevo paradigma de fabricación de vacunas, por lo que la caracterización de cómo se producen las proteínas recombinantes y la distribución de estas podría ayudar a mejorar de manera eficiente esta tecnología. Primero, al estudiar la expresión proteica sobre la membrana de las células transfectadas, demostramos que las proteínas recombinantes se producían de forma heterogénea dentro de la población de células, revelando que las tres proteínas estaban

organizadas en pequeños grupos a lo largo de la membrana que co-localizan con el tiempo. Sucesivamente, caracterizamos la distribución de las proteínas los VLP partícula a partícula, mostrando una mayor expresión de HA en comparación con NA y M2, mientras que muestra una leve heterogeneidad inter- e intra-partícula. Esta caracterización a nivel molecular demostró que DNA-PAINT es una herramienta poderosa para estudiar y describir nuevos sistemas de producción de vacunas, monitoreando la expresión recombinante de proteínas en las células y la liberación de partículas virales para mejorar el desarrollo de vacunas recombinantes.

Por último, seguimos demostrando el potencial del uso de dSTORM para identificar antivirales y la presencia de diferentes virus en otras preparaciones. Para ello estudiamos otras estructuras virales y antivirales como la presencia de la Hepatitis B y Hepatitis Delta en tejidos de parafina de pacientes, la interacción de análogos de ácido siálico sobre cuatro cepas de influenza y la monitorización de la captación de nanovacunas por células presentadoras de antígeno del sistema inmunitario, obteniendo información detallada y única de cómo estos virus y antivirales interactúan, con el objetivo de poder implementar estos estudios en la producción inteligente de antivirales y vacunas.

En general, SMLM ha demostrado ser una aproximación ideal para caracterizar virus y sistemas antivirales, ajustándose perfectamente a los requisitos para nuevos estudios virales y desarrollo de antivirales. En resumen, mediante el uso de la microscopía de súper-resolución se pudo caracterizar la distribución de proteínas clave de la gripe y del virus de la hepatitis, su maduración y su interacción con anticuerpos monoclonales, antivirales y células, resolviendo modelos imposibles de resolver con microscopía convencional y demostrando lo potente y esencial que es la microscopía de súper-resolución en el estudio de vacunas y antivirales.

Referencias

1. Webster, R. G. & Govorkova, E. A. Continuing challenges in influenza. *Ann. N. Y. Acad. Sci.* **1323**, 115–139 (2014).

2. Monto, A. S. & Webster, R. G. Influenza pandemics: History and lessons learned. in *Textbook of Influenza* 20–34 (John Wiley & Sons, Ltd, 2013). doi:10.1002/9781118636817.ch2.

3. Wu, C.-Y. *et al.* Mammalian Expression of Virus-Like Particles for Advanced Mimicry of Authentic Influenza Virus. *PLoS ONE* **5**, e9784 (2010).

4. Shaw, M. L., Stone, K. L., Colangelo, C. M., Gulcicek, E. E. & Palese, P. Cellular Proteins in Influenza Virus Particles. *PLOS Pathogens* **4**, e1000085 (2008).

5. Vajda, J., Weber, D., Brekel, D., Hundt, B. & Müller, E. Size distribution analysis of influenza virus particles using size exclusion chromatography. *J Chromatogr A* **1465**, 117–125 (2016).

6. Ustinov, N. B., Zavyalova, E. G., Smirnova, I. G. & Kopylov, A. M. The Power and Limitations of Influenza Virus Hemagglutinin Assays. *Biochemistry Mosc.* **82**, 1234–1248 (2017).

7. Rumlová, M. & Ruml, T. In vitro methods for testing antiviral drugs. *Biotechnol Adv* **36**, 557–576 (2018).

8. Payne, S. Methods to Study Viruses. *Viruses* 37–52 (2017) doi:10.1016/B978-0-12-803109-4.00004-0.

9. Guliy, O. I., Zaitsev, B. D., Larionova, O. S. & Borodina, I. A. Virus Detection Methods and Biosensor Technologies. *BIOPHYSICS* **64**, 890–897 (2019).

10. Nathan, L. & Daniel, S. Single Virion Tracking Microscopy for the Study of Virus Entry Processes in Live Cells and Biomimetic Platforms. *Physical Virology* **1215**, 13–43 (2019).

11. Carravilla, P., Nieva, J. L. & Eggeling, C. Fluorescence Microscopy of the HIV-1 Envelope. *Viruses* **12**, (2020).

12. Kiss, B. *et al.* Single-particle virology. *Biophys Rev* **12**, 1141–1154 (2020).

13. Gwosch, K. C. *et al.* MINFLUX nanoscopy delivers 3D multicolor nanometer resolution in cells. *Nature Methods* **17**, 217–224 (2020).

14. Gunzenhäuser, J., Olivier, N., Pengo, T. & Manley, S. Quantitative Super-Resolution Imaging Reveals Protein Stoichiometry and Nanoscale Morphology of Assembling HIV-Gag Virions. *Nano Lett.* **12**, 4705–4710 (2012).

15. Grove, J. Super-Resolution Microscopy: A Virus' Eye View of the Cell. *Viruses* **6**, 1365–1378 (2014).

16. Pereira, C. F., Rossy, J., Owen, D. M., Mak, J. & Gaus, K. HIV taken by STORM: Super-resolution fluorescence microscopy of a viral infection. *Virol J* **9**, 84 (2012).

17. Chojnacki, J. & Eggeling, C. Super-resolution fluorescence microscopy studies of human

immunodeficiency virus. *Retrovirology* **15**, (2018).

18. Lehmann, M. *et al.* Quantitative Multicolor Super-Resolution Microscopy Reveals Tetherin HIV-1 Interaction. *PLoS Pathog* **7**, (2011).

19. Lehmann, M., Lichtner, G., Klenz, H. & Schmoranzer, J. Novel organic dyes for multicolor localization-based super-resolution microscopy. *J Biophotonics* **9**, 161–170 (2016).

20. Rust, M. J., Bates, M. & Zhuang, X. Sub-diffraction-limit imaging by stochastic optical reconstruction microscopy (STORM). *Nat Meth* **3**, 793–796 (2006).

21. Jungmann, R. *et al.* Multiplexed 3D cellular super-resolution imaging with DNA-PAINT and Exchange-PAINT. *Nature Methods* **11**, 313–318 (2014).

22. Schnitzbauer, J., Strauss, M. T., Schlichthaerle, T., Schueder, F. & Jungmann, R. Super-resolution microscopy with DNA-PAINT. *Nat. Protocols* **12**, 1198–1228 (2017).

23. Archetti, I. Appearances associated with filamentous forms of influenza viruses. *Arch Gesamte Virusforsch* **6**, 29–35 (1955).

24. Vijayakrishnan, S. *et al.* Cryotomography of Budding Influenza A Virus Reveals Filaments with Diverse Morphologies that Mostly Do Not Bear a Genome at Their Distal End. *PLOS Pathogens* **9**, e1003413 (2013).

“Don't just give up,

Life is about getting knocked down over and over, but still getting up each time.

If you keep getting up, you win.”

Ai Yazawa, Nana

Chapter 1: Introduction: "Towards a super-resolution microscopy characterization of influenza: from antivirals to recombinant vaccines"

This chapter contains part of the submitted and accepted review: Towards a quantitative single particle characterization by super resolution microscopy: from virus structures to antivirals design. Arista-Romero M., Pujals S. and Albertazzi L. (2021). Frontiers in Bioengineering and Biotechnology.

As the author of this review I organized and summarized all the literature found regarding super-resolution studies of viral structures with super-resolution microscopy and single-particle techniques, as well as select and create the figures and the whole structure of the review.
The manuscript was written also in collaboration with my supervisors S. Pujals and L. Albertazzi.

1.1 Influenza virus

Viruses are even present risks against all types of animals, including human beings. One of the viruses that most infections produces every winter season is influenza virus, and ancestral disease that generates respiratory infection in mammals and domestic poultry and generally emerges from zoological reservoirs like birds and bats[1]. The effects of influenza in our society is remarkable, being the cause of at least 5 pandemics between the XX century and the XXI century, causing more than 60 million deaths[2] and creating the need of seasonal yearly vaccination for susceptible population.

From the four types of influenza virus (A, B, C and D), influenza A is the only one that causes pandemics and epidemics almost every year[3]. The symptoms of influenza disease can vary from mild fever, cough, sore throat, headaches and stomach problems to more severe complications such as pneumonia, multi-organ failure, encephalitis or myocarditis[4,5]. The Center for Disease Control and Prevention (CDC) from U.S. estimated than every season, only in the U.S., up to 45 million people are affected by influenza, between 140,000 and 810,000 are hospitalized and deaths oscillate between 12,000 and 61,000[6]. Further, according to the World Health Organization (WHO), seasonal influenza may result in approximately between 290,000 to 650,000 deaths worldwide yearly[7,8]. Apart from the seasonal epidemics of the virus, influenza

has the strong capability to create deadly pandemics that can spread strongly among the worldwide population. An example is found in 2009, where the influenza strain Pdm09 infected almost 15% of the total population of the world within only 18 months with an estimated 283,000 deaths due to respiratory and cardiovascular failure[9,10].

The lack of a universal vaccine against the virus and the potential ability to create pandemics, impossible to control by current available antivirals, increased the interest to develop new tools to analyse influenza treatments and new target structures, which can open the pathway to discovery the future universal vaccine against all strains of influenza.

1.1.1 Influenza A biology

Influenza A viruses (IAV) belong to the family of *Orthomyxoviridae* and are enveloped viruses with 8 segments of negative-stranded RNA[11]. All the RNA segments synthesize in total 11 proteins that comprise the final virus structure and allow the life cycle of it (Figure 1.1). Three of these proteins are transmembrane proteins that are inserted on the outside of the lipid membrane of the envelope: hemagglutinin (HA), neuraminidase (NA) and ion channel matrix protein 2 (M2); further, underneath the membrane we can also find the matrix protein 1 (M1)[12]. This lipid membrane is obtained from the cell membrane of the host cell, containing both cholesterol-enriched lipid rafts and non-lipid rafts. HA and NA are anchored to the lipid rafts while M2 is not tightly associated with this region[13].

HA, NA and M2 are the three proteins involved in the infectivity of the virus and are key elements in the infection and release of new influenza virus.

HA is the major protein of the envelope (~80% of the total protein of IAV) consisting in a homotrimeric glycoprotein receptor in form of spikes that recognize sialic acid (SA) and allows the adhesion with host cells. Each subunit of the homotrimers contains two polypeptide chains with different important roles: HA1 binds to the receptor sites and HA2 contains the fusion peptide[14].

The second most present protein is NA (~17% of the total protein), a glycoside hydrolase enzyme forming tetrameric spikes, with the role of cleaving surfaces receptors and allowing the virus to reach the target in lungs[15], and lastly, we find the protein M2 (16-20 molecules/virion), a tetramer proton selective ion channel with a critical role in disassembly and bud release[16].

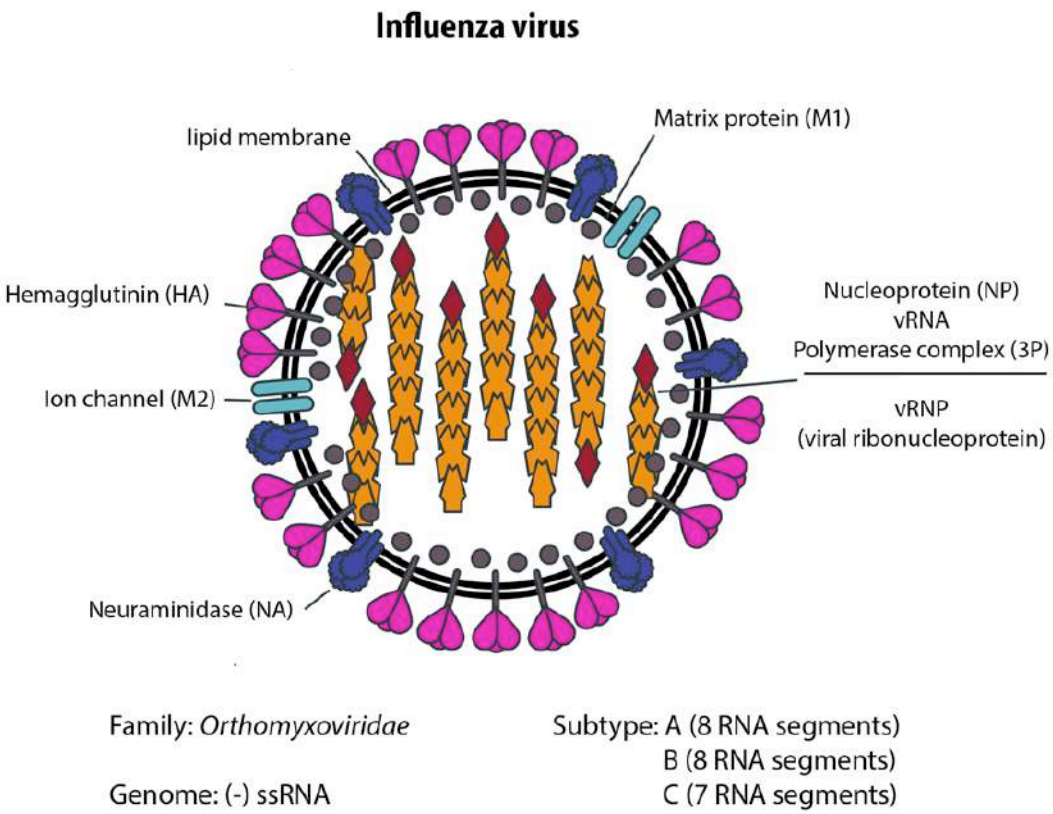

Figure 1.1: Influenza virus morphology. Influenza particle consists of a bilipid membrane with 3 transmembrane proteins (Hemagglutinin (HA), neuraminidase (NA) and Ion channel (M2)). Inside the viral particle, 8 segments of RNA are protected by ribonucleoproteins (vRNP) consisted in nucleoprotein (NP) and polymerase complex (3P complex). The vRNP interacts on the inside strongly with the matrix protein (M1).

Underneath the membrane, we can find the matrix protein M1, a lipid-binding protein that has essential roles in the uncoating/disassembly, nuclear import and export of the ribonucleoproteins (vRNP), transport, assembly and budding of the virus. M1 interacts internally with the cytoplasmic tails of M2, HA and NA and the rest of the cytoplasmic proteins inside the viral particle, specially the viral vRNP[11,17]. Lastly, the viral core consist in the genetic material RNA bonded to the vRNP along with small amounts of the nuclear export protein (NEP) and the polymerases complex (3P: PB1, PB2, PA).

The classification of IAV depends on the subtype of the proteins HA and NA, since they suffer several antigenic modifications, with 18 HA and 11 NA subtypes identified so far[18]. By combining them, it can be found up to 198 different subtypes of IAV where H1N1 and H3N2 are the most commonly found in humans.

1.1.1.1. Influenza life cycle

Unlike most common RNA viruses, IAV replicates in the nucleus, so the virus has to overcome several barriers during the infection to reach the nucleus with all the fragments of RNA intact in order to replicate properly[19]. In general, the infection cycle can be divided into seven steps (Figure 1.2): a) adhesion of virus particles to the cell, b) endocytosis and endosomal trafficking to the nucleus, c) fusion of endosomal membranes and uncoating d) importing the viral genome into the nucleus and expression of proteins and RNA, e) transportation of newly synthesized proteins and RNA to the membrane and assembly, f) budding of the new virus and g) release by cleavage of sialic acid.

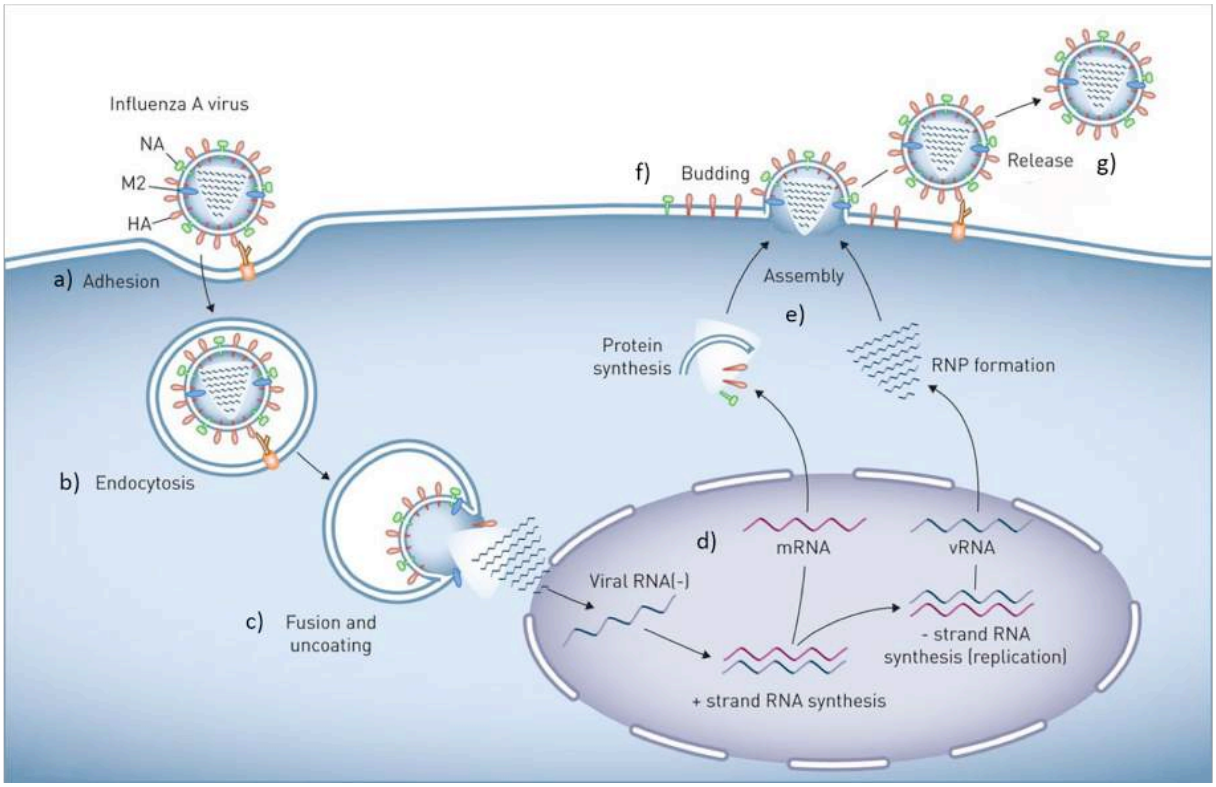

Figure 1.2: Replication of influenza A virus. Binding of hemagglutinin (HA) with sialic acid (a) triggers the endocytosis of the IAV (b). A change in the pH allows the interaction between the lipid membrane of the IAV and the endosome producing a fusion of membranes (c), uncoating the virus and letting the RNA to release to the cytoplasm safely. This RNA will go to the nucleus to be express and replicated (d). The newly synthesize proteins and genetic material will be assembly on the membrane of the host cell (e) and released by budding (f). NA cleavages the interactions between HA and sialic acid, in order to produce a fully active virus (g). Modified from reference [20]

The viral journey starts with the protein HA binding to host cells through a specific interaction against sialic acid (SA) receptors, which are localized in the membrane and are attached to the galactose of the glycans on the cell surface by α2–6 or α2–3 linkages. This interaction is specific enough to be able to discriminate between sugars and strains of IAV; while swine and human influenza preferentially bind to terminal SA residues in an α2–6 linkage (SAα2,6Gal), avian influenza binds specificity to terminal SA residues in an α2–3 linkage (SAα2,3Gal)[21,22].

Upon the attachment to the receptors of the host cells, IAV internalizes in the cell by receptor-mediated endocytosis, clathrin and not clathrin-mediated[19,23]. The endosomes evolve from early endosomes to late endosomes while the endosomes are transported to the perinuclear region by an actin dependent transport[24,25]. During this maturation process of the endosomes, the pH inside the endosome drops from 6.8 to 4.8 triggering the fusion process by the conformational change of the protein HA (HA2 chain) that starts exposing the fusion peptide[11]. This peptide can enter inside the endosomal membrane layer[26], helping the fusion of both membranes and releasing the whole content of the viral core into the cytoplasm (Figure 1.2.c). At the same time, in acidic state M2 opens the ion channel and starts acidifying the interior of the virion. This acidification dissociates the interaction of M1 with the membrane and thus the interaction between the vRNP and M1, allowing the complex of vRNP to be released inside the cytoplasm[27]. Once vRNPs are released, the whole complex is transported into the nucleus through the nuclear pore complex for transcription and replication of the genetic material (Figure 1.2.d).

In the nucleus, the polymerase 3P complex uses the negative sense RNA to produce mRNA and viral RNA (vRNA). The mRNA goes to the cytoplasm to be translated into proteins while the new vRNA is repack with the vRNPs in the cytoplasm as well[17]. Newly synthesized viral proteins and vRNP are transported to the budding site in the membrane using a well-organized interconnected network of transport proteins (Figure 1.2.e), where beta actin microfilaments are involved[27] (Figure 1.3).

The assembly and budding process of new viruses requires all three viral components of the membrane (HA, NA and M2) as well as M1 and the vRNPs[11](Figure 1.3). HA and NA concentrate mainly in the lipid rafts areas of the membrane, while M2 is localized in the non-lipid rafts areas[16]. All the assembly of the virus happens in this process, where M1 interacts inside the membrane with the vRNP and the budding process starts.

During this budding, the membrane bends due to the curvature of the membrane produced by HA[28,29] and all the components accumulate around this area. The closure of the neck of the bud is done by M2 mainly, since it facilitates the cleavage by bringing together the flexible lipids in non-lipid rafts in the neck of the bud[16,30] (Figure 1.3A arrows).

The produced viruses are not completely released yet (Figure 1.2.g). HA is linked to the plasma membrane by the interaction HA/SA, so for the fully release of the virions this interaction must be cut by the action of the NA. This cleavage releases the newly produced viruses, fully active and able to infect other cells[28,31].

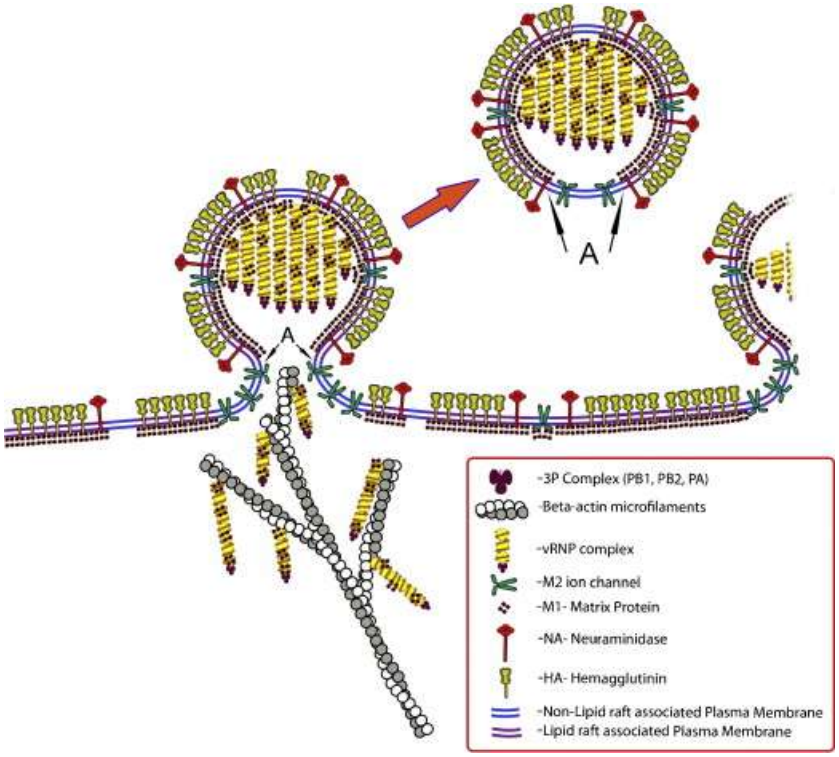

Figure 1.3: Schematic illustration of the budding and pinching process of IAV on the host membrane after the replication and the translation of all the proteins and genetic material. The three transmembrane proteins are inserted in the host membrane (HA, NA and M2) on the outside of the cell, while M1 interacts on the other side of the membrane with the vRNP in lipid rafts. The protein M2 (A and arrows) plays an important role in the pinching process in order to close the virion in the non-lipid raft region. Reproduced from reference [16] Copyright © 2009 Elsevier B.V.

1.1.1.2 Influenza morphology

The morphology of influenza A virus is determined by the main proteins HA, NA, M1 and M2 during the budding process[16,28]. This implies that influenza viruses are highly pleomorphic and the shape and size of the virus depends on the strain of influenza and the differential features of their proteins as well as the nature of the host cell[32].

The general shape is spherical or elliptical with an average diameter of 120 nm but ranging from 80-170 nm. The aspect ratio (ratio major/minor axis) is usually between 1:2 to 1:4 but bigger or smaller ratios can be found as well[11](Figure 1.4 A). Some strains, like A/Udorn/72 (H3N2), feature filaments and elongated virions than grown from the membrane of the cells and do not detach, reaching up to 20 μm in length (Figure 1.4 B)[33-35].

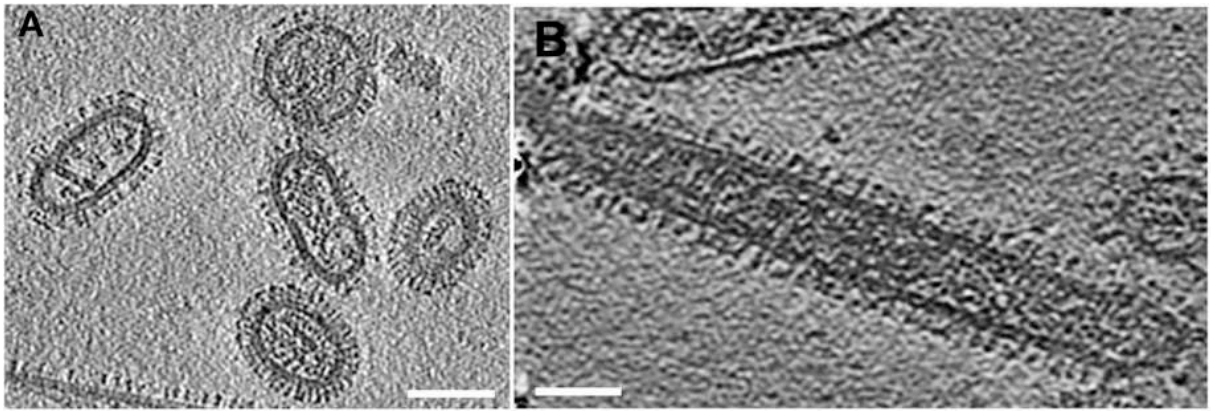

Figure 1.4: Cry-electron tomography of 2009 H1N1 pandemic influenza virus. Tomographic slices (around 5 nm thick) show the heterogeneity of the viral structures. A) Spherically and elongated shaped influenza virions. B) Long filamentous virion. Scale bar 100 nm. Adapted from reference [36]. Copyright © 2006 National Academy of Sciences.

Other factors determine the final shape and size of the virus such as the polarity of the epithelial cells, the lipid that conforms the host cell or the most important, if the strain is laboratory adapted or comes from fresh virus isolated from an animal and never grown i*n vitro*[16,37]. Furthermore the morphology of influenza strains can vary strongly depending on how the virus is grown and in which cells are grown. What all authors agree is that IAV never has the same shape and their physical structure can vary strongly between strains and inside the same population[38].

1.1.2 Common treatments against influenza

The annual influenza epidemic causes important mortality, especially in elderly population or patients with other pathologies[39]. The first approach to avoid the spread of IAV is vaccination, however, due to the antigenic drift of IAV, every year the strain that have prevalence during the sickness season (September-January) is slightly different from the season before[40]. The new strain is different enough to not be recognized from the immune system of vaccinated patients, losing the immunity memory of the population.

Since the production of a new yearly vaccine is quite time-consuming, the development of universal and broad-spectrum prophylactic and therapeutic antivirals is necessary to effectively stop the spread in the first stages of the epidemic[41]. All together, we can find 3 main strategies to fight against IAV:

-Small molecules and analogues
-Monoclonal antibodies
-Vaccines

1.1.2.1 Small molecules and analogues

Currently we can find broad-spectrum antiviral drugs that are effective against multiple strains of influenza but with limitations[42]. Historically, the two main targets are M2 ion channel and neuraminidase NA:

-M2 inhibitors: M2 was the first target for developing antivirals with two "first generation" drugs against influenza in the market: amantadine (Symmetrel; Endo Pharmaceuticals) and rimantadine (Flumadine, Forest Pharmaceuticals)[42], both derivative from adamantane (Figure 1.5 A). The main structure of both consist in an amine that can intercalate in the ion channel M2[43], avoiding the acidification of the inside of the virion during the fusion and uncoating step (Figure 1.2.c). This blockage results in an unsuccessful release of the vRNP into the cytoplasm of the host cell, avoiding the replication and translation of the RNA.

Even thought they have been employed since 1976, their used is not longer recommended in clinical use for patients, since can produce side effects on the central nervous system (amantadine is used as Parkinson's disease treatment) and also rapidly emerged drug-resistant virus variants[44].

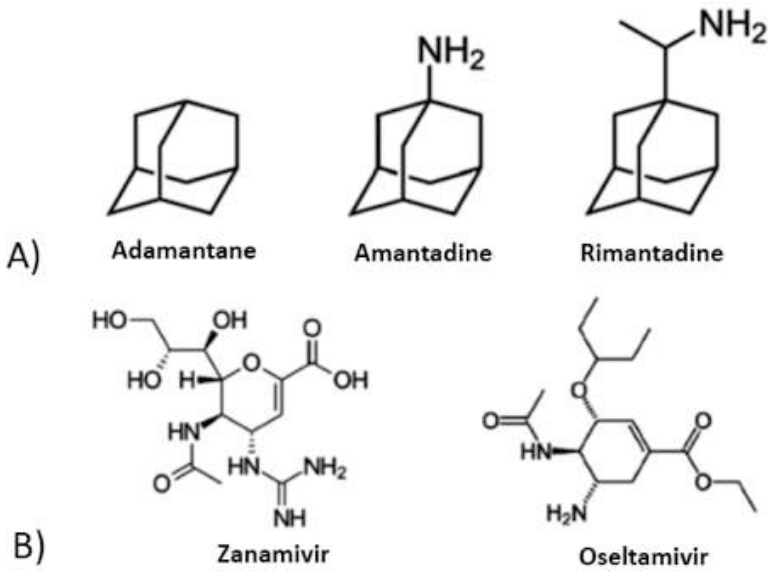

Figure 1.5: A) Adamantane and its amine derivatives amantadine and rimantadine. B) Viral neuraminidase inhibitors: zanamivir and seltamivir. Reproduced from reference [42]. Copyright ©2014 ACTA ABP.

-NA inhibitors: second generation of antivirals that block the neuraminidase activity at the end of the replication cycle of IAV, avoiding the cut of the sialic acid bound to HA. Hence, the viruses produced will not be released and will not be able to infect new cells (Figure 1.2.g)[42]. A strong advantage of this second generation is that the structure of the protein NA between the influenza A and B is highly conserved, also within all the subtypes of influenza[45], displaying a broad spectrum activity.

The two main drugs found in the market are Zanamivir (Relenza, GlaxoSmithKline) and Oseltamivir (Tamiflu, Roche) (Figure 1.5 B), both synthetic analogues of sialic acid (SA) that compete with the natural ligand in the active site of NA, interacting and blocking the activity of the enzyme. Even though the promising broad activity spectrum of NA inhibitors, resistant mutants arose as a consequence of the well know drug-induced selective pressure[46].

-HA inhibitors: new approaches for developing antiviral drugs are focusing on conserved features of the infection of influenza, such as the interaction between SA and HA, essential for the entrance of the virus onto the host cell, thus will have less possibilities to mutate for resistances, since this interaction must be conserved.

These new analogues of SA are being developed to compete with SA for the binding to HA, in order to avoid the recognition of the virus to the host cell, and therefore avoiding the whole

infection from the beginning (Figure 1.2.a). Some strategies include the use of peptides blocking HA1 and HA2[47] or using small molecules bound to 6-sialyllactose[48], a SA analogue with stronger affinity towards HA that can attach to the virus receptors strongly.

Finally, other targets of interest for developing antivirals are drugs that inhibit the polymerase of influenza like Favipiravir (T-705, Toyama Chemical)[49] with again a broad action against influenza virus A, B and C.

-**Multivalency:** a new promising approach towards the development of more powerful antivirals consists in taking advantage of the multivalent binding of small antivirals. This system is based on multiple, simultaneous and strong but reversible binding of *m*-valent ligands and *n*-valent receptors (where $m,n > 1$)[50]. The main idea is using multivalent inhibitors instead of individual small antivirals (Figure 1.6) to not only bind and block the receptors of influenza but also to inhibit completely the pathogen adhesion to the cell surface. Small analogues of sialic acid or blockers of NA could be combined in the same structure creating a shield that could surround the virus.

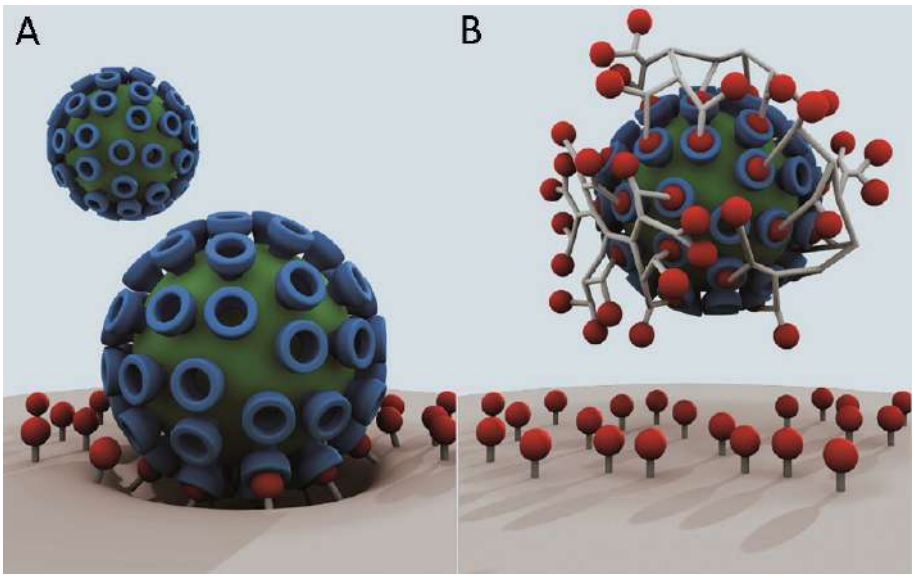

Figure 1.6: Models of interactions between virus (green) and antivirals (red). A) No inhibition. Normal binding between the virus and the receptors displayed on host cells. B) Multivalent inhibition. Blockage of the interaction between the virus and the receptors. Modified from reference [50].Copyright ©2016 Bhatia, American Chemical Society.

Lauster D. et al. used this approach to develop a multivalent peptide-nanoparticle in order to inhibit IAV[51]. Using a biocompatible polyglycerol (PG)-based dendritic scaffold covalent conjugated to peptides analogues to SA, they could block 90% of IAV infection *in vitro* in nanomolar concentrations. Papp I. et al did a similar approach in 2011 where they used polyglycerol-based nanoparticles conjugated to SA to block up to 80% of the infection of IAV *in vitro*[52].

1.1.2.2 Monoclonal antibodies

An important tactic to avoid influenza infection implies the use of external monoclonal antibodies in order to produce a passive immunization[53]. This therapy can be used alone for the treatment of drug resistant influenza infection or in combination with other antivirals in severe infections, specially for at-risk population such as immunocompromised[54,55].

This passive immunotherapy requires antibodies that matches perfectly the targets and are able to block either the virus or the spread of the infection. This is the reason why is desirable the identification and design of antibodies that can bind with high affinity and neutralize several strains at the same time. These antibodies are commonly design against external parts of the proteins HA, M2 and NA and would block the infection of IAV by binding strongly to the proteins of influenza, thus blocking their activity (Figure 1.7)[22].

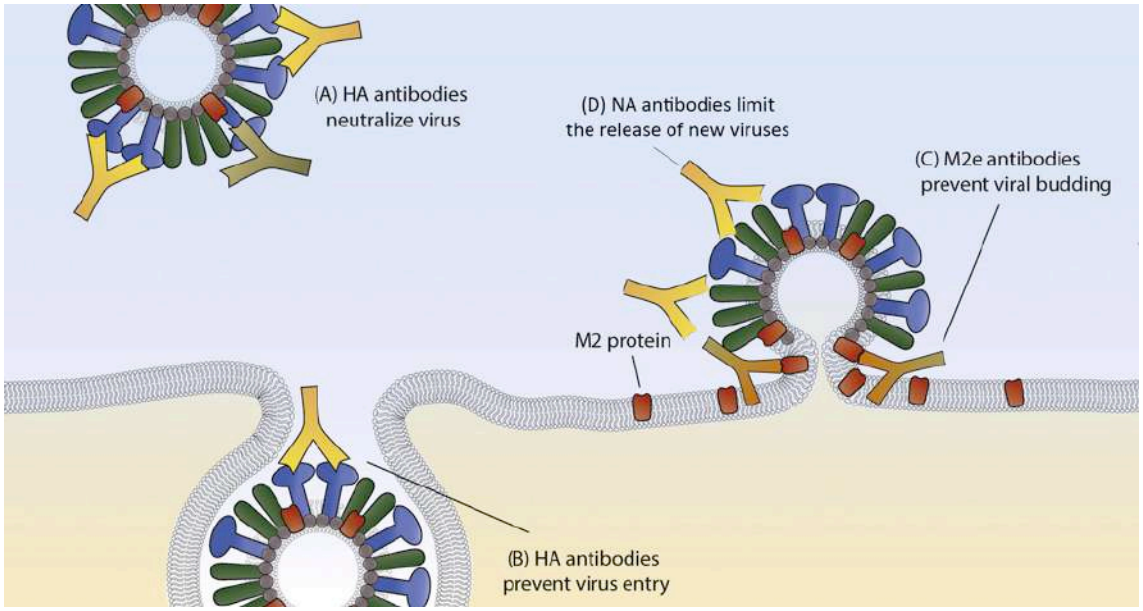

Figure 1.7: The effect of different monoclonal antibodies against HA, NA and M2 on the infection cycle of IAV. A) Antibodies against HA block the attachment of the virus to the host cell and B) HA antibodies prevent the virus entry

blocking the fusion peptide. C) Antibodies against the external domain of M2 interfere with virus budding and also block the ion channel avoiding the fusion of the virus with the endosome. D) Antibodies against NA do not prevent infection but limit the release of virus from infected cells. Modified from reference [56]. Copyright © 2015 Soema, Elsevier B.V.

-**Anti-HA:** one of the most promising targets for the development of influenza antibodies are antibodies anti-HA, since seventeen subtypes of HA share between 40% to 60% of amino acid sequence[57], thus broad spectrum antibodies could be design. Following a similar approach as the HA inhibitors, by blocking HA at the beginning of the infection, the virus will not be able recognize SA and thus will not bind and enter host cells (Figure 1.7A,B), avoiding the infection completely.

The first high spectrum anti-HA antibody against influenza was developed in the 90's by Okuno Y. et al., a monoclonal antibody that could neutralize in vitro and in vivo 5 subtypes of HA[58,59]. From this first discovery, several anti-HA antibodies have been developed with promising prospective (Table 1.1), some of them entering the phase II of clinical trials alone and in combination with Oseltamivir as a potential treatment for resistant patients[60], proving the potential use of passive immunotherapy using anti-HA antibodies.

Antibody	Target	Type of influenza	Development	Reference
CR9114	HA stem	Influenza B	Pre-clinical	61
CR6261	HA stem	Influenza A (6 subtypes)	Phase I	62,63
CR8020	HA stem	Influenza A (H3N2)	Phase I	64,65
MHAA4549A	HA stem	Influenza A (H3N2)	Phase II	66,60

Table 1.1: Recent discovery of broad-spectrum anti-HA antibodies that are under clinical studies for use in clinics[55].

-**Anti-M2:** the second candidate for developing therapeutic antibodies is M2, targeting the external part of the protein called M2e that is remarkably conserved and very small (24 amino acids)[67]. M2 protein is highly expressed on infected cells but is virtually absent on virions, so blocking M2e will not produce the neutralization of the virus but will avoid the release of new viruses, blocking the budding process in the membrane (Figure 1.7C)[57]. As expected, M2e antibodies that are in clinical trial phase I are not efficient neutralizing the particle of influenza but show significant therapeutic efficacy *in vivo*[68] .

-**Anti-NA:** in the same line than inhibitors of NA, anti-NA antibodies will not block the infection of influenza, but by inhibiting its enzymatic function will avoid the release of new viral particles (Figure 1.7D)[69]. The potential feature of these antibodies is the fact that NA has a lower rate of evolution compared to HA and its active site is highly conserved[70]. This is why several researches have highlighted the efficacy of antibodies against NA to block influenza disease like Doyle T. et al, who taking advantage of the universal conserved sequence of NA located between amino acids 222-230 developed an universal anti-NA monoclonal antibody that could block the infection of all 9 NA subtypes of IAV and both types of influenza B virus[71,72].

Although the monoclonal antibody treatment is very promising, the lack of genetic stability in influenza is still a problem to overcome, since the interaction antibody-target must be very tight and specific so the fast mutation of the virus can decrease the effectiveness of the immunotherapy.

1.1.2.3 Vaccines

Antivirals and monoclonal antibodies are very useful as first line treatment to avoid the spread of influenza, but the only way to obtain long and successful protection in the population is the immunity obtained from vaccines. The first vaccine against influenza was developed and approved in 1945[73]. It consisted on formalin inactivated virus grown in hen eggs and was proved to be 70% efficient in the protection against H1N1. From that first vaccine, a large diversity of influenza vaccines has been approved during the years and a whole system to produce them has been established, thanks to the new technology and methodology to test vaccine candidates[74-76].

The most used seasonal influenza vaccine is the trivalent vaccine, composed of the 3 circulating seasonal influenza virus strains: 2 IAV types (H3N2 and H1N1) and a B type[74]. For the development of these vaccines, researchers can work either with whole influenza viruses (WIV) or with fragments from the virus (Figure 1.8).

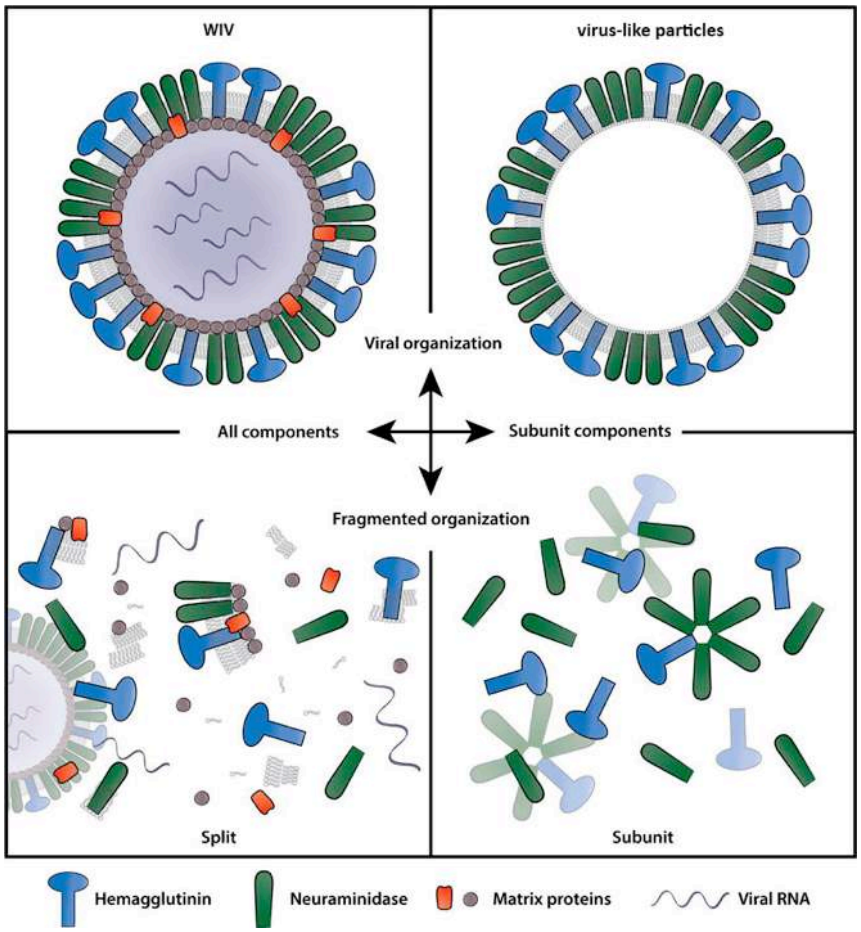

Figure 1.8: Types of vaccines produced from IAV. Modified from reference [56]. Copyright © 2015 Soema, Elsevier B.V.

-Whole influenza virus vaccine:

In case the vaccine consists on WIV, there are two variants of vaccines to work with: live attenuated or inactivated virus. In both cases the virus is grown in mammalian cells, generally in fertilized hen's eggs. After the incubation and amplification, the fluid containing virus is harvested from the eggs[77]. Attenuated vaccines use these viruses decreasing the virulence with mutations or chemicals and are administrated to the patients by the intranasal pathway, mimicking the natural route of the infection, thus producing a controlled immune response at the site of infection[56]. For inactivated influenza vaccines, these viruses are killed in order to avoid the interaction of the virus with the body. To keep them intact they are killed using heat or chemicals such as formaldehyde or formalin.

-Split or subunits vaccines:

Due to the side effects that WIV produces in some patients, currently the vaccine preparations focus on split or subunits of the virus (Figure 1.8). For this, after the inactivation of the virus,

the particle is disrupted using detergent treatments or diethyl ether[56]. In case of split vaccines, the preparation will contain all viral protein and rest of lipid membrane, while in subunit vaccines the proteins of influenza are purified and selected.

These two types of vaccines are currently the most common and widely used (Fluzone ®, Fluad, Agrippal CLS Limited® or Influvac Mylac®), although the production has some limitations. Influenza vaccines produced in allantoic fluids of eggs can generate allergies in persons with intolerance against egg proteins and also it shows some difficulties scaling up or even cross-contaminations[74]. To overcome these disadvantages, other platform of production are under study, but right know only one cell-based vaccine produced in MDCK cells is approved by FDA in EU and USA (Flucelvax, Segirus)[78].

-Recombinant and mRNA vaccines:

Currently the industry is starting to focus attention on other type of vaccines based on the expression of recombinant proteins[79,80]. Recombinant proteins can be produced in a safe environment with the DNA or mRNA of the virus but lacking the risks and the need of a laboratory with class II security and without the virus particle involve[81]. Also allows the production of a wider array of influenza protein antigens, which can induce broader immune responses that the ones obtained from split and subunits from WIV[82-84].

mRNA vaccines consist in the use of mRNA from a protein of the virus to induce the immunity. In this case, the mRNA covered by lipid membrane is administrated to the patient, so the recombinant proteins will be produced from the cells of the subject[85,83,86]. This is the approach followed by the new COVID-19 vaccines developed by Moderna, AstraZeca and Pzifer[87].

In other cases, recombinant proteins are produced and isolated prior the administration of the vaccine. They can be produced as isolated subunits (Figure 1.8), which comprise several subunits of proteins of influenza that can be combined in the final formulation or in form of empty virus called virus-like particles (VLP).

In the market we can already find examples of both types of vaccines: trivalent recombinant baculovirus-expressed vaccine Flublok®[88](Protein sciences, Sanofi Pasteur) and the first VLP vaccine sell in the world called CadiFlu-S, found in the Indian market by CPL Biologicals.

1.1.2.3.1 VLPs as vaccines

Virus-like particles (VLPs) are structures that mimic the viral particles without the genetic material[89-91]. They assemble spontaneously from recombinant viral proteins express on host cells due to the self-assembly capacity of the viral proteins to bud and release by themselves[92].

The production of VLPs is quite simple and very well establish. Depending on the properties, they can be produced in bacteria, yeast, insects, mammalian cells and cell-free systems[93]. Influenza VLPs are generally produced in mammalian and insect cells by transfection of DNA plasmids with the main 4 proteins of the influenza envelope (Figure 1.9). These proteins are express using the transcription and translation machinery of the host cell and they will be glycosylated by the Golgi before inserting into the host cell membrane, in a similar way normal infection produce viral proteins. In this case, the viral proteins on the membrane interact by self-assembly and produce the viral particle by budding, releasing a virus-like particle without any genetic material on it[94].

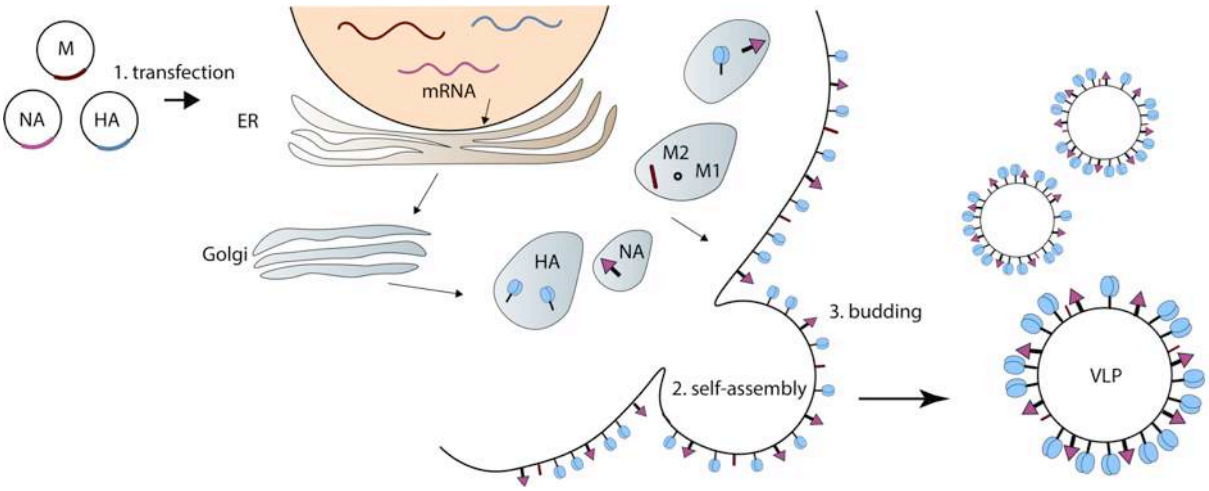

Figure 1.9: Scheme of influenza virus-like particle (VLP) expression using 4 proteins of influenza (HA-hemagglutinin, NA-neuraminidase, M-tandem of M1 and M2 ion channel). 1- Plasmids are introduced in the cell by transfection and they are translated intro proteins through the glycolisation in the Golgi. 2- The 4 proteins produced (HA, NA, M1 and M2) are inserted into the membrane and interact by self-assembly, producing the viral particle. 3- Thanks to the interaction of the 4 proteins, the VLP particle will be form by budding and released. The genetic material is not necessary for the budding and release process of the VLPs.

As commented before, influenza vaccine produced from embryonated hen eggs must be produced every year, so the development and production times are critical. The whole process of production generally takes several months and the resulting vaccine can be often obtained in

low yields[95]. VLP vaccines, on the contrary, are faster, safer, cheaper to produced and display several characteristics that made them perfect for vaccine usage[93,94]:

-Their multivalent nature

-Their capacity to bind to antigen presenting cells via HA-SA interaction[96]

-The display of the native HA and NA mimicking the surface of an infective influenza virus

-The lack of genetic material

Several studies have proved that Influenza VLPs containing NA, HA and M1 provided a broader immune response compared to whole inactivated IAV or recombinant HA alone[97,98], confirming the potential use of this recombinant structures in the development of vaccines. In fact, we are starting to see commercially available VLPs vaccines against influenza such as CadiFlu-S from CPL biological or promising phase II clinical trials like Novavax trivalent VLP vaccine and Medicago's plant-based VLPs MDG-2271[99-101].

Overall, vaccine production and antiviral development need to be in continuous growth and study to improve the immunity and fight against influenza disease, which is in continuous mutation within the year. New single-particle methods to study the effects of these treatments could help characterizing the antiviral effect, the immunity and the recombinant protein distribution at single-particle level to distinguish the best approach against influenza[102].

1.2 Nanostructural characterization of viruses

From the discovery of viruses by Dmitri Ivanowsky and Martinus Beijerinck in 1892 and 1898 respectively[103], viral characterization has become a key element to understand and fight viral infections and pandemics. Viruses have been intensely studied with biochemical techniques such as ELISA, Western blots, PCRs and hemagglutination assays to understand the protein composition and the affinity towards antivirals and target cells[90,104-107]. Nevertheless, these techniques measure of viral particles in bulk at the same time, leading to a lack of understanding of protein structures and the spatial distribution of the viral proteins of within the particle[108,109]. Microscopy contributes to fill this gap by studying structure and function of viruses in space and time. Fluorescence microscopy in particular allows visualization of multiple viral proteins thanks to its multicolour ability, and is in fact one of the main tools of modern virology [110,111]. However, due to the small size of viruses, usually smaller than 200 nm, conventional fluorescence techniques are lacking sufficient resolution power to resolve individual viral structures.

From the first image of a virus obtained in 1938 and 1939[112,113], electron microscopy (EM), transmission electron microscopy (TEM), scanning electron microscopy (SEM) and cryo-electron microscopy (cryo-EM)[11] have been the main microscopy techniques used to study and characterize viruses[114], virus-like particles[115], viral glycoproteins[116] and viral inhibitors[117,118] focusing mainly on the size distribution of the viral particles[91]. However, traditional morphological studies require the negative staining of the sample under extreme conditions. Due to the exposure of the sample to heavy metals, non-physiological pH, dehydration and sectioning, the shape and morphology of the virus particle can suffer modifications and artefacts, leading to irregular virus shapes and broken structures (Figure 1.10 C)[37,119-121]. These drawbacks were overcome by cryo-EM, a technique that fixes the sample by freezing. However, this is a quite delicate process that also could generate artifacts[122,34].

Additionally, studying the distribution of the proteins along the particle is quite complicated, only done using immunogold labelling that is also affected by the negative staining and thus cannot represent the whole distribution of all proteins at the same time (Figure 1.10 A-B)[123,104], since generally gold nanoparticles aggregates, not covering the whole virus surface[121].

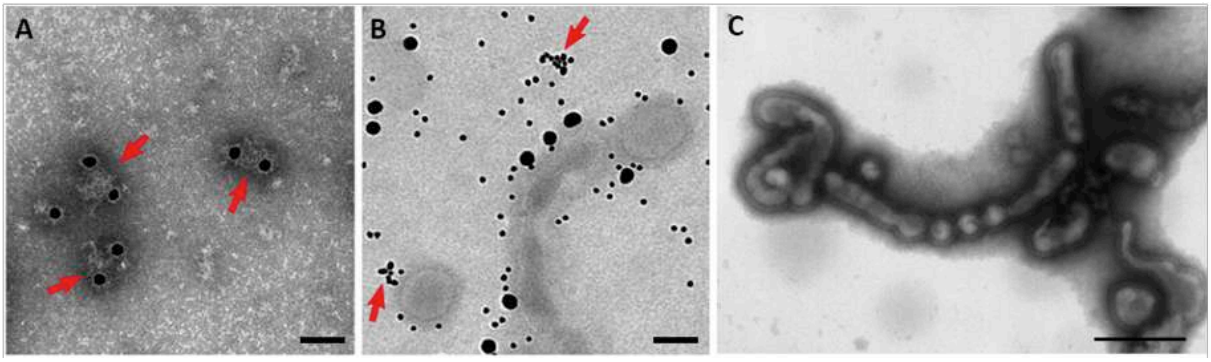

Figure 1.10: Artefacts and troubleshooting errors regarding the preparation of virus sample for electron microscopy (TEM) with or without immunogold labelling. A) Flublok influenza vaccine immunolabelled with 25 nm gold labels, too big to surround all the vaccine structure. B) Influenza H1N1 immunolabelled with 10 nm gold nanoparticles against HA. Red arrows show aggregates and background, also a not evenly distributed nanoparticles along the virus particle. Scale bar: 100 nm. C) Negative staining of H1N1 virions shows artefacts and irregular shapes not related to the virus. Scale bar: 200 nm. Modified from references [121] and [37]. Copyright © 2019 Gulati, John Wiley & Sons, Inc.; Copyright ©2012 Noda.

Despite the individual disadvantages of each technique, in general the main drawback of electron microscopy is the lack of multicolour characterization and specific labelling of all the proteins on the viral structure, information that can be obtained with fluorescence probes.

Related studies have been done using confocal microscopy focusing mainly on how infected cells respond to infections and antivirals[124-128], but since viruses are smaller than 200 nm, it is impossible to study the virus architecture using conventional fluorescence microscopes with immunostaining; this is why super-resolution microscopy techniques are needed to understand and quantify viral protein distribution and cell-virus interaction.

In the current thesis we are presenting a type of super-resolution microscopy technique that has the potential to surpass these limitations and break the diffraction limit to study viral structures at single-particle level called super-molecule localization microscopy (SMLM)

1.2.1 Super-resolution microscopy

As commented before, fluorescence microscopy is an important and well-used technique in all fields due to the versatility of the sample preparation and target labelling, however, there is a strong limitation in terms of resolution, since you cannot distinguish two structures closer than 250 nm due do the diffraction limit of the light, described in the 1873 by Abbe[129] and later by Rayleigh[130] (Figure 1.11).

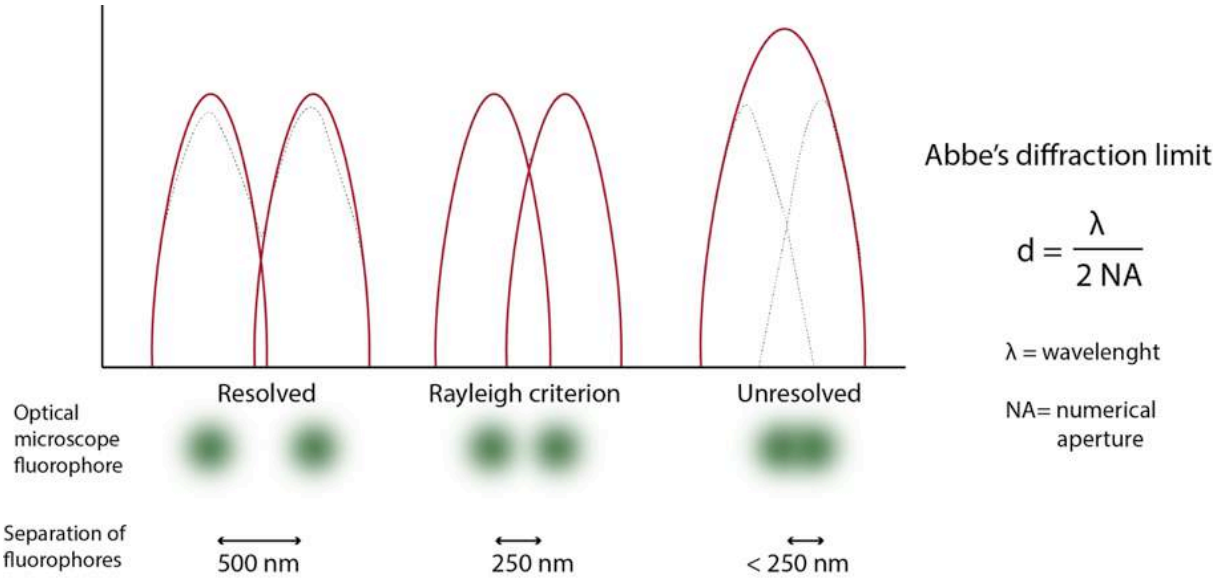

Figure 1.11: Abbe's diffraction limit and Rayleigh criterion. The minimum angular separation between two dyes (d ≈ 250 nm) is determined by the wavelength of the excitation light (λ) and the numerical aperture (NA) of the optical lenses, usually between 1.4-1.6. The Rayleigh criterion specifies the minimum separation between two light sources that may be resolved into distinct objects (>250 nm). Inspired by reference [131].

These restrictions handicap the study of virus interaction with host cells, antivirals and immune system as well as the protein distribution of the virions and vaccines. To overcome this limitation, super-resolution microscopy (SRM) has burst in the last years as a powerful technique to image in the nanoscale different types of cells and materials[132,133].

SRM is a family of different microscopic techniques that embrace the same goal: break the diffraction limit of the light, previously described, to achieve resolutions between 1 nm to 100 nm[134]. The whole family of SRM methods are based on different principles and instruments[135]. With these differential characteristics, three main types of SRM can be framed: stimulated emission depletion (STED)[136], structured illumination microscopy(SIM)[137] and single molecule localization microscopy (SMLM)[138,139]. The distinctive technical differences between the SRM techniques are explained in detail in several reviews previously published, which described intensively the strength and weakness of each microscopy[133,140,141].

Due to the higher spatial resolution and potential use in molecular quantification, we selected SMLM for the studies in the present thesis.

1.2.1.1 Single molecule localization microscopy

Single molecule localization microscopy (SMLM) allows the analysis of the spatial arrangements of molecules beyond the diffraction limit by the localization of fluorophores[142]. The enhanced of resolution depends on the sample preparation and dye selection, being usually around 10-20 nm lateral and 50 nm axial resolution[143,144].

For achieving this new resolution, SMLM would build up the final super-resolution image, literally molecule by molecule by detecting each fluorophore independently. Using a total internal reflection fluorescence microscope (TIRF) and a powerful laser the system can turn “off” the emission of fluorescence of most of the dyes, switching “on” some of them at once stochastically in multiple cycles of “on-off” (i.e. blinking) (Figure 1.12.A), making sure that the fluorophores on the “on state” are individually recognized and isolated. These single fluorophores would be localized by a Gaussian fitting and a post-process point spread function (PSF) in order to recognize their point of emission (Figure 1.12B red cross).

By recording the blinking emission of all fluorophores in a video and fitting a Gaussian on all dyes individually recognized, we are able to reconstruct a super-resolution image from a low-resolution sample (Figure 1.12.C)[145].

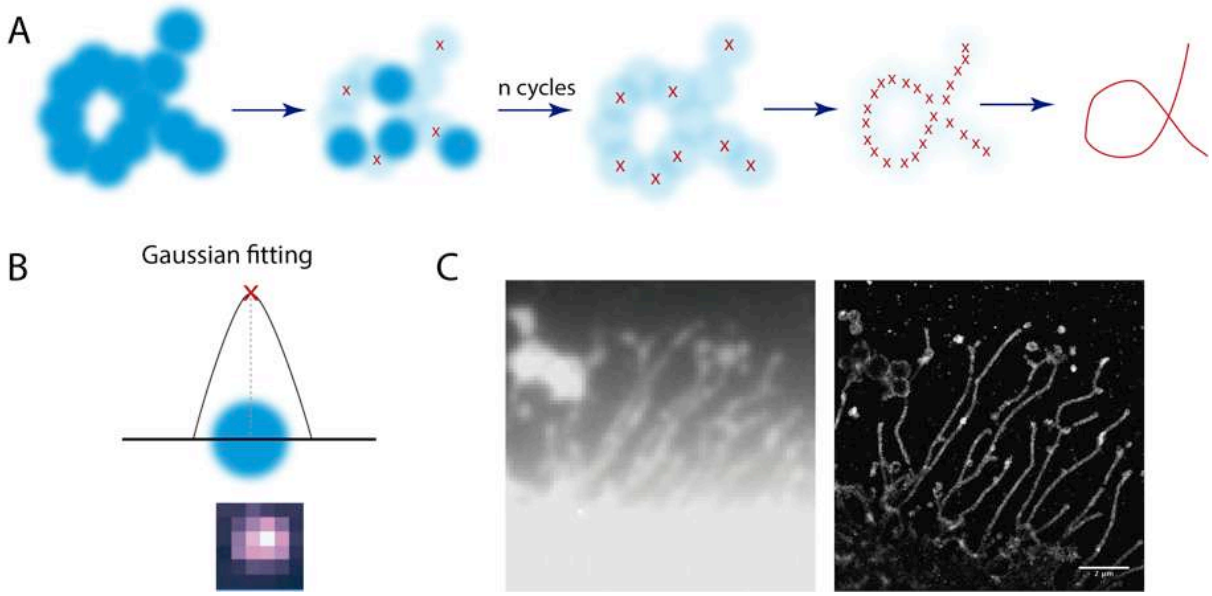

Figure 1.12: Principle of single molecule localization microscopy. A) In order to identify single fluorophores in the sample, dyes will overcome a switching cycle where they will be in a cycle of "on" and "off" called "blinking", where most of the dyes will be off while some of them stochastically will be "on" and able to be recognized alone. This process will last several cycles, recognizing the emitter in each cycle. B) To recognize the point of emission of the dye, the software would fit a Gaussian on each isolated dye in order to fit with accuracy the centre of the dye. C) Example of dSTORM image of a viral structure of influenza, next to a low-resolution image of the same structure.

There are several advantages of using SMLM and one of them is the ability to perform multicolour images, something impossible to achieve with the single-particle techniques previously explained. By multicolour acquisition it is possible to characterize the spatial distribution of 2 or more proteins of the virus among the viral particle[146,147]. Moreover, the main advantage feature of SMLM is the possibility to quantify the amount of labelled proteins that are in the analysed area, performing multicolour-quantifications at single particle level. This opens the possibility to measure the amount of proteins clustered in certain areas of the viral particle and infected cell membrane and how it changes with time, like the study performed by Gunzenhäuser et al. on HIV-1[148].

We can find two types of SMLM depending on how the system induces the dyes to start the cycle of blinking: direct stochastic optical reconstruction microscopy (dSTORM) and point accumulation imaging in nanoscale topography with DNA (DNA-PAINT).

1.2.1.2 dSTORM

Developed in 2006 by Rust M.J. et al.[138] dSTORM used photoswitchable dyes and a specific buffer based on glucose oxidase, catalase and mercaptoethylamine (MEA) that oxide-reduce the dye and induce photochemical reactions that would allow the fluorophore to be intermittently "on-off" for a limit of time, achieving resolutions of 20 nm.

The main advantages of using dSTORM is the sample preparation, since the dye selection can be easily found commercially either alone or in secondary antibodies, nonetheless there is a lack of multicolour imaging options, since few dyes can work together in dSTORM nor follows the same photoswitchable cycle[147]. To overcome that limitation we also focused on DNA-PAINT.

1.2.1.3 DNA-PAINT

Developed in 2014 by Jungmann R.[149,150], this novel SMLM is a variation of PAINT[151] and identifies the centre of each fluorophore by the transient and specific binding of two short sequences of DNA, one bound to the target and the other to a dye. This transient binding has a Kd that mimics the "on-off" cycle needed in SMLM to recognize the point of emission, thus the centre of the target.
With this approach, we can obtain long acquisition and multiplexed images by changing the DNA probe, achieving up to 124-colour images[152-154]. Furthermore, since the Kd keeps constant in all probes, the quantification of targets can be performed by quantitative points accumulation in nanoscale topography (qPAINT)[154] developed too by Jungmann R. in 2016, obtaining resolutions around 10 nm[155,149]. This technique had been successfully applied on nanostructures such as exosomes[156], membrane receptors[157] and cellular structures[158,159].

dSTORM and DNA-PAINT are very powerful techniques that can work *in vitro* samples[,133,132,150]. In fact, dSTORM has a wide path on the study of biological samples including several viruses like HIV[126,160-162]; for instance with STORM it had been studied the pathway of the virus HIV during it infection cycle, visualizing the matrix and the capsid proteins before and after the interaction with cells, confirming the size and cell interactions previously analysed with EM[146,163-166].

Influenza have been also studied with several SRM techniques, such as dSTORM[167], where it must be highlighted the work of Vahey M.D et al[15] that in 2019 studied the protein distribution of Influenza A virus with dSTORM, describing the tendency of NA to concentrate on the viral

poles when the virus is elongated, organizing in small clusters to optimize the mucus penetration in the lungs. Further, with a combination of several SRM techniques such as dSTORM and STED, Sieben et al. quantified and characterized the cluster distribution on the membrane of two of the factors involved in the virus-cell binding of IAV: attachment factors (AF) and epidermal growth factor receptor (EGFR)[168].

All in all, within the last decade SRM have been the protagonist of outstanding research in terms of viral structure characterization[160,165,169]. In this context, dSTORM and DNA-PAINT are super-resolution techniques that would allow us to reach the nanoscale and study different features of influenza at single-protein and single-particle level.

As commented before, antivirals and vaccine development is in continuous improvement and development due to the need of new approaches against viruses. We propose that with a better understanding of the viral structures and influenza infection processes, better vaccines and drugs can be developed with a rational design, in order to avoid new pandemics. Using super-resolution microscopy it could be possible to characterize the distribution of key proteins of different viruses, its maturation and their interaction with monoclonal antibodies, antivirals and cells, resolving models impossible to be resolved with conventional microscopy.

1.3 References

1. Webster, R. G. & Govorkova, E. A. Continuing challenges in influenza. *Ann. N. Y. Acad. Sci.* **1323**, 115–139 (2014).

2. Monto, A. S. & Webster, R. G. Influenza pandemics: History and lessons learned. in *Textbook of Influenza* 20–34 (John Wiley & Sons, Ltd, 2013). doi:10.1002/9781118636817.ch2.

3. CDC. Types of Influenza Viruses. *Centers for Disease Control and Prevention* https://www.cdc.gov/flu/about/viruses/types.htm (2019).

4. CDC. Flu Symptoms & Complications. *Centers for Disease Control and Prevention* https://www.cdc.gov/flu/symptoms/symptoms.htm (2019).

5. Carrat, F. *et al.* Time Lines of Infection and Disease in Human Influenza: A Review of Volunteer Challenge Studies. *Am. J. Epidemiol.* **167**, 775–785 (2008).

6. CDC. Burden of Influenza. *Centers for Disease Control and Prevention* https://www.cdc.gov/flu/about/burden/index.html (2020).

7. WHO | Burden of disease. *WHO* http://www.who.int/influenza/surveillance_monitoring/bod/en/.

8. Iuliano, A. D. *et al.* Estimates of global seasonal influenza-associated respiratory mortality: a modelling study. *The Lancet* **391**, 1285–1300 (2018).

9. Dawood, F. S. *et al.* Estimated global mortality associated with the first 12 months of 2009 pandemic influenza A H1N1 virus circulation: a modelling study. *Lancet Infect. Dis.* **12**, 687–695 (2012).

10. Kelly, H. *et al.* The Age-Specific Cumulative Incidence of Infection with Pandemic Influenza H1N1 2009 Was Similar in Various Countries Prior to Vaccination. *PLOS ONE* **6**, e21828 (2011).

11. Nayak, D., Shivakoti, S., Balogun, R. A., Lee, G. & Zhou, Z. H. Structure, disassembly, assembly, and budding of influenza viruses. in *Textbook of Influenza* 35–56 (John Wiley & Sons, Ltd, 2013). doi:10.1002/9781118636817.ch3.

12. Samji, T. Influenza A: Understanding the Viral Life Cycle. *Yale J. Biol. Med.* **82**, 153–159 (2009).

13. Scheiffele, P., Rietveld, A., Wilk, T. & Simons, K. Influenza viruses select ordered lipid domains during budding from the plasma membrane. *J. Biol. Chem.* **274**, 2038–2044 (1999).

14. Tamm, L. K. Hypothesis: spring-loaded boomerang mechanism of influenza hemagglutinin-mediated membrane fusion. *Biochim. Biophys. Acta* **1614**, 14–23 (2003).

15. Vahey, M. D. & Fletcher, D. A. Influenza A virus surface proteins are organized to help penetrate host mucus. *eLife* **8**, (2019).

16. Nayak, D. P., Balogun, R. A., Yamada, H., Zhou, Z. H. & Barman, S. Influenza virus morphogenesis and budding. *Virus Res.* **143**, 147–161 (2009).

17. Resa-Infante, P., Jorba, N., Coloma, R. & Ortín, J. The influenza RNA synthesis machine. *RNA Biol.* **8**, 207–215 (2011).

18. Virk, R. K., Gunalan, V. & Tambyah, P. A. Influenza infection in human host: challenges in making a better influenza vaccine. *Expert Rev. Anti Infect. Ther.* **14**, 365–375 (2016).

19. Edinger, T. O., Pohl, M. O. & Stertz, S. Entry of influenza A virus: host factors and antiviral targets. *J. Gen. Virol.* **95**, 263–277 (2014).

20. Herold, S., Becker, C., Ridge, K. M. & Budinger, G. R. S. Influenza virus-induced lung injury: pathogenesis and implications for treatment. *Eur. Respir. J.* **45**, 1463–1478 (2015).

21. Rogers, G. N., Pritchett, T. J., Lane, J. L. & Paulson, J. C. Differential sensitivity of human, avian, and equine influenza A viruses to a glycoprotein inhibitor of infection: selection of receptor specific variants. *Virology* **131**, 394–408 (1983).

22. Sandbulte, M. R., Spickler, A. R., Zaabel, P. K. & Roth, J. A. Optimal Use of Vaccines for Control of Influenza A Virus in Swine. *Vaccines* **3**, 22–73 (2015).

23. Barrow, E., Nicola, A. V. & Liu, J. Multiscale perspectives of virus entry via endocytosis. *Virol. J.* **10**, 177 (2013).

24. Baharom, F. *et al.* Visualization of early influenza A virus trafficking in human dendritic cells using STED microscopy. *PLOS ONE* **12**, e0177920 (2017).

25. Kummer, S., Avinoam, O. & Kräusslich, H.-G. IFITM3 Clusters on Virus Containing Endosomes and Lysosomes Early in the Influenza A Infection of Human Airway Epithelial Cells. *Viruses* **11**, (2019).

26. Cross, K. J., Langley, W. A., Russell, R. J., Skehel, J. J. & Steinhauer, D. A. Composition and functions of the influenza fusion peptide. *Protein Pept. Lett.* **16**, 766–778 (2009).

27. Manzoor, R., Igarashi, M. & Takada, A. Influenza A Virus M2 Protein: Roles from Ingress to Egress. *Int. J. Mol. Sci.* **18**, (2017).

28. Rossman, J. S. & Lamb, R. A. Influenza virus assembly and budding. *Virology* **411**, 229–236 (2011).

29. Chlanda, P. & Zimmerberg, J. Protein–lipid interactions critical to replication of the influenza A virus. *FEBS Lett.* **590**, 1940–1954 (2016).

30. Chen, B. J., Leser, G. P., Jackson, D. & Lamb, R. A. The influenza virus M2 protein cytoplasmic tail interacts with the M1 protein and influences virus assembly at the site of virus budding. *J. Virol.* **82**, 10059–10070 (2008).

31. Dou, D., Revol, R., Östbye, H., Wang, H. & Daniels, R. Influenza A Virus Cell Entry, Replication, Virion Assembly and Movement. *Front. Immunol.* **9**, 1581 (2018).

32. Roberts, P. C. & Compans, R. W. Host cell dependence of viral morphology. *Proc. Natl. Acad. Sci. U. S. A.* **95**, 5746–5751 (1998).

33. Vijayakrishnan, S. *et al.* Cryotomography of Budding Influenza A Virus Reveals Filaments with Diverse Morphologies that Mostly Do Not Bear a Genome at Their Distal End. *PLOS Pathog.* **9**, e1003413 (2013).

34. Dadonaite, B., Vijayakrishnan, S., Fodor, E., Bhella, D. & Hutchinson, E. C. Filamentous influenza viruses. *J. Gen. Virol.* **97**, 1755–1764 (2016).

35. Calder, L. J., Wasilewski, S., Berriman, J. A. & Rosenthal, P. B. Structural organization of a filamentous influenza A virus. *Proc. Natl. Acad. Sci.* **107**, 10685–10690 (2010).

36. Harris, A. K. *et al.* Structure and accessibility of HA trimers on intact 2009 H1N1 pandemic influenza virus to stem region-specific neutralizing antibodies. *Proc. Natl. Acad. Sci.* **110**, 4592–4597 (2013).

37. Noda, T. Native Morphology of Influenza Virions. *Front. Microbiol.* **2**, (2012).

38. Harris, A. *et al.* Influenza virus pleiomorphy characterized by cryoelectron tomography. *Proc. Natl. Acad. Sci.* **103**, 19123–19127 (2006).

39. Hayden, F. G. & deJong, M. D. Human influenza: Pathogenesis, clinical features, and management. in *Textbook of Influenza* 371–391 (John Wiley & Sons, Ltd, 2013). doi:10.1002/9781118636817.ch24.

40. CDC. How Flu Viruses Can Change. *Centers for Disease Control and Prevention* https://www.cdc.gov/flu/about/viruses/change.htm (2019).

41. Yang, J., Huang, Y. & Liu, S. Investigational antiviral therapies for the treatment of influenza. *Expert Opin. Investig. Drugs* **28**, 481–488 (2019).

42. Król, E., Rychłowska, M. & Szewczyk, B. Antivirals--current trends in fighting influenza. *Acta Biochim. Pol.* **61**, 495–504 (2014).

43. Leonov, H., Astrahan, P., Krugliak, M. & Arkin, I. T. How do aminoadamantanes block the influenza M2 channel, and how does resistance develop? *J. Am. Chem. Soc.* **133**, 9903–9911 (2011).

44. Dong, G. *et al.* Adamantane-resistant influenza a viruses in the world (1902-2013): frequency and distribution of M2 gene mutations. *PloS One* **10**, e0119115 (2015).

45. Yen, H.-L. *et al.* Importance of neuraminidase active-site residues to the neuraminidase inhibitor resistance of influenza viruses. *J. Virol.* **80**, 8787–8795 (2006).

46. Samson, M., Pizzorno, A., Abed, Y. & Boivin, G. Influenza virus resistance to neuraminidase inhibitors. *Antiviral Res.* **98**, 174–185 (2013).

47. Chen, Q. & Guo, Y. Influenza Viral Hemagglutinin Peptide Inhibits Influenza Viral Entry by Shielding the Host Receptor. *ACS Infect. Dis.* **2**, 187–193 (2016).

48. Kwon, S.-J. *et al.* Nanostructured glycan architecture is important in the inhibition of influenza A virus infection. *Nat. Nanotechnol.* **advance online publication**, (2016).

49. Furuta, Y. *et al.* T-705 (favipiravir) and related compounds: Novel broad-spectrum inhibitors of RNA viral infections. *Antiviral Res.* **82**, 95–102 (2009).

50. Bhatia, S., Camacho, L. C. & Haag, R. Pathogen Inhibition by Multivalent Ligand Architectures. *J. Am. Chem. Soc.* **138**, 8654–8666 (2016).

51. Lauster, D. *et al.* Multivalent Peptide–Nanoparticle Conjugates for Influenza-Virus Inhibition. *Angew. Chem. Int. Ed Engl.* **56**, 5931–5936 (2017).

52. Papp, I. *et al.* Inhibition of influenza virus activity by multivalent glycoarchitectures with matched sizes. *Chembiochem Eur. J. Chem. Biol.* **12**, 887–895 (2011).

53. Chaisri, U. & Chaicumpa, W. Evolution of Therapeutic Antibodies, Influenza Virus Biology, Influenza, and Influenza Immunotherapy. *BioMed Res. Int.* **2018**, (2018).

54. Laursen, N. S. & Wilson, I. A. Broadly neutralizing antibodies against influenza viruses. *Antiviral Res.* **98**, 476–483 (2013).

55. Shriver, Z., Trevejo, J. M. & Sasisekharan, R. Antibody-Based Strategies to Prevent and Treat Influenza. *Front. Immunol.* **6**, 315 (2015).

56. Soema, P. C., Kompier, R., Amorij, J.-P. & Kersten, G. F. A. Current and next generation influenza vaccines: Formulation and production strategies. *Eur. J. Pharm. Biopharm.* **94**, 251–263 (2015).

57. Corti, D. & Lanzavecchia, A. Broadly Neutralizing Antiviral Antibodies. *Annu. Rev. Immunol.* **31**, 705–742 (2013).

58. Okuno, Y., Isegawa, Y., Sasao, F. & Ueda, S. A common neutralizing epitope conserved between the hemagglutinins of influenza A virus H1 and H2 strains. *J. Virol.* **67**, 2552–2558 (1993).

59. Smirnov, Y. A. *et al.* An epitope shared by the hemagglutinins of H1, H2, H5, and H6 subtypes of influenza A virus. *Acta Virol.* **43**, 237–244 (1999).

60. A Study of MHAA4549A in Combination With Oseltamivir Versus Oseltamivir in Participants With Severe Influenza A Infection - Full Text View - ClinicalTrials.gov. https://clinicaltrials.gov/ct2/show/NCT02293863.

61. Dreyfus, C. *et al.* Highly conserved protective epitopes on influenza B viruses. *Science* **337**, 1343–1348 (2012).

62. Throsby, M. *et al.* Heterosubtypic neutralizing monoclonal antibodies cross-protective against H5N1 and H1N1 recovered from human IgM+ memory B cells. *PloS One* **3**, e3942 (2008).

63. Assessment of CR6261, a Monoclonal Antibody Against the Influenza A Virus - Full Text View - ClinicalTrials.gov. https://clinicaltrials.gov/ct2/show/NCT01406418.

64. Ekiert, D. C. *et al.* A Highly Conserved Neutralizing Epitope on Group 2 Influenza A Viruses. *Science* **333**, 843–850 (2011).

65. Assessment of CR8020, a Monoclonal Antibody Against Influenza A Viruses - Full Text View - ClinicalTrials.gov. https://clinicaltrials.gov/ct2/show/NCT01756950.

66. McBride, J. M. *et al.* Phase 2 Randomized Trial of the Safety and Efficacy of MHAA4549A, a Broadly Neutralizing Monoclonal Antibody, in a Human Influenza A Virus Challenge Model. *Antimicrob. Agents Chemother.* **61**, (2017).

67. Neirynck, S. *et al.* A universal influenza A vaccine based on the extracellular domain of the M2 protein. *Nat. Med.* **5**, 1157–1163 (1999).

68. Ramos, E. L. *et al.* Efficacy and safety of treatment with an anti-m2e monoclonal antibody in experimental human influenza. *J. Infect. Dis.* **211**, 1038–1044 (2015).

69. Krammer, F. *et al.* NAction! How Can Neuraminidase-Based Immunity Contribute to Better Influenza Virus Vaccines? *mBio* **9**, (2018).

70. Gubareva, L. & Mohan, T. Antivirals Targeting the Neuraminidase. *Cold Spring Harb. Perspect. Med.* (2020) doi:10.1101/cshperspect.a038455.

71. Doyle, T. M. *et al.* Universal anti-neuraminidase antibody inhibiting all influenza A subtypes. *Antiviral Res.* **100**, 567–574 (2013).

72. Doyle, T. M. *et al.* A monoclonal antibody targeting a highly conserved epitope in influenza B neuraminidase provides protection against drug resistant strains. *Biochem. Biophys. Res. Commun.* **441**, 226–229 (2013).

73. Stöhr, K. Influenza vaccine production. in *Textbook of Influenza* 352–370 (John Wiley & Sons, Ltd, 2013). doi:10.1002/9781118636817.ch23.

74. Wong, S.-S. & Webby, R. J. Traditional and New Influenza Vaccines. *Clin. Microbiol. Rev.* **26**, 476–492 (2013).

75. Reina, J. & Reina, N. Universal influenza vaccination: Future prospects. *Vacunas Engl. Ed.* **20**, 72–81 (2019).

76. McMillan, C. L. D., Young, P. R., Watterson, D. & Chappell, K. J. The Next Generation of Influenza Vaccines: Towards a Universal Solution. *Vaccines* **9**, (2021).

77. How Influenza (Flu) Vaccines Are Made | CDC. https://www.cdc.gov/flu/prevent/how-fluvaccine-made.htm (2019).

78. Cell-Based Flu Vaccines | CDC. https://www.cdc.gov/flu/prevent/cell-based.htm (2020).

79. Sgrulletti, M. *et al.* One step closer to influenza vaccine inclusiveness. *Pediatr. Allergy Immunol. Off. Publ. Eur. Soc. Pediatr. Allergy Immunol.* **31 Suppl 26**, 69–71 (2020).

80. Tripp, R. A. & Tompkins, S. M. Recombinant vaccines for influenza virus. *Curr. Opin. Investig. Drugs Lond. Engl. 2000* **9**, 836–845 (2008).

81. Sedova, E. S. *et al.* Recombinant Influenza Vaccines. *Acta Naturae* **4**, 17–27 (2012).

82. Mardanova, E. S. & Ravin, N. V. Plant-produced Recombinant Influenza A Vaccines Based on the M2e Peptide. *Curr. Pharm. Des.* **24**, 1317–1324 (2018).

83. Rockman, S., Laurie, K. L., Parkes, S., Wheatley, A. & Barr, I. G. New Technologies for Influenza Vaccines. *Microorganisms* **8**, (2020).

84. Mathew, N. R. & Angeletti, D. Recombinant Influenza Vaccines: Saviors to Overcome Immunodominance. *Front. Immunol.* **10**, (2020).

85. Pardi, N., Hogan, M. J., Porter, F. W. & Weissman, D. mRNA vaccines — a new era in vaccinology. *Nat. Rev. Drug Discov.* **17**, 261–279 (2018).

86. Pascolo, S. Messenger RNA-based vaccines. *Expert Opin. Biol. Ther.* **4**, 1285–1294 (2004).

87. An mRNA Vaccine against SARS-CoV-2 — Preliminary Report | NEJM. https://www.nejm.org/doi/10.1056/NEJMoa2022483.

88. Baxter, R. *et al.* Evaluation of the safety, reactogenicity and immunogenicity of FluBlok® trivalent recombinant baculovirus-expressed hemagglutinin influenza vaccine administered intramuscularly to healthy adults 50–64 years of age. *Vaccine* **29**, 2272–2278 (2011).

89. Durous, L., Rosa-Calatrava, M. & Petiot, E. Advances in influenza virus-like particles bioprocesses. *Expert Rev. Vaccines* **18**, 1285–1300 (2019).

90. Wu, C.-Y. *et al.* Mammalian Expression of Virus-Like Particles for Advanced Mimicry of Authentic Influenza Virus. *PLoS ONE* **5**, e9784 (2010).

91. McCraw, D. M. *et al.* Structural analysis of influenza vaccine virus-like particles reveals a multicomponent organization. *Sci. Rep.* **8**, 1–16 (2018).

92. Hema, M., Vishnu Vardhan, G. P., Savithri, H. S. & Murthy, M. R. N. Chapter 6 - Emerging Trends in the Development of Plant Virus-Based Nanoparticles and Their Biomedical Applications. in *Recent Developments in Applied Microbiology and Biochemistry* (ed. Buddolla, V.) 61–82 (Academic Press, 2019). doi:10.1016/B978-0-12-816328-3.00006-4.

93. Kalkhoran, B. F. A Short Review on Virus-Like Particles as Vaccine and Delivery Systems. in (2017).

94. Haynes, J. R. Influenza virus-like particle vaccines. *Expert Rev. Vaccines* **8**, 435–445 (2009).

95. Naskalska, A. & Pyrć, K. Virus Like Particles as Immunogens and Universal Nanocarriers. *Pol. J. Microbiol.* **64**, 3–13 (2015).

96. Guo, L. *et al.* Enhancement of mucosal immune responses by chimeric influenza HA/SHIV virus-like particles. *Virology* **313**, 502–513 (2003).

97. Bright, R. A. *et al.* Influenza virus-like particles elicit broader immune responses than whole virion inactivated influenza virus or recombinant hemagglutinin. *Vaccine* **25**, 3871–3878 (2007).

98. Hodgins, B., Pillet, S., Landry, N. & Ward, B. J. Prime-pull vaccination with a plant-derived virus-like particle influenza vaccine elicits a broad immune response and protects aged mice from death and frailty after challenge. *Immun. Ageing A* **16**, 27 (2019).

99. Novavax Trivalent VLP Vaccine for Seasonal Influenza. *Clinical Trials Arena* https://www.clinicaltrialsarena.com/projects/novavax-vlp-vaccine/.

100. Evaluate the Safety and Immunogenicity of a Seasonal Influenza Virus-Like Particle (VLP) Vaccine in Older Adults - Full Text View - ClinicalTrials.gov. https://clinicaltrials.gov/ct2/show/NCT01014806.

101. Flu season: 169m vaccine doses available for current US influenza season. https://www.pharmaceutical-technology.com/comment/with-influenza-seasons-starting-earlier-and-lasting-longer-more-efficient-vaccines-are-needed/.

102. Kiss, B. *et al.* Single-particle virology. *Biophys. Rev.* **12**, 1141–1154 (2020).

103. Artenstein, A. W. The discovery of viruses: advancing science and medicine by challenging dogma. *Int. J. Infect. Dis.* **16**, e470–e473 (2012).

104. Shaw, M. L., Stone, K. L., Colangelo, C. M., Gulcicek, E. E. & Palese, P. Cellular Proteins in Influenza Virus Particles. *PLOS Pathog.* **4**, e1000085 (2008).

105. Vajda, J., Weber, D., Brekel, D., Hundt, B. & Müller, E. Size distribution analysis of influenza virus particles using size exclusion chromatography. *J. Chromatogr. A* **1465**, 117–125 (2016).

106. Ustinov, N. B., Zavyalova, E. G., Smirnova, I. G. & Kopylov, A. M. The Power and Limitations of Influenza Virus Hemagglutinin Assays. *Biochem. Biokhimiia* **82**, 1234–1248 (2017).

107. Rumlová, M. & Ruml, T. In vitro methods for testing antiviral drugs. *Biotechnol. Adv.* **36**, 557–576 (2018).

108. Payne, S. Methods to Study Viruses. *Viruses* 37–52 (2017) doi:10.1016/B978-0-12-803109-4.00004-0.

109. Guliy, O. I., Zaitsev, B. D., Larionova, O. S. & Borodina, I. A. Virus Detection Methods and Biosensor Technologies. *Biophysics* **64**, 890–897 (2019).

110. Nathan, L. & Daniel, S. Single Virion Tracking Microscopy for the Study of Virus Entry Processes in Live Cells and Biomimetic Platforms. *Phys. Virol.* **1215**, 13–43 (2019).

111. Carravilla, P., Nieva, J. L. & Eggeling, C. Fluorescence Microscopy of the HIV-1 Envelope. *Viruses* **12**, (2020).

112. von Borries, B., Ruska, E. & Ruska, H. Bakterien und Virus in Übermikroskopischer Aufnahme. *Klin. Wochenschr.* **17**, 921–925 (1938).

113. Ruska, H., von Borries, B. & Ruska, E. Die Bedeutung der Übermikroskopie für die Virusforschung. *Arch Gesamte Virusforsch* **1**, 155-169. (1939).

114. Leser, G. P. & Lamb, R. A. Lateral Organization of Influenza Virus Proteins in the Budozone Region of the Plasma Membrane. *J. Virol.* **91**, (2017).

115. McCraw, D. M. *et al.* Structural analysis of influenza vaccine virus-like particles reveals a multicomponent organization. *Sci. Rep.* **8**, 10342 (2018).

116. Wu, N. C. & Wilson, I. A. Structural Biology of Influenza Hemagglutinin: An Amaranthine Adventure. *Viruses* **12**, (2020).

117. Liu, C. *et al.* The Architecture of Inactivated SARS-CoV-2 with Postfusion Spikes Revealed by Cryo-EM and Cryo-ET. *Struct. Lond. Engl. 1993* (2020) doi:10.1016/j.str.2020.10.001.

118. Zhou, Q. F. *et al.* Structural basis of Chikungunya virus inhibition by monoclonal antibodies. *Proc. Natl. Acad. Sci. U. S. A.* (2020) doi:10.1073/pnas.2008051117.

119. Mollenhauer, H. H. Artifacts caused by dehydration and epoxy embedding in transmission electron microscopy. *Microsc. Res. Tech.* **26**, 496–512 (1993).

120. Ayache, J., Beaunier, L., Boumendil, J., Ehret, G. & Laub, D. Artifacts in Transmission Electron Microscopy. *Sample Prep Handb Transm Electron Microsc* (2010) doi:10.1007/978-0-387-98182-6_6.

121. Gulati, N. M., Torian, U., Gallagher, J. R. & Harris, A. K. Immunoelectron Microscopy of Viral Antigens. *Curr. Protoc. Microbiol.* **53**, e86 (2019).

122. Passmore, L. A. & Russo, C. J. Specimen preparation for high-resolution cryo-EM. *Methods Enzymol.* **579**, 51–86 (2016).

123. Murtey, M. D. Immunogold Techniques in Electron Microscopy. *Mod. Electron Microsc. Phys. Life Sci.* (2016) doi:10.5772/61719.

124. Howell, D. N. & Miller, S. E. Identification of viral infection by confocal microscopy. *Methods Enzymol.* **307**, 573–591 (1999).

125. Lorin, V. *et al.* Antibody Neutralization of HIV-1 Crossing the Blood-Brain Barrier. *mBio* **11**, (2020).

126. Witte, R., Andriasyan, V., Georgi, F., Yakimovich, A. & Greber, U. F. Concepts in Light Microscopy of Viruses. *Viruses* **10**, (2018).

127. Sieczkarski, S. B. & Whittaker, G. R. Influenza Virus Can Enter and Infect Cells in the Absence of Clathrin-Mediated Endocytosis. *J. Virol.* **76**, 10455–10464 (2002).

128. Soudani, N., Hage-Sleiman, R., Karam, W., Dbaibo, G. & Zaraket, H. Ceramide Suppresses Influenza A Virus Replication In Vitro. *J. Virol.* **93**, (2019).

129. Abbe, E. Beiträge zur Theorie des Mikroskops und der mikroskopischen Wahrnehmung. *Arch. Für Mikrosk. Anat.* **9**, 413–468 (1873).

130. Lord Rayleigh Sec R., L. R. S. R. XV. On the theory of optical images, with special reference to the microscope. *Lond. Edinb. Dublin Philos. Mag. J. Sci.* **42**, 167–195 (1896).

131. Thorley, J. A., Pike, J. & Rappoport, J. Z. Chapter 14 - Super-resolution Microscopy: A Comparison of Commercially Available Options. in *Fluorescence Microscopy* (eds. Cornea, A. & Conn, P. M.) 199–212 (Academic Press, 2014). doi:10.1016/B978-0-12-409513-7.00014-2.

132. Pujals, S., Feiner-Gracia, N., Delcanale, P., Voets, I. & Albertazzi, L. Super-resolution microscopy as a powerful tool to study complex synthetic materials. *Nat. Rev. Chem.* **3**, 68–84 (2019).

133. Sahl, S. J., Hell, S. W. & Jakobs, S. Fluorescence nanoscopy in cell biology. *Nat. Rev. Mol. Cell Biol.* **advance online publication**, (2017).

134. Gwosch, K. C. *et al.* MINFLUX nanoscopy delivers 3D multicolor nanometer resolution in cells. *Nat. Methods* **17**, 217–224 (2020).

135. Schermelleh, L., Heintzmann, R. & Leonhardt, H. A guide to super-resolution fluorescence microscopy. *J. Cell Biol.* **190**, 165–175 (2010).

136. Hell, S. W. & Wichmann, J. Breaking the diffraction resolution limit by stimulated emission: stimulated-emission-depletion fluorescence microscopy. *Opt. Lett.* **19**, 780–782 (1994).

137. Gustafsson, M. G. L. Surpassing the lateral resolution limit by a factor of two using structured illumination microscopy. *J. Microsc.* **198**, 82–87 (2000).

138. Rust, M. J., Bates, M. & Zhuang, X. Sub-diffraction-limit imaging by stochastic optical reconstruction microscopy (STORM). *Nat. Methods* **3**, 793–796 (2006).

139. Hess, S. T., Girirajan, T. P. K. & Mason, M. D. Ultra-High Resolution Imaging by Fluorescence Photoactivation Localization Microscopy. *Biophys. J.* **91**, 4258–4272 (2006).

140. Thorley, J. A., Pike, J. & Rappoport, J. Z. Chapter 14 - Super-resolution Microscopy: A Comparison of Commercially Available Options. in *Fluorescence Microscopy* (eds. Cornea, A. & Conn, P. M.) 199–212 (Academic Press, 2014). doi:10.1016/B978-0-12-409513-7.00014-2.

141. Huszka, G. & Gijs, M. A. M. Super-resolution optical imaging: A comparison. *Micro Nano Eng.* **2**, 7–28 (2019).

142. Hess, S. T., Girirajan, T. P. K. & Mason, M. D. Ultra-High Resolution Imaging by Fluorescence Photoactivation Localization Microscopy. *Biophys. J.* **91**, 4258–4272 (2006).

143. Schermelleh, L. *et al.* Super-resolution microscopy demystified. *Nat. Cell Biol.* **21**, 72–84 (2019).

144. Nieuwenhuizen, R. P. J. *et al.* Measuring image resolution in optical nanoscopy. *Nat. Methods* **10**, 557–562 (2013).

145. Sauer, M. & Heilemann, M. Single-Molecule Localization Microscopy in Eukaryotes. *Chem. Rev.* (2017) doi:10.1021/acs.chemrev.6b00667.

146. Lehmann, M. *et al.* Quantitative Multicolor Super-Resolution Microscopy Reveals Tetherin HIV-1 Interaction. *PLoS Pathog.* **7**, (2011).

147. Lehmann, M., Lichtner, G., Klenz, H. & Schmoranzer, J. Novel organic dyes for multicolor localization-based super-resolution microscopy. *J. Biophotonics* **9**, 161–170 (2016).

148. Gunzenhäuser, J., Olivier, N., Pengo, T. & Manley, S. Quantitative Super-Resolution Imaging Reveals Protein Stoichiometry and Nanoscale Morphology of Assembling HIV-Gag Virions. *Nano Lett.* **12**, 4705–4710 (2012).

149. Jungmann, R. *et al.* Multiplexed 3D cellular super-resolution imaging with DNA-PAINT and Exchange-PAINT. *Nat. Methods* **11**, 313–318 (2014).

150. Schnitzbauer, J., Strauss, M. T., Schlichthaerle, T., Schueder, F. & Jungmann, R. Super-resolution microscopy with DNA-PAINT. *Nat. Protoc.* **12**, 1198–1228 (2017).

151. Sharonov, A. & Hochstrasser, R. M. Wide-field subdiffraction imaging by accumulated binding of diffusing probes. *Proc. Natl. Acad. Sci. U. S. A.* **103**, 18911–18916 (2006).

152. Agasti, S. S. *et al.* DNA-barcoded labeling probes for highly multiplexed Exchange-PAINT imaging. *Chem. Sci.* (2017) doi:10.1039/C6SC05420J.

153. Wade, O. K. *et al.* 124-Color Super-resolution Imaging by Engineering DNA-PAINT Blinking Kinetics. *Nano Lett.* **19**, 2641–2646 (2019).

154. Jungmann, R. *et al.* Quantitative super-resolution imaging with qPAINT. *Nat. Methods* **13**, 439–442 (2016).

155. Dai, M., Jungmann, R. & Yin, P. Optical imaging of individual biomolecules in densely packed clusters. *Nat. Nanotechnol.* **11**, 798–807 (2016).

156. Chen, C. *et al.* Profiling of Exosomal Biomarkers for Accurate Cancer Identification: Combining DNA-PAINT with Machine- Learning-Based Classification. *Small* **15**, 1901014 (2019).

157. Cremers, G. A. O., Rosier, B. J. H. M., Riera Brillas, R., Albertazzi, L. & de Greef, T. F. A. Efficient Small-Scale Conjugation of DNA to Primary Antibodies for Multiplexed Cellular Targeting. *Bioconjug. Chem.* **30**, 2384–2392 (2019).

158. Strauss, S. *et al.* Modified aptamers enable quantitative sub-10-nm cellular DNA-PAINT imaging. *Nat. Methods* **15**, 685–688 (2018).

159. Schlichthaerle, T. *et al.* Site-Specific Labeling of Affimers for DNA-PAINT Microscopy. *Angew. Chem. Int. Ed.* **0**,.

160. Grove, J. Super-Resolution Microscopy: A Virus' Eye View of the Cell. *Viruses* **6**, 1365–1378 (2014).

161. Chojnacki, J. & Eggeling, C. Super-resolution fluorescence microscopy studies of human immunodeficiency virus. *Retrovirology* **15**, 41 (2018).

162. Hanne, J., Zila, V., Heilemann, M., Müller, B. & Kräusslich, H.-G. Super-resolved insights into human immunodeficiency virus biology. *FEBS Lett.* **590**, 1858–1876 (2016).

163. Pereira, C. F., Rossy, J., Owen, D. M., Mak, J. & Gaus, K. HIV taken by STORM: Super-resolution fluorescence microscopy of a viral infection. *Virol. J.* **9**, 84 (2012).

164. Muranyi, W., Malkusch, S., Müller, B., Heilemann, M. & Kräusslich, H.-G. Super-resolution microscopy reveals specific recruitment of HIV-1 envelope proteins to viral assembly sites dependent on the envelope C-terminal tail. *PLoS Pathog.* **9**, e1003198 (2013).

165. Pereira, C. F., Rossy, J., Owen, D. M., Mak, J. & Gaus, K. HIV taken by STORM: Super-resolution fluorescence microscopy of a viral infection. *Virol. J.* **9**, 84 (2012).

166. Pham, S. *et al.* Cryo-electron microscopy and single molecule fluorescent microscopy detect CD4 receptor induced HIV size expansion prior to cell entry. *Virology* **486**, 121–133 (2015).

167. Touizer, E., Sieben, C., Henriques, R., Marsh, M. & Laine, R. F. Application of Super-Resolution and Advanced Quantitative Microscopy to the Spatio-Temporal Analysis of Influenza Virus Replication. *Viruses* **13**, (2021).

168. Sieben, C., Sezgin, E., Eggeling, C. & Manley, S. Influenza A viruses use multivalent sialic acid clusters for cell binding and receptor activation. *PLoS Pathog.* **16**, e1008656 (2020).

169. Chojnacki, J. & Eggeling, C. Super-resolution fluorescence microscopy studies of human immunodeficiency virus. *Retrovirology* **15**, (2018).

Objectives and Thesis Content

In **Chapter 1** it has been described the problematic of influenza virus in our society and the lack of full blockers for the infection. The need of development of new universal antivirals and vaccines highlights the lack of information of the influenza viral structure and how antivirals are affecting the viral structure in the nanoscale. Likewise, vaccine improvement is still in need of single-molecule characterization to boost the production and optimization of newly developed approaches.

Hence, the main aim of this thesis is the use and optimization of novel single-molecule localization microscopy techniques to characterize the viral composition of viral structures and vaccines at single-particle level.

In this framework, each chapter embraces the study with super-resolution microscopy of a different viral structure, antiviral or vaccine, as well as the required optimization and validation of the novel single-molecule localization microscopy approaches needed for these studies.

In this context, the objective of **Chapter 2** was to perform dSTORM imaging to characterize the *in vitro* effects of three monoclonal antibodies against the protein M2 of influenza on viral filaments, along with describing their effects on the filament integrity and the influence of this deformity on the spread of the infection and influenza virulence.

Next, the objective of **Chapter 3** was to implement, optimize and validate the novel super-resolution technique DNA-PAINT to characterize and quantify the distribution of targeting ligands at the nanoscale. The initial optimization was performed on commercially available nanoparticles for its further implementation on cells and viral structures.

The objective of **Chapter 4**, following the optimization performed in **Chapter 3,** was to apply DNA-PAINT imaging in the study of the production of recombinant viral proteins of influenza and the resulting isolated virus-like particles (VLP). Hence, the main goal was to quantify and characterize the distribution of three recombinant proteins of influenza along the cell membrane and on the VLP structure at single-particle level.

Moreover, the aim of **Chapter 5** was the optimization of dSTORM imaging acquisition to characterize the presence of hepatitis B and Delta virus on paraffin-fixed tissues extracted from cirrhotic patients, to increase the resolution and sensitivity on thick samples.

The objective of **Chapter 6** focused on the characterization of the antiviral activity of a multivalent antiviral based on analogues of sialic acid. This characterization comprised in vitro inhibition assays using several different strains of influenza in combination with imaging with super-resolution microscopy.

Finally, in **Chapter 7** the objective was to perform super-resolution microscopy for the intracellular localization of nanovaccines internalized by dendritic cells, to explore the interaction of the nanovaccine and dendritic cells with time and to identify the internalization pathway.

Chapter 2: Super-resolution microscopy characterization of the effects of therapeutic antibodies in the filament inhibition of influenza A virus

This chapter reproduces almost literally the article: Super-resolution microscopy reveals significant impact of M2e-specific monoclonal antibodies on influenza A virus filament formation at the host cell surface. Kolpe A., Arista-Romero M.*, Schepens B., Pujals S., Saelens X., and Albertazzi L. (2019). Scientific Reports, 9(1), 4450. http://doi.org/10.1038/s41598-019-41023-51.*

As a co-author, my contribution to this paper was the super-resolution microscopy acquisitions and all the quantifications performed on the filaments, while Dr. A Kolpe, co-author of the paper, prepared the monoclonal antibodies and the viral samples. The manuscript was written also in collaboration with Dr. B. Schepens and my two supervisors Dr. S. Pujals and Dr. L. Albertazzi.

2.1 Introduction

As explained in chapter 1, influenza virus budding results in the formation of filamentous, bacilliform or spherical particles, depending on the virus strains that are used. Infection with A/WSN/33 (H1N1), for example, predominantly gives rise to spherical virions, whereas infection of cells with the strain A/Udorn/72 (H3N2) produces a mixture of spherical and filamentous virions (Figure 2.1)[2-6].

Filamentous influenza virions are thought to be the predominant form in the upper respiratory tract of influenza patients[4,7,8] and were also detected in 2009 H1N1 pandemic virus isolates[9]. Indeed, the general view is that primary human influenza virus isolates are filamentous in appearance, but convert into predominantly spherical virions after serial passage in embryonated chicken eggs[10]. Nevertheless, spherical and filamentous virus particles are equally infectious *in vitro* [4,11].

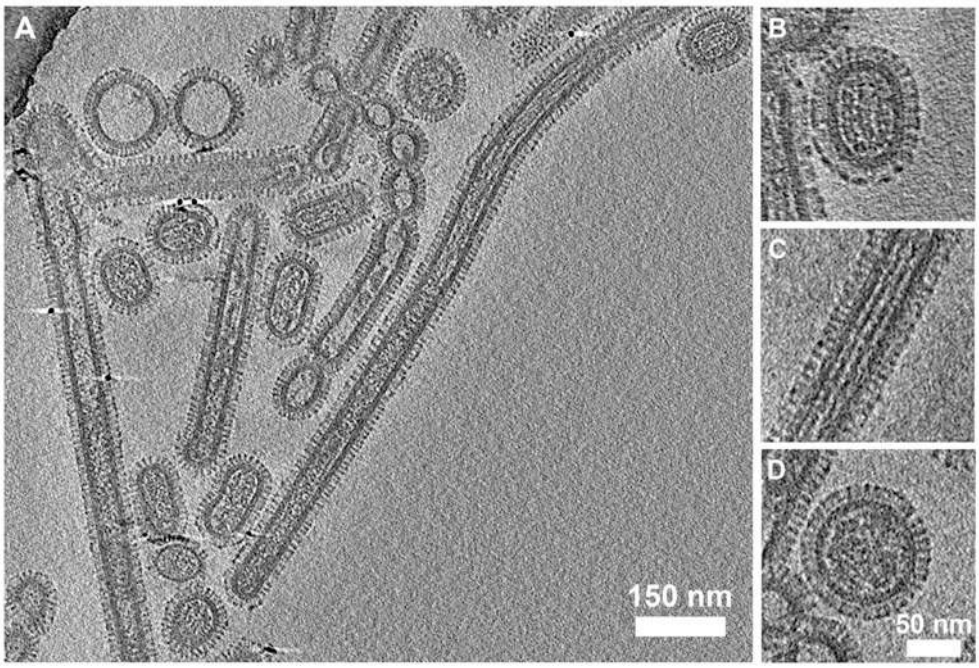

Figure 2.1: Cryoelectrontomgraphy of influenza A/Udorn/72 H3N2 displaying three distinct morphologies. A) All the virion structures. B) Bacilliform shape. C) Filament shape. D) Spherical shape. Modified from reference [3]. Copyright: © 2013 Vijayakrishnan et al. CC.

Previous studies have suggested that the protein M2, as well as M1 protein[11,12,13], are involved in this filament formation[4,14,15]. In particular, an amphipathic alpha helix in the cytoplasmic part of M2 has been proposed to contribute to the formation and stability of filamentous virion formation[16].

Antibodies directed against the extracellular portion of M2 (M2e) (described in chapter 1) can protect against experimental influenza A virus challenge *in vivo* by an Fcγ Receptor-dependent mechanism[17,18]. However, some influenza A virus strains are also susceptible to a *in vitro* antiviral effect of M2e-specific IgGs by a direct interaction and blockage of the M2 protein[19]. In this case, M2e-specific IgGs perturb critical interactions between the M1 and M2 proteins, which in turn affect the interaction of M1 with the viral ribonucleoprotein complexes; as a consequence, virions assembly is compromised[20]. Rossman et al. tested this evidence, observing that the effect of an M2e-specific monoclonal antibody (MAb) 14C2 against the influenza strain A/Udorn/72 resulted in a loss of filament formation and reduction of the infectivity of the virus *in vitro*[4,19]. This M2e-specific antibody-mediated fragmentation of filamentous virions appears to be due to the induction of a conformational change in the M2 protein, which alters membrane

curvature[14,4]. Furthermore, the treatment of infected cells with M2e-specific MAb 14C2 antibody was also shown to inhibit viral assembly and release[21].

Due to the small size of the influenza particles (approximately 100 nm in width) and the filaments formed on infected cells, the characterization of the detailed effects of MAbs M2e on these structures is almost impossible using conventional fluorescence microscopy techniques, such as confocal microscopy, due to the diffraction limit. As explained in chapter 1, studies of the budding process of influenza viruses have been performed using electron microscopy (Figure 2.1)[3,22] with several limitations due to the complexity of the sample preparation, requiring also expensive and sensitive materials. To overcome those limitations and facilitate the acquisition of precise images of budding influenza virions, we used direct stochastical optical reconstruction microscopy (dSTORM), which it has never been used deeply to study the role of M2 in filament formation and structures[23].

All in all, in this chapter we have investigated the effect of three M2e-specific MAbs on influenza A virus plaque formation and infectivity *in vitro*. We utilized confocal and super-resolution dSTORM microscopy to characterize filaments formation that is associated with influenza A/Udorn/72 replication. We further investigated M2e-specific antibody-induced perturbation of filament formation and fragmentation of pre-existing filaments in influenza A/Udorn/72 infected cells.

2.2 Results and discussion

2.2.1 Inhibition *in vitro* assays of M2e-specific MAbs

The M2-specific mouse IgG1 MAb 14C2 was previously shown to be able to inhibit influenza A/Udorn/72 virus plaque growth and infectivity *in vitro*[4,19,24]. In line with this, to prove that the selected M2e-specific IgG MAbs were able to inhibit influenza, we performed plaque growth and infectivity assays *in vitro*.

The three MAbs selected were 37 (IgG1) and 65 (IgG2a), both directed against a similar part of M2e (encompassing residues Thr4-Trp15), and MAb 148 (IgG1) directed against Ser2-Thr9 (Table 2.1), all of them previously described in the literature. For a better understanding of the inhibition of influenza and its relation to filament formation, we employed two strains of

influenza: the filamentous strain Udorn (A/Udorn/72) and PR8 (A/PR8/34) a non-filamentous strain as negative control.

Name of MAb	Epitope specificity	Isotype	References
MAb 37	Influenza M2e	IgG1	25
MAb 65	Influenza M2e	IgG2a	25, 26
MAb 148	Influenza M2e	IgG1	25
Control MAb	Hepatitis B core	IgG1	25

Table 2.1: Monoclonal antibodies used in the study

First, we studied the capability of the three MAb to block viral infection *in vitro* on both strains of influenza by measuring the size and number of viral plaques formed after the incubation of each MAb at 100 µg/ml for 72 hours on infected cells. The decrease in number of plaques and size is directly related to a lower amount of viral infection. As seen in Figure 2.2 A and B, the plaque size was visually and statistically significantly smaller in the presence of all three M2e-specifc MAbs compared to the control antibody (isotype). In contrast, M2e-specific MAbs 65, 37, 148, did not affect the plaque growth of PR8 virus either in number of plaques or size.

Further, we also measured the total amount of new viral particles produced from threated Udorn infected cells using a multicycle growth setup (Figure 2.2 C), where the medium containing newly released virus in presence of MAb was titrated by plaque assay. We could observe that all three M2e-specific MAbs reduced the amount of newly produced infectious Udorn virus equally, where the plaque formation units (pfu) decreased from 10^6 to 10^4.

Hence, M2e-specific MAbs could bind to the external M2 protein expressed on the surface of Udorn infected cells. This interaction not only blocked Udorn influenza infection but also avoided the release of new influenza particles *in vitro*.

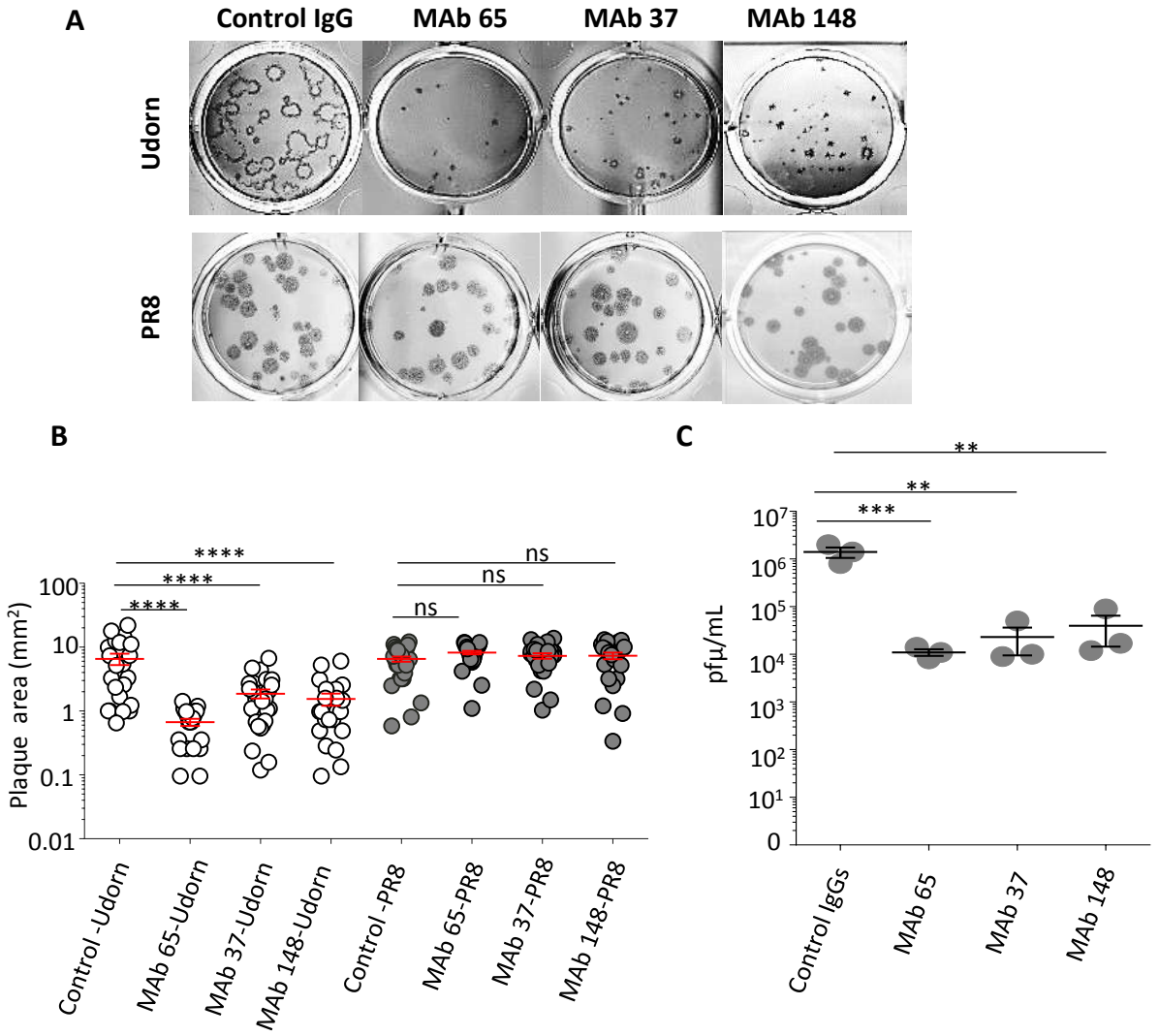

*Figure 2.2: Inhibition of influenza infection by three M2e IgGs (65, 37, 148), in vitro. A) Plaque assay performed in MDCK cells infected with Udorn (A/Udorn/72) or PR8 (A/PR8/34) incubated with a control IgG and M2e MAb 65, 37 or 148 after 72h of incubation. B) Quantification of the plaque size after 72h of incubation. The graph shows the area of each plaque and the bars represent the mean area ± SEM. C) Production of active virions after the treatment by plaque assay: plaque formation unit (pfu) produced from infected cells with Udorn and treated with each MAb (100 µg/ml) after 24 hours. Non-significant (ns), ** p ≤ 0.01, *** p ≤ 0.001; ****p ≤ 0.0001.*

Despite that PR8 and Udorn viruses have similar M2 sequence, only Udorn strain was sensitive to the *in vitro* inhibition by the three anti-M2e MAbs tested, where the three MAbs had similar effects, since none of them have a significantly strongest outcome than the other. Interestingly, once we characterized the binding affinity of the three MAbs to the M2 expressed on the surface of Udorn virus-infected cells by a cellular ELISA (Figure 2.3) we estimated that MAbs

65, 37 and 148 had a Kd of 2.073 nM, 6.957 nM, and 14.82 nM, respectively, denoting that the different affinities did not affect the *in vitro* blockage of influenza.

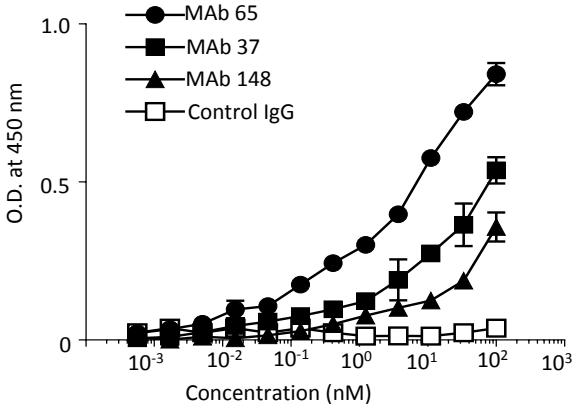

	MAb65	MAb 37	MAb 148
Kd	2.073 nM	6.957 nM	14.82 nM

Figure 2.3: Affinity assay of each MAb against the strain Udorn performed by an ELISA. Kds obtained from the assay are shown in the table under the graph.

These experiments led us to conclude that M2e-specific MAbs bind to the M2e expressed on the surface of A/Udorn/72 virus-infected cells and can reduce infectivity and plaque growth of this filamentous strain *in vitro* equally, independently to the differential affinity of the MAbs towards M2 protein; on the other hand, these MAbs did not have any effect on a non-filamentous strain like A/PR8/34. Unfortunately, whether filamentous virion morphology is a prerequisite for *in vitro* susceptibility to M2e-specific IgGs antibodies remains to be determined.

2.2.2 Characterization of A/PR8/34 and A/Udorn/72 infected cells by dSTORM

Before testing the effects of the MAbs previously studied on the filament formation of infected cells, we wanted to characterize the surface of Udorn and PR8 infected cells with dSTORM. The fact that most laboratory strains of influenza present as spherical or kidney shaped virions, the fragility of long filamentous structure as well as the limitations of conventional light microscopy techniques, can explain why filamentous influenza virions are poorly studied; therefore, we wanted to prove that dSTORM allowed visualizing and characterizing such filaments, overcoming those limitations and gaining detailed insight in the morphology of those filaments.

For this purpose, we performed dSTORM imaging of MDCK cells fixed and immunostained against HA, the most abundant membrane protein present in influenza A virus (IAV) (Figure

2.4). The images obtained revealed filamentous structures that emerged from the surface of the Udorn infected cells, whereas infection with PR8 virus did not result in the formation of such structures. Further, in order to characterize the membrane of a negative control cell, we stained the membrane of an uninfected cell with wheat germ agglutinin (WGA-mock). This way we identified the filament formation in Udorn infected cells as thin and long filaments with several microns length while, as expected, PR8 and mock sample did not show those long filament on their membrane but only small filopodia, a natural feature of MDCK cells.

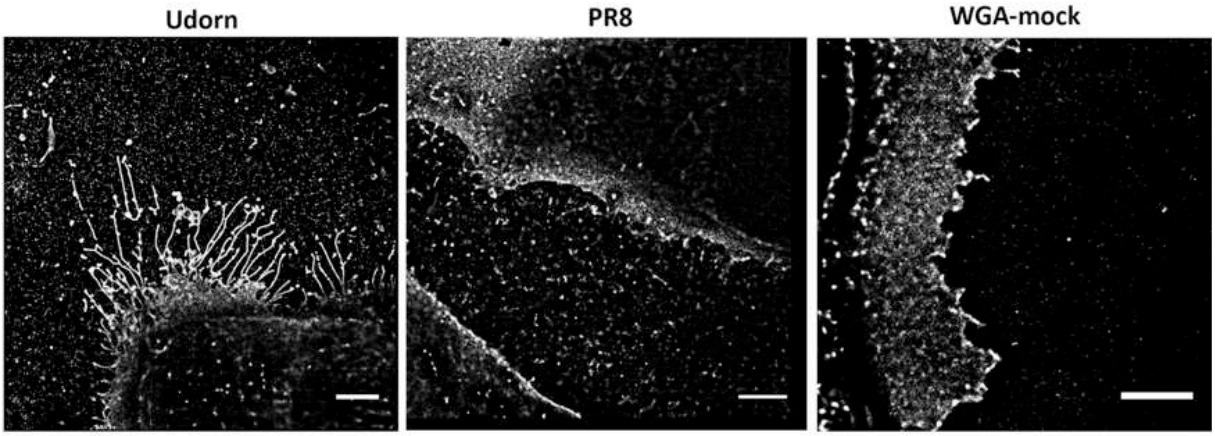

Figure 2.4: dSTORM imaging of A/Udorn/72 and A/PR8/34 infected MDCK cells revealing the filament formation in Udorn strain and the lack of it in PR8. dSTORM images of MDCK cells infected by Udorn or PR8 staining against the protein HA. To compare the membrane structure, a negative control (mock) was stained with membrane staining (WGA). Scale bar 5 µm.

Further, we also wanted to understand and characterize the role of the protein M2 on the filament formation. HA is the most abundant membrane protein in IAV, NA is approximately 10-fold less and M2 is scarcely represented[27,28]. However, it was known that M2 is highly expressed on the plasma membrane of infected cells but not in the final viral virion[29,30], so we investigated if M2 is detectable at the sites of budding filaments on infected cells, given its involvement in filament formation and budding of virions. For this purpose, influenza Udorn virus-infected MDCK cells were stained with M2e-specific IgG1 MAb 37 at 24 h after infection and then analysed by dSTORM (Figure 2.5).

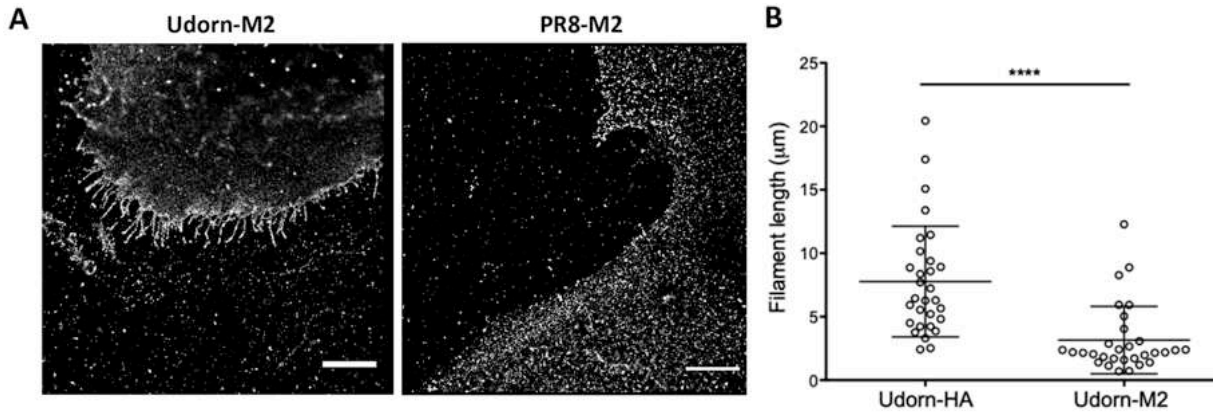

*Figure 2.5: A) dSTORM images of MDCK cells infected by Udorn or PR8 staining against the protein M2. Scale bar 5 µm. B) Graph of the length of the filaments stained against HA and M2 in Udorn sample (n=30). Scale bar 5 µm. **** $p \leq 0.0001$*

As seen in the images obtained (Figure 2.4 and Figure 2.5 A), HA and M2 were both present in Udorn filaments using super-resolution dSTORM microscopy, revealing filaments with a length of 2-20 µm length and a width of 80-250 nm (Figure 2.5 B). Filaments were traced to their origin on the cell surface using super-resolution dSTORM imaging, where M2 was observed mainly in the basilar part of budding filaments in Udorn infected cells (Figure 2.5 A). The length of Udorn HA-containing filaments was significantly longer than the M2 positive filaments (Figure 2.5 B), since M2 was only present on the basilar part of the filaments while HA was found along the whole filament of influenza. If we also compared the presence of M2 on Udorn-infected cells with PR8-infected cells we observed how M2 is only present on the membrane of PR8, confirming its role in the filament formation.

Finally, taking into account that dSTORM is a versatile and powerful technique that implemented in the study of viral structures enriched the comprehension of influenza features, we were able to reveal different filament structures, including branched filaments and filaments with enlarged oval/round structures (Figure 2.6). With super resolution microscopy we characterized the latter structures that had an apparent width of 230 to 663 nm and have been described previously as Archetti bodies[3,31,32](Figure 2.6 Left), only previously seen with electron microscopy. Also, the dSTORM images showed long filaments or long HA-containing protrusions connected neighbouring cells (Figure 2.6 Right), that were also previously reported[33].

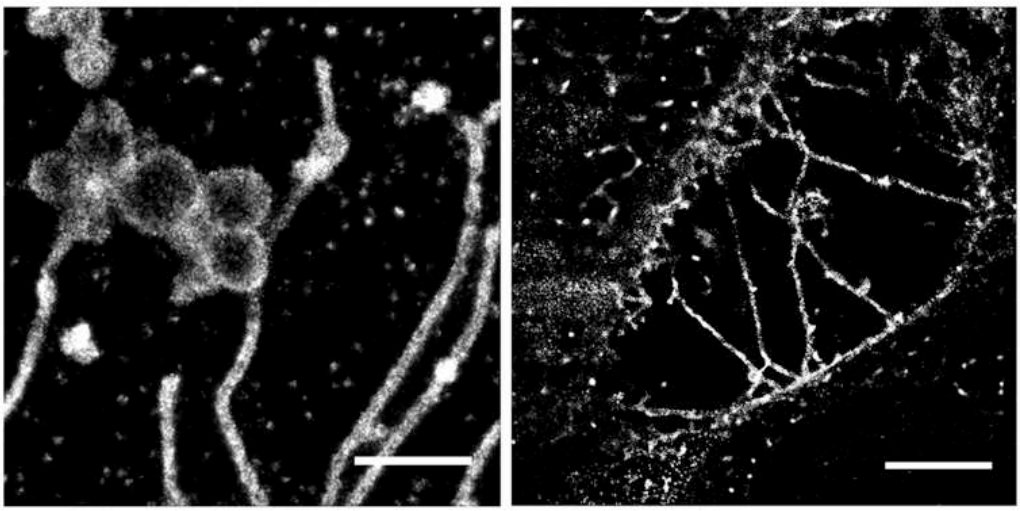

Figure 2.6: Influenza features characterized by dSTORM on Udorn samples: left Archetti bodies (scale 1 µm), right: protrusions and connexions between cells (scale 5 µm).

Taken together, super-resolution dSTORM microscopy proved to be a useful tool to study the detailed structure and protein distribution in filaments that emerge from influenza A virus infected cells.

2.2.3 Characterization of the effect of MAbs on filament formation by confocal and dSTORM

Previous studies demonstrated that the M2-specific antibody 14C2 could restrict *in vitro* growth and assembly of the Udorn virus, prevented filament formation, and caused the fragmentation of pre-existing filaments[21]. Contrarily, the inhibition of the M2 ion channel function with amantadine did not affect the filament formation by Udorn infected cells, whereas this drug prevents the post-entry fragmentation of filamentous virions in the endosomes [2,4,19].

Therefore, in order to know whether our M2e-specific IgGs could also perturb the filament formation, we infected MDCK cells with a high dose of Udorn IAV (5 multiplicity of infection (MOI)) at the same time that they were incubated with MAbs 65, 37, 148 or control IgG at concentrations of 20 or 100 µg/ml. This way cells would start the viral infection and filaments formations while were interacting with the MAbs at different concentrations. Further, cells were fixed and immunostained after 24 hours and the outcome was analysed by confocal microscopy (Figure 2.7) and subsequently by dSTORM imaging (Figure 2.8).

Although confocal microscopy cannot achieve lower resolution than 250 nm, could help in the study of the filament inhibition by MAb. By combining these two microscopy techniques, we wanted to gain a detailed insight in the morphology of those filaments and prove the importance of the applicability of super-resolution microscopy in viral studies.

Confocal images (Figure 2.7) showed a limited resolution of the filament formation around Udorn-infected cells, being distinguishable only a decrease of filament presence in the surroundings of the cell. In order to perform an analysis of the decreased production of filaments, the ratio of the perimeter of a cell to the surface of that cell was used as a parameter to study the level of filament formation on cells. The perimeter/pixel count ratio was significantly lower in M2e-specific MAb 37 and MAb 65 treated cells, confirming that inhibition of filament formation by M2e-specific MAbs.

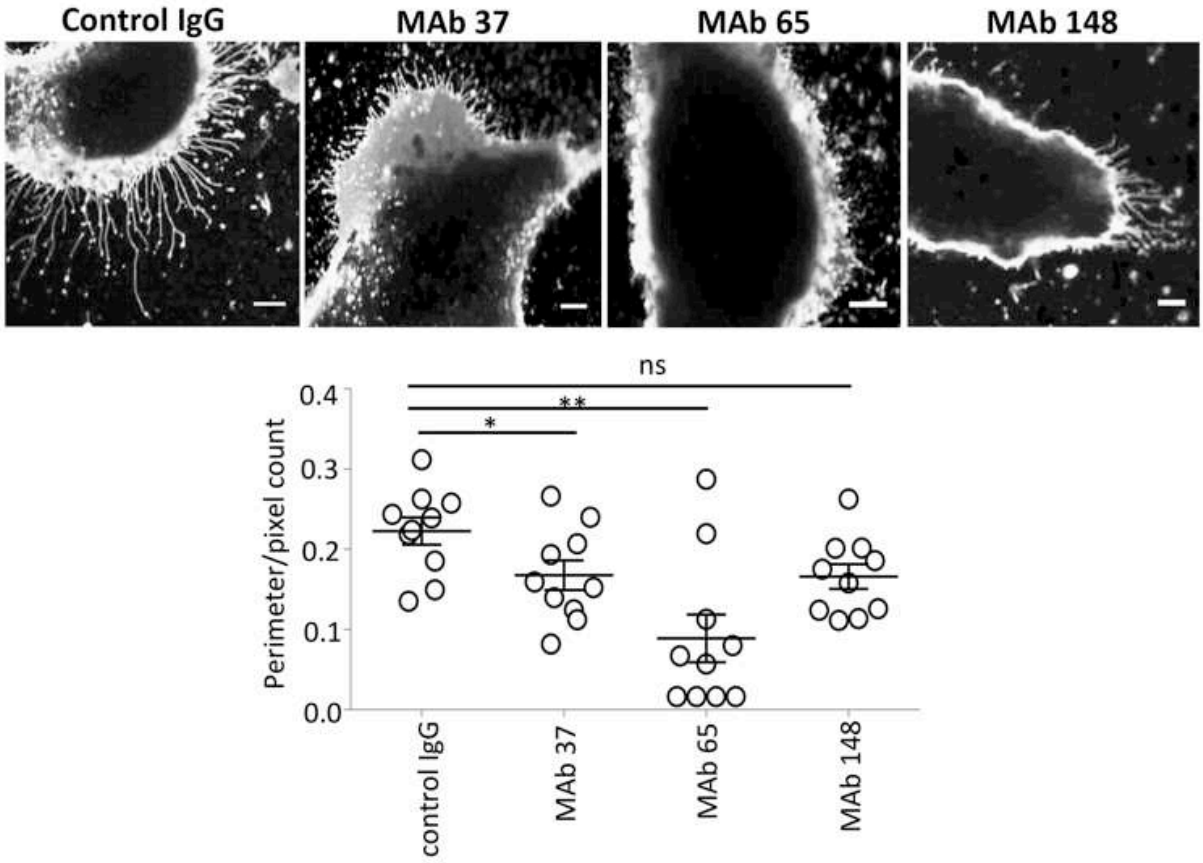

*Figure 2.7: Confocal imaging of MDCK cells infected at 5 multiplicity of infection (MOI) with Udorn and treated with different MAb (MAb 37, MAb 65 and MAb 148) at 20 µg/ml for 24 hours. The negative control consisted on incubation with a control IgG. Measurements of the perimeter/pixel count of the area of surface. Scale bar 5 µm. One-way ANOVA with multiple comparisons correction (Kruskal-Wallis test). Non-significant (ns), * p ≤ 0.05; ** p ≤ 0.01; ***p ≤ 0.001.*

Thanks to the dSTORM images we studied and measure how the shape of the filaments changed strongly compared to the negative control (Figure 2.8). Comparing the control with the treatments with the MAbs, we could perceive that numerous long filaments were observed at cell surfaces when Udorn virus-infected cells were treated with isotype control IgG (negative control).

In contrast, all samples treated with MAb filaments showed a strong different phenotype compared to the negative control filaments. The most significant change was noticed with MAb 65 treated cells but not exclusively. Filaments formed after the incubation of MAbs displayed a very different filament profile compared to the control antibody treatment: the filaments were shorted, broken and wider (Figure 2.8). Also in some cases (Figure 2.8 MAb 65) filaments were completely defective and did not look like filament at all, but protrusions with a triangle shape. In addition, these structures were not protruding in parallel but they were curved and produced branches along the filament. Most new filaments appear weaker and easier to break, whereas filaments from negative control are long and not broken at all.

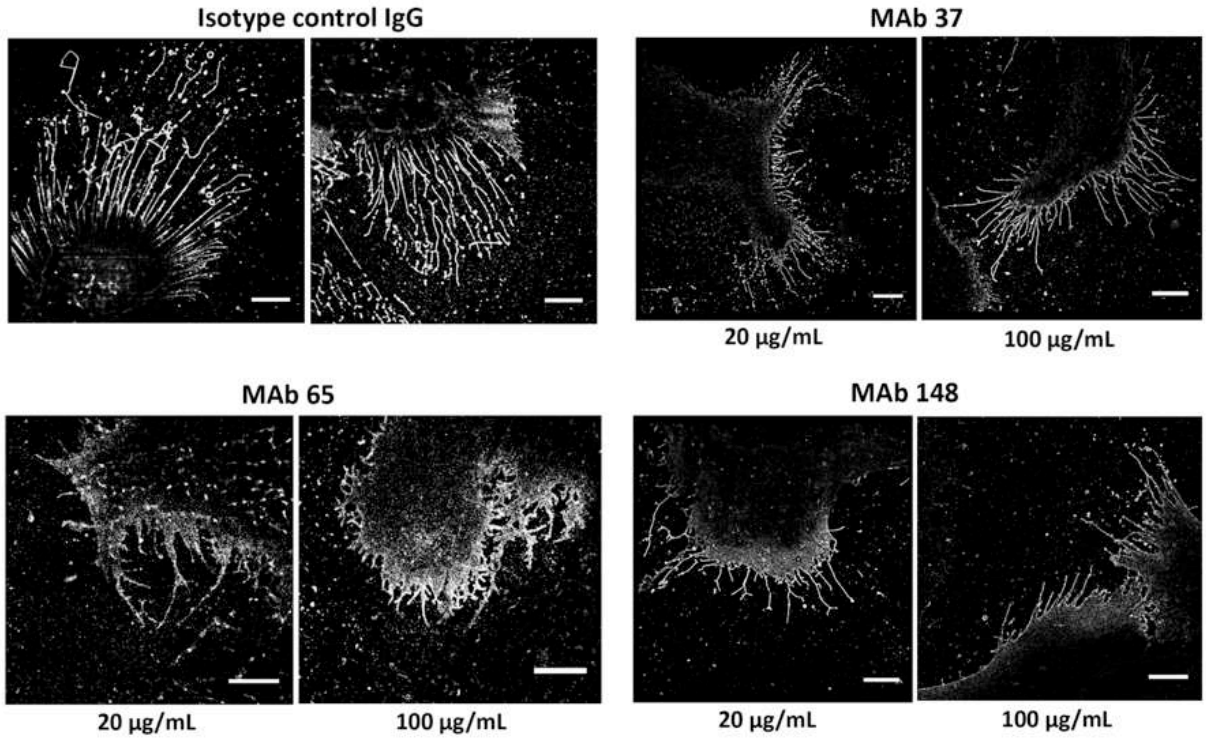

Figure 2.8: dSTORM images of MDCK cells infected at 5 multiplicity of infection (MOI) with Udorn and treated with different MAb at different concentrations (20 µg/ml and 100 µg/ml) for 24 hours. The negative control consisted on incubation with a control IgG. Scale bar 5 µm.

These detailed descriptions of the filament depletion could only be performed by dSTORM imaging, while confocal microscopy displayed difficulties in identifying the structure differences in the nanoscale, proving the need of the implementation of super-resolution microscopy in viral structure studies.

Since the changes of the phenotype in the filaments after the incubation with the M2e-specific MAbs characterized with dSTORM were very clear, we decided to quantify these changes by measuring the width and length of the filaments, the two most remarkable features. To ensure a correct measurement, we developed a criterion for selecting the filaments to be counted in order to have a representative collection of samples: the filaments selected should have the same width along the filament, be intact (not broken), lack branches and the structure would be fully reconstructed.

For this purpose we analysed cells that were infected at 5 MOI and we tested two different concentrations (100 and 20 µg/ml) of the M2e-specific MAbs. We counted in total 60 filaments from 7-9 different cells per condition with an average of 8 filaments per cell. To study the distribution of all filaments per condition, we plotted the full length and width of all filaments measured individually (Figure 2.9).

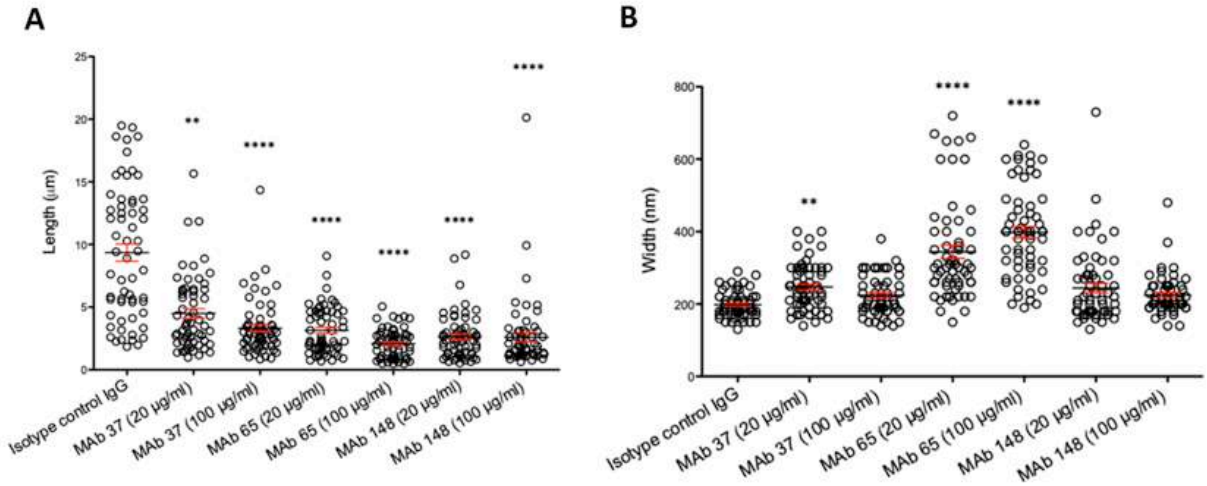

*Figure 2.9: Filament quantification of each condition, counting the filaments that were not broken, had a consistent width and without branches (n=60). A) Representation of the length (µm). B) Representation of the width (nm). One-way ANOVA. Non-significant (ns), ** p ≤ 0.01; *** p ≤ 0.001; ****p ≤ 0.0001.*

The length of the filaments of the negative control showed a wide size distribution, ranging between 2 and 20 μm. When the M2e-specific MAbs were applied at 20 μg/ml, we observed a decrease in length and an increase of the homogeneity of all samples (between 0.5 and 10 μm). Increasing the concentration of the MAbs to 100 μg/ml produced smaller filaments with similar sizes and the samples were more homogeneous (Figure 2.9 A). Performing an ANOVA test on this data, we saw how these differences between al populations of filaments treated with MAbs in comparison to the negative control are statistically significant in all cases. Thus, treatment of Udorn virus infected cells with the M2-MAbs produced a more homogeneous population of filaments that, furthermore, were much shorter.

The width is the second feature that was measured (Figure 2.9 B). The negative control showed a homogeneous width of the filaments of around 170 nm. Cells treated with MAb 65 produced filaments with variable widths, where the average width was around 250 nm and ranged from 100 nm to 610 nm as deduced from the dSTORM imaging (Figure 2.9 B). The distribution of width of these filaments showed an increase of distribution of diameter when cells are treated with MAb 65 (both concentrations) and MAb 37 (20 μg/ml). The ANOVA test indicated a statistically significant difference between the population of filaments in the negative control and MAb 65. On the contrary, incubation of infected cells with MAb 148 presented with a very small increase in the heterogeneity of the filaments. Similar results were obtained with the incubation of MAb 37 at high concentrations (100 μg/ml), where the width was not dramatically changed by the incubation with these two MAbs.

To finalize, we also measured the aspect ratio (length/diameter) of each filament (Figure 2.10). The aspect ratio decreased dramatically with the treatment, being also almost 9 times smaller in filaments with MAb 65 (100 μg/ml) than the aspect ratio in the negative control. In the rest of conditions the aspect ratio is 4 times smaller than in the negative control. With this information we could notice that cells treated with MAb 65 produced shorter and wider filaments, as previously quantified separately.

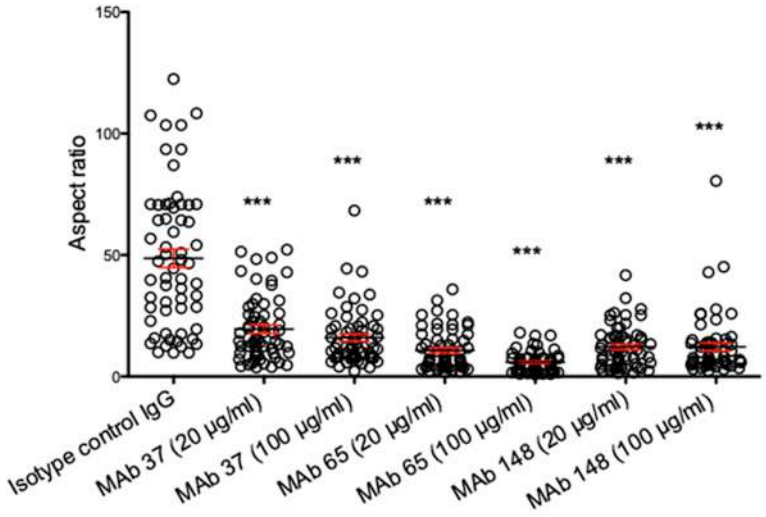

*Figure 2.10: Filament quantification of each condition, counting the filaments that were not broken, had a consistent width and without branches (n=60), representation of the aspect ratio (length/width). The negative control consisted on incubation with a control IgG. One-way ANOVA. Non-significant (ns), ** p ≤ 0.01; *** p ≤ 0.001; ****p ≤ 0.0001.*

Taking together these measurements, we confirmed that the incubation with the three different MAbs tested produced a decrease in the filament formation and depletion in the filament development. This depletion was observed stronger when MAb 65 was tested at highest concentrations (100 µg/ml) and when the viral content is extremely high (5 MOI), displaying a strong decrease in the aspect ratio and the length of the filaments and an increased of width due to the malformation occurred. This depletion was not as strongly produced when MAb 37 and MAb 148 was incubated at both concentrations, especially the increased in the width of the filaments. Notably, these are sub-diffraction features that were not accessible with confocal microscopy (Figure 2.7).

All in all, in order to understand the filament inhibition process by MAbs we observed copious amounts of filaments when cells were infected with high MOI (MOI 5) of Udorn virus. Accordingly, to fully understand the mechanism of inhibition of filament formation driven by MAbs, we tested if the inhibition produced by MAbs was performed also at low viral charges. For this purpose, we infected cells with 300, 90 and 30 plaque forming units (pfu), equivalent to 0.1, 0.03 and 0.01 MOI respectively, and then we characterized by dSTORM if the filaments formed were also inhibited by MAb 37 and 65 at 100 µg/ml, incubated during the influenza infection as before (Figure 2.11).

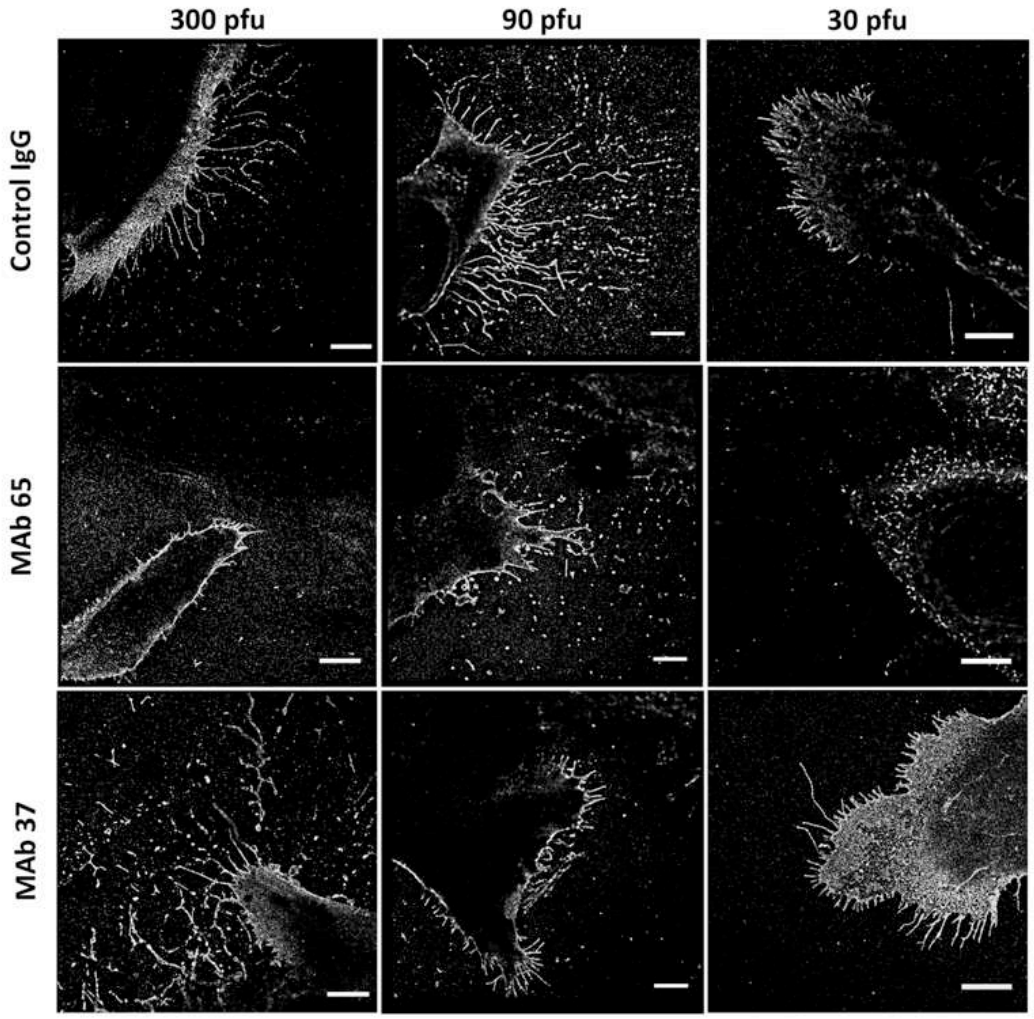

Figure 2.11: dSTORM images of MDCK cells infected with different amounts of Udorn strain IAV 300, 90 or 30 plaque forming units (pfu) (equivalent to 0.1, 0.03 and 0.01 MOI respectively) and treated with MAb 65 and 37 MAb 100 µg/ml for 24 hours. Scale bar 5 µm.

As observed in the Figure 2.11, the negative control still displayed long and thin filaments at low viral charges (Figure 2.11 Control IgG), with a decreased in the filament definition as viral content decreases, especially 30 pfu where the Udorn-infected cell displayed shorted filaments.

Interestingly, the treatment with M2e-specific antibodies 65 and 37 inhibited as well the filament formation. In the case of MAb 65 the inhibition was so strong at low viral charges that at 30 pfu the infection was almost inexistent and filaments were not formed properly. In case of MAb 37 the inhibition of filament formation is subtler and similar at all three pfu tested. Thereupon, MAbs did not need a minimum viral expression on the membrane to block filament formation, especially MAb 65, the most efficient monoclonal antibody tested.

From these results identified by dSTORM, we could determine that M2e therapeutic antibodies did not block the initial entrance and infection of the influenza virus, but interacts with the M2 protein located on the surface of the infected cell resulting in short and defective influenza filaments.

In general, the inhibition of filament formation was most apparent in MAb 65 treated cells, which also strongly inhibited plaque growth of Udorn *in vitro* and profoundly deformed the shape and width of the filaments.

2.2.4 Characterization of the effect of MAbs on pre-existing filaments by dSTORM

In order to obtain further information about the role of MAb in the binding and interaction with filament structure itself, we wanted to finish this chapter by testing if MAbs produced an effect on the filament integrity after filaments were fully formed. In the results previously described, infected cells were incubated with M2e specific MAbs 37, 65 and 148 throughout infection cycle (24 hours), therefore it did not allow us to distinguish whether M2e-specific MAbs treatment blocks the formation of filamentous particles only or if it has also a direct effect on pre-existing filamentous particles.

With this purpose we infected MDCK cells with Udorn at 5 MOI, led the filaments be formed for 24 hours post infection (HPI) and incubate the MAbs after for only 1 hours, followed by fixation and immunostaining (Figure 2.12).

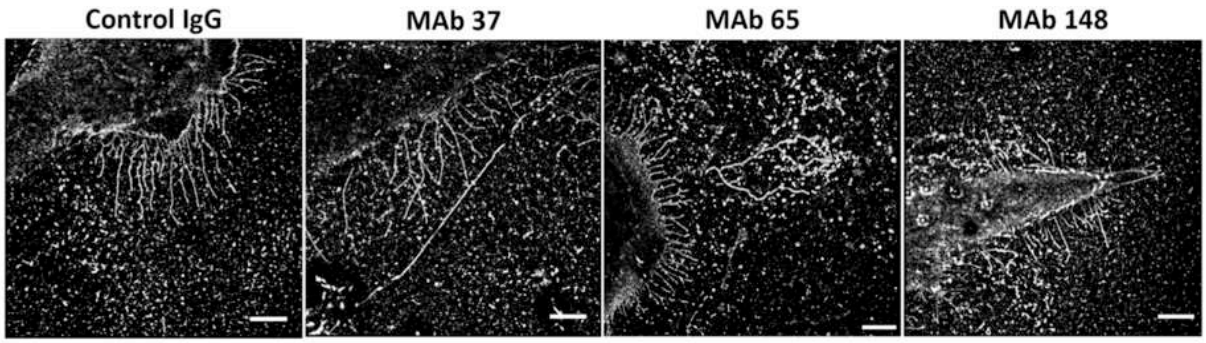

Figure 2.12: dSTORM images of MDCK cells infected for 24 hours with Udorn IAV 5 MOI, and incubated with the three MAbs 37, 65 and 148 at 100 µg/ml for 1 hour. The negative control consisted on incubation with a control IgG. Scale bar 5 µm.

As seen in the images, the treatment with the isotype control IgG had no effect on the pre-existing filaments (Figure 2.12 Control IgG), although this concrete sample had more noise on the glass due to the influenza virus release and sample manipulation. The treatment with MAbs after the production of filaments on cells produced visible breakages on existing filaments, showing in the images rests of long filaments resting next to infected cells but completely broken in pieces in all MAbs incubations.

Quantifying the length of the filaments that remained connected to the cells, using the same criterion as before (Figure 2.13), we observed how the filaments left on the cells were much shorted, with a length between 0.5 μm and 4 μm in the case of MAbs 65 and slightly longer filaments (up to 9 μm) with MAb 37 and 148. On the other hand, the negative control with the Isotype IgG showed a similar distribution than before, with filaments from 4 μm to 20 μm.

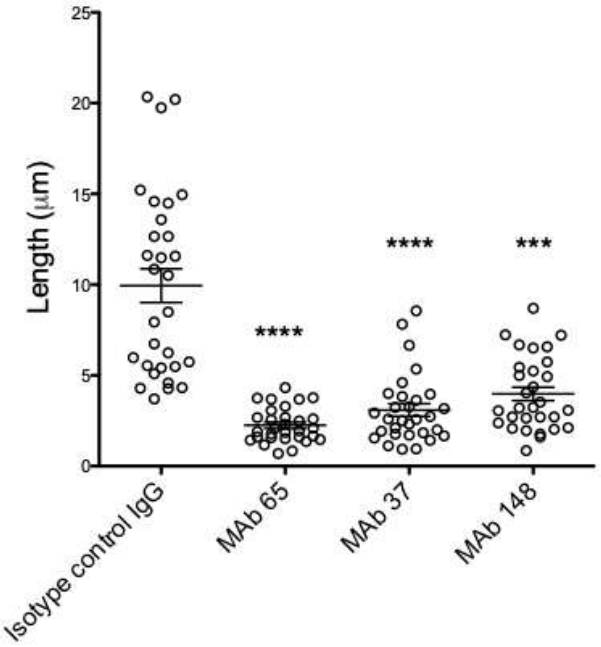

*Figure 2.13: Representation of the length (μm) of all filaments quantified (n=30) from infected cells HPI 24 and treated with MAb (100 μg/ml). The negative control consisted on incubation with a control IgG. One-way ANOVA with multiple comparisons correction (Kruskal-Wallis test). *** p ≤ 0.001; ****p ≤ 0.0001.*

Taking these results into account, we believed than fragmentation is a specific consequence of M2e-specific IgGs binding to the M2 protein in pre-existent filaments. The specific interaction between the protein M2, located in the base of the filaments, and the M2e-specific MAbs increase the fragility of the structures and further breaking them. Again we experimented an

increment of breakage of filaments with MAb 65, proving again that this MAb is the one that produced more effects on filament inhibition and fragmentation *in vitro*.

This strong effect on the filament depletion carried out by MAb 65 was observed in detailed, infecting MDCK cells with 5 MOI of Udorn and incubating the M2e MAb at different time points from the beginning of the infection: 6, 12 and 24 HPI. Right after the incubation for 1 hour with the MAb 65, the sample was either fixed (24 HPI) and immunostained or the sample was incubated to achieve a total infection time of 24 hours from the outset of the infection (6 HPI and 12 HPI).

As displayed in Figure 2.14, when MDCK cells were incubated with isotype control IgG it was observed a normal filament development with long and thin features. Observing the filaments formed when MAb 65 was present at different HPI, it was confirmed the familiar strong deficiency filament formation as observed previously. Independently the time point, MAb 65 could interact with M2 expressed on the surface of the filament and deplete their formation, interfering in the integrity of previously formed filaments.

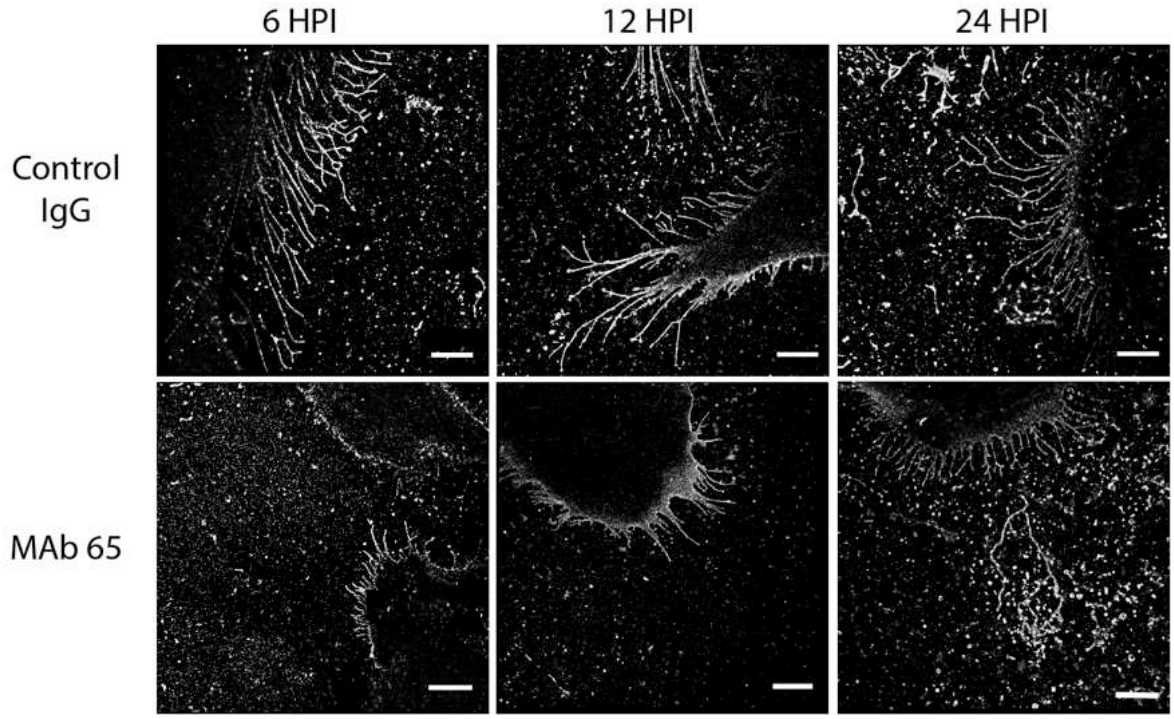

Figure 2.14: dSTORM images of MDCK cells infected for different hours post infection (6, 12 and 24 HPI) with Udorn IAV 5 MOI and incubated with MAbs 65 at 100 µg/ml for 1 hour right after the post-infection time. The negative control consisted on incubation with a control IgG. Scale bar 5 µm.

All in all, using super-resolution microscopy we confirmed our hypothesis than M2e-specific IgG could affect the influenza filament formation by blocking the correct development of the filaments at different stages of the infection and filament formation, remarking the fact that M2 plays a crucial role in filament formation and integrity. From the three M2e-specific MAb tested, MAb 65 proved to be the most efficient interfering with M2 on the membrane and avoiding the filament formation, which in combination with the plaque assays performed, confirmed the strong connection between the decrease in the infectivity of the viral particle and the truncated filament formation. However it was not established if this strong inhibition given by MAb 65 was due to the lower K_D displayed (Figure 2.3) of the epitope accessibility.

2.3 Conclusions

In this chapter we tested the *in vitro* the effects of M2e-specific IgGs on the filament formation and fragmentation in the strain Udorn of influenza using super-resolution microscopy imaging.

In general, the M2e-specific MAbs appeared to blunt filament formation and resulted in shorter and wider filaments compared to control MAb treated cells (Figure 2.15). This decrease was most apparent with MAb 65, which was able to almost fully inhibit the formation of filaments. Not only a decrease in size was seen but also a defective structure of filament formation, where filaments did not look thin and long but protrusions with triangle shape. MAb 148 and MAb 37 also inhibited the progression of the filamentous formation but less strongly, producing branched filaments as well. This could be related both to antibody affinity and to the positioning of the epitope on the M2e structure, but to determine which one we would need further experiments.

Besides, this lack of filament formation is strongly related to a decrease in influenza infectivity and viral particles release, suggesting that Udorn filaments play a crucial role in the release of newly synthetized viral particles. It has been suggested that long filaments on the surface of infected cells may be important for cell-to-cell transmission of virus[3,34]. The M2e-specific IgGs may perhaps reduce or prevent cell-to-cell transmission of virus (which would result in a reduced plaque size *in vitro*) through inhibition of filament formation and fragmentation of pre-existing filaments on the surface of infected cells.

In summary, we used super-resolution dSTORM imaging technique to characterize A/Udorn/72 virus filaments morphology, studied antibody mediated inhibition of filament formation and

fragmentation of pre-existing filaments on the surface of infected cells. Our data demonstrate that M2 is an important player in the formation of filaments on the surface of infected cells and super-resolution dSTORM microscopy proved to be a valuable tool to study structural details on the plasma membrane or budzone viral components of filaments during IAV replication.

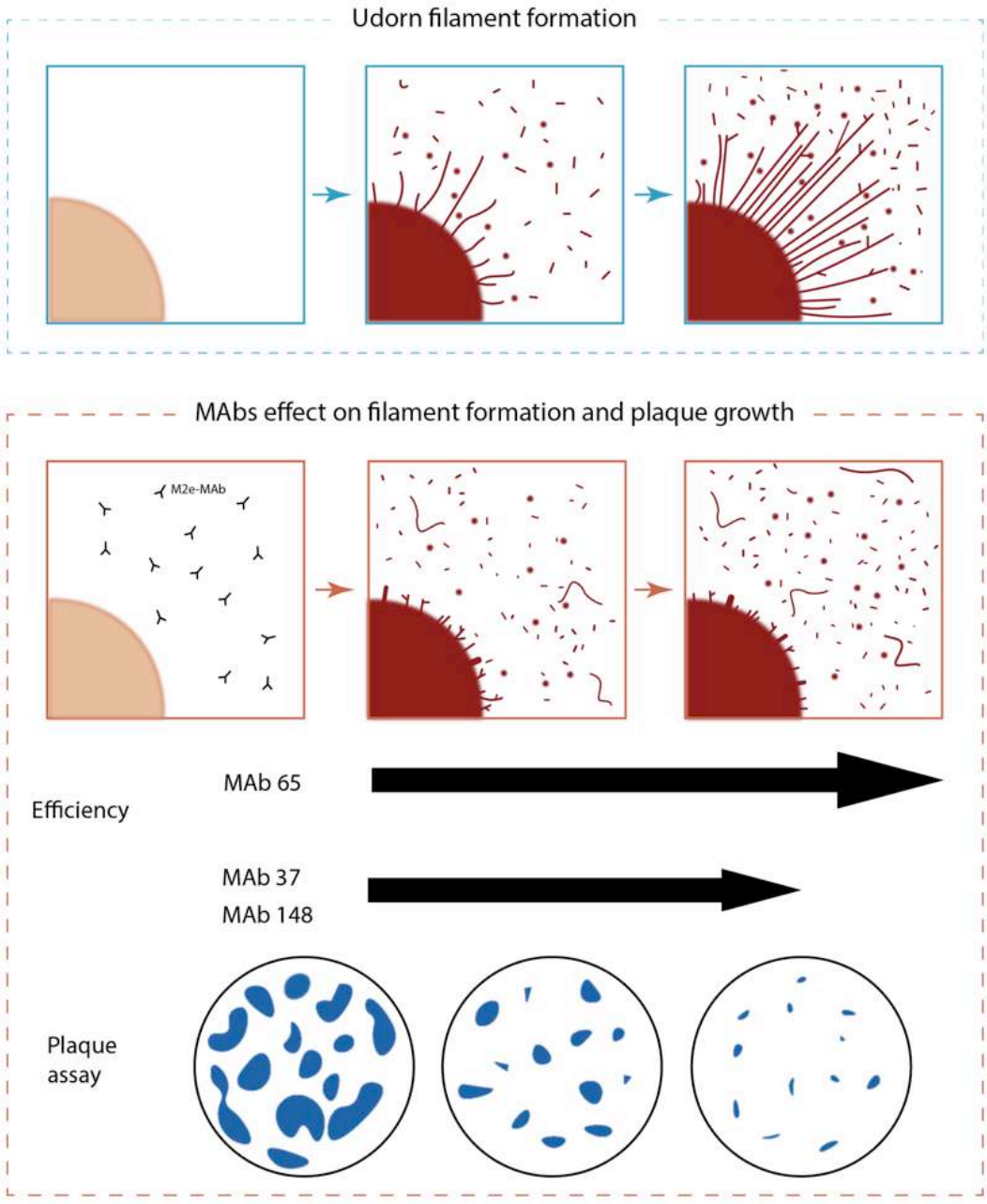

Figure 2.15: Scheme of the correlation between filament formation and viral plaque formation in influenza A/Udorn/72 virus infected cells. The different M2e-specific MAbs affect the progression of filament formation and plaque growth with variable efficiency in MDCK cells infected.

2.4 Perspectives

There is an incognita about how influenza filaments could produce viral particles and if the assembly and the budding of the virus is performed along the filament or in the apical part, basically due to the difficulty of studying such thin structures beyond the diffraction limit.

There are some models suggested by Vijayakrishnan et al. based on cryo-EM, where it is proposed that viral ribonucleoproteins (vRNPs) of influenza are organized differently depending on the structure and the type of filament, either along the whole filament or packed organized at the leading end of the filament[3]. However, they claimed to not be able to confirm the functionality of those different filaments organizations found due to the difficulty of creating pure preparation of long filaments, suggesting also that the structures that resemble vRNPs could not be vRNPs at all.

We propose that by using super-resolution microscopy, we could overcome those limitations and study with immunostaining the right composition of the filaments of influenza, likewise characterizing the types of filaments that contain all proteins of influenza. In this chapter, dSTORM have proved to be a strong and robust super-resolution microscopy technique, which in combination with the right selection of dyes (usually 568 nm and 647 nm dyes) would allow 2-colour super-resolution images.

Hence, we propose that performing multicolour imaging could help elucidating the viral content of the filaments of influenza. Applying this study in more samples and expanding it with the immunostaining of more proteins it would be possible to distinguish the functionality and composition of all influenza filaments, thanks to the versatility of dSTORM.

2.5 Materials and methods

2.5.1 Viruses culture

The virus culture and preparation was done in Xavier Saelens lab, in VIB-Ghent, by Dr. Annasaheb Kolpe.

Influenza A A/Udorn/307/72 (H3N2) and A/Puerto Rico/8/34 (H1N1) virus strains were amplified on Madin-Darby canine kidney (MDCK) cells in serum-free Dulbecco's Modified Eagle medium (DMEM) supplemented with non-essential amino acids, 2 mM L-glutamine and

0.4 mM sodium pyruvate) in the presence of 2 μg/mL TPCK-treated trypsin (Sigma) at 37°C in 5% CO_2. 96 hours after virus inoculation, the culture medium was collected, and cell debris was removed by centrifugation for 10 min at 2,500 g at 4°C, and the virus was pelleted from the supernatants by overnight centrifugation at 30,000 g at 4°C. The pellet was resuspended in sterile 20% glycerol in PBS, aliquoted and stored at −80°C until used.

2.5.2 Monoclonal antibodies and polyclonal antibodies and their epitope specificity

Synthesis and selection of monoclonal antibody was done in Xavier Saelens lab in VIB-Ghent by Dr. Annasaheb Kolpe, as described previously [25,26] and described in Table 2.1.

The MAbs were purified from the hybridoma supernatant by protein A sepharose (GE Healthcare). The affinity of MAb 37 MAb 65, and MAb 148 for M2e was determined by ELISA as per method described[25]. Convalescent anti-A/Udorn/72 mouse serum was prepared by infecting BALB/c mice with A/Udorn/72 virus. Briefly, 6-8 weeks old female BALB/c mice were anesthetized by intraperitoneal injection with a mixture of ketamine (10 mg/kg) and xylazine (60 mg/kg) and infected by intranasal administration of 50 μl PBS containing 1 x 10^5 PFU of A/Udorn/72 virus. 4 weeks after infection the mice were anesthetized and then terminally bled. Serum was prepared from the blood, heat inactivated at 56°C for 30 min and stored at -20 °C. The convalescent mouse serum has high A/Udorn/72 hemagglutination inhibition titers (HAI titer = 1280). All animal experiments were conducted according to the national (Belgian Law 14/08/1986 and 22/12/2003, Belgian Royal Decree 06/04/2010) and European legislation (EU Directives 2010/63/EU, 86/609/EEC). All experiments on mice and animal protocols were approved by the ethics committee of Ghent University (permit number EC2014-074).

2.5.3 Infection of MDCK cells and immunostaining

The virus infection of MDCK cells was done in Xavier Saelens lab, in VIB-Ghent by Dr. Annasaheb Kolpe.

MDCK cells were seeded at 3 × 10^3 cells per well in an 8 well μ-Slide (Cat. No. 80826, ibidi GmbH, Germany) for super-resolution dSTORM microscopy or at 3 x 10^5 in 12 well plates (Corning, USA, REF 353043) for multiple cycle infection. The cells were treated with either MAb 65, 37, 148 or control IgG at concentrations of 20 or 100 μg/mL for 30 minutes prior to mock infection or infection with A/Udorn/72 at MOI 5 for filament analysis. For multiple cycle

infection, MDCK cells were infected at MOI 0.01 in serum-free medium containing TPCK-treated trypsin (2 µg/mL, Sigma) and incubated with serum-free medium for 24h at 37°C. 24 hours after infection, the medium was harvested from 12 well plates and titrated by plaque assay.

The cells from 8 well µ-Slides were then washed with LPS-free PBS and fixed with 2% paraformaldehyde (PFA) at room temperature for 20 min. The cells were blocked with 1% bovine serum albumin (BSA) solution in PBS for 1 hour at room temperature and stained at room temperature for 1 hour with 1/500 diluted convalescent mouse serum against A/Udorn/72. An Alexa Fluor 647 Donkey anti-Mouse IgG (1/600; Invitrogen) was used as fluorescently labeled secondary antibody. The samples were visualized using a Leica TCS SP5 II confocal microscope (Leica Microsystems, Germany) or Zeiss LSM 780 (Carl Zeiss, Germany) with 40x magnification. For membrane staining with wheat germ agglutinin (WGA), MDCK cells were grown on Ibidi® labtecks at a confluence of 60%. After 24 hours, the cells were fixed with 4% paraformaldehyde for 15 minutes and then washed with PBS. After fixation the cells were stained with WGA-568 (Vector laboratories) at 0.4 µg/mL in PBS for 10 minutes. Then the cells were washed 3 times for 5 minutes with PBS. Subsequently, the cells were visualized under the super-resolution microscope or confocal microscopy.

2.5.4 Plaque and plaque size reduction assays

The plaque assay was done in Xavier Saelens lab, in VIB-Ghent by Dr. Annasaheb Kolpe.

Confluent monolayers of MDCK cells in 12 well plates were infected with 20-50 plaque forming units (PFU) of virus for 1 h at 37°C. The cells were washed thoroughly and overlaid with 1.2 % of Avicel RC-591 (FMC Biopolymer) alone or with MAb 65, MAb 37, MAb 148 or isotype control (IgG1+ IgG2a) at 100 µg/mL supplemented with 2 µg/mL of TPCK-treated trypsin (Sigma). The cells were then incubated for 72 h at 37°C in 5% CO_2. Avicel was subsequently removed and the cells were fixed with 4% PFA for 15 min. After permeabilization (10x Permeabilization buffer diluted in bi-distilled water, eBioscience), the cells were stained with 1/2000 diluted polyclonal goat anti-influenza ribonucleoprotein (RNP) (Biodefense and Emerging Infections Resources Repository, NIAID, NIH, NR-4282) followed by donkey-anti-goat IgG HRP-linked antibody (Santa Cruz Biotechnology, cat no. SC2020). After washing, TrueBlue peroxidase substrate (KPL) was used to visualize the plaques. The wells were also scanned and the plaque size was determined using Image J Analysis Software.

2.5.5 Super-resolution optical imaging (dSTORM)

Immuno-stained samples were used to acquire dSTORM images. Cells that had been fixed and stained in ibidi® labteck slides were washed once with PBS, after which 300 µl of STORM buffer was added. The STORM buffer consists of an oxygen scavenging system (0.5 mg/ml glucose oxidase, 40 µg/ml Catalase), 5% w/v glucose and cysteamine 100 mM in PBS.

Images were acquired using a Nikon N-STORM 4.0 system configured for total internal reflection fluorescence imaging. Excitation inclination was tuned to adjust focus and to maximize the signal-to-noise ratio. Alexa-647 and WGA-568 fluorophores were excited by illuminating the sample with a 647 nm (160 mW) and 561 (80 mW) laser, respectively, built into the microscope. During acquisition the integration time was 10ms. For the measurements with Alexa-647 20,000 frames were acquired in the 647 channel. The total time required to acquire one image was about 5 min. For the measurements with WGA-568 40,000 frames were acquired in the 561 channel. The total time required to acquire one image was about 10 minutes. Fluorescence was collected by means of a Nikon x100, 1.4 NA oil immersion objective and passed through a quad-band-pass dichroic filter (97335 Nikon). Images were recorded onto a 256 x 256 pixel region (pixel size 160 nm) of a sCMOS camera (Hamamatsu). Single-molecule localization sequences were analysed with the STORM plug-in of NIS element Nikon software.

2.5.6 Statistical analyses

Data were analysed using GraphPad Prism version 7 for Windows and OS (GraphPad Software, San Diego California; www.graphpad.com). The results are shown as individual data points with the mean ± SEM. Statistical analysis of the differences in viral titers, plaque size and *in vitro* viral kinetics were performed using the One-way ANOVA with multiple comparisons correction (Kruskal–Wallis test). For the quantification of filaments by super resolution microscopy, the acquired images were analysed using the software ImageJ. We created the following criterion for selecting the filaments to be counted: filaments should have the same width along the entire structure, not be broken or branched. 60 filaments per condition were quantified, with an average of 8 filaments per cell. 43,4% of filaments of each cell did not pass the criterion of selection. The length and width of the filaments were count manually using the ImageJ software. The length was measured after selecting the corresponding scale (0.16 µm/pixel) and the width was obtained by plotting the profile of the filament in ImageJ. Measurements were plotted as dot plot graphics using Graphpad prism software. A value of $p \leq 0.05$ was considered

statistically significant. The following statistical values and symbols are used throughout the manuscript; non-significant (ns) $p > 0.05$, * $p \leq 0.05$, ** $p \leq 0.01$, *** $p \leq 0.001$; ****$p \leq 0.0001$.

2.6 References

1. Kolpe, A. *et al.* Super-resolution microscopy reveals significant impact of M2e-specific monoclonal antibodies on influenza A virus filament formation at the host cell surface. *Sci. Rep.* **9**, 4450 (2019).
2. Rossman, J. S., Leser, G. P. & Lamb, R. A. Filamentous Influenza Virus Enters Cells via Macropinocytosis. *J. Virol.* **86**, 10950–10960 (2012).
3. Vijayakrishnan, S. *et al.* Cryotomography of Budding Influenza A Virus Reveals Filaments with Diverse Morphologies that Mostly Do Not Bear a Genome at Their Distal End. *PLOS Pathog.* **9**, e1003413 (2013).
4. Rossman, J. S. *et al.* Influenza Virus M2 Ion Channel Protein Is Necessary for Filamentous Virion Formation. *J. Virol.* **84**, 5078–5088 (2010).
5. Badham, M. & Rossman, J. Filamentous Influenza Viruses. *Curr. Clin. Microbiol. Rep.* **3**, (2016).
6. Cox, J. C., Hampson, A. W. & Hamilton, R. C. An immunofluorescence study of influenza virus filament formation. *Arch. Virol.* **63**, 275–284 (1980).
7. Chu, C. M., Dawson, I. M. & Elford, W. J. Filamentous forms associated with newly isolated influenza virus. *Lancet Lond. Engl.* **1**, 602 (1949).
8. Kilbourne, E. D. & Murphy, J. S. Genetic studies of influenza viruses. I. Viral morphology and growth capacity as exchangeable genetic traits. Rapid in ovo adaptation of early passage Asian strain isolates by combination with PR8. *J. Exp. Med.* **111**, 387–406 (1960).
9. Neumann, G., Noda, T. & Kawaoka, Y. Emergence and pandemic potential of swine-origin H1N1 influenza virus. *Nature* **459**, 931–939 (2009).
10. Choppin, P. W. & Tamm, I. Studies of two kinds of virus particles which comprise influenza A2 virus strains. II. Reactivity with virus inhibitors in normal sera. *J. Exp. Med.* **112**, 921–944 (1960).
11. Roberts, P. C., Lamb, R. A. & Compans, R. W. The M1 and M2 proteins of influenza A virus are important determinants in filamentous particle formation. *Virology* **240**, 127–137 (1998).
12. Burleigh, L. M., Calder, L. J., Skehel, J. J. & Steinhauer, D. A. Influenza A Viruses with Mutations in the M1 Helix Six Domain Display a Wide Variety of Morphological Phenotypes. *J. Virol.* **79**, 1262–1270 (2005).

13. Elleman, C. J. & Barclay, W. S. The M1 matrix protein controls the filamentous phenotype of influenza A virus. *Virology* **321**, 144–153 (2004).

14. Rossman, J. S., Jing, X., Leser, G. P. & Lamb, R. A. Influenza virus M2 protein mediates ESCRT-independent membrane scission. *Cell* **142**, 902–913 (2010).

15. Smirnov YuA, null, Kuznetsova, M. A. & Kaverin, N. V. The genetic aspects of influenza virus filamentous particle formation. *Arch. Virol.* **118**, 279–284 (1991).

16. McCown, M. F. & Pekosz, A. Distinct domains of the influenza a virus M2 protein cytoplasmic tail mediate binding to the M1 protein and facilitate infectious virus production. *J. Virol.* **80**, 8178–8189 (2006).

17. Neirynck, S. *et al.* A universal influenza A vaccine based on the extracellular domain of the M2 protein. *Nat. Med.* **5**, 1157–1163 (1999).

18. El Bakkouri, K. *et al.* Universal vaccine based on ectodomain of matrix protein 2 of influenza A: Fc receptors and alveolar macrophages mediate protection. *J. Immunol. Baltim. Md 1950* **186**, 1022–1031 (2011).

19. Zebedee, S. L. & Lamb, R. A. Influenza A virus M2 protein: monoclonal antibody restriction of virus growth and detection of M2 in virions. *J. Virol.* **62**, 2762–2772 (1988).

20. Zebedee, S. L. & Lamb, R. A. Nucleotide sequences of influenza A virus RNA segment 7: a comparison of five isolates. *Nucleic Acids Res.* **17**, 2870 (1989).

21. Noda, T. *et al.* Architecture of ribonucleoprotein complexes in influenza A virus particles. *Nature* **439**, 490–492 (2006).

22. Yi, H. *et al.* Native immunogold labeling of cell surface proteins and viral glycoproteins for cryo-electron microscopy and cryo-electron tomography applications. *J. Histochem. Cytochem. Off. J. Histochem. Soc.* **63**, 780–792 (2015).

23. Kim, D. *et al.* Correlative Stochastic Optical Reconstruction Microscopy and Electron Microscopy. *PLOS ONE* **10**, e0124581 (2015).

24. Hughey, P. G. *et al.* Effects of Antibody to the Influenza A Virus M2 Protein on M2 Surface Expression and Virus Assembly. *Virology* **212**, 411–421 (1995).

25. Van den Hoecke, S. *et al.* Hierarchical and Redundant Roles of Activating FcγRs in Protection against Influenza Disease by M2e-Specific IgG1 and IgG2a Antibodies. *J. Virol.* **91**, (2017).

26. Cho, K. J. *et al.* Structure of the extracellular domain of matrix protein 2 of influenza A virus in complex with a protective monoclonal antibody. *J. Virol.* **89**, 3700–3711 (2015).

27. Calder, L. J., Wasilewski, S., Berriman, J. A. & Rosenthal, P. B. Structural organization of a filamentous influenza A virus. *Proc. Natl. Acad. Sci.* **107**, 10685–10690 (2010).

28. Hutchinson, E. C. *et al.* Conserved and host-specific features of influenza virion

architecture. *Nat. Commun.* **5**, 4816 (2014).

29. Lamb, R. A., Zebedee, S. L. & Richardson, C. D. Influenza virus M2 protein is an integral membrane protein expressed on the infected-cell surface. *Cell* **40**, 627–633 (1985).

30. Leser, G. P. & Lamb, R. A. Influenza virus assembly and budding in raft-derived microdomains: a quantitative analysis of the surface distribution of HA, NA and M2 proteins. *Virology* **342**, 215–227 (2005).

31. Archetti, I. Appearances associated with filamentous forms of influenza viruses. *Arch. Gesamte Virusforsch.* **6**, 29–35 (1955).

32. Dadonaite, B., Vijayakrishnan, S., Fodor, E., Bhella, D. & Hutchinson, E. C. Filamentous influenza viruses. *J. Gen. Virol.* **97**, 1755–1764 (2016).

33. Roberts, K. L., Manicassamy, B. & Lamb, R. A. Influenza A virus uses intercellular connections to spread to neighboring cells. *J. Virol.* **89**, 1537–1549 (2015).

34. Roberts, P. C. & Compans, R. W. Host cell dependence of viral morphology. *Proc. Natl. Acad. Sci. U. S. A.* **95**, 5746–5751 (1998).

Chapter 3: Nanoscale mapping functional sites on nanoparticles by Points Accumulation for Imaging in Nanoscale Topography (PAINT)

This chapter reproduces almost literally the article: Nanoscale Mapping Functional Sites on Nanoparticles by Points Accumulation for Imaging in Nanoscale Topography (PAINT). Delcanale P., Miret-Ontiveros B., Arista-Romero M., Pujals S., Albertazzi L. ACS Nano. 2018;12(8):7629-7637. doi:10.1021/acsnano.7b09063[1].

My contribution to this paper was the optimization and implementation of the DNA-PAINT imaging technique with P. Delcanale on nanoparticles in vitro, including the oligo selection, the labeling of the nanoparticles and the initial imaging acquisition settings. P. Delcanale and B. Miret-Ontiveros performed all the quantifications and the design of the Matlab code for the analysis while I performed DNA-PAINT on cells, optimizing the immunostaining and parameters for this technique. The manuscript was written also in collaboration with our supervisors S. Pujals and L. Albertazzi.

3.1 Introduction

As described in Chapter 1, super-resolution microscopy is emerging as a revolutionary tool in nanomedicine and virology. Thanks to the resolution and sensitivity of these imaging techniques, the number, size, morphology and spatial distribution of nanostructures on cells and synthetic samples can be directly revealed with high accuracy and multiple colours *in vitro* [2,3,4].

Particularly, single-molecule localization microscopy (SMLM) not only possesses the ability to spatially resolve subdiffraction-sized objects, but also to quantify those specific targets previously labelled. In this context, SMLM has been applied in a broad variety of biological samples, such as in the quantification of biomolecules and receptors inside cells[5-10] and in the identification of protein distribution on viral particles. In concrete, several studies using 2-colour STORM allowed the visualization of the cluster distribution of several proteins of HIV-1[11-14],vaccinia virus[15] and influenza[16], even quantifying the protein cluster size with time.

Nevertheless, the imaging and quantification of all the proteins displayed on viral nanostructures using nanoscopy remains poorly explored. The distribution and accessibility of

proteins on viral particles is of extreme importance for the design of virus-like particles and viral structures for vaccination approaches, due to the need of homogeneous and constant present of viral proteins along the viral particle. Indeed, this mentioned imaging and quantification of functional molecules using SMLM is also poorly explored on synthetic nanostructures such as commercially available nanoparticles[17-21], due to the challenges and limitations of dSTORM in terms of multi-colouring, resolution and quantification of proteins[22-24].

In chapter 1 we introduced an alternative SMLM technique namely DNA point accumulation for imaging in nanoscale topography (DNA-PAINT), which has been proposed exploiting the selectivity and programmability of DNA hybridization[25-28]. As previously explained, unlike other SMLM techniques such as STORM, in DNA-PAINT the fluorescence blinking allowing the localization of single molecules is due to the transient interaction between two complementary single DNA strands, rather than to the photoswitching of a fluorescent probe. Being independent from a dye's photophysics to produce the fluorescence blinking, DNA-PAINT is gifted with negligible photobleaching and high multiplexing ability[29], thus providing among the best spatial resolution achievable with fluorescence microscopy (~5 nm)[30]. DNA-PAINT has been applied to image synthetic DNA-origami[25,31] and multiple cellular components like tubulin[32], exosomes[33] and membrane receptors[34], while its use for viral structures is barely exploded.

Hence, in this chapter we developed a method based on DNA-PAINT to map the active sites on the surface of nanoparticles, providing an estimation of the number and distribution of the functionalities on a single-particle basis.

This optimized and validated mapping of active sites on the surface of nanoparticles can be applied to study the active sites on other types of bionanomaterials with similar size and protein distribution such as viral particles, liposomes and exosomes[33]. Accordingly, we demonstrated the applicability of our procedure in nanoparticles (NPs) with different sizes and functionalization with emphasis on moieties, such as antibodies and streptavidin, relevant for the fields of drug delivery, molecular sensing[2,35] and important for its further application in biological samples.

Thanks to the features of DNA-PAINT, functionalized NPs were imaged in three dimensions and with high multiplexing. Spatial distribution and functional heterogeneity of the active sites

on the surface of the nanomaterial were directly explored at the level of single particles. Using a quantitative PAINT (qPAINT) approach, initially developed by Yin, Jungmann et al[36] we were able to obtain robust quantification of the number of available functional sites on the surface of NPs at the single-molecule and single-particle level.

All in all, the implementation, optimization and validation of DNA-PAINT exposed in this chapter would allow us to perform similar approaches on biological samples and viral structures.

3.2 Results and discussion

3.2.1 Characterization of the distribution of single ligands on nanoparticles by DNA-PAINT

First, NPs with functional groups were loaded with a PAINT probe. Such probe consists on a binder portion, such as the native ligand of the functional molecule or an antibody, conjugated with a short oligonucleotide DNA strand (Figure 3.1). This allows assigning one docking strand for every functional binding site on the NP. Very relevantly, only the functional molecules that are properly exposed to the solvent will be recognized by the docking strand, thereby providing a highly selective identification of the active sites. This is of crucial importance, as many reports have highlighted the issues of wrongly oriented antibodies for targeting and molecular diagnostics[37-40]. Notably, as there is no need for direct labelling that implies a covalent conjugation of fluorophores to the protein of interest, this method allows performing super-resolution on the native material.

Subsequently, a complementary fluorescently labelled oligonucleotide DNA strand (imager strand, Figure 3.1 PAINT imaging) is added to the solution. Transient binding between docking and imager strand, driven by DNA hybridization, allows imaging and localization of single molecules and reconstruction of a super-resolution image. Such an image contains information about the distribution and number of active binding sites that can be analysed using the qPAINT algorithm, among others.

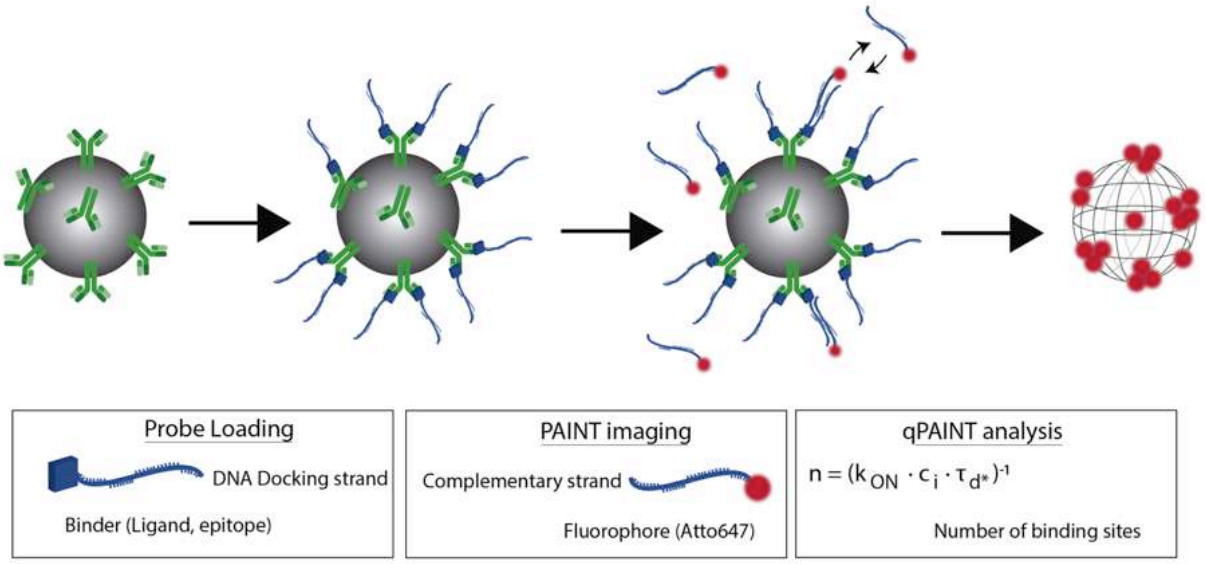

Figure 3.1: diagram of DNA-PAINT approach. Functional sites of the nanoparticle can be labelled with antibodies or natural ligands such as biotin, bound to a binder containing a DNA docking strand. This docking strand is complementary to the PAINT imaging probe, consisting in a dye (Atto647) and a small sequence of DNA. Only the available functional sites will bind to the imaging strand, thus will be visible, while the functional sites that are no available won't be detected. The binding of the docking strand and the imaging strand is transient and allow the localization of the point of emission with SMLM and quantify the amount of functional sites on the particle.

For our first approach, we imaged two types of nanoparticles using our DNA-PAINT methodology. First, streptavidin particles of 300 nm (Figure 3.2) were imaged using a biotin-docking DNA probe and an optimized concentration of imager strand (0.1 nM) in solution, to avoid overloading of the densely packed docking sites on the NP surface. The retrieved localizations reconstructed full circles corresponding to the projection in two dimensions of the NPs (Figure 3.2A-C, green). Evidently, DNA-PAINT was able to solve the structures with nanometric resolution, revealing both the intraparticle distribution of binding sites and the differences among particles in terms of number of localizations (Figure 3.2 D).

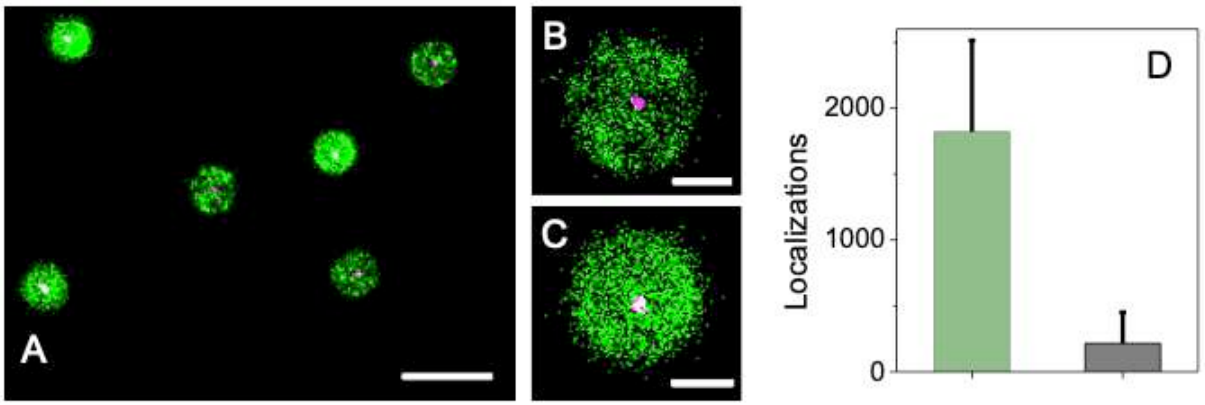

Figure 3.2: DNA-PAINT images of streptavidin-coated NPs saturated with biotin-docking strands in a large field (A, scale bar 500 nm) and in close-ups (B and C, scale bar 150 nm). DNA-PAINT localizations are shown in green, while localizations in magenta are due to NP-conjugated Cy3 dyes, which were used for the mechanical drift correction and to indicate the centre of NPs. D) Number of DNA-PAINT localizations per NP for correct (green) and wrong (grey) docking-imager pairing.

Secondly, with a similar approach we imaged immune-functionalized microspheres (~3.2 μm) by saturating the anti-digoxigenin antibodies exposed on their surface with digoxigenin-conjugated docking strands, exploiting the high affinity of the antibody-antigen pair. An imager strand (0.5 nM) was then added in solution to obtain the single-molecule localizations and the DNA-PAINT images (Figure 3.3). As for streptavidin-coated NPs, DNA-PAINT images of microspheres offer functional information since the retrieved localizations reflected the presence of docking sites on the irradiated region of the particle. Notably, if the antigen-binding site of an antibody is not properly exposed to the solvent for features such as improper orientation[37,38,39], it is not imaged by the docking-imager strand system, so the presence of localizations reflects the amount of available active sites, a crucial issue for immunoparticles.

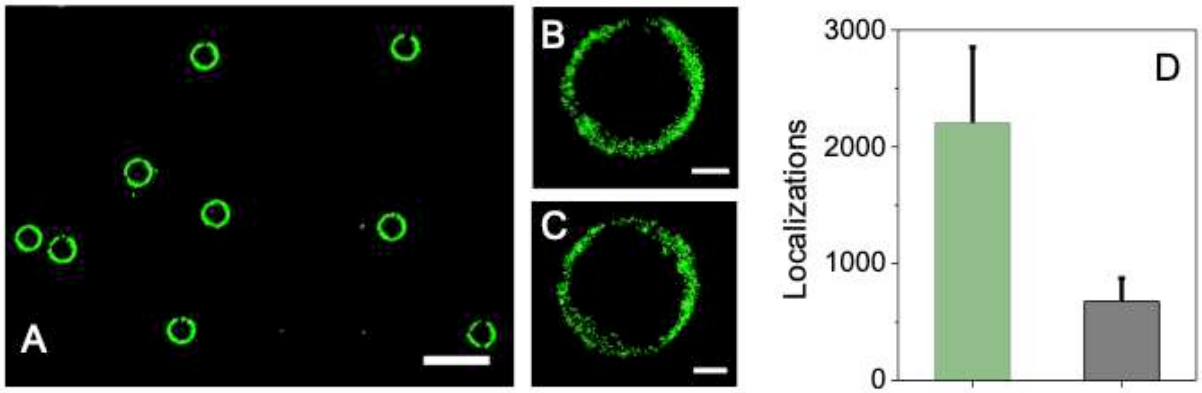

Figure 3.3: DNA-PAINT images of anti-digoxigenin coated microspheres saturated with digoxigenin-docking strands in a large field (E, scale bar 5 µm) and in close-ups (B-C scale bar 500 nm). DNA-PAINT localizations are shown in green. D) Number of DNA-PAINT localizations within the focal plane per microsphere for correct (green) and wrong (grey) docking-imager strands pairing.

Given the presence of free imager strands in solution, specific and controllable interaction between imager and docking strands is a key issue in DNA-PAINT. To check the specificity of docking-imager strand recognition in our systems, we performed control experiments where NPs and microspheres were saturated with docking strands whose oligonucleotide sequence was not complementary to the one of the imager strand (wrong pairing), and we compared the number of DNA-PAINT localizations with the one obtained with correct pairing. Both for streptavidin-coated NPs (Figure 3.2D) and for antibody-coated microspheres (Figure 3.3D), the wrong pairing gives significant lower localizations, indicating that the specific binding is predominant. The decreased difference between correct and wrong pairing observed for antibody-coated particles in comparison with streptavidin-coated NPs was attributed to a different density of biofunctionalization, as reported by the manufacturer. Indeed, when functionalization density is low, more surface is available for nonspecific interactions.

Our method allows the investigation of NP properties at single-particle level, obtaining information about heterogeneity of properties that are hard to obtain with ensemble methods. We, therefore, carried out a semi-quantitative analysis on the size and number of localizations for functionalized NPs. The size of single particles was evaluated from the subdiffraction images by means of a clustering algorithm and subsequent fitting of the clusters. NPs were homogeneous in size: the population distribution shows a Gaussian profile with most NPs sized between 300 and 360 nm (Figure 3.4 A).

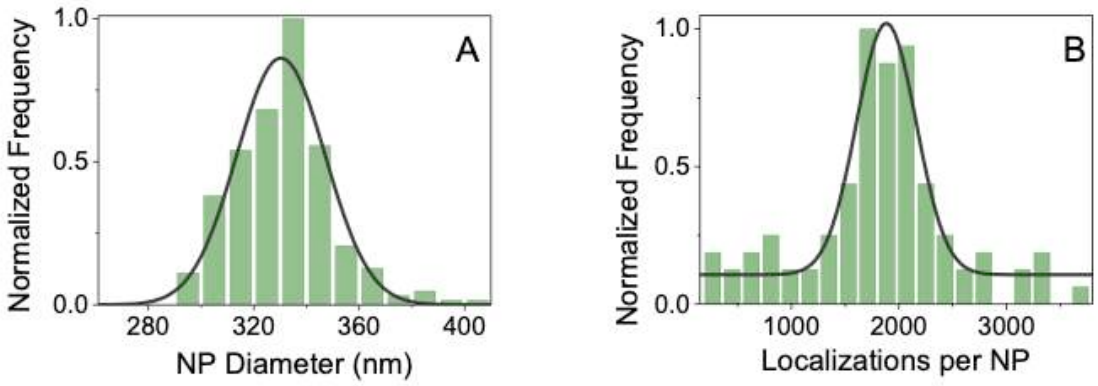

Figure 3.4: Distributions of the NP diameter (A, green) and the number of localizations per NP (B, green) obtained from DNA-PAINT images of streptavidin-coated NPs saturated with biotin-docking strands. The grey lines represent the results of the fitting with a Gaussian model.

Information about NP functionalization can be also extracted as a first approximation by evaluating the number of localizations per NP, which reflects the amount of active functional sites. The distribution of the number of localizations per NP (Figure 3.4 B) shows an average of 1800 localizations, but with considerable variability within the single NPs, with a non-negligible amount of NPs showing a number of localizations outside the main Gaussian-distributed population, below 1000 and above 3000. This is qualitatively appreciable also in Figure 3.2, where NPs of the same size, but differing in the number and distribution of localizations were individuated. These results point out a marked heterogeneity in the amount of sites on the NPs in spite of the geometrical homogeneity of the NPs, which implies relevant consequences on their functionality.

Besides inter-particle heterogeneities, intraparticle information can also be obtained with DNA-PAINT imaging. To explore this possibility, we prepared a sample in which the intraparticle heterogeneity of binding site distribution was artificially enhanced by exposing aggregated streptavidin-coated NPs to a solution of docking strand, resulting in less homogeneous functionalization. DNA-PAINT imaging (Figure 3.5 A and C) revealed the presence of a clustered intraparticle distribution of localizations of many NPs, reflecting a heterogeneous organization of the functional sited on the NP surface.

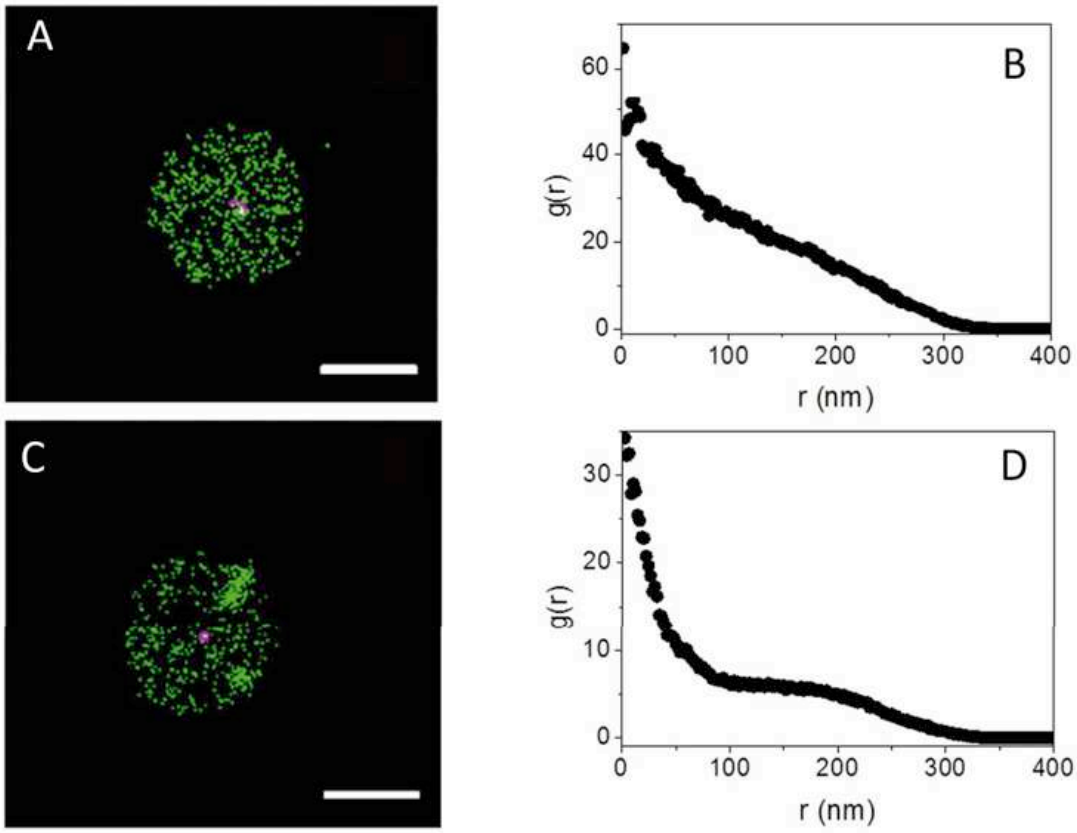

Figure 3.5: DNA-PAINT images of representative streptavidin-coated NPs loaded with biotin-docking strands (A and C scale bar 200 nm) and their corresponding pair autocorrelation functions g(r) (B and D). DNA-PAINT localizations are shown in green while localizations in magenta are due to NP-conjugated Cy3 dyes, which were used for the mechanical drift correction and to indicate the NPs centre.

This was further appreciated by inspecting the autocorrelation function obtained from NP localizations, which is an effective tool to quantify spatial organization in heterogeneous systems (Figure 3.5 C and D). By loading streptavidin-coated NPs with biotin-docking strand in a heterogeneous way led us to differentiate between population of NPs with homogeneous intra-particle distribution or heterogeneous intraparticle distribution. A rather homogeneous intra-particle distribution of localizations (Figure 3.5 A-B) produced an autocorrelation function that smoothly decreases to zero within a distance corresponding to the NP size. On the other hand, when intra-particle localizations are distributed heterogeneously, like in clusters (Figure 3.5 C-D), the resulting autocorrelation function displays a wavier trend, that is typically associated to clustered or patterned distributions.

To sum up, the ability of DNA-PAINT to address intra- and inter-particle heterogeneity at the single molecule level allows for the characterization with significant detail.

3.2.2 Multiplexed and 3D Characterization of the distribution of ligands on nanoparticles

Further, exploiting the stability of the system, we were able to acquire three-dimensional DNA-PAINT images of functionalized NPs, where the z-coordinates were obtained by astigmatism (Figure 3.6 A). As expected, NPs showed a spherical shape with a rather homogeneous distribution of localizations in the three dimensions.

Moreover, we wanted to test the highly multiplexed imaging with DNA-PAINT that was recently demonstrated on synthetic DNA structures and fixed cellular components[31]. In this approach developed by Jungmann et al., every target structure was labelled with docking strands having different oligonucleotide sequences. Sequentially, each complementary imager strand, bearing the same dye, was added in solution to acquire one image and then washed out. A multicolour image was then produced, by merging and assigning a false colour to every image obtained with a different imager strand.

In order to prove the viability of this approach for functional nanomaterials, we applied four different probe combinations to streptavidin-coated NPs: in three of them, the streptavidin solution was saturated with three different biotin-docking strands, respectively; in the fourth solution, NPs were exposed to all three biotin-docking strands at the same time, so that the streptavidins were saturated by a mixture of the three types of docking. The four populations were then mixed and imaged by adding sequentially the complementary imager strands using a fluidic device (Figure 3.6 B-F).

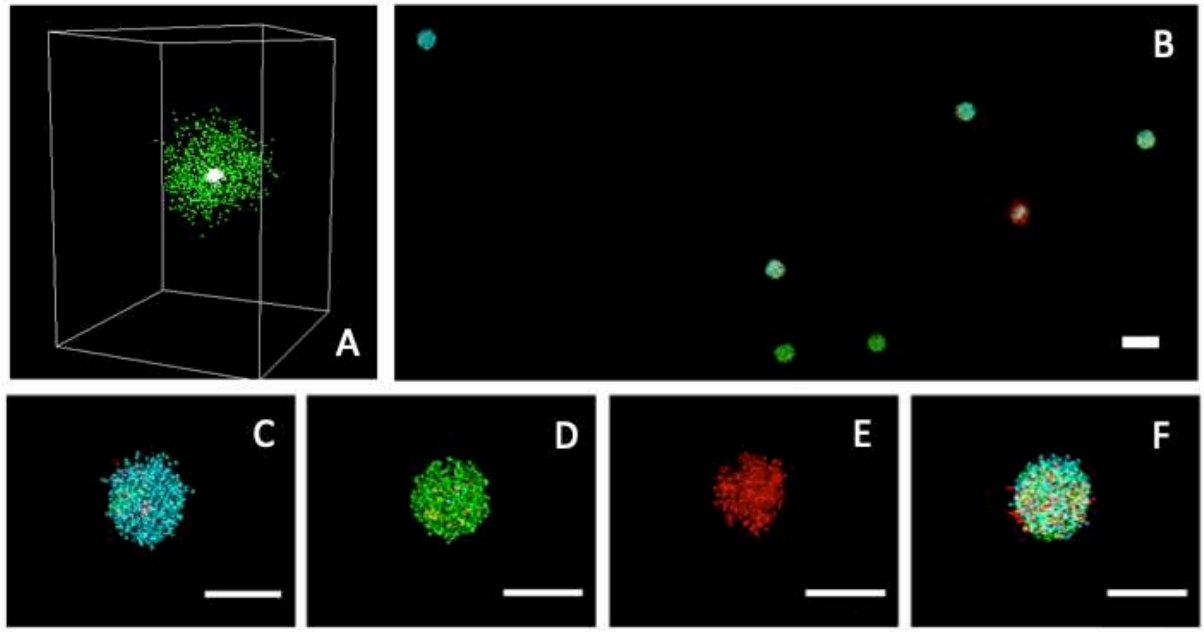

Figure 3.6: A) Three-dimensional DNA-PAINT image of a streptavidin-coated NP saturated with biotin-docking strands. B-F) multiplexed DNA-PAINT imaging of streptavidin-coated NPs loaded with different biotin-docking strands. Different false colours are assigned to localizations obtained with imager strand 1 (cyan), 2 (green), and 3 (red) in the multicolour image (B, scale bar 600 nm). Close-ups of selected NPs loaded with docking strand 1 (C), 2 (D) 3 (E) and 1, 2, 3 together (F) are shown. (Scale bar 300 nm).

The four populations are distinguishable with minimal cross-talk in the multicolour image, as can be appreciated in Figure 3.6 C-F; three particles functionalized with three different docking strands appear with different colours (cyan, green and red), while a particle functionalized with all three docking strands appears white, due to the superposition of the three colours (Figure 3.6F).

These results demonstrated that a highly multiplexed imaging of a functional material is possible with DNA-PAINT. Remarkably, multicolour DNA-PAINT imaging extends the possibilities of detecting an intraparticle distribution for multiple types of docking sites. This was proved by considering separately the three single-colour images of the same NPs loaded simultaneously with the three docking strands (Figure 3.7). The single-colour images displayed different intraparticle distributions for the different docking sites: while in some cases single-colour localizations were rather homogeneously distributed within the NP area, for many NPs the localizations segregate into clusters that were different for the three single-colour channels.

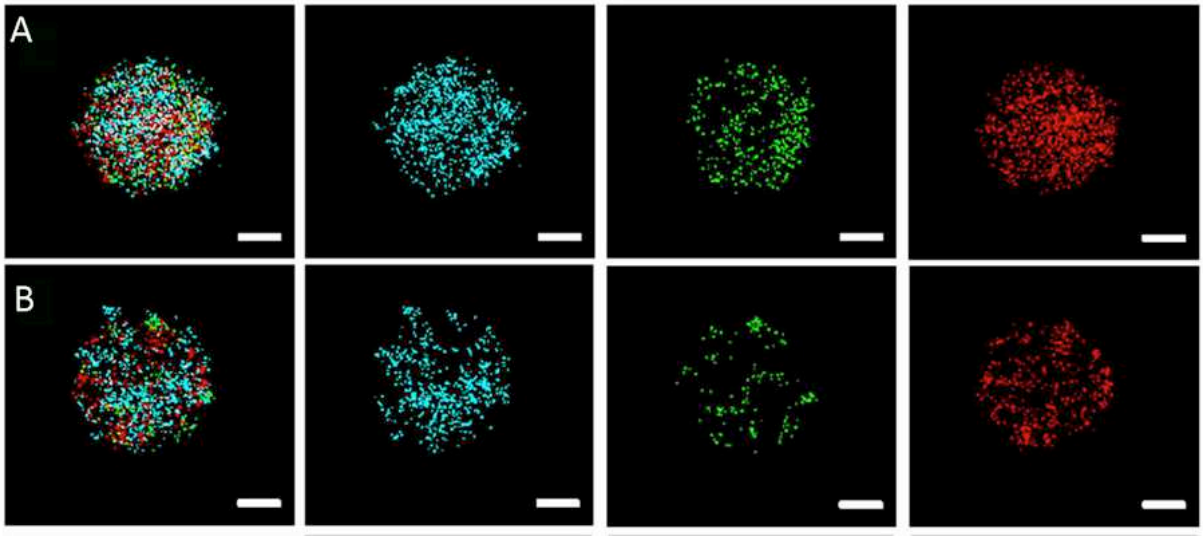

Figure 3.7: Multiplexed DNA-PAINT imaging of streptavidin-coated NPs loaded simultaneously with three different biotin-docking strands. Different false colours are assigned to localizations obtained with imager strand 1 (cyan), 2 (green) and 3 (red). For each NP (A, B) the image resulting from the superimposition of the three colours (left column) and the corresponding single-colour channels (right columns) are shown. Scale bars 100 nm.

The selectivity of DNA hybridization allowed the specific mapping of different docking sites on the NPs decorated with the same surface biomolecules, such as the streptavidin-biotin pair. However, functional particles often exhibit different surface biomolecules, typically multiple antibodies that should be effectively targeted by multiplexed imaging.

We therefore applied multiplexed DNA-PAINT to NPs coated with two different antibodies: anti-digoxigenin and anti-biotin. Antibody-coated particles were first exposed to a solution containing the two antigens, digoxigenin and biotin, bearing two different DNA docking strands to allow the targeting of the available sites of antibodies. Then, DNA-PAINT imaging was performed introducing sequentially the complementary imager strand (Figure 3.8 A). Two-colour images of different antibody-coated particles are shown on Figure 3.8 B-D, where green localizations map the anti-digoxigenin active sites, while red localizations map anti-biotin active sites.

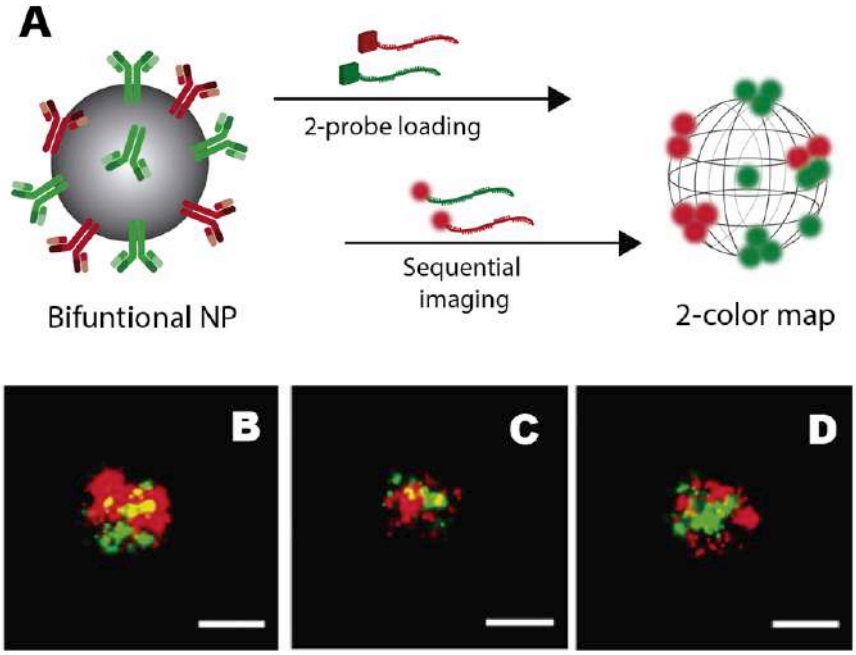

Figure 3.8: A) Representation of the multiplexed immunolabelling of the nanoparticles. B-D) Multiplexed DNA-PAINT images of particles coated with anti-digoxigenin and anti-biotin antibodies, loaded with digoxigenin-docking strand 1 and biotin-docking strand 2 (scale bar 300 nm). False colour assigned to localizations with imager strand 1 (green) and 2 (red).

This result demonstrates than multiplexed DNA-PAINT selectively discriminated different antibody-antigen pairs. Thus, mapping of active sited for different biofunctionalizations on a particle's surface is possible. Additionally, as previously demonstrated for streptavidin-coated NPs, the intraparticle distribution of the active sites of different biomolecules can be clearly recognized. Indeed, clustered distributions of the localizations for the two colours are appreciable for the particles shown in Figure 3.8.

3.2.3 Quantification of functional sites on NPs by qPAINT

Finally, we used the qPAINT approach previously developed[36] to obtain a robust estimation of the exact number of functional sites on the NP surface. Unlike other quantification methods based on SMLM, qPAINT relies on stable and well-controllable kinetic information, i.e., the dark time between binding events, to retrieve the number of docking sites.

We applied this approach to directly count the available functional sites on the surface of NPs, the exact number of which is hard to obtain by visual inspection of subdiffraction resolution images and is often retrieved by indirect ensemble techniques[35,41].

The parameter of interest for qPAINT is the mean dark time (τ_{d*}) between fluorescence events in intensity versus time traces. τ_{d*} is obtained experimentally from the cumulative distribution function (CDF) of individual dark times, and it is related to the number of available docking sites (n) by the equation $n= (k_{ON}c_i\tau_{d*})^{-1}$, where k_{oN} is the second-order association rate of the docking-imager pair and c_i is the concentration of imager strand solution.

Importantly, qPAINT relies on a calibration to determine the value for the imager strand's influx rate parameter ($k_{ON}c_i$). While c_i is easily controllable in an experiment, the value of k_{ON} can be obtained considering the reversible binding kinetics of a single docking site (n = 1) exposed to a know c_i. Under these calibration conditions, $\tau d^* = (k_{ON}c_i)^{-1}$.

In our system, calibration is ideally carried out on NPs exposing a single active docking site. A sample was then prepared exposing the streptavidin-coated NPs to a low concentration (0.5 nM) of biotin-docking strand. The loaded NPs were then imaged with DNA-PAINT adding 5 nM of complementary imager strand to maximize the signal-to-noise ratio. These conditions allowed obtaining images of NPs decorated with only a few active docking sites, but clearly distinguishable from the background due to nonspecific interactions (Figure 3.9).

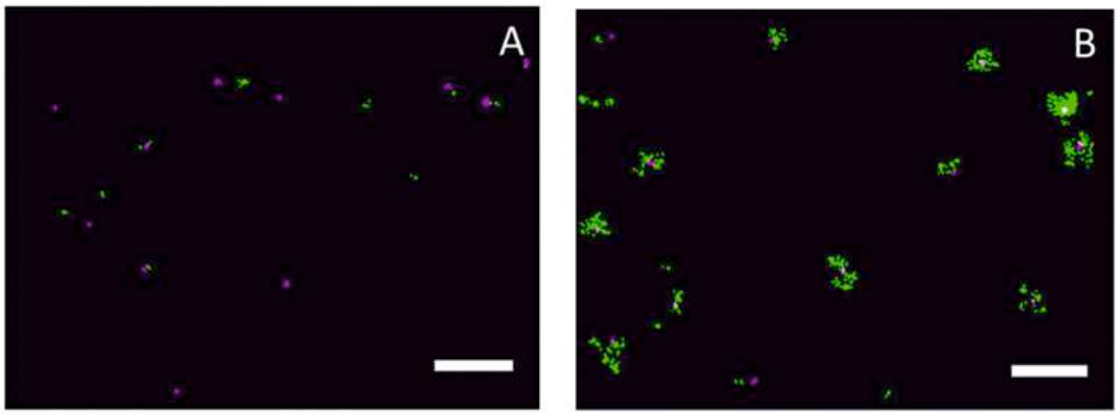

Figure 3.9: Comparison between two DNA-PAINT images of NPs obtained with wrong pairing (A) and correct pairing (B) of docking and imager strands for calibration of qPAINT. Localizations are shown in green. Magenta indicates the centre of the NPs. Scale bars 1 µm.

Calibration NPs were then selected with the following criteria: (I) a single spot of localizations was clearly identifiable; (II) the retrieved size of the spot was consistent with the one of a subdiffraction-sized docking site (with few tens of nm, fwhm of the spots about 25 nm); (III) the spot was located within the NP area (the image of a representative NP used for calibration is shown in Figure 3.10A).

The number of localizations for the selected NPs was between 20 and 40, above the level of the nonspecific background determined with the wrong pairing control (Figure 3.9 A). The τd^* values for the calibration NPs were then determined by fitting the CDF with an exponential model. An example is shown in Figure 3.10 B and yielded a value for the K_{ON} of 3.3 X 10^6 M^{-1} s^{-1}, very consistent with previously reported values (2 X 10^6 M^{-1} s^{-1}) obtained in similar DNA-PAINT experiments on DNA-Origami[25,36].

Using this in situ calibration, we quantified the actual number of available functional docking sites on the surface of NPs exposed to increasing concentrations of biotin-docking strand, from 0.5 mM to 10 µM (Figure 3.10 C). NPs appeared saturated when exposed to docking strand concentrations above 100 nM, and they showed an average of 550 functional sites available on the surface, even with a high variability between the individual NPs (Figure 3.10 D).

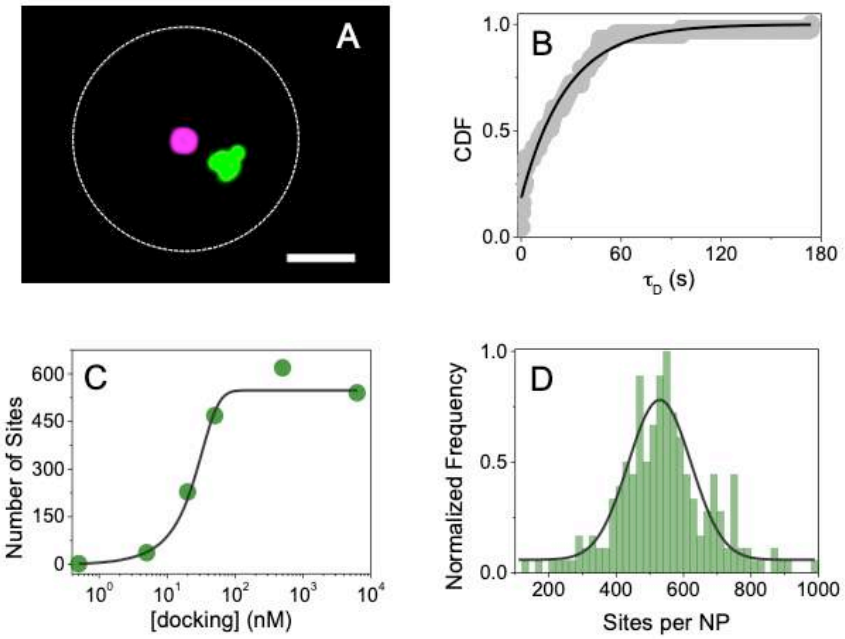

Figure 3.10: Calibration and calculations of qPAINT on streptavidin-coated NP. A) DNA-PAINT image of a streptavidin-coated NP used for qPAINT calibration. The NP is loaded with a single available biotin-docking strand.

B) Cumulative distribution function (CDF) of individual dark times obtained for a calibration NP (grey circles). The black line shows the result of the fitting with an exponential model. C) Number of available docking sites per NP retrieved with qPAINT. D) Normalized distribution for the number of available docking sites per NP retrieved by qPAINT for NPs saturated with biotin-docking strands (green).

This value is line with an approximate geometrical estimation (approximately 800 sites per NP), based on the average area covered by streptavidin, as determined by atomic force microscopy[42] and considering four sites available per streptavidin. The difference with our qPAINT result can be explained by the presence of nonactive sites on the streptavidin coating the NPs. Moreover, when NPs were exposed to lower biotin-docking strand concentrations (0.5-50 nM), the number of available sites increases with the expected linear trend at increasing the docking concentration.

These results show the ability of qPAINT to provide a direct estimation of the number of active sites on a functional NP and its heterogeneity among a NP population.

3.3 Conclusions

In this chapter we tested how sensitive is DNA-PAINT for studying functional sites on nanoparticles, in order to characterize the ligand distribution and available sites in the nanoscale.

We demonstrated that the DNA-PAINT method proved to be a sensitive tool for geometrical and functional characterizations of nanomaterials, offering minimally invasive optical imaging with subdiffraction resolution, together with highly selective recognition of available functional sites on the material's surface.

Multiplexed DNA-PAINT imaging allowed the discrimination of different populations of NPs having the same size but different surface functionalization. Remarkably, the possibility of selective multiplexed imaging was first explored for streptavidin-coated NPs and then demonstrated for particles having different functional biomolecules, where multiplexing efficiently mapped different antibody-antigen pairs. Moreover, counting the available functional sites on single streptavidin-coated NPs was demonstrated using a qPAINT approach with a robust in situ calibration.

Importantly, this approach is independent of the choice of a specific dye or exogenous labelling system. Indeed, the docking strands spontaneously target the active functional sites exploiting the native molecule-ligand interaction, without the need for direct conjugation with a fluorescent reporter. The possibility to selectively count only the active sites of functional biomolecules on a material is a distinctive feature of qPAINT. However, the effective targeting of these sites is of crucial importance in qPAINT as in other quantitative techniques, and should be carefully considered.

Furthermore, DNA-PAINT provided quantitative insights about the distribution of the available functional sites at both inter- and intraparticle levels, offering additional information for a rational design of these nanomaterials. Interestingly, the presence of a clustered organization of the active sites was identified for many NPs. Multiple physicochemical reasons can be at the origin of this heterogeneity. Steric barriers, protein-protein obstacles or wrong orientation of the biomolecules at the particle surface are likely to reduce the uniform exposure of the sited to the solvent, creating recognizable intraparticle, along with interparticle heterogeneity. This is in line with qPAINT results, which indicate that only a fraction of the potential binding sites on the streptavidin-coated NPs are effectively saturated with biotin-docking strands, and thus were counted.

This mapping method based on DNA-PAINT is generally applicable to a wide range of nanomaterials with different size, shape, functionalization systems and nature, allowing to gain direct quantitative characterization of a functional nanomaterial at the level of a single molecule, which is of primary interest for drug delivery or biosensing applications.

3.4 Perspectives

DNA-PAINT proved to be a successful technique to study nanomaterials. The perspective of this technique is very broad since it led us to study single molecules in the nanoscale with a multiplexing approach, almost impossible in STORM due to the limitation of the dye selection.

Although DNA-PAINT was previously proved to be viable in vitro[29,31,36], we wanted to test the possibility to study biological and viral structures by the implementation of this system. Instead of using natural targets against a protein, as we did in NPs with biotin-streptavidin interaction, we optimized this technique using secondary antibodies that contained docking strands

chemically attached by a maleimide link[32]. The main advantage of this approach is the facility to employ this technique to any type of cell target and sample by an immunostaining protocol.
To test this applicability, we immunostained fixed HeLa cells with primary antibodies against mitochondria and tubulin, followed by the corresponding secondary antibody with ~2.4 docking strains. Next, we added the first imager into the cells to acquire the super-resolution image in that area, so we could reconstruct the structure of the mitochondria; following, we washed the sample in the same position and added the second imager, imaging the tubulin in the same plane and position on the cell, co-localizing both structures inside the cells (Figure 3.11).

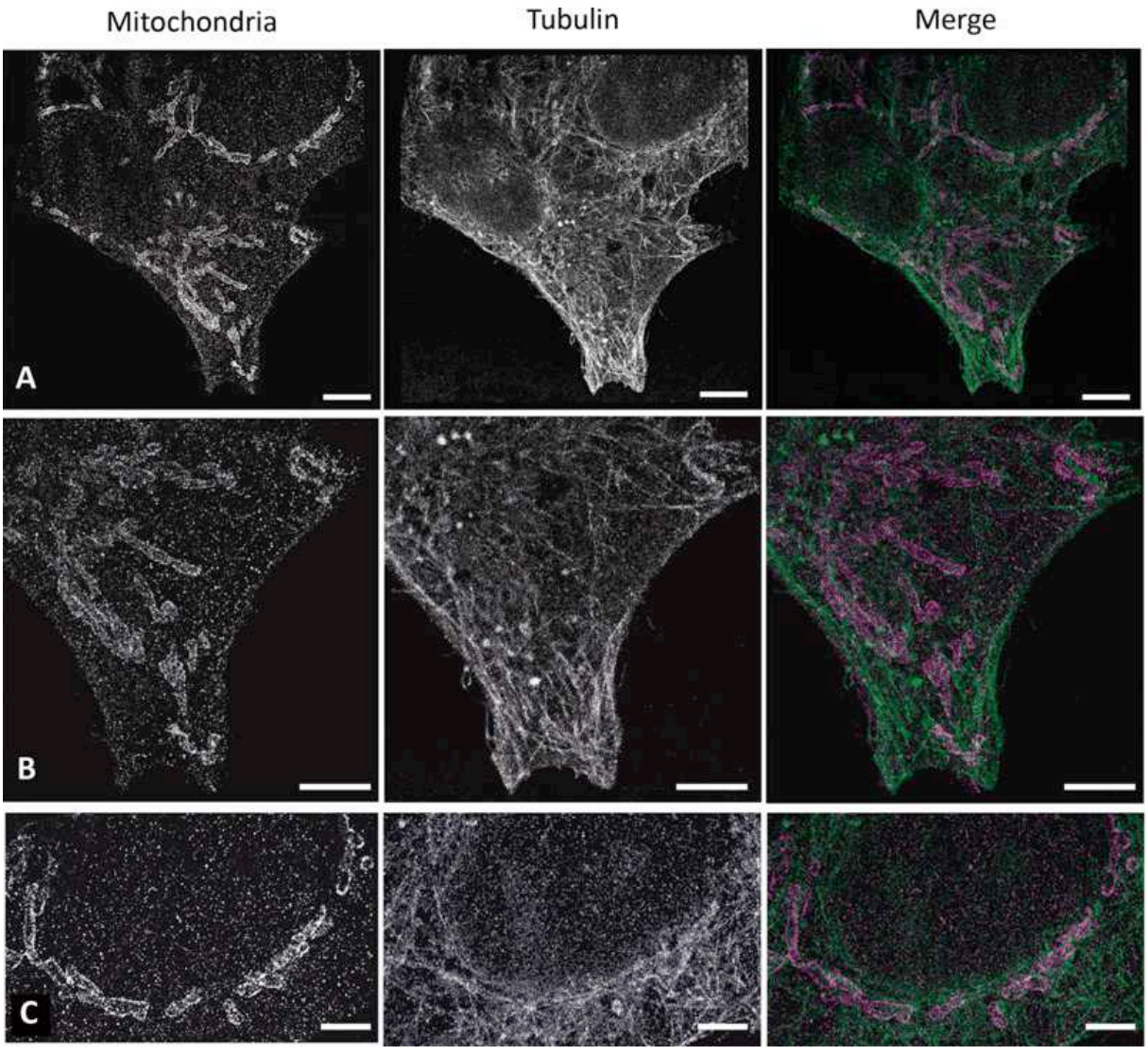

Figure 3.11: Reconstructed DNA-PAINT images of tubulin and mitochondria on HeLa cells. A) View of the whole cell immunostained against Tom20 (mitochondria) and tubulin using DNA-PAINT. Artificial colours were given in the merge image, where magenta represents the mitochondria and green the tubulin. (Scale bar 5 µm). B) Close-up in the bottom part of the cell. Artificial colours were given in the merge image, magenta (mitochondria) and green (tubulin)

(Scale bar 5 μm). C) close-up of the nucleus area. Artificial colours were given in the merge image, magenta (mitochondria) and green (tubulin) (Scale bar 2 μm).

As seen in Figure 3.11, mitochondria were perfectly shaped with DNA-PAINT, being able to identify single mitochondrion spread in the cell and specially around the nucleus (Figure 3.11 B-C). Further, we imaged the filaments of tubulin located mainly in the bottom extension of the cell (Figure 3.1 B middle). By co-localizing both images and assigning them an artificial colour we studied the position of both proteins in the same portion of the cell. This technique could be expanded to other proteins in order to study different cell structures without any limitation in terms of "colours"[29], it is just needed to select a new docking strand sequence with the complementary imager sequence.

This cell approach is very promising and easy to achieve, since with a regular immunostaining we performed multiplexing super-resolution images of structures inside the cell. The quality of the primaries and secondary antibodies is essential to be able to reconstruct successfully the structures. This phenomenon is observed in the Figure 3.11 (Tubulin), where the primary antibody did not have good quality, creating noise in the sample and a lack of definition. On the other hand, mitochondria antibody produced defined and specific images of mitochondria.

Further, since we wanted to implement multicolour DNA-PAINT on viral structures, we followed a similar approach but to study the composition and distribution of 2 proteins of influenza: hemagglutinin (HA) and viral ribonucleoproteins (vRNPs) on the previously studied Udorn filaments (chapter 2).

As observed in Figure 3.12, performing multicolour DNA-PAINT against HA and vRNPs it allowed us to study the heterogeneity distribution of both proteins within the population of filaments observed. In concrete, we could find 3 types of profiles of protein content on the filaments (Figure 3.12): A) all filaments only contain HA, but none of them has RNPs, thus they will not contain genetic material; B) half of the filaments that contain HA have as well RNPs, finding a whole region without vRNPs; C) all filaments have HA and RNPs on them, presumably with genetic material.

Applying this study in more samples and studying with more proteins would be possible to distinguish the functionality and composition of all influenza filaments, thanks to the versatility of DNA-PAINT that would allow us to image with super-resolution the distribution of all

proteins of influenza in these structures. Combining the possibilities to study functional sites in nanostructures and the possibility to perform in vitro images with DNA-PAINT, we implemented this technique in the next chapter to study the protein distribution of viral particles with the same precision that we studied NPs.

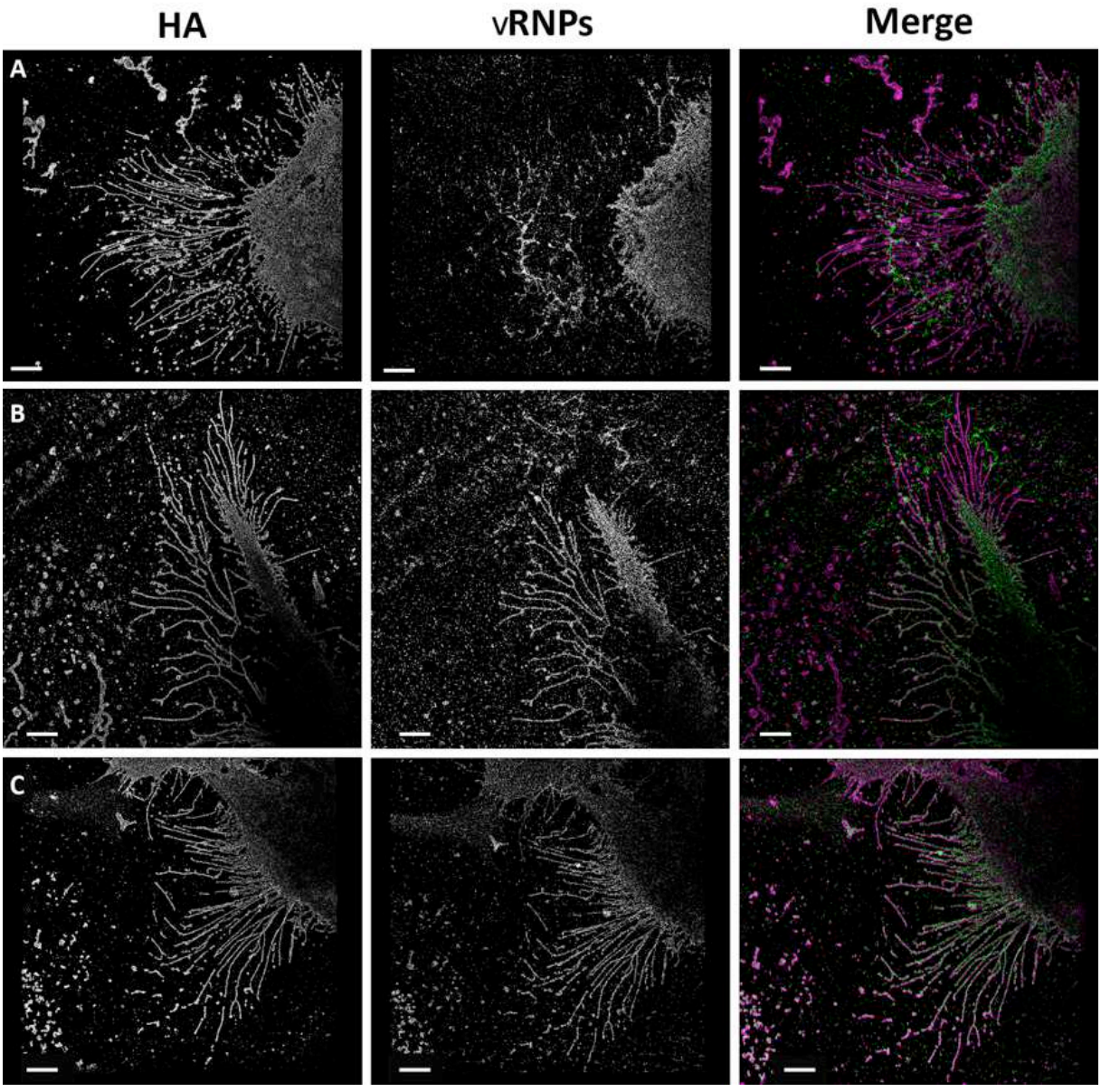

Figure 3.12: Multicolour DNA-PAINT on MDCK cells infected with Udorn influenza virus and immunostained against HA and viral ribonucleoproteins (vRNPs). Left: HA, middle: vRNPs, right: merge (purple HA, green RNPs). We can find different profiles of filament content: A) All filaments contain HA but none of them RNPs; B) Half filaments contain HA and RNPs at the same time; C) All filaments contain HA and RNPs. Scale bar = 5 µm.

3.5 Materials and methods

3.5.1 Materials

3.5.1.1 Nanoparticles

Streptavidin-coated and carboxyl-polystyrene nanoparticles (0.32 μm, 1% w/v), together with anti-digoxigenin-coated microspheres (3.2 μm, 0.5% w/v), were obtained by Spherotech.

3.5.1.2 List of oligos: docking and imagers

The list of DNA oligos used in this project is shown in Table 3.1, obtained from Dr. Ralf Jungmann [31,32] and purchased from Integrated DNA Technologies (IDT).

Number sequence	Docking	Imager
P1	Thiol C6SS/biotin or digoxigenin/- TTA TAC ATC TA–3'	5'–CTA GAT GTA T–Atto647 -3'
P2	Thiol C6SS/biotin/- TTA TCT ACA TA–3'	5'–TAT GTA GAT C–Atto647 -3'
P3	Thiol C6SS /biotin/- TTT CTT CAT TA–3'	5'–GTA ATG AAG A–Atto647 -3'

Table 3.1: list of sequences and DNA used to perform DNA-PAINT.

All oligos were diluted in TE buffer (10 mN Tris-Cl, 0.1 mM EDTA pH 8) at 1 mM and stored at -20°C.

Docking strands 1 and 3, with the respective imager strands, were used in one colour DNA-PAINT imaging; docking strands 1, 2 and 3, with the respective imager strands, were used for multicolour DNA-PAINT.

3.5.1.3 Buffers

Sterile phosphate-buffered saline (PBS) buffer pH=7.4 was used for sample preparation. Specific buffers were used for imaging: buffer B (5mM Tris-HCl, 10 mM $MgCl_2$, 1 mM EDTA, 0.05% Tween-20, pH=8) for imaging streptavidin and antibody-coated NPs; buffer C (PBS with 500 mM NaCl, pH=8) for anti-digoxigenin-coated microspheres and fixed cells.

3.5.2 Nanoparticle preparation

3.5.2.1 Labelling of NPs with Cy3

The commercial suspension of streptavidin-coated NPs (10 mg/ml) was diluted in sodium bicarbonate pH = 8.5 to a concentration of 0.2 mg/ml, with 200 nM Cy3. The suspension was kept under moderate shaking in the dark for 4h before washing three times with PBS to remove unconjugated dyes. Finally, the solution of Cy3-labeled NPs was concentrated to 1 mg/ml in PBS buffer and stored in the dark at 4ºC. The estimated number of Cy3 dyes per NP is about 30.

3.5.2.2 Coating of NPs with antibodies

Surface groups of carboxyl-NPs in PBS buffer were first activated with 1-ethyl-3(3-(dimethylamino)-propyl) carbodiimide hydrochloride and N-hydroxysuccinimide in equivalent amounts and further incubated with a mixture of anti-digoxigenin and anti-biotin antibodies for 4 h at room temperature and under moderate shaking. The coated particles were then washed three times with PBS to remove unconjugated antibodies and stored at 4ºC.

3.5.2.3 Loading of docking strands to NPs

Cy3-labeled streptavidin-coated NPs were diluted in PBS to 0.25 mg/ml in the presence of biotinylated DNA docking strand. The solution was kept under moderate shaking for 30 min at 4ºC in dark conditions, then washed three times with PBS to remove unconjugated docking strands, concentrated five times, sonicated to reduce particle aggregation, and used fresh. Antibody-coated NPs were diluted in PBS in the presence of premixed digoxigenin-docking strand 1 and biotin-docking strand 2 in large excess. The solution was kept under moderate shaking for 30 min at 4ºC, then washed three times with PBS to remove unconjugated docking strands, concentrated to a volume compatible with the imaging chamber, sonicated and used fresh.

3.5.2.4 Loading of docking strands to NPs with artificially enhanced heterogeneity

Cy3-labeled streptavidin-coated NPs were diluted in PBS to 0.35 mg/ml and then centrifuged at max speed for 20 min to obtain a tight pellet. The supernatant was removed and the NPs in the pellet were exposed to an excess of biotinylated DNA docking strand in solution for 15 min. the pellet was not resuspended during incubation with docking strands. Then, the solution containing the docking strands was removed and the NPs were washed twice with PBS to remove unconjugated docking strands, concentrated five times, sonicated to reduce particle aggregation and used fresh.

3.5.2.5 Loading of docking strands to microspheres

The commercial suspension of anti-digoxigenin-coated microspheres (1 mg/ml) was concentrated twice and then further diluted with PBS buffer to a concentration of 0.5 mg/ml in the presence of digoxigenin-conjugated DNA docking strand. The solution was kept under moderate shaking for 30 min at 4ºC in dark conditions, then washed three times with PBS to remove unconjugated docking strands, concentrated five times, sonicated to reduce particle aggregation and used fresh.

3.5.2.6 Imaging chamber

A flow chamber (volume approx. 40 µl) was assembled from a glass slide and a coverslip (24 x 24 nm, thickness 0.15 mm) separated by double-sided tape. Coverslips were precleaned by sonication in water and in pure acetone and dried under a nitrogen flow. This prevented the presence of impurities on the glass, facilitating the absorption of the particles. No coating agents were used. Loaded NPs or microspheres were added to the chamber and allowed to absorb on the glass for 30 min.

Only for the imaging of antibody-coated NPs were fiducial marker beads with white emission (Tetraspeck 0.1 µm) added and allowed to adsorb on the glass for 10 min. PBS buffer promoted the adsorption of the particles. Then, the chamber was washed with PBS and with the imaging buffer to remove unabsorbed particles. Finally, a solution containing the imager strand in imaging buffer was flowed in and the chamber was sealed to avoid evaporation.

For multicolour DNA-PAINT measurements, an analogous procedure was carried out using a commercial flow channel slide (Ibidi µ-Slide) equipped with a custom flow system consisting of two syringes to inject and remove the solutions, respectively.

After collecting a DNA-PAINT image of the sample using a first imager strand, the sample was washed with an excess of imaging buffer until no significant emission was detectable by the microscope camera. Then, a solution containing a second imager strand was injected for the acquisition of another image in the same field of view. The produce took a few minutes and was repeated for three different imager strand solutions without removing the chamber from the microscope sample holder.

3.5.3 Ligation of the docking strand with secondary antibodies

The DNA labelling of antibodies was done via maleimide-PEG2-succinimidyl ester adapted from Dr. Ralf Jungmann[32]. The list of antibodies and dockings bound is shown in Table 3.2.

Antibody	Docking sequence
Goat anti-mouse IgG (H+L) (115-005-003)	P1 Thiol C6SS- TTA TAC ATC TA–3'
Goat anti-mouse IgG (H+L) (115-005-003)	P3 Thiol C6SS- TTT CTT CAT TA–3'
Goat anti-rabbit IgG (H+L) (111-005-003)	P2 Thiol C6SS- TTA TCT ACA TA–3'

Table 3.2: list of secondary antibodies and docking sequence bound

The reduction of the thiolated DNA for the maleimide reaction was done incubating 30 µl 1 mM of thiolated DNA in 70 µl of freshly prepared DTT solution (250 mM DTT, 1.5 mM EDTA and 0.5x PBS, pH 7.2) for 2 h at RT covered with aluminium foil on a shaker.

At the same time the maleimide linker was bound to the secondary antibody. For this, the cross-linker solution of maleimide-PEG2-susccinimidyl ester was prepared at 10 mg/ml in DMF and added in to the secondary antibody in a 10:1 molar ratio, being careful to only add a maximum volume 5 µl of cross-linker solution to avoid adding too much DMF. The antibody with the linker was incubated for 90 min at 4ªC on a shaker covered in aluminium foil.

Before the incubation of the thiolated DNA and the DTT solution finished, a Nap-5 column was equilibrated with H_2Omq filled to the top three times. Then, DNA-DTT solution was added to the column and immediately added 400 µl of H_2Omq. Once 400 µl of solution passed through, 1 ml of H_2Omq was added and the fractions were collected. The first 4 fractions consisted on three drops of the flow-through, the following 4 fractions consisted on two drops and the last eight fractions consisted in one drop.

In order to select only the fractions with DNA and not the ones with DTT, 25 µl of BCA mix was added to the fractions, starting from the last fraction collected. If DTT is present, the solution turned purple, discarding those tubes. Once no colour change was visible the remaining fractions were measured using the NanoDrop spectrophotometer. The fractions that showed the highest concentrations were collected together and concentrated using Amicon spin filters (3kDa) at 14,000g 4ºC during 30 min. After discarding the flow-through, the spin filter was

inverted and recovered in a new empty tube spinning for 6 min at 1,000g 4ºC. The concentration was measured again in the NanoDrop spectrophotometer and being >700 ng/µl.

After the antibody-cross linker reaction was complete, the linker was removed using a Zeba desalting column. For this purpose, the storage solution of the column was removed by centrifugation at 1,500g for 1 min at 4ºC, following by a wash with 300 µl of PBS and centrifugation at 1,500g for 1 min at 4ºC. The antibody-cross linker solution was added to the Zeba column and spin at 1,500g for 2 min at 4ºC in a new clean eppendorf. The flow-through was measured with the NanoDrop spectrophotometer, obtaining a concentration >1.5 mg/ml.
Both solutions already purified and concentrated were mixed with a 10:1 molar ratio of the thiolated DNA to antibody overnight on a shaker, covered in aluminium foil in a cold room.

In order to remove the excess of not bound DNA, an Amicon spin filter (100 kDa) was used. For this, the filter was washed first with 1x PBS for 10 min at 14,000g at 4ºC. after discarding the flow-through, the antibody-DNA solution was added, plus 300 µl of PBS and span at 14,000g for 5 min at 4ºC. In a new tube, the invert filter was centrifuged at 1,000g at 4ºC. After adjusting the volume to 100 µl with 1x PBS, the concentration was measured with the NanoDrop spectrophotometer. The antibody solution could be storage at 4ºC.

3.5.4 DNA-PAINT microscopy acquisition

3.5.4.1 Optical setup

DNA-PAINT imaging was carried out with a Nikon N-STORM system configured for total internal reflection (TIRF), using a Perfect Focus System. Irradiation under TIRF conditions allowed to selectively observe fluorescence emission from particles on the glass slide, reducing the background contributions. After laser excitation (647 or 561 nm), fluorescence was collected by a 100x 1.49 NA oil immersion objective; it passed through a quad-band dichroic mirror (97337 Nikon) and was collected by a Hamamatsu ORCA Flash 4.0 CMOS camera (pixel size 160 nm). A movie was produced where blinking generated by molecule emission appears like circular spots lasting a few acquisition frames. Three-dimensional measurements were carried out with the astigmatism method: a cylindrical lens was introduced in the light path, producing optical aberrations (elongation and inclination) of the detected fluorescence spots depending on the z-position of the emitter.

3.5.4.2 For nanoparticle imaging

Cy3-labeled streptavidin-coated NPs were saturated by incubation with an excess of biotin-docking strand (10 µM). Figures Figure 3.2, Figure 3.5, Figure 3.6 were obtained with 0.1 nM imager strand; imaging was performed under TIRF conditions using a 647 nm laser (power ~80 mW) for the excitation of the imager strands; emission was detected on a 256 x 256 pixel region of the camera for 50,000 frames at a rate of 20 Hz (camera exposure time 50 ms); a 561 nm laser (~0.4 mW) was used for Cy3 excitation; one frame in the 561 channel was collected every 100 frames in the 647 channel. The time for the acquisition of one image was around 40 min. The three-dimensional image in Figure 3.6A was collected under the same conditions (for 20,000 frames at 20 Hz): a single stack was acquired setting the focus on the plane of nanoparticles adsorbed on the glass. Antibody coated NPs of Figure 3.8 were obtained with 0.5 nM imager strand; imaging was performed under TIRF conditions using 647 nm laser (power 80 mW) for the excitation of imager strand; emission was detected on a 512 x 512 pixel region of the camera for 20,000 frames at a rate of 20 Hz. Fiducial marker emission was detected in 561 channel. The acquisition of a single colour image required approx. 20 min.

3.5.4.3 For NP quantitative imaging

For acquisition of Figure 3.10 A Cy3-labeled streptavidin-coated NPs were incubated with 0.5 nM biotin-docking strand and imaged with 5 nM imager strand. For the results reported in Figure 3.10 C the NPs were incubated with increasing biotin-docking strand concentration (0.5, 5, 20, 50, 500 and 6250 nM) and then imaged with 5 nM (for 0.5 nM docking), 0.5 nM (for 5 nM docking), or 0.1 nM (for 20, 50, 500 and 6250 nM docking) imager strand. The distribution of Figure 3.10 D was obtained using the qPAINT data for NPs exposed to the higher concentration (6250 nM) of docking. All the qPAINT experiments were performed under TIRF conditions using a 647 nm laser (power ~80 mW) for the excitation of the imager strands; emission was detected on a 256 x 256 pixel region of the camera for 10,000 frames or 15,000 frames at a rate of 10 Hz (camera exposure time 100 ms); a 561 nm laser (~0.3 mW) was used for Cy3 excitation; one frame in the 561 channel was collected every 100 frames in the 647 channel. The time for the acquisition of one image was approx.. 25 min. Temperature was controlled at 25°C; no photobleaching was detected during measurements.

3.5.4.4 For microsphere imaging

In Figure 3.3, anti digoxigenin-coated microspheres were saturated with an excess of digoxigenin-docking strand (5 µM) and were imaged with 0.5 nM imager strand; imaging was performed using a 647 nm laser (power ~80 mW) and setting the focus close to the middle plane of the spheres; emission was detected on a 512 x 512 pixel region of the camera for 10,000 frames at a rate of 10 Hz (camera exposure time 100 ms). The time for acquisition of an image was approx.. 17 min.

3.5.4.5 For cell imaging

Mitochondria and tubulin:

HeLa cells were obtained from Dr. Conxita Solans's lab at CSIC in Barcelona. HeLa cells were seeded at 2.5 x 10^4 cells per well in a 24 well plate for production of VLPs or 2 x 10^3 cells per well in a 8 well glass-bottom µ-Slide (Cat. No. 80826, Ibidi GmbH, Germany) overnight at 37ºC and 5% of CO_2 to achieve 85% of confluence prior to performing the immunostaining experiments.

Cells were fixed with 4% of paraformaldehyde in PBS for 10 min and then followed by a permeabilization of cell membrane using 0.2% Triton X-100 for 10 min at RT. After washing 3 times with PBS 1x 5 min each, cells were incubated with 1% BSA for 30 min at RT. Primary antibodies (mouse Anti-Tom20 Abcam, rabbit Anti-tubulin Abcam) were diluted at 15 µg/ml in 1% BSA PBS 1x and incubated for 1h at RT. After washing with PBS 1x 3 times, secondary antibody (anti-mouse docking 1, anti-rabbit docking 2) was diluted at 30 µg/ml and added to the cells for 1 h at RT.

Influenza filaments:

For DNA-PAINT cells, MDCK infected cells were fixed with 2% PFA for 20 min. After washing with PBS, they were permeabilized for 10 min with 0.2% Triton X-100 in PBS followed by blocking with 3% BSA in PBS for 30 min. Primaries antibodies, mouse anti-H2 and goat anti-RNPs, were incubated for 1 hour at RT at 1/500 dilution in 1% BSA, followed by 3 washed with PBS. After, secondary antibodies for DNA-PAINT, anti-mouse docking 1 and anti-goat docking 3, were incubated at 20 µg/ml in PBS for 1 hour at RT, followed by 3 washes with PBS.

Images were acquired using a Nikon N-STORM 4.0 system configured for total internal reflection fluorescence imaging (TIRF). Excitation inclination was tuned to adjust focus and to

maximize the signal-to-noise ratio. Imager was added at 1 nM. Atto-647 was excited by illuminating the sample with a 647 nm (80 mW) laser, built into the microscope. During acquisition the integration time was 80ms. For the measurements with Atto-647 15,000 frames were acquired in the 647 channel. The total time required to acquire one image was about 30 min. Fluorescence was collected by means of a Nikon x100, 1.4 NA oil immersion objective and passed through a quad-band-pass dichroic filter (97335 Nikon). Images were recorded onto a 256 x 256 pixel region (pixel size 160 nm) of a sCMOS camera (Hamamatsu).

3.5.5 Analysis

3.5.5.1 DNA-PAINT image reconstruction

The NIS elements Nikon software generates a list of localizations by Gaussian fitting the florescence spots of blinking dyes in the acquired move of diffraction-limited images. To avoid overcounting, blinkings detected in consecutive frames are counted as single by the software. For three-dimensional imaging the z-coordinate of the localization is retrieved from the ellipticity and the inclination of the elongated spots.

3.5.5.2 NP conjugation with Cy3 and drift correction

The fluorescence emission of NP-conjugated Cy3 is spectrally distinguishable from that of the imager strand and was thus acquired on a different channel for two purposes: (I) it allowed the correction of the mechanical drift during image acquisition; (II) since the Cy3 dyes labelling the same NP are simultaneously emitting upon photoexcitation, the resulting clusters of Cy3 localizations in the reconstructed image correspond, with an uncertainty of a few tens of nm, to the centre of the NP. This is an important parameter for further analysis, especially when few docking strands are available on the NP surface. Finally, the amount of Cy3 dyes per NP is rather low and there is no evidence that it significantly affects the docking-imager interaction.

For streptavidin-coated-NPs, thanks to the emission of the NP-conjugated Cy3, the NPs themselves acted as subdiffraction-sized fiducial markers for the correction of the mechanical drift, without the need for introduction of additional probes. The low frequency (100 times lower than for imager strand excitation) and power of Cy3 excitation ensured negligible bleaching of the dyes during image acquisition. To obtain the multicolour images of Figure 3.6 B and Figure 3.11, the drift corrected one-colour images of the same field of view, acquired using different imager strands, were merged and aligned using ImageJ software, exploiting the clusters of Cy3 localizations to align the centres of the single NP. For immune-functionalized particles of

micrometric size, the correction for the mechanical drift was obtained with a tool integrated in the Nikon analysis software based on localization autocorrelation, while for antibody-coated NPs fiducial markers beads were used for drift correction and alignment of single colour images.

3.5.5.3 NP size

The list of localizations in the 647 channel (imager strand) was analysed using a Matlab script to obtain the size of NPs from the DNA-PAINT images: a mean-shift clustering algorithm was applied to identify clusters of localizations corresponding to NPs; aggregates or clusters with unrealistic shape were filtered out, and the mass centre of the selected clustered localizations was calculated. Typically, between 1000 and 3000 localizations in the NP area were obtained for saturated NPs. Under these conditions, the radius of each NP was estimated by a full circle model as the distance from the mass centre comprising 90% of the cluster localizations.

3.5.5.4 Localization counting

For loaded NPs, the list of localizations in both the 647 (imager strand) and 561 (Cy3) channel was analysed by a Matlab script. First, clusters of localizations in the 561 channel were identified using a mean-shift clustering algorithm. These clusters roughly indicate the centre of each NP, with an uncertainty of a few tens of nm. A further filter was applied to remove particle aggregates or clusters with an unrealistic shape or size. Then, the localizations in the 647 channel located within a distance of 210 nm from the NP centre were identified, so that the number of 647 localizations and their (x,y,t) coordinates are stored for each NP. The distance value was optimized considering the NP diameter (~330 nm) and the localizations uncertainty.

Due to their larger size than NPs, the number of localizations in the focal plane for loaded microspheres was easily obtained using the statistic tool of the Nikon analysis software, which allows counting the localizations within a region of interest.

3.5.5.5 qPAINT Analysis on NPs

Having identified the (x,y,t) coordinates of 647 localizations belonging to each NP, a binary intensity versus time trace was reconstructed for each NP, assigning a value of 0 to the frames without localizations and a value of 1 to the frames with one localization. The individual dark times, corresponding to consecutive 0 values in the reconstructed time trace, were individuated for each NP, allowing obtaining the correspondent empirical CDF, which was then fitted with the exponential model $y(t) = 1 - Ae^{-t/\tau_{d^*}}$. Thus, the value of the mean dark time τ_{d^*} was retrieved as an optimized parameter in the fitting process for each NP. Finally, the number of binding

sites (n) was calculated for each NP from the equation $n = (k_{ON} c_i \tau_{d^*})^{-1}$, using the value for the second-order association rate (k_{ON}) established by calibration and the known imager concentration (c_i) of the sample.

3.5.5.6 Pair autocorrelation analysis

In order to study the intraparticle distribution of 647 localizations and to determine the average localization precision of our signals, an analysis based on pair autocorrelation of the retrieved 647 localizations was performed. First, the list of 647 localization coordinates for single NPs was converted into a binary image of the single particles using a Matlab script. The pixel size was set to 2 nm for analysis of intraparticle distributions and 1 nm for analysis of the precision. Then, pair autocorrelation analysis of the images was performed using a previously developed Matlab function[5,43].

3.5.5.7 Precision

To experimentally assess the precision in our imaging system, we performed a pair autocorrelation analysis on DNA-PAINT images of the NPs selected for qPAINT calibration, i.e., exposing a single active functional site. These showed a significant correlation at short distances (roughly below 50 nm), which was attributed to over-counting, i.e., multiple localizations of the same docking molecule due to different binding events. Under these conditions, the retrieved autocorrelation functions g(r) can be fitted with a Gaussian model $g(r) = Ae^{-r^2/4\sigma^2}$. The average value retrieved for the parameter σ, which is often considered as a good estimate of the precision[44], was 11 nm, corresponding to a fwhm of about 25 nm. The values are comparable to other SMLM results and confirm that the selected particles expose a single functional site. Remarkably, this constitutes an in situ measurement of the precision, which accounts for contributions, such as residual mobility of the docking molecule or incomplete correction of the drift, that generally are not taken into account when determining the precision from fitting signals of artificially obtained isolated objects, such as single fluorophores spread on glass.

3.6 References

1. Delcanale, P., Miret-Ontiveros, B., Arista-Romero, M., Pujals, S. & Albertazzi, L. Nanoscale Mapping Functional Sites on Nanoparticles by Points Accumulation for Imaging in Nanoscale Topography (PAINT). *ACS Nano* **12**, 7629–7637 (2018).
2. van der Zwaag, D. *et al.* Super Resolution Imaging of Nanoparticles Cellular Uptake and Trafficking. *ACS Appl Mater Interfaces* **8**, 6391–6399 (2016).
3. Shang, L. *et al.* Protein-based fluorescent nanoparticles for super-resolution STED imaging of live cells. *Chem Sci* **8**, 2396–2400 (2017).
4. Chen, X. *et al.* Probing cell internalisation mechanics with polymer capsules. *Nanoscale* **8**, 17096–17101 (2016).
5. Veatch, S. L. *et al.* Correlation Functions Quantify Super-Resolution Images and Estimate Apparent Clustering Due to Over-Counting. *PLOS ONE* **7**, e31457 (2012).
6. Sengupta, P. *et al.* Probing protein heterogeneity in the plasma membrane using PALM and pair correlation analysis. *Nat. Methods* **8**, 969–975 (2011).
7. Sengupta, P. & Lippincott-Schwartz, J. Quantitative analysis of photoactivated localization microscopy (PALM) datasets using pair-correlation analysis. *Bioessays* **34**, 396–405 (2012).
8. Lee, S.-H., Shin, J. Y., Lee, A. & Bustamante, C. Counting single photoactivatable fluorescent molecules by photoactivated localization microscopy (PALM). *Proc. Natl. Acad. Sci. U.S.A.* **109**, 17436–17441 (2012).
9. Ehmann, N. *et al.* Quantitative super-resolution imaging of Bruchpilot distinguishes active zone states. *Nat Commun* **5**, 4650 (2014).
10. Stone, M. B., Shelby, S. A. & Veatch, S. L. Super-Resolution Microscopy: Shedding Light on the Cellular Plasma Membrane. *Chem. Rev.* **117**, 7457–7477 (2017).
11. Muranyi, W., Malkusch, S., Müller, B., Heilemann, M. & Kräusslich, H.-G. Super-Resolution Microscopy Reveals Specific Recruitment of HIV-1 Envelope Proteins to Viral Assembly Sites Dependent on the Envelope C-Terminal Tail. *PLOS Pathogens* **9**, e1003198 (2013).
12. Lehmann, M. *et al.* Quantitative Multicolor Super-Resolution Microscopy Reveals Tetherin HIV-1 Interaction. *PLoS Pathog* **7**, (2011).
13. Pereira, C. F., Rossy, J., Owen, D. M., Mak, J. & Gaus, K. HIV taken by STORM: Super-resolution fluorescence microscopy of a viral infection. *Virol J* **9**, 84 (2012).
14. Pham, S. *et al.* Cryo-electron microscopy and single molecule fluorescent microscopy detect CD4 receptor induced HIV size expansion prior to cell entry. *Virology* **486**, 121–133 (2015).

15. Gray, R. D. M. *et al.* Nanoscale polarization of the entry fusion complex of vaccinia virus drives efficient fusion. *Nature Microbiology* **4**, 1636–1644 (2019).

16. Vahey, M. D. & Fletcher, D. A. Influenza A virus surface proteins are organized to help penetrate host mucus. *Elife* **8**, (2019).

17. Feiner-Gracia, N. *et al.* Super-Resolution Microscopy Unveils Dynamic Heterogeneities in Nanoparticle Protein Corona. *Small* **13**, (2017).

18. Clemments, A. M., Botella, P. & Landry, C. C. Spatial Mapping of Protein Adsorption on Mesoporous Silica Nanoparticles by Stochastic Optical Reconstruction Microscopy. *J. Am. Chem. Soc.* **139**, 3978–3981 (2017).

19. Albertazzi, L. *et al.* Probing exchange pathways in one-dimensional aggregates with super-resolution microscopy. *Science* **344**, 491–495 (2014).

20. Belfiore, L., Spenkelink, L. M., Ranson, M., van Oijen, A. M. & Vine, K. L. Quantification of ligand density and stoichiometry on the surface of liposomes using single-molecule fluorescence imaging. *J Control Release* **278**, 80–86 (2018).

21. Pujals, S., Feiner-Gracia, N., Delcanale, P., Voets, I. & Albertazzi, L. Super-resolution microscopy as a powerful tool to study complex synthetic materials. *Nature Reviews Chemistry* **3**, 68–84 (2019).

22. Durisic, N., Cuervo, L. L. & Lakadamyali, M. Quantitative super-resolution microscopy: pitfalls and strategies for image analysis. *Curr Opin Chem Biol* **20**, 22–28 (2014).

23. Sauer, M. Localization microscopy coming of age: from concepts to biological impact. *J. Cell. Sci.* **126**, 3505–3513 (2013).

24. Shivanandan, A., Deschout, H., Scarselli, M. & Radenovic, A. Challenges in quantitative single molecule localization microscopy. *FEBS Letters* **588**, 3595–3602 (2014).

25. Jungmann, R. *et al.* Single-Molecule Kinetics and Super-Resolution Microscopy by Fluorescence Imaging of Transient Binding on DNA Origami. *Nano Lett.* **10**, 4756–4761 (2010).

26. Seeman, N. C. & Sleiman, H. F. DNA nanotechnology. *Nature Reviews Materials* **3**, 1–23 (2017).

27. Hariri, A. A., Hamblin, G. D., Gidi, Y., Sleiman, H. F. & Cosa, G. Stepwise growth of surface-grafted DNA nanotubes visualized at the single-molecule level. *Nat Chem* **7**, 295–300 (2015).

28. Lo, P. K. *et al.* Loading and selective release of cargo in DNA nanotubes with longitudinal variation. *Nat Chem* **2**, 319–328 (2010).

29. Agasti, S. S. *et al.* DNA-barcoded labeling probes for highly multiplexed Exchange-PAINT imaging. *Chem Sci* **8**, 3080–3091 (2017).

30. Dai, M., Jungmann, R. & Yin, P. Optical visualisation of individual biomolecules in

densely packed clusters. *Nat Nanotechnol* **11**, 798–807 (2016).

31. Jungmann, R. *et al.* Multiplexed 3D cellular super-resolution imaging with DNA-PAINT and Exchange-PAINT. *Nature Methods* **11**, 313–318 (2014).

32. Schnitzbauer, J., Strauss, M. T., Schlichthaerle, T., Schueder, F. & Jungmann, R. Super-resolution microscopy with DNA-PAINT. *Nat. Protocols* **12**, 1198–1228 (2017).

33. Chen, C. *et al.* Profiling of Exosomal Biomarkers for Accurate Cancer Identification: Combining DNA-PAINT with Machine- Learning-Based Classification. *Small* **15**, 1901014 (2019).

34. Cremers, G. A. O., Rosier, B. J. H. M., Riera Brillas, R., Albertazzi, L. & de Greef, T. F. A. Efficient Small-Scale Conjugation of DNA to Primary Antibodies for Multiplexed Cellular Targeting. *Bioconjug. Chem.* **30**, 2384–2392 (2019).

35. Pérez-López, B. & Merkoçi, A. Nanoparticles for the development of improved (bio)sensing systems. *Anal Bioanal Chem* **399**, 1577–1590 (2011).

36. Jungmann, R. *et al.* Quantitative Super-Resolution Imaging with qPAINT using Transient Binding Analysis. *Nat Methods* **13**, 439–442 (2016).

37. Saha, B., Evers, T. H. & Prins, M. W. J. How antibody surface coverage on nanoparticles determines the activity and kinetics of antigen capturing for biosensing. *Anal. Chem.* **86**, 8158–8166 (2014).

38. Saha, B., Songe, P., Evers, T. H. & Prins, M. W. J. The influence of covalent immobilization conditions on antibody accessibility on nanoparticles. *Analyst* **142**, 4247–4256 (2017).

39. Parolo, C. *et al.* Design, preparation, and evaluation of a fixed-orientation antibody/gold-nanoparticle conjugate as an immunosensing label. *ACS Appl Mater Interfaces* **5**, 10753–10759 (2013).

40. van Reenen, A., de Jong, A. M. & Prins, M. W. J. How Actuated Particles Effectively Capture Biomolecular Targets. *Anal. Chem.* **89**, 3402–3410 (2017).

41. Zamora-Gálvez, A., Morales-Narváez, E., Mayorga-Martinez, C. C. & Merkoçi, A. Nanomaterials connected to antibodies and molecularly imprinted polymers as bio/receptors for bio/sensor applications. *Applied Materials Today* **9**, 387–401 (2017).

42. Neish, C. S., Martin, I. L., Henderson, R. M. & Edwardson, J. M. Direct visualization of ligand-protein interactions using atomic force microscopy. *Br. J. Pharmacol.* **135**, 1943–1950 (2002).

43. Sengupta, P., Jovanovic-Talisman, T. & Lippincott-Schwartz, J. Quantifying spatial organization in point-localization superresolution images using pair correlation analysis. *Nat Protoc* **8**, 345–354 (2013).

44. Deschout, H. *et al.* Precisely and accurately localizing single emitters in fluorescence microscopy. *Nat. Methods* **11**, 253–266 (2014).

Chapter 4: Nanostructural characterization of recombinant viral proteins with super-resolution microscopy: from cells to virus-like particles

This chapter reproduces almost literally the submitted article: Nanostructural characterization of recombinant viral proteins with super-resolution microscopy: from cells to virus-like particles. Arista-Romero M., DelCanale P., Pujals S., and Albertazzi L. (2021).

4.1 Introduction

As explained in chapter 1, influenza virus-like particles (VLPs) consist in small structures that mimic the viral particle with multicomponent organization yet without genetic material[1,2], and are currently under study for their promising role as vaccines[3-9]. Since their discovery in the mid 60's[10,11], the study of these structures have increased over time (Figure 4.1.A), attracting researches from several fields to study and characterize VLPs, proving the strong interest and versatility of this recombinant system.

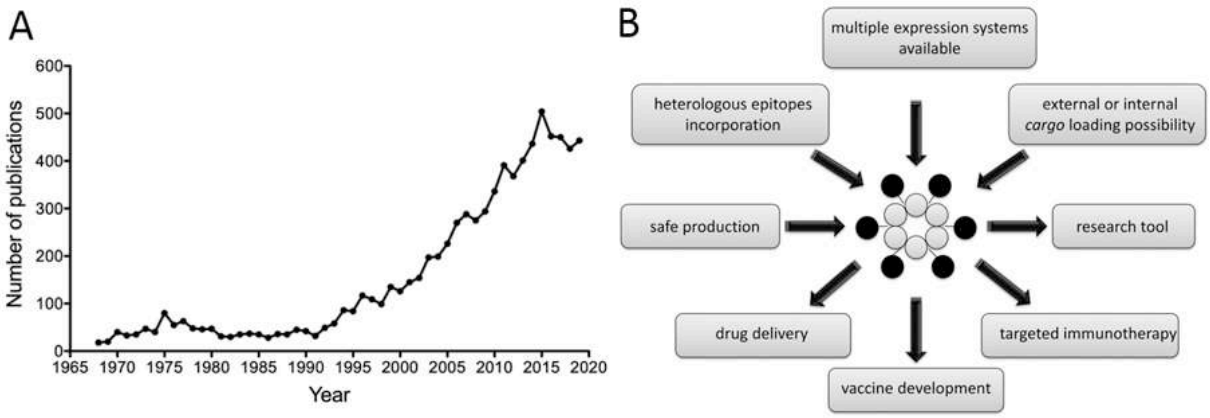

Figure 4.1: A) Total number of publications from PubMed regarding VLPs, in time. B) Diagram of potential uses of VLPs and possible synthesis modifications. Reproduced from reference [12], Copyright © 2015, PJM ONLINE .

One good advantage of using VLPs is their capacity to be produced by multiple expression systems either for high throughput synthesis or small-scale production according the needs, always in safety conditions. Thus, they are easily charged with different cargos or modified with different proteins like GFP. For these reasons researchers study VLPs to be used as drug delivery vectors, molecular imaging tools, vaccines and targeted immunotherapy (Figure

4.1.B)[12-14]. All in all, VLPs and recombinant vaccines are considered as the new frontier to develop universal vaccines[5,15-17]. An example is found in the vaccines developed against COVID-19 in 2020, consisting of mRNA vectors that produce recombinant proteins in the cells of vaccinated patients[18,19,20].

The whole process of production of envelope VLPs in mammalian cells is quite straightforward since only needs cells expressing recombinant proteins of the virus, which would self-assemble releasing empty viruses[21-24]. From all the expression systems for the production of recombinant VLPs, mammalian cells seems the most promising due to their enormous advantages, such as the similarities of membrane composition and native post-translational modifications of the glycoproteins[1,2,25-28]. However, these cells have the drawback of displaying a low yield of protein expression combined with a lack of control of the total protein expression, a feature that is not found in other systems like insect cells. This is why in most cases insect cells are used as a VLP expression system[29,30]. Through the infection of a baculovirus, recombinant proteins are produced from insect cells, usually the Sf9 cell line, in an easily scale-up downstream process[31]. Even though its possibilities, it still has several drawbacks such as a cross-contamination of the baculovirus in the resultant VLP mixture and lack of lipid membrane similarities[32].

Hence, due to the possible use of mammalian cells as expression systems, mammalian cell lines have been modified or enhanced to increase the expression yield of influenza VLPs[33-36]. However, in most cases the resulting purified VLPs are characterized in bulk by DLS, ELISA, Western-blot and with electron microscopy, not paying especial attention to the cells producing recombinant proteins and lacking precision in the measurements at single-particle and single-protein level, crucial information to optimize recombinant expression and VLP synthesis.

Owing to the small size of influenza VLPs and viral recombinant proteins (≤100 nm) it is impossible to characterize the protein expression and distribution on cells and VLPs with conventional fluorescent microscopy due the diffraction limit of the light (250 nm)[37,38]. As commented in previous chapters, single-molecule localization microscopy (SMLM) has appeared in the last decade as a powerful super-resolution microscopy technique to study and characterize viral structures[39-42].

As explain and tested in detail in chapter 3, DNA-PAINT[43] demonstrated to be a sensitive tool for geometrical and functional characterization for small structures such as nanomaterials, allowing the recognition of functional sites on the surface of nanoparticles. This technique not

only allowed the multiplexed visual characterization of the intra- and inter-particle distribution of antibodies or proteins along the surface of particle, but also permitted their quantification in the total population of nanoparticles at single-particle level. Thanks to this validation, we were able to carry out the mapping and the measurement of functional proteins in the nanoscale on viral structures such as VLPs.

Hence, in this chapter we characterized with DNA-PAINT the nanostructural distribution of the three main proteins of influenza on recombinant cells and the resulting VLPs, semi-quantifying at single-particle level the total amount of the three proteins expressed on both structures and their distribution in the nanoscale to monitor the main steps of VLP formation. Overall, we could prove that DNA-PAINT is an extremely powerful SMLM technique that provides solid information about recombinant protein expression at levels never studied.

4.2 Results and discussion

The workflow followed in this chapter is exhibited in Figure 4.2. Firstly, to perform DNA-PAINT with secondary antibodies (Figure 4.2B), the antibodies selected were labelled with a DNA-docking strand following the protocol from Schnitzbauer et al.[44], where each antibody contained approximately 2.5 docking sequences. Subsequently, to acquire the super-resolution image it is added the imager, a complementary DNA strand fluorescently labelled with Atto-647N, similarly as we did in chapter 3. The transient binding between the DNA strands of the docking and the imager allows the imaging and the localization of the proteins targeted by the antibody complex, as a result of the reconstruction of the super-resolution image.

Each imager would target a different secondary antibody, thus, to acquire images with different imager strands sequentially in the same field, we employed a chamber-tubing system connected to a pump for washing and exchanging the imager while the sample was still in the microscope. The localizations retrieved were directly correlated to the total amount of proteins expressed on the area measured, consequently, semi-quantifying the expression of the three proteins of PR8 influenza studied: hemagglutinin (HA), neuraminidase (NA) and matrix 2 (M2). According to the literature[2,7,22], the main proteins present on the envelope of influenza (HA, NA, M2 and M1) are necessary to produce VLPs. Thus we employed the same concentration of three different plasmids to produce VLPs: HA, NA and M, containing M1 and M2 (Figure 4.2 A).

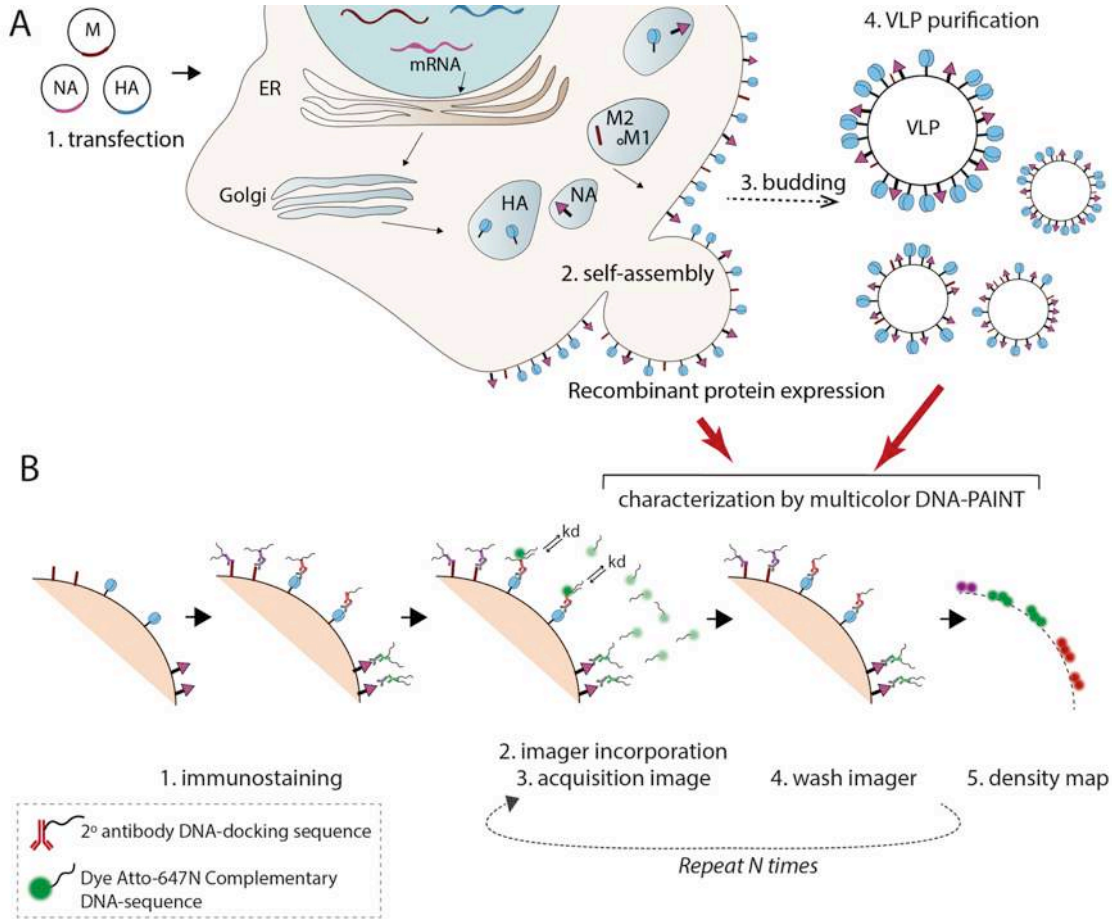

Figure 4.2: Diagram of the workflow followed for the characterization of recombinant viral proteins with DNA-PAINT. A) (1) Cos7 cells were transfected with 3 different plasmids containing the 3 main envelope proteins of influenza PR8 strain. The proteins would interact by self-assembly (2) and produce the virus-like particles (VLP) by budding from the membrane (3). VLPs were then purified by ultracentrifugation with sucrose gradient (4). B) Both fixed cells expressing the recombinant proteins and the VLPs purified were immunostained with primary and secondary antibodies, the last ones bound to a small sequence of DNA called docking. To image with DNA-PAINT, the Atto-647N bound to a small sequence complementary to the docking, called imager, was added on the sample and it was imaged. After the acquisition of the image, the imager is washed out and it could be added a second imager with the complementary sequence of a different docking, repeating this process N times. After the image acquisition, the analyses and post-process of the image would reveal a density map and the localizations in X, Y of the single targets.

4.2.1 Characterization of recombinant expression on mammalian cells

Firstly, we characterized the recombinant viral expression on mammalian cells with DNA-PAINT. Hence, Cos7 cells were transfected with the three different plasmids at the same time and with the same concentration. Prior performing DNA-PAINT, we identified the timeline of the post-transfection (p.t.) expression of recombinant proteins. For this, we checked the

protein expression after 24 hours and 48 hours p.t. using conventional fluorescence microscopy (Figure 4.3).

To avoid crosstalk between the fluorophores selected, we immunostained against only two proteins at a time using secondary antibodies bound to Alexa647 and Alexa488, naming the samples immunostained as staining 1 (NA and HA were imaged in the same sample) and staining 2 (NA and M2 were imaged in the same sample). Besides, the fluorescence expression was measured to compare the expression of proteins and the percentage of transfected cells with time (Figure 4.4). As observed in Figure 4.3A, just after 24 hours p.t. the recombinant proteins were observed highly expressed on the surface of the cells, at similar intensities and co-localizing (Figure 4.4A).

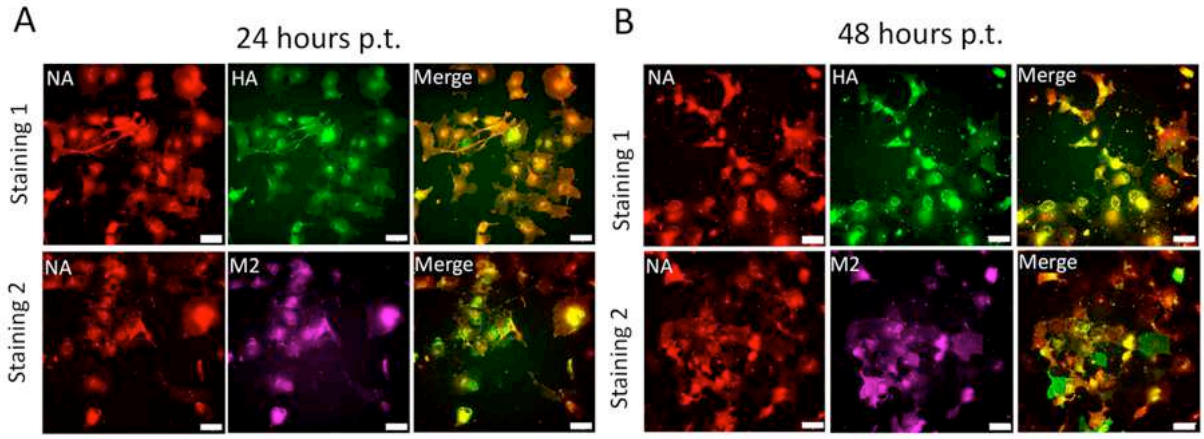

Figure 4.3: Fluorescence microscopy images of cells fixed after 24h and 48h post-transfection (p.t.). Two different immunostaining were made: staining 1= cells were immunostained against HA and NA (Alexa-647 and Alexa-488 respectively; staining 2= cells were immunostained against M2 and NA (Alexa-647 and Alexa-488 respectively. A) Images of cells fixed after 24h p.t. In staining 1 NA is displayed in red, while HA is displayed in green. Merged colours display cells co-expressing both proteins. Staining 2 displays NA in red and M2 in magenta. B) Images of cells fixed after 48h p.t. the same artificial colours were applied as A. Scale bar: 50 µm.

Similarly, at 48 hours p.t. (Figure 4.3B) cells were expressing similar amounts of recombinant proteins, indicating that the recombinant expression started after 24 hours p.t. and maintained with time. If we observe the intensity of the fluorescence (mean) in Figure 4.4 A, we detected that indeed the amount of immunostained proteins was quite similar at 24h and 48h p.t. However, the percentage of transfected cells increased with time (Figure 4.4 B), achieving up to 80% of transfected cells at 48h p.t., the time point where VLPs are released from transfected cells normally[23,27].

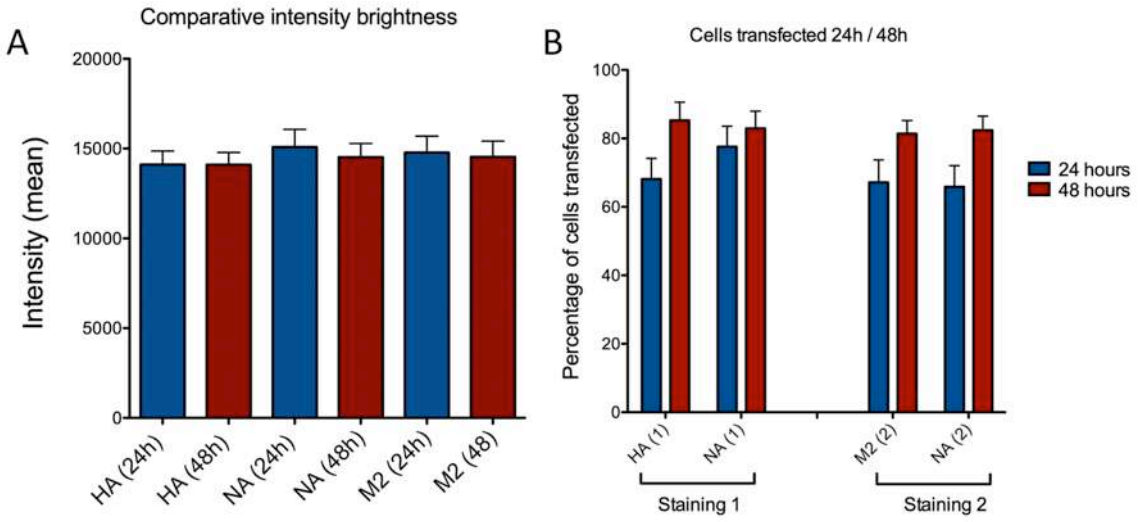

Figure 4.4: Measurements retrieved from the fluorescence images obtained of cells after 24h and 48h post-transfection. A) Mean intensity of fluorescence (n=50). B) Percentage of cells transfected at 24h p.t. and 48h p.t. (n=400). Error bars: SEM.

Thus, to monitor the recombinant protein production with DNA-PAINT, we selected both time points to further track the expression and the interaction of the recombinant proteins expressed prior the self-assembly of the VLPs.

To perform DNA-PAINT imaging, we transfected Cos7 cells with the three plasmids at the same time and after 24h or 48h p.t. we fixed the cells and immunostained them with primary and the secondary antibodies containing the docking strands. Next, to acquire the super-resolution image, we added an optimized concentration of each imager sequentially (1.5 nM) in the same field and with the same focus, paying special attention to the washing steps between imagers.

Figure 4.5A-B shows the super-resolution images obtained for each protein in the same region of the membrane. In general, the three proteins displayed visual homogeneous distribution along the surface both at 24h p.t. (Figure 4.5) and at 48h p.t. (Figure 4.5B).

Thanks to DNA-PAINT it was possible to image three different proteins in the same area of the cell using the same parameters for the super-resolution image acquisition, allowing the comparison of the localizations obtained. These retrieved localizations from the super-resolution reconstructions were defined within the membrane area, obtaining the density of localizations (localizations/μm^2) per protein and per cell at both time points. The density of

localization correlates to the amount of protein presented in the area measured, semi-quantifying the protein expression from the same cell.

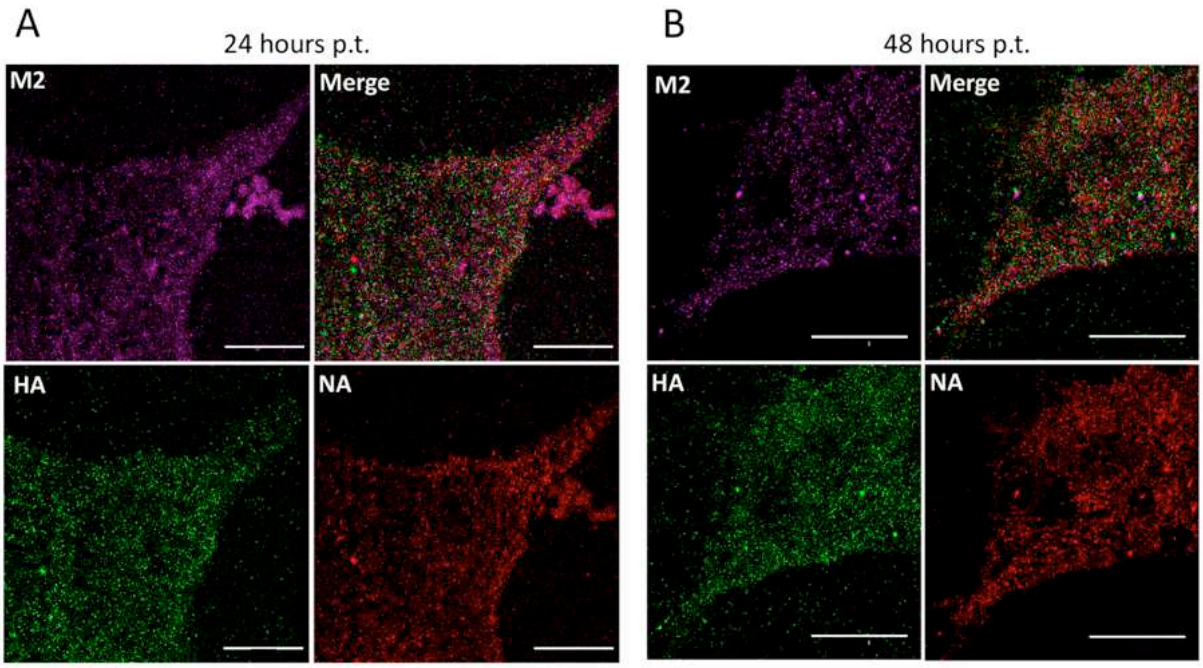

Figure 4.5: DNA-PAINT imaging of cells expressing recombinant proteins after 24 hours or 48 hours post transfection (p.t.). A) Super-resolution images of cell expressing the three proteins of influenza (HA (green), NA (red), M2 (magenta) and the merged of the three of them) after 24 hours p.t.. The images show a portion of the cell membrane. Scale bar: 5 μm. B) Super-resolution images of cell expressing the three proteins of influenza (HA (green), NA (red), M2 (magenta) and the merged of the three of them) after 48 p.t.. The images show a portion of the cell membrane. Scale bar: 5 μm.

These localizations were plotted in two different graphs: the localization/μm^2 of each protein within the population of cells (Figure 4.6A), and the localizations/μm^2 of the three proteins expressed within the same cell (3D plot, Figure 4.6 B).

When we examined the localizations of each protein in the whole population of cells analysed (Figure 4.6A), we observed that, independently the time point, each protein displayed a different density value, ranging between 100 localizations/μm^2 to up to 400 localizations/μm^2 in some cases. In other words, each cell expressed a different amount of each protein within the population of cells at 24h and 48h p.t. Besides, there was not a substantial difference between the amount of proteins at 24h and 48h, which could be due to the extreme biological differences between the protein productions seen. These results proved how heterogeneous is this recombinant expression system.

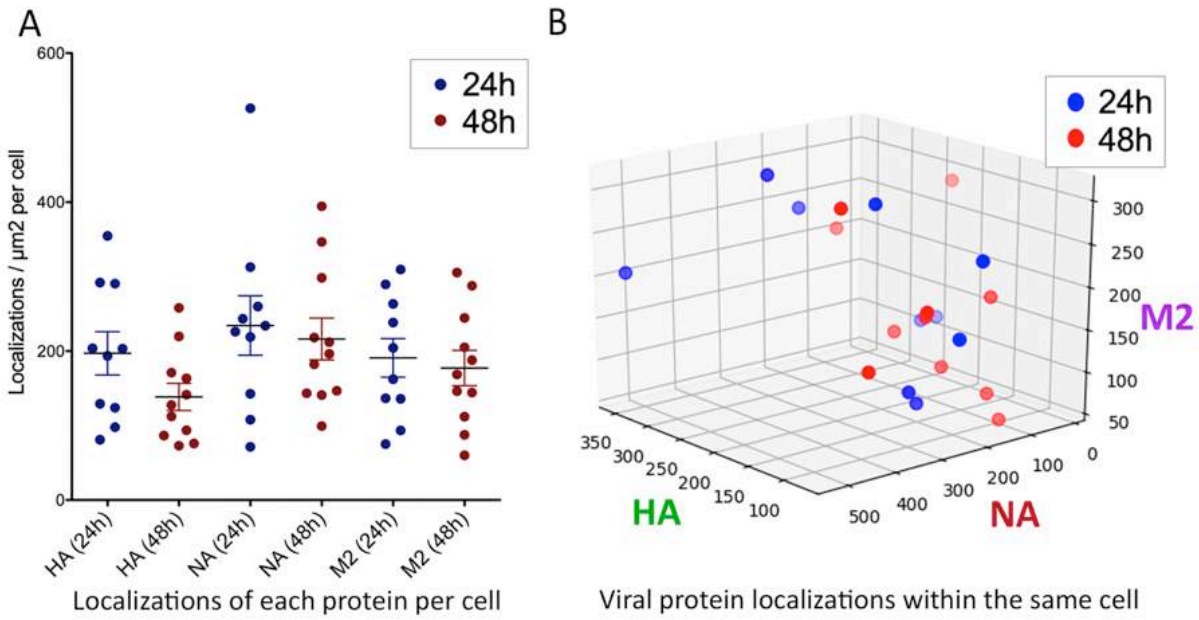

Figure 4.6: Localizations retrieved from the super-resolution analysis of mammalian protein expression with DNA-PAINT. A) Localizations of each protein per cell: quantification of the amount of localizations/µm^2 of HA, NA and M2 at 24h and 48h p.t. in the whole population of cells (n=10). Each dot correspond to a cell analysed. Blue: 24h p.t., Red: 48h p.t... Mean and SEM. B) Viral protein localizations within the same cell: semi-quantification of the three recombinant proteins expressed within the same cell (n=10). Blue: 24h p.t., Red: 48h p.t... The axes HA, NA and M2 represent the amount of localizations/µm^2 per each protein. Each dot corresponds to a cell analysed.

Thanks to the multicolour ability of DNA-PAINT we could relate and compare the density (localizations/µm^2) of the three proteins expressed within the same cell at the same time (Figure 4.6 B). We observed that each single cell expressed the proteins at different levels without any correlation, not displaying a consistent recombinant expression of the three proteins transfected simultaneous.

All in all, from these preliminary results we confirmed that DNA-PAINT could measure the recombinant expression of the viral recombinant proteins, relating the amount of localizations with the amount of protein expressed. We further corroborated the heterogeneity of expression of this system, previously mentioned in the literature, confirming that the three transfected proteins were express at completely different levels, despite of being transfected at the same time and with the same concentrations.

4.1.1 DNA-PAINT characterization of the cluster distribution

Moreover, observing a close-up of the merged areas on the super-resolution images (Figure 4.7A), we detected that proteins arranged in small groups, sometimes overlapping with each other (arrowheads). In order to measure the observed differences in protein arrangement with time, we carried out an analysis on the size of the organized localizations identified, by using a cluster algorithm that would measure and classified defined clusters of localizations.

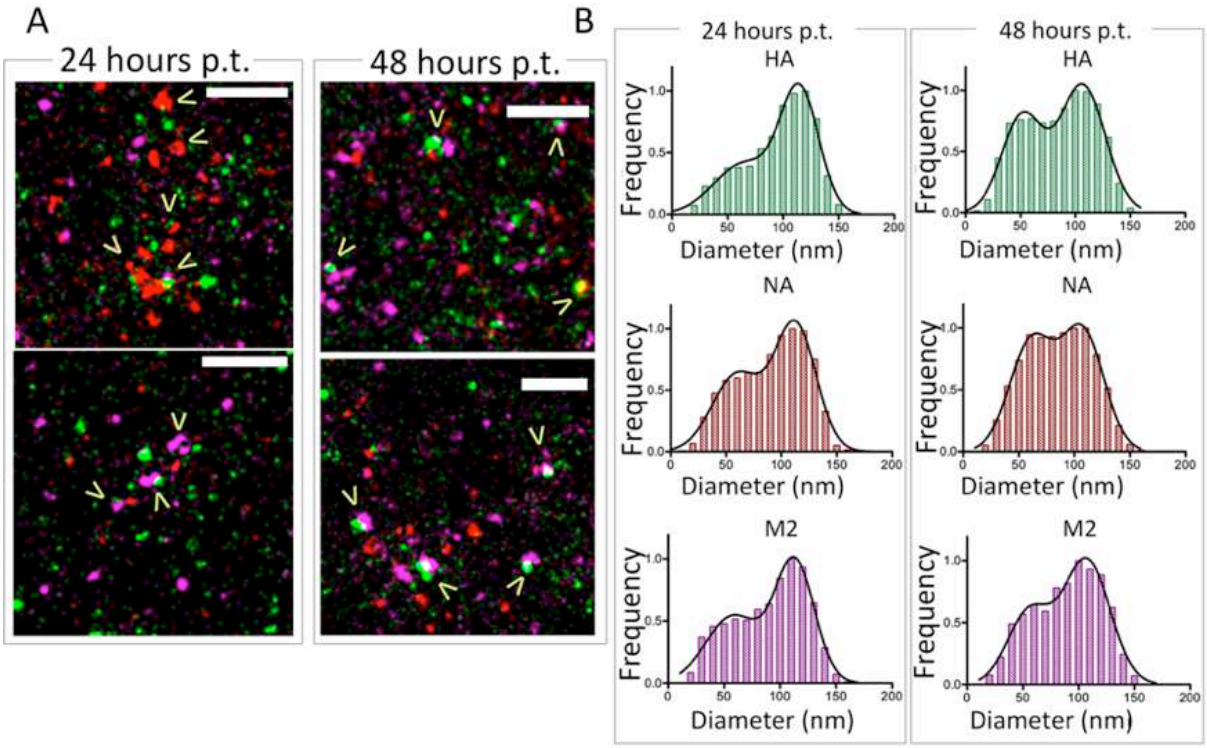

Figure 4.7: Recombinant protein distribution along the membrane of cells at 24h and 48h post-transfection (p.t.) measured with DNA-PAINT. A) Close-up super-resolution images of the merge of the 3 proteins expressed within the same cell at 24h p.t. and 48h p.t.. The arrowheads indicate the bigger cluster agglomerations and co-localizations. Scale bar 500 nm. Red: NA, Magenta: M2, Green: HA. B) Cluster size distribution of each protein expressed in the whole population of cells at 24h and 48h p.t. The distribution of the diameter (nm) showed two populations fitting a two-Gaussian model (black line). n=6000

In general, the diameters of the clusters of the three proteins oscillated between 50 nm to 150 nm (Figure 4.7B). Observing the distribution of the diameters, we detected that at 24h p.t., the diameter distribution of the clusters identified of NA and M2 displayed a two-Gaussian distribution with two main populations, 50-60 nm and 100-110 nm. In the case of HA, the first peak was subtler and most of the clusters found had a peak at 110 nm.

To study in detail the two populations found we divided the clusters analysed into the two populations observed (0-70 nm and 71-170 nm) (Figure 4.8). With this new layout we confirmed that both populations followed a Gaussian distribution with different amplitude. Likewise, we identified that 70-77% of the clusters presented a size distribution between 71-170 nm (Figure 4.9).

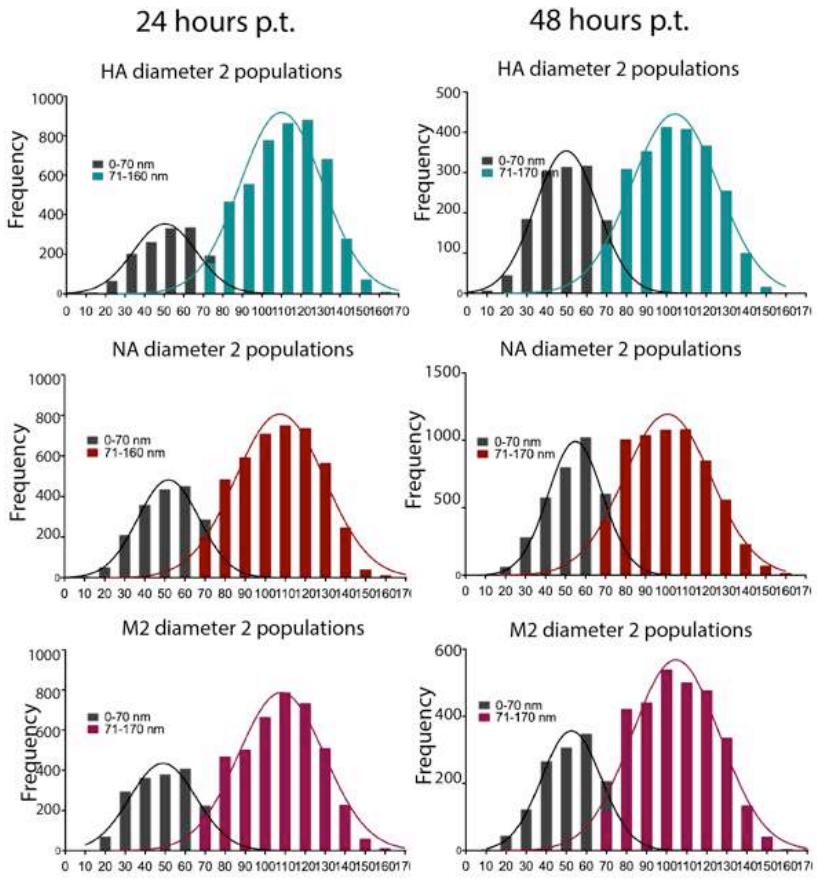

Figure 4.8: Cluster size distribution of the population of clusters. Frequency distribution of the diameter of the clusters at 24h and 48h divided by size to distinguish the two populations (0-70 nm and 71-170 nm). Grey colour represents the population of 0-70 nm and each colour (blue, red, magenta) represents the population of 71-170 nm of HA, NA and M2 respectively. n=6000.

Furthermore, these distributions changed with time, and at 48h p.t. the peaks of both populations started to balance, especially HA and NA where the two-Gaussian populations displayed similar amplitude (Figure 4.7B, Figure 4.8). The average size of the population of clusters at 24h and 48h was quite similar (both presented peaks at 70 nm and 100 nm), however, at 48h p.t. the amount of the second population (71-170nm) decreased by 10% in the

three proteins (Figure 4.9). We hypothesized that this decreased could be related to the VLP production; while small clusters remained constant in time, big aggrupation of proteins were forming VLPs and had been released at 48h p.t.

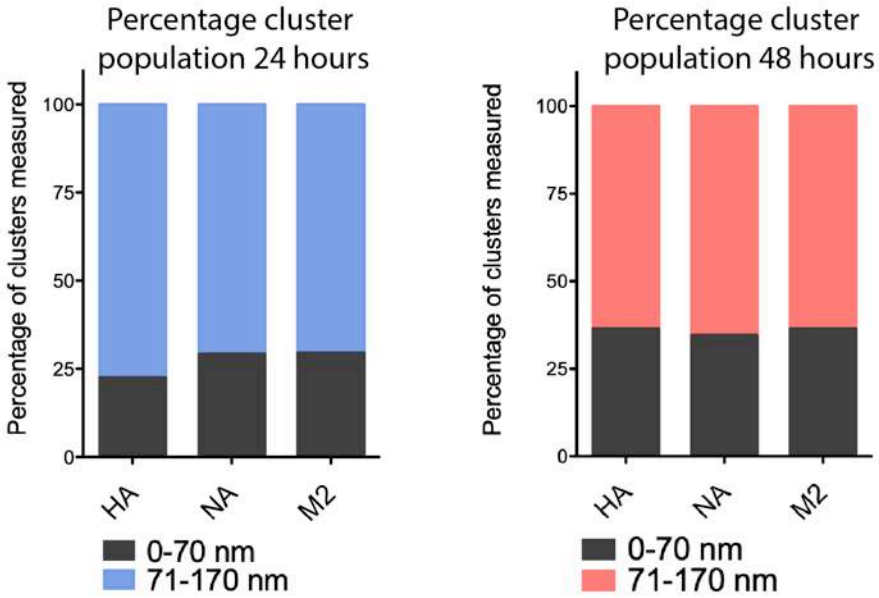

Figure 4.9: Percentage of the populations of clusters (0-70 nm and 71-170 nm) for each protein (HA, NA and M2) at 24h p.t. and 48h p.t. n=6000.

To confirm this concept, we measured the percentage of colocalization of the localizations retrieved (Figure 4.10). For this purpose we applied a Clus-DoC analysis, developed by Pageon et al.[45]. Details are explained on methods but to summarize, this analysis consist in creating a density map of the localizations of the two proteins to analysed. These density maps are compared and valuated, so a DoC value is assigned to each of the localizations based on their colocalization (1 correlated, -1 anticorrelated, 0 non-correlated). To obtain the percentage of colocalization, we selected a DoC threshold of 0.4, since is the optimal DoC value to include the localizations that are colocalizing but distant 10 nm, the resolution of DNA-PAINT. Importantly, this analysis only allowed measuring the percentage of colocalization between two proteins, comparing the effect of one on the other and contrariwise.

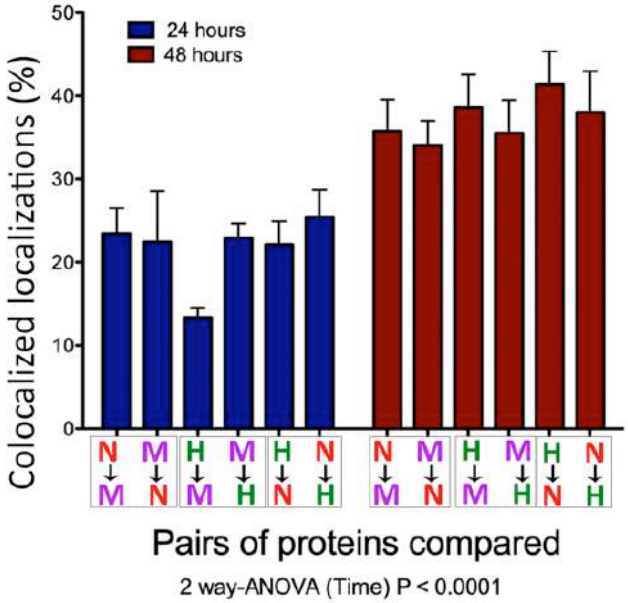

*Figure 4.10:Percentage of colocalizations of the localizations of the three pair proteins within the same cell (n=3). The comparisons are done in pairs, studying the present of density clusters of one protein on top of the other protein and vice versa (protein 1 → protein 2; protein 2 → protein 1). N indicated NA, M indicated M2 and H indicated HA. 2-way ANOVA test on the factor "time", extremely significant *** P<0.0001.*

As observed in Figure 4.10 three pairs of proteins were compared, obtaining two percentages of colocalization for each pair. The general percentage of co-localization of proteins at 24h p.t. oscillated between 12-22%. Except HA compared to M2, which exhibited an unexpected low colocalization, the remaining comparisons presented similar percentages of colocalization. We interpreted that this even value is an indicator of a more random distribution of the clusters of proteins. However, at 48h p.t. the colocalization boosted up to ~40% even in the comparison between HA and M2. This increase of the percentage of colocalizations was statistically significant (P<0.0001) and concurrent to the decreased of big clusters of proteins, fact that we interpreted as the production and release of VLPs. Overall, using DNA-PAINT we observed the distribution of the three recombinant proteins expressed on the membrane, describing their cluster arrangement with time. At 48h p.t., the time point at which VLPs are starting to be released from the cell, the recombinant proteins organized in big and co-localized clusters, releasing from the membrane.

In brief, our method allowed the imaging and localization of recombinant viral proteins on cell membrane in the nanoscale, not only retrieving semi-quantitative information about the amount of protein produced but also correlating the amount of all proteins expressed within the same

cell at single-cell level. Further, these localizations were used for the quantification of the clusters formed on the membrane, and the interaction of the three proteins. This way we were able to describe the evolution and colocalization of recombinant proteins on the membrane with time.

4.1.2 DNA-PAINT characterization of the protein distribution on VLPs

Besides cells recombinant approaches, multiplexing DNA-PAINT characterization and quantification of small structures has been deeply described on nanoparticles[46] and exosomes[47], similar structures than influenza VLPs. For this purpose we produced, isolated and labelled the VLPs resulting from Cos7 cells previously studied, to describe the distribution of the recombinant proteins at single-particle level. To make sure the VLPs produced were properly isolated, we measured with dynamic light scattering (DLS) all the fractions recovered from the ultracentrifugation sucrose gradient (data not shown) to select the fraction with lower polydispersity (PDI) and right size (~100 nm) (fraction corresponding to 42-45% sucrose). Finally, the size of the recovered VLPs was determined with conventional techniques such as DLS, transmission electron microscopy (TEM) and super-resolution microscopy (dSTORM), measuring between 75-105 nm, depending on the technique employed (Figure 4.11).

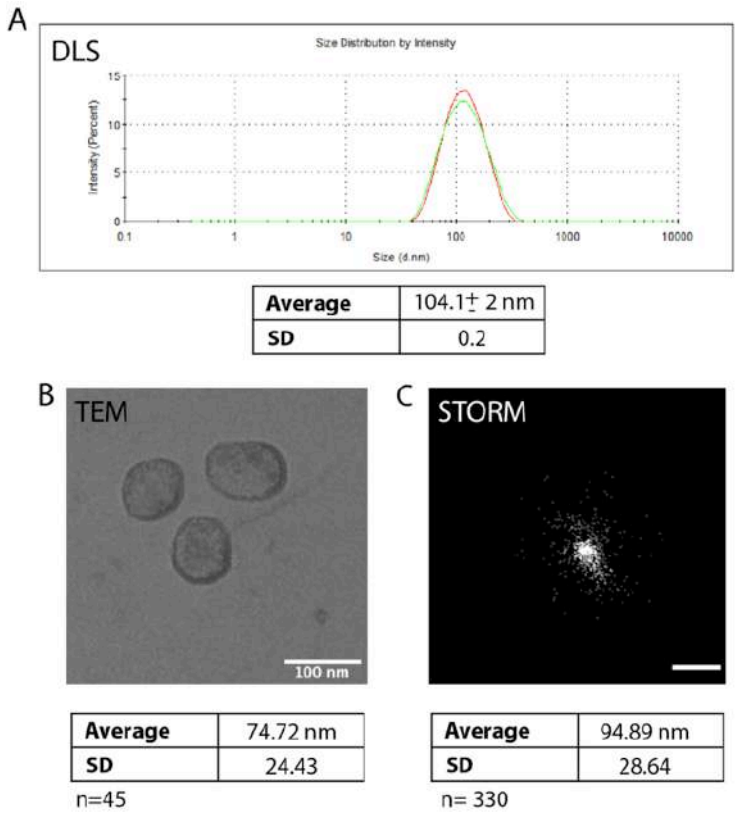

Figure 4.11: Measurements of the size of VLPs purified after ultracentrifugation with conventional techniques. A) Dynamic light scattering (DLS) measurements showing an average of 104,1 nm in diameter. B) Transmission electron microscopy (TEM) image of the VLPs purified, measuring an average of 75 nm in width. C) Stochastic Optical Reconstruction microscopy (STORM) image of VLP purified and immunostained against the protein HA with primary antibody mouse anti-HA and secondary antibody anti mouse-Alexa647. The average width is 95 nm. Scale bar: 100 nm

To perform the multiplexing DNA-PAINT, VLPs were labelled with a hydrophobic dye (DiI) to mark their position, being used as a reference of the centre of the particle. The immunostaining was performed in solution, using ultracentrifugation for washing the unlabelled antibodies. Due to an overlapping in the host of the primary antibodies of HA and M2 (both mouse-primary antibodies), it was not possible to perform a three-label immunostained as previously done on cells. Instead, we divided the protein identification in two pairs of proteins (similarly as Figure 4.3): HA and NA, M2 and NA, performing 2 separate experiments with the same conditions (1nM imager concentration). VLPs with the corresponding primary and secondary antibodies were incubated after washing on top of a clean glass-bottom petry-dish for 30 min, followed by the adding of the imager with the previously described tubing system.

After the image acquisition, a post analysis was performed with the retrieved localizations. Using the signal obtained from DiI for marking each VLP, we obtained the total number of

localizations of each protein per VLP, by fitting a size and shape criterion (not bigger than 120 nm and ellipse fitting). Further, the images obtained were merged and an artificial colour was assigned to each protein (green HA, red NA and magenta M2).

First, we focus attention to the study of HA and NA. Figure 4.12 A shows the reconstructed images obtained for HA (green) and NA (red) on VLP. As commented, the distribution of the localizations of HA and NA was studied together on the same VLP, observing that both proteins formed small clusters along the structure in some cases or a more evenly distribution on other cases. Generally, this population of VLPs displayed a strong heterogeneity intra-particle and inter-particle within the population of VLPs studied.

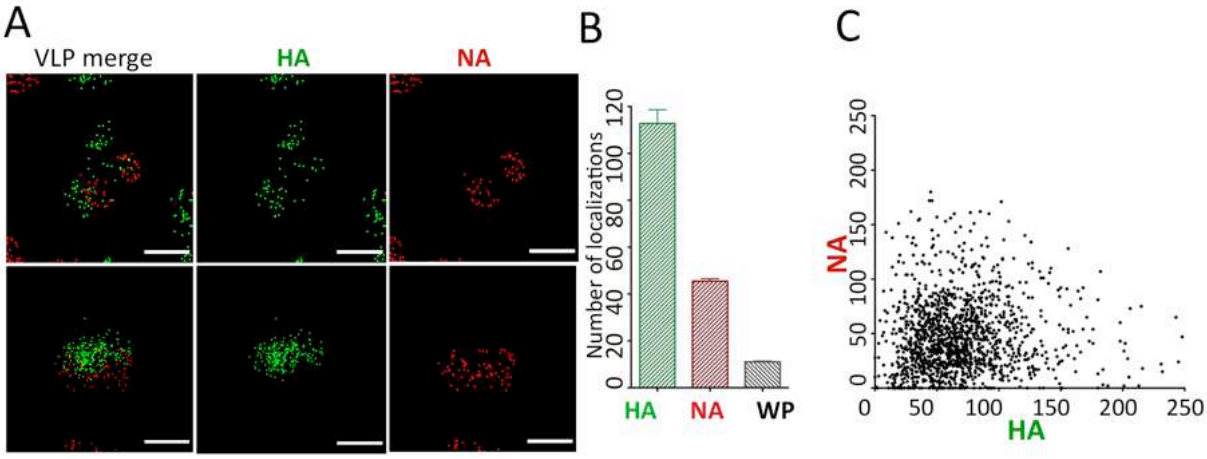

Figure 4.12: DNA-PAINT characterization of HA and NA on the resulting VLPs obtained at 48h post-transfection. A) VLPs immunostained against HA and NA. Each dot is a localization found around the reference (not shown). Scale bar 100 nm. Localizations retrieved from super-resolution analysis of VLPs B) Average of localizations of HA and NA per VLP. WP represents the negative control or wrong pairing (WP), imager mispairing on VLP (Mean and SEM). C) Localizations of NA and HA within the same VLP. N=1200.

The average of the total amount of localization per VLP of both proteins is displayed in Figure 4.12 B. In this case, HA showed an average of ~120 localizations per VLP while NA had ~56 localizations. When we plotted the distribution of the localizations (Figure 4.13) in the whole population of VLPs measured, we observed that they followed a Gaussian distribution with HA displaying a broader distribution than NA.

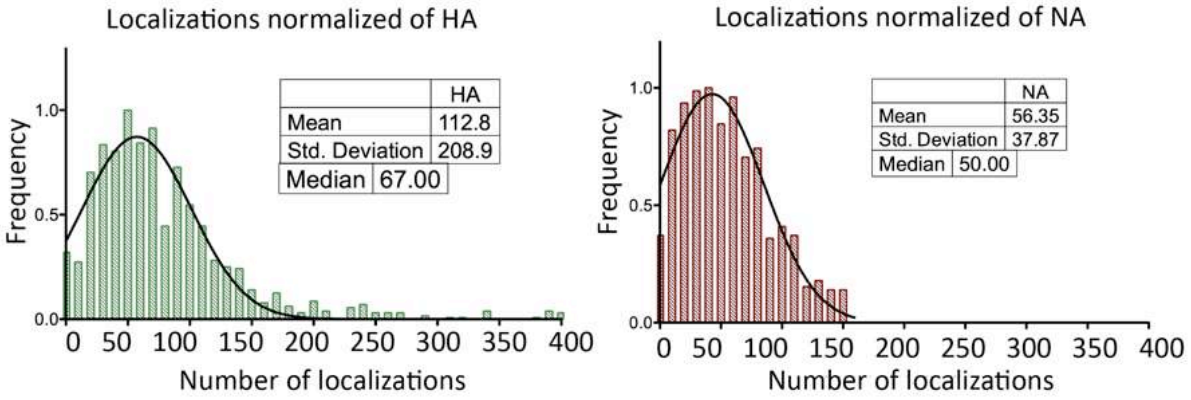

Figure 4.13: Frequency distribution of the localizations of HA and NA within the VLP population, showing a Gaussian distribution. NA was measured in two different experiments and in both experiments the mean and the median are very similar, proving the strong replicability of DNA-PAINT.

Furthermore, since we measured the amount of localizations at single-particle level, we could match the amount of both proteins within the same VLP (Figure 4.12 C), observing the lack of correlation between the amounts of localizations of NA and HA. Each VLP contained a different amount of proteins, confirming the enormous heterogeneity of the recombinant protein presence in the population of VLPs.

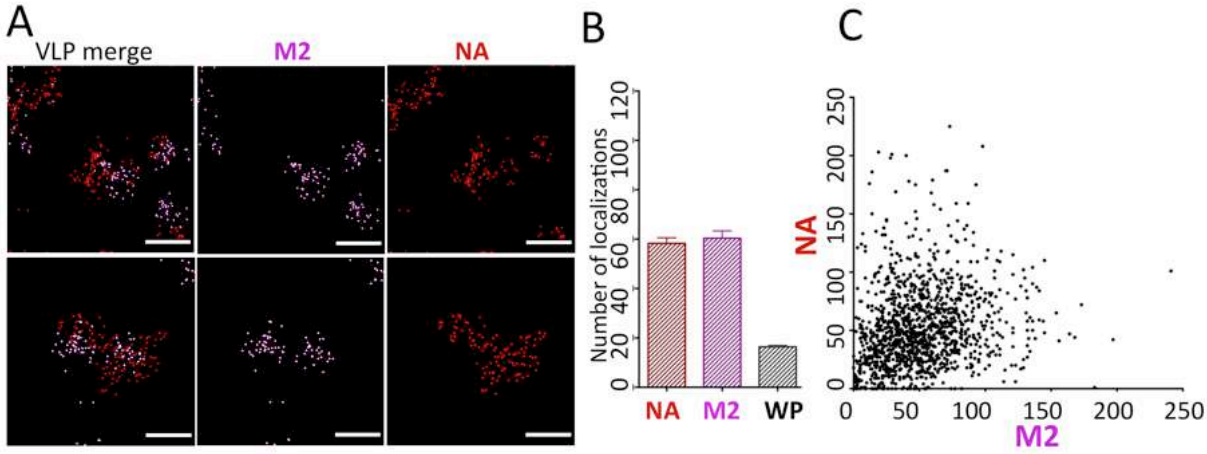

Figure 4.14: DNA-PAINT characterization of NA and M2 on the resulting VLPs obtained at 48h post-transfection. A) VLPs immunostained against NA and M2. Each dot is a localization found around the reference (not shown). Scale bar 100 nm. Localizations retrieved from super-resolution analysis of VLPs B) Average of localizations of NA and M2 per VLP. WP represents the negative control or wrong pairing (WP), imager mispairing on VLP (Mean and SEM). C) Localizations of NA and M2 within the same VLP. N=1200.

Similarly, the pair M2 and NA was observed. As seen in Figure 4.14 A, both proteins organized in small groups or clusters along the particle, exhibiting heterogeneity intra-particle and inter-particle. Moreover, NA and M2 revealed identical localizations on the surface (Figure 4.14 B), both containing ~60 localizations with a Gaussian distribution (Figure 4.15). In this case, comparing the presence of both proteins within the same VLP particle (Figure 4.14 C) it displayed a soft correlation of the incidence of both proteins, however, the population is so big (n=1200) that is complicated to calculate a proper correlation test for both localizations.

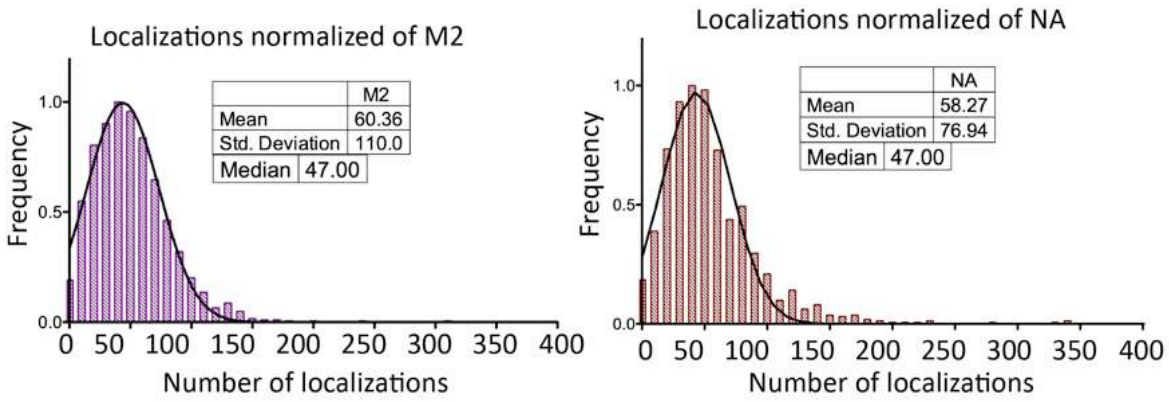

Figure 4.15: Frequency distribution of the localizations of M2 and NA within the VLP population, showing a Gaussian distribution. NA was measured in two different experiments and in both experiments the mean and the median are very similar, proving the strong replicability of DNA-PAINT.

To make sure the imagers were not binding randomly to the VLP structure or to the surrounding areas, we measured the amount of localizations using an imager with a DNA-strand not complementary to the ones used in the VLP, marked as wrong pairing (WP) (Figure 4.16). The centre of the VLP was imaged again using DiI as a fiducial marker for the correction of the mechanical drift and identification of the VLP particle. In general, WP gave significant lower localizations in both experiments, where the localizations are randomly distributed along the glass due to the stickiness of the dye proving how robust and specific is the imaging DNA-PAINT system.

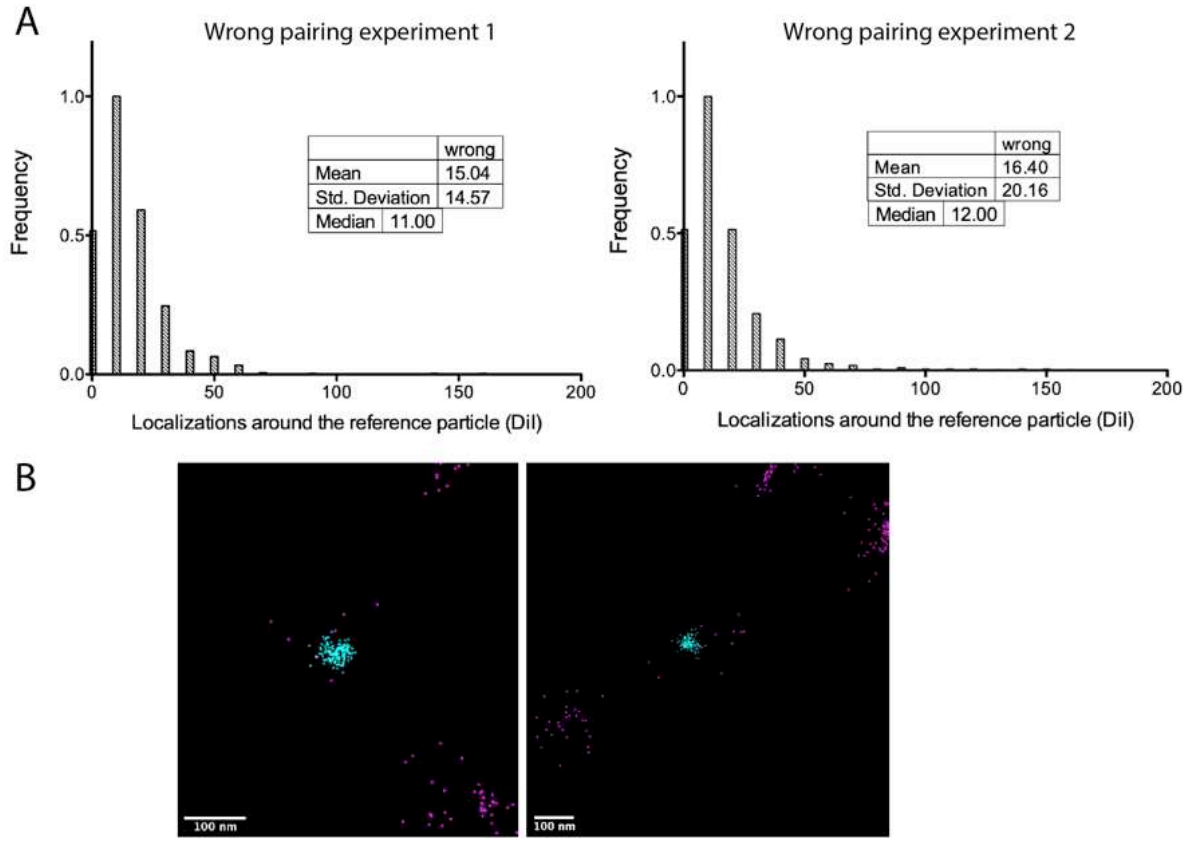

Figure 4.16: DNA-PAINT of VLPs using a wrong pairing. For experiment 1, VLPs were immunostained anti-HA (docking 1) and anti-NA (docking 2); Imager 3 (complementary to docking 3) was imaged at 1.5 nM in PAINT buffer as wrong pairing. For experiment 2, VLPs were immunostained anti-M2 (docking 3) and anti-NA (docking 2); Imager 1 (complementary to docking 1) was imaged at 1.5 nM in PAINT buffer as wrong pairing. A) Frequency distribution of the localizations obtained under wrong pairing of DNA-PAINT docking and imager strands (negative control). B) Images of the wrong imager (magenta) around a particle of VLP (cyan).

Taking all these data into consideration, we observed that the amount of localizations containing the VLPs was not aligned with the amount of localizations measured on cells. Whereas cells displayed a similar profile of expression of the three proteins on the membrane, in VLPs it was observed that HA was doubly expressed than NA and M2. Thus, the protein content of VLPs was not correlated to the amount of expression from mammalian cells. This could be explained by the self-assembly nature of the VLP formation, where VLPs star to self-assembly and interact with certain amounts of proteins.

All in all, with DNA-PAINT it was possible to characterize at single-particle level the allocation of the recombinant proteins, observing their distribution intra-particle and inter-particle and semi-quantifying the amount of localizations of both proteins within the same VLP, proving the

heterogeneity expression and protein content of the three proteins in the total population of VLPs. These results confirmed the potential use of DNA-PAINT to characterize the nanostructural distribution of the proteins of big batch of vaccines and VLPs at single-particle level.

4.3 Conclusions

In conclusion, DNA-PAINT proved to be a robust, sensitive and versatile tool to characterize the recombinant viral protein expression. Thanks to the multiplexing ability of DNA-PAINT we were able to semi-quantify the expression of three different recombinant proteins on biological samples using exactly the same conditions in terms of laser power, type of dye and lack of photobleaching.

Firstly, we successfully characterized the heterogeneous expression of the three proteins of influenza transfected at the same time on Cos7 cells, comparing the expression on the same surface area with time. The results confirmed how heterogeneously recombinant proteins are expressed on mammalian cells, not only within the population but also within the same cell when the proteins are expressed at the same time.

Thus, we characterized the distribution of the proteins while are organizing in clusters on the membrane, achieving resolutions of 10-15 nm that allowed the identification of two populations of clusters, small (60-70 nm) and big (100-110nm), in different proportions that changed with time. Concurrently, the localizations retrieved in the super-resolution analysis allowed a colocalization analysis, observing that with time the clusters increased the percentage of colocalization. All the information obtained would help describing the recombinant expression model, and even though the expression of the proteins was quite heterogeneous, the protein distribution and interaction stayed balanced; most of the proteins displayed similar sizes and percentages of colocalizations that changed evenly in time.

Furthermore, DNA-PAINT provided single-particle insights of the recombinant proteins on VLPs formed from Cos7 cells, allowing the semi-quantification and visualization of the distribution of the proteins along the particle, offering single-particle measurements of the two proteins characterized at VLP level. Remarkably, NA and M2 presented similar features in terms of amount of localizations and cluster distribution along the particle while HA was doubly expressed. These localizations per VLP were not correlated to the one observed in cells,

indicating that VLP content is not related to the total amount of protein expressed on cells but to the viral budding mechanism. Visualizing where are the proteins distributed on the VLP at single-particle level would led us to understand how heterogeneous is the population of VLPs intra-particle and inter-particle, critical feature for clinical approaches.

This nanocharacterization and semi-quantification based on DNA-PAINT is a powerful tool to study and define new vaccines systems, thus would permit the monitor of the recombinant protein expression on cells, crucial information to improve the development of recombinant vaccines such as the newly introduced COVID-19 vaccine. Being able to measure and visualize the distribution of the recombinant proteins produced would help selecting the best expression system and thus, optimize it.

4.4 Perspectives

As commented in detail at the beginning of the chapter, VLPs have a potential role in the vaccine development industry due to their similarities with full viruses. Hence, the main goal of this chapter was to implement DNA-PAINT, a super-resolution technique, to study in detail the VLP protein content for their application in different roles in the pharmaceutical industry. However, VLPs are not only being in the focus for developing universal vaccines, but also for other interesting pharmacological approaches.

New trends in nanomedicine and nanotechnology are focus on using drug delivery with nanoparticles or nanocarriers to target specific cells to be treated. In the need of looking for new materials for targeting efficiently, the use of VLPs has been strongly purpose due to the specific interaction target-cell driven by VLPs, using the same mechanisms that an influenza virus uses to interact and infect cells. Other advantages of using VLPs as drug delivery vectors are the biocompatibility, low toxicity and degradability. Since VLPs are produced in mammalian or insect cells, neither their proteins nor membrane are toxic and thus are easily degradable by the proteolytic mechanism of the cell, thus they can protect genetic materials and small peptides the same way they virus protect their own nucleic acids (Figure 4.17).

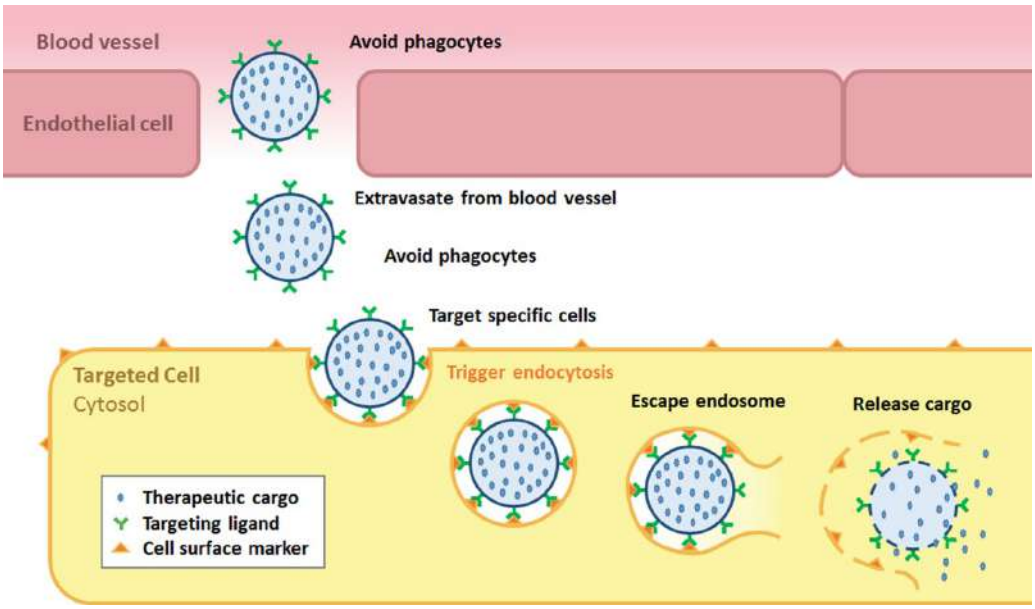

Figure 4.17: Diagram of targeted drug delivery using VLPs. The VLPs need to avoid the immune system and phagocytes, be able to extravasate from the blood vessels and arrive at target cells where a specific interaction would allow the VLPs to internalize in the cell and release the cargo. Reproduced from reference [48] Copyright © 2016 John Wiley & sons, Inc.

Therefore, VLPs have been proposed to envelope drugs, small molecules, nucleic acids and dyes[49]. We can find some examples of successfully delivery of mRNAs and small peptides using VLPs of the bacteriophage PP7 virus into mouse prostate cancer cells[50] or in vitro delivery of siRNA to osteoblast cells in rats using VLPs of John Cunningham virus (JC) from the polyomavirus family[51].

Even though the potential use of VLPs as drug delivery vectors and drug carriers, there are several limitations to take into account, since VLPs are derived from viruses with their own restrictions and idiosyncrasies. To overcome some of these challenges, modifications of the external part of the VLPs have been suggested and tested:

-Pre-existing immunity against influenza virus: Most of the population has antibodies against most commons strains of influenza due to the continuous contract against this virus. This leads to VLPs not being suitable for repetitive administration. The immune response of the person receiving the treatment can be increased with multiple and repetitive administration, lacking effectiveness and thus not being suitable for long-term treatments[52]. The most promising approach to overcome this immunity response is to use masking agents such as polyethylene glycol (PEG)[12,53].

-Targeting specificity: the natural tropisms of viruses present a disadvantage when targeting cells that are not the naturally targeted, such as cancer cells. For this, external modification of the surface of the VLPs may be necessary, adding antibody fragments[54], transferrin[55], DNA aptamers[56] or biotin[57].

-Efficient cargo loading and retention: the cargo has to be charged in high concentrations and maintaining the stability of the VLPs, to avoid leakage during the transportation and the storage. Two strategies are followed to load the cargo into VLPs: covalent and non-covalent methods.

Therefore, not only VLPs need to be modified and optimize but also due to their small size, new mechanisms are needed to identify the protein content, the targeting specificity and the cargo loading. Hence, we propose to use DNA-PAINT as a crucial step to characterize VLPs for performing drug delivery.

This way, we want to produce a batch of different VLPs as promising drug delivery vectors. By using DNA-PAINT we would be able to identify the protein content, distinguishing also the interactions with the target cells. Additionally, we would visualize with SRM the pathway that the VLPs follows once are internalized by host cells, using the same approach we followed in chapter 7, where we studied the nanoparticle uptake of a nanovaccine. With this detailed insight in the drug delivery mechanisms of VLPs vectors, we could unveil the optimizations needed to make it through clinical stages.

4.5 Materials and methods

4.5.1 Plasmid amplification and isolation

Influenza plasmids PHW2000 (Figure 4.18) HA, NA and M (M1/M2) were donated by Dr. Kenny Roose and Anout Smet from the groups of Dr Nico Callewaert and Dr Xavier Saelens from VIB-UGENT Center for Medical Biotechnology.

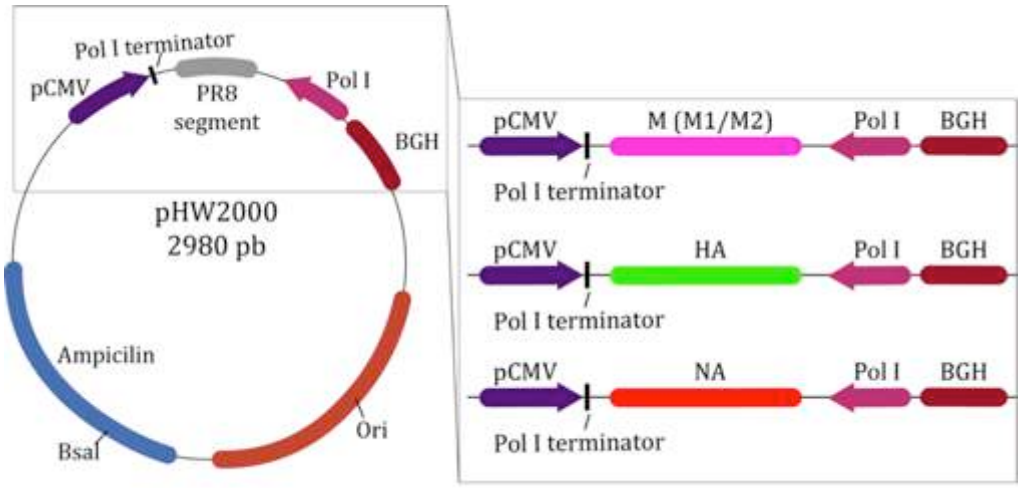

Figure 4.18: plasmid map of pHW2000 and the insert of each protein, described and developed by Ref [58] and optimized [59,60,61,62].

These plasmids were introduced into competence *E.coli* DH5α bacteria cells by transformation. For this, frozen competence cells of *E.coli* were thawed on ice, where 200 µl of the cells were mixed with 1 µl of plasmid (at least 15 ng of DNA) and kept together on an ice bath for 10 min. Right after, a heat shock was performed to the competence cells at 42ºC for 1 min and put again in an ice bath for at least 1 min. 800 µl of LB medium was added to the mixture of cells and plasmid and incubated at 37ºC in a shaker for 1 h. Then, 100 µl of the mixture was seeded on a LB-ampicillin plate and cells were spread using a bent tip until the agarose absorbed the mixture. The agarose plates were incubated at 37ºC overnight.

Then, one colony from the plate was picked and put into 10 ml LB-ampicillin in an Erlenmeyer and was led grow at 37ºC on a shaker for 8 hours. After this time, a dilution of 1:1000 of the culture was done into 150 ml LB-ampicillin and led it grow overnight at 37ºC on a shaker.

The optical density at 600 nm (OD_{600}) of the overnight culture was then measured and the plasmid was isolated following the instruction of the GeneJET plasmid Midiprep kit from Thermo fisher (K0481).

4.5.2 Cell culture transfection

Cos7 cells were used in these sets of experiments and were donated by the GEMAT group from IQS, directed by Dr. Salvador Borros. Cos7 cells were seeded at 1 x 10^5 cells per well in a 24 well plate for production of VLPs or 2.5 x 10^4 cells per well in a 8 well µ-Slide (Cat. No. 80826, ibidi GmbH, Germany) for fluorescence microscopy and DNA-PAINT microscopy, overnight at 37ºC and 5% of CO_2 to achieve 85% of confluence prior to performing the transfection experiments.

The day after, complexes of lipofectamine 2000 (Thermo fisher) and plasmids of DNA were prepared as indicated in Table 4.1 and were mixed as following: the total amount of DNA was mixed with 100 µl or 200 µl (half the final volume) of serum-free DMEM (no FBS added). At the same time, lipofectamine 2000 was mixed with 100 µl or 200 µl of serum-free DMEM with the pipette. Then, the whole volume of lipofectamine 2000 diluted was put on top of the dilution of DNA plasmid, mixing gently for several seconds and then incubated together for 5 minutes at RT. Then, cells seeded on wells were washed with 1x PBS and incubated with the plasmid-lipofectamine complex solution for 4 h at 37ºC 5% CO_2. Negative control was performed without DNA plasmid or with a DNA plasmid that produced proteins not related to influenza proteins plus lipofectamine.
Subsequently, cells were washed carefully with 1x PBS and incubated with full DMEM for 24 or 48 hours at 37ºC and 5% CO_2.
The negative control is performed with a pDOL plasmid expressing LacZ.

	8 well µ-Slide	**24 well plate**
Number of cells per well	2 x 10^3	1 x 10^5
Total amount of DNA per well	2 µg	4 µg
Amount of DNA per plasmid per well	0.66 µg	1.3 µg
Amount of lipofectamine 2000 per well	0.8 µl	2 µl
Final volume per well	200 µl	400 µl

Table 4.1: table of combination of lipofectamine-DNA transfection mixture

4.5.3 Purification of VLPs and DiI staining

Cells seeded in 24 well plates, transfected and incubated for 48 hours post-transfection were used to purify the VLPs produced. For this, the supernatant of these cells was filtered (cutoff 0.45 µm) and centrifuged at 2,500g for 30 min at 4ºC to remove cell debris. The VLP recovered in the supernatant were stained with 10 µM of DiI for 30 min in a shaker at RT in the dark.
After incubation with DiI, the suspension was loaded on top of 20-60% continuous sucrose gradient and centrifuged at 125,000g (35,000 RPM) for 2 h at 4ºC in a Beckman SW41 rotor. A total of 6 fractions of 2 ml were collected manually from the top to the bottom. Each fraction was diluted 1/3 with PBS and centrifuged at 40,000 rpm for 1 h at 4ºC. The pellet containing VLPs was resuspended in 50 µl of PBS and kept at 4ºC in the dark.

4.5.4 VLP imaging with TEM

VLP purified samples were incubated with 2% PFA for 30 min and absorbed on freshly glow discharged carbon-grid for 20 min. Subsequently, grids were washed 3 times with deionized water during 1 min for the first wash and 30 seconds for the two remaining. Washed samples were stained with 2% uranyl acetate for 5 min, air dried and observed using a Jeol J1010 (80 kV) TEM microscope.

4.5.5 Determination of VLP size by DLS

VLP size measurements of all purified fractions were determined by dynamic light scattering (DLS) at 4ºC with a Zetasizer Nano ZS ZEN 3600 (Malvern Instruments Ltd, United Kingdom, 4-mW laser) using a wavelength of 633 nm. Correlation functions were collected at a scattering angle of 90ºC, and particle sizes were calculated using the Malvern particle sizing software (DTS version 5.03). The value was recorded as the mean of three measurements and each measurement was determined from the average of 12 cycles in a disposable plastic cuvette. The size distribution was given by polydispersity index (PDI, a value between 0 and 1).

4.5.6 Conjugation of the docking strand with secondary antibodies

The DNA labeling of antibodies was done via maleimide-PEG2-succinimidyl ester as described in previous works[44]. The list of antibodies and conjugated DNA docking sequences is shown in Table 4.2, while the complementary sequences for the imagers are displayed in Table 4.3. DNA oligonucleotides were purchased from Integrated DNA technologies (IDT).

Antibody	**Docking sequence**
Goat anti-mouse IgG (H+L) (115-005-003)	P1 Thiol C6SS- TTA TAC ATC TA–3’
Goat anti-mouse IgG (H+L) (115-005-003)	P3 Thiol C6SS- TTT CTT CAT TA–3’
Goat anti-rabbit IgG (H+L) (111-005-003)	P2 Thiol C6SS- TTA TCT ACA TA–3’

Table 4.2: list of secondary antibodies and docking sequence bound

Number sequence	Docking	Imager
P1	Thiol C6SS - TTA TAC ATC TA–3'	5'–CTA GAT GTA T–Atto647N -3'
P2	Thiol C6SS - TTA TCT ACA TA–3'	5'–TAT GTA GAT C–Atto647N -3'
P3	Thiol C6SS - TTT CTT CAT TA–3'	5'–GTA ATG AAG A–Atto647N -3'

Table 4.3: Sequence of the DNA-docking and Imager for DNA-PAINT acquisition images.

A resume of the protocol is the following:
The reduction of the thiolated DNA for the maleimide reaction was done incubating 30 µl 1 mM of thiolated DNA in 70 µl of freshly prepared DTT solution (250 mM DTT, 1.5 mM EDTA and 0.5x PBS, pH 7.2) for 2 h at RT. At the same time, the maleimide linker was bound to the secondary antibody. For this, the cross-linker solution of maleimide-PEG2-susccinimidyl ester was prepared at 10 mg/ml in DMF and added to the secondary antibody in a 10:1 molar ratio. The antibody with the linker was incubated for 90 min at 4ªC on a shaker.

Before the incubation of the thiolated DNA and the DTT solution finished, a Nap-5 column was equilibrated with ddH_2O. Then, DNA-DTT solution was purified added on top of the column with ddH_2O. The first fractions of the flow-through were collected and measured using the NanoDrop spectrophotometer (ND-1000). The fractions that showed the highest concentrations were collected together and concentrated using Amicon spin filters (3kDa). The concentration was measured again in the NanoDrop spectrophotometer and being >700 ng/µl. After the antibody-cross linker reaction was complete, the linker was removed using a Zeba™ desalting column at 1,500g for 2 min at 4ºC. The flow-through was measured with the NanoDrop spectrophotometer, obtaining a concentration >1.5 mg/ml. Purified solutions of thiolated DNA and antibody were mixed with a 10:1 molar ratio and gently shaken overnight at 4°C. In order to remove the excess of not bound DNA, an Amicon spin filter (100 kDa) was used. Finally, the volume was adjusted to 100 µl with 1x PBS, the concentration was measured spectroscopically with a NanoDrop and the antibody solution was stored at 4ºC.
The final concentration of the purified antibodies was ~ 6 mg/ml with a ratio docking/Ab ~2.5.

4.5.7 Cell immunostaining for microscopy

Cells 24h and 48 h after transfection were fixed with 4% of paraformaldehyde for 10 min at RT. After 3 washes with PBS, the sample was blocked for 30 min with 0.3M Glycine in PBS (Merck Chem) and with 3% BSA-PBS for other 30 min. After blocking, primary antibodies (Table 4.4)

mouse anti-HA and rabbit anti-NA were incubated at 4 µg/ml together with 3% BSA for 1 h. Following the incubation, cells were washed 3 times with 1x PBS for 5 min each and then incubated with secondary antibody.

For fluorescence microscopy

Anti-rabbit Alexa Fluor 488 and anti-mouse Alexa Fluor 647 (A-11008 and A-21239) were diluted at 8 µg/ml in 3% BSA and incubated for 1 h at RT in the dark. Cells were washed 3 times with 1x PBS and imaged immediately with the fluorescence microscope.

For DNA-PAINT

Docking strand conjugated secondary antibodies anti-mouse docking 1 and anti-rabbit docking 2 were diluted at 12 µg/ml in 3% BSA and incubated for 1 h at RT in the dark. Right after, for staining the protein M2 (antibody anti-mouse cross-reactivity), secondary antibodies were washed and the sample was blocked by using anti-mouse (Unconjugated; Jackson Immunoresearch Goat anti-mouse) at 20 µg/ml for 1 h in 3% BSA at RT. With this step the free epitomes from the mouse anti-HA abs presented in the sample would be blocked to avoid cross-reactivity with a new immunostaining using anti-mouse docking 3.
After 3 washes with 1x PBS, primary antibody mouse anti-M2 (ab5416) at 4 µg/ml in 3% BSA was incubated on cells for 1h at RT. Subsequently, 3 washes with 1x PBS for 5 min was performed and then the incubation with the secondary anti-mouse docking 3 12 µg/ml in 3% BSA for 1 h at RT. Cells were washed 3 times with 1x PBS for 5 min and imaged. PAINT buffer consist on 1x PBS 500 mM NaCl 1 nM imager.

Primary antibodies used:
-Primary antibody anti neuraminidase (Influenza A H1N1 A/Puerto Rico/8/1934) ABIN1841889 antibodies-online
-Primary antibody anti Hemagglutinin (Influenza A H1N1 A/Puerto Rico/8/1934) 11684-MM05 sinobiological
-Primary antibody anti M2 protein (Influenza A H1N1) ab5416 abcam

Table 4.4: list of primary antibodies used in this project.

4.5.8 VLP immunostaining for microscopy

VLPs were immunostained in solution. For this, 20 µl of VLPs were diluted to a final volume of 100 µl with PBS and incubated with 7 µg/ml of primary antibody anti-influenza (anti-HA with anti-NA and anti-M2 with anti-NA) at 4ºC on a shaker overnight. To wash, the sample was centrifuged at 40,000 rpm (98,600 g) using a TLA-55 rotor for 1h at 4ºC and the pellet was resuspended in 100 µl of PBS with 20 µg/ml of secondary antibody bound to docking 1,2 or 3 for 1h at RT in the dark in a shaker. Subsequently the solution was washed by centrifugation at 40,000 rpm for 1h at 4ºC and the pellet was resuspended in 50 µl of PBS.

4.5.8.1 For DNA-PAINT

We used Nunc-glass petry dish (40.4 mm 150680 Thermofisher). Dishes were washed with ethanol and dried with nitrogen. The suspension of VLPs was incubated on top of the glass covered with a piece of parafilm for 30 min. After incubation, PAINT buffer is added on top while parafilm is removed. PAINT buffer consist on 1x PBS 500 mM NaCl 1.5 nM imager.

4.5.8.2 For dSTORM

Secondary antibody is anti-mouse alexa647. After second wash with ultracentrifugation, VLPs were incubated on the microscopy slide.

The microscopy slide was prepared by washing the coverslips 10 min with acetone and 10 min with ethanol by sonication, followed by drying with nitrogen. The slide was assembled using two stripes of double-sided adhesive tape that secured the coverslip (150 µm thickness 24x24 mm size) on a glass slide forming a flow chamber. immunostained VLPs (approx. 35 µl) were pipetted in the chamber and incubated for 10-15 min in the dark at room temperature. Then, unbound VLPs were washed out using of PBS and dSTORM buffer was added prior to imaging. The STORM buffer consists of an oxygen scavenging system (0.5 mg/ml glucose oxidase, 40 µg/ml Catalase), 5% w/v glucose and cysteamine 100 mM in PBS.

4.5.9 Fluorescence microscopy

The fluorescence images were obtained with a epifluorescence microscope Nikon Eclipse Ti2 series, equipped with CoolLED led excitation system. Images were obtained with a 40x oil immersion objective and using a camera exposure time of 100 ms. For Alexa488, excitation wavelength was set at 490 nm, while for Alexa647 the excitation wavelength was set at 660 nm.

Collected images were analysed with ImageJ software to measure the fluorescence intensity on cells..

4.5.10 Super-resolution microscopy on cells and on VLPs

Super-resolution images were acquired using a Nikon N-STORM 4.0 system configured for total internal reflection fluorescence imaging (TIRF). A highly inclined excitation condition, close to TIR, was employed to reduce background contributions. DNA imager strands, bearing Atto-647N, and DiI fluorophores were excited with a 647 nm (80 mW) laser and 561 (0.4 mW) laser, respectively. Camera integration time was set to 80 ms. For DNA-PAINT measurements 15,000 frames were acquired in the 647 channel and 150 frames were acquired in the 561 channel. The total time required to acquire one image was about 30 min. VLPs themselves acted as subdiffraction-sized fiducial for the correction of the mechanical drift using the DiI in the 561 channel. Fluorescence was collected by means of a Nikon x100, 1.4 NA oil immersion objective and passed through a quad-band-pass dichroic filter (97335 Nikon). Images were recorded onto a 256 x 256 pixel region (pixel size 160 nm) of a sCMOS camera (ORCA Flash 4.0 Hamamatsu). Single-molecule localization sequences were analyzed with the STORM plug-in of NIS element Nikon software.

After each acquisition, imager containing solution was washed with PBS using the tubing system and a pump (Chemyx, Nexus Fusion 200) at a rate of 0.7 ml/min and fresh imager was added with the pump in DNA-PAINT buffer (1x PBS 500 mM NaCl 1 nM imager for cells, 1.5 nM for VLPs) for further acquisitions.

4.5.11 Quantitative analysis of SMLM images

4.5.11.1 Cells and VLPs clustering measurements

A quantitative analysis of DNA-PAINT images of VLPs and recombinant proteins was performed in Matlab, using previously developed scripts. Preliminarily, the results of single-molecule analysis obtained with Nikon NIS-elements software are imported in Matlab and the list of (x,y,t) coordinates of each localization is extracted for further processing.

In a first approach (Figure 4.7, Figure 4.8 and Figure 4.9), a single channel (647 channel) is considered, comprising DNA-PAINT localizations. A mean-shift clustering algorithm (bandwidth 100 nm) is applied to identify clusters of localizations that correspond to isolated VLPs or clusters of proteins. False positive such as aggregates; clusters with unrealistic shape or with a few localizations (<10) are removed. Finally, the number of localizations in the selected clusters, together with clusters size and centre are calculated. The radius of selected VLP clusters is estimated by a circular model and corresponds to the distance from the centre comprising 90% of cluster localizations.

In a second approach (From Figure 4.12 to Figure 4.16), two channels are considered: a main channel (647 channel), comprising DNA-PAINT localizations, and a reference channel (561 channel), used for drift correction in NIS-elements), comprising localizations from DiI. First, clusters of localizations in the reference channel are identified using a mean shift-clustering algorithm. These clusters roughly identify the centre position of the VLPs loaded with DiI, with an uncertainty of a few tens of nanometres. Then, DNA-PAINT localizations, belonging to the main channel, that are located within a distance of 120 nm from the VLP centres are selected and counted. The Matlab scripts are available elsewhere with a detailed description[63]. The results of clustering have been carefully checked by visual inspection.

4.5.11.2 Localization density in cells

Results shown in Figure 1 and Figure S3 are obtained with a custom Matlab script that calculates the surface density of DNA-PAINT localizations located within a manually selected region of interest (ROI). Localizations are selected in ROIs corresponding to cell covered areas while excluding localizations outside cell, i.e. due to non-specific sticking of imager strands on glass. Because cells are not always easily recognizable in reconstructed DNA-PAINT images of membrane proteins, especially at low expression levels, the selection of ROIs is performed on a corresponding low-resolution reference image, where cell profiles are clearly recognized. First, the list of DNA-PAINT localizations, obtained with Nikon NIS-elements software, and a reference low-resolution image, captured on the same field of view, are loaded and aligned. Then, polygonal ROIs can be manually drawn by the user on the reference image and DNA-PAINT localizations within each ROI are automatically selected and counted. Localization density within each ROI is calculated as the number of selected localizations divided by the ROI area.

4.5.11.3 Clus-DoC analysis

To perform Clus-DoC analysis a single list of the localizations of the two proteins to compare is needed. The DNA-PAINT localizations referring to two different proteins are acquired in different images and must be aligned and merged in a single list prior to Clus-DoC analysis. To perform the alignment, the raw acquisition videos obtained from the Nikon microscope were analysed with Picasso software, developed by Schnitzbauer et al.[44]. After the analysis, the two images were rendered and aligned using fiducial beads as reference. The outputs were combined in a single list and analysed with Clus-DoC analysis developed by Pageon et al.[45]. with the following parameters: L radius 20 nm, Rmax 500 nm, step 10, col-ocalized threshold 0.4, min. co-localized points 10. The Clus-DoC test generates density maps of the localizations at

increasing radius sizes of each molecule, starting from a radius of 20 nm up to 500 nm. These two density maps would be compared using colocalizing algorithms such as Spearman correlation, assigning a DoC value to each localization according the colocalization: 1 correlated, -1 anti-correlated, 0 not correlated (Figure 4.19). To retrieve the percentage of colocalization, a threshold of 0.4 DoC is selected so the localizations with >0.4 DoC would count as "colocalized". This threshold is selected in base of the minimum DoC value obtained after shifting 10 nm two colocalized images.

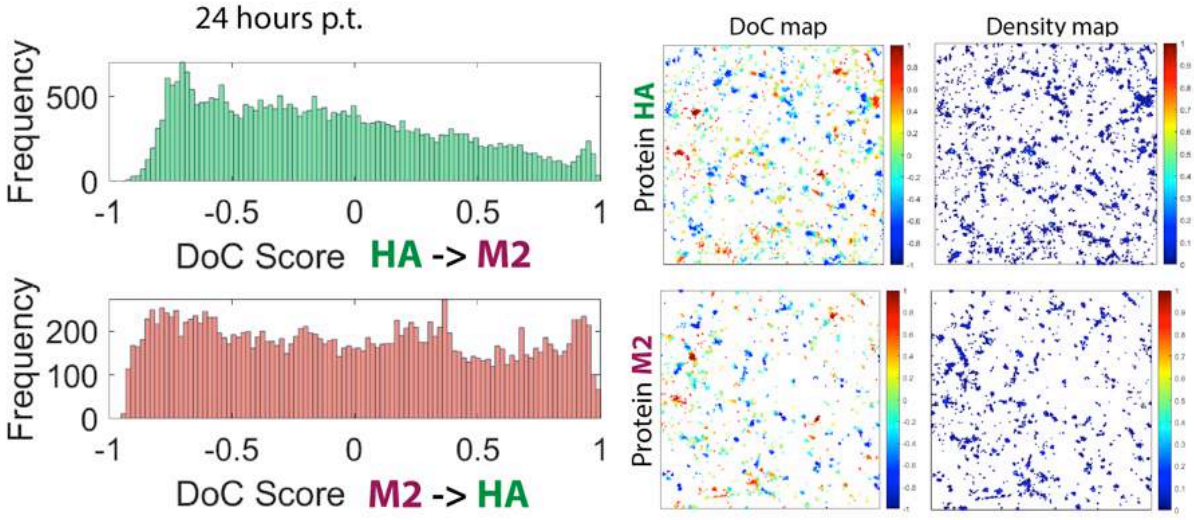

Figure 4.19: Output of the Clus-DoC analysis developed by Pageon et al.[45]. Left: Frequency distribution of the DoC scores of all localization presented in the region of interest measured of the proteins compared. DoC scores are given to each localization based on their colocalization (1 correlated, -1 anticorrelated, 0 non-correlated). Right: DoC maps and density maps of both proteins, obtained during the analysis. The density maps are maps that represent the distribution of the localizations in the area and are used to compare the colocalization; the colour code represent normalized relative density. DoC maps are a colorimetric representation of the DoC values given to each localization. Red → 1, Blue → -1. The Clus-DoC algorithm prepares a density map to identify the distribution of the localizations and them compared the distribution of both proteins. After comparing the density maps, it is added a DoC value and it is created a new DoC map with the DoC scores. DoC scores are extrapolated and plot in frequency distribution and tables.

4.5.12 Statistical analysis

Data were analysed using GraphPad Prism version 7 (GraphPad Software, San Diego California; www.graphpad.com). The results are shown as columns with the mean ± SD. Statistical analysis of the differences in colocalization of localizations was performed using the Two-way ANOVA with multiple comparisons correction (Bonferroni test). For the DLS purification fractions measurement, a 1-way ANOVA was performed with a multiple comparison correction

(Bonferroni). A value of $p \leq 0.05$ was considered statistically significant. The following statistical values and symbols are used throughout the manuscript; non-significant (ns) $p > 0.05$, * $p \leq 0.05$, ** $p \leq 0.01$, *** $p \leq 0.001$; ****$p \leq 0.0001$.

4.5.13 Imaging software

DNA-PAINT Images (Fig 2, 3 and 4) were artificially merged and coloured by ImageJ. VILs images (Fig 4) had applied a Gaussian blur filter to make localizations more visible.

4.6 References

1. McCraw, D. M. *et al.* Structural analysis of influenza vaccine virus-like particles reveals a multicomponent organization. *Sci. Rep.* **8**, 1–16 (2018).
2. Wu, C.-Y. *et al.* Mammalian Expression of Virus-Like Particles for Advanced Mimicry of Authentic Influenza Virus. *PLoS ONE* **5**, e9784 (2010).
3. Kang, S. M., Pushko, P., Bright, R. A., Smith, G. & Compans, R. W. Influenza Virus-Like Particles as Pandemic Vaccines. in *Vaccines for Pandemic Influenza* 269–289 (Springer, Berlin, Heidelberg, 2009). doi:10.1007/978-3-540-92165-3_14.
4. Fuenmayor, J., Gòdia, F. & Cervera, L. Production of virus-like particles for vaccines. *New Biotechnol.* **39**, 174–180 (2017).
5. Kang, S.-M., Kim, M.-C. & Compans, R. W. Virus-like particles as universal influenza vaccines. *Expert Rev. Vaccines* **11**, 995–1007 (2012).
6. Wang, Y., Deng, L., Kang, S.-M. & Wang, B.-Z. Universal influenza vaccines: from viruses to nanoparticles. *Expert Rev. Vaccines* **17**, 967–976 (2018).
7. Haynes, J. R. Influenza virus-like particle vaccines. *Expert Rev. Vaccines* **8**, 435–445 (2009).
8. Kang, H.-J. *et al.* Influenza M2 virus-like particle vaccination enhances protection in combination with avian influenza HA VLPs. *PloS One* **14**, e0216871 (2019).
9. Kim, K.-H. *et al.* Virus-Like Particles Are a Superior Platform for Presenting M2e Epitopes to Prime Humoral and Cellular Immunity against Influenza Virus. *Vaccines* **6**, (2018).
10. Blumberg, B. S., Alter, H. J. & Visnich, S. A 'NEW' ANTIGEN IN LEUKEMIA SERA. *JAMA* **191**, 541–546 (1965).
11. Bayer, M. E., Blumberg, B. S. & Werner, B. Particles associated with Australia antigen in the sera of patients with leukaemia, Down's Syndrome and hepatitis. *Nature* **218**, 1057–1059 (1968).

12. Naskalska, A. & Pyrć, K. Virus Like Particles as Immunogens and Universal Nanocarriers. *Pol. J. Microbiol.* **64**, 3–13 (2015).

13. Georgens, C., Weyermann, J. & Zimmer, A. Recombinant virus like particles as drug delivery system. *Curr. Pharm. Biotechnol.* **6**, 49–55 (2005).

14. Hill, B. D., Zak, A., Khera, E. & Wen, F. Engineering Virus-like Particles for Antigen and Drug Delivery. *Curr. Protein Pept. Sci.* **19**, 112–127 (2018).

15. Syomin, B. V. & Ilyin, Y. V. Virus-Like Particles as an Instrument of Vaccine Production. *Mol. Biol.* **53**, 323–334 (2019).

16. Ninyio, N. N. *et al.* Virus-like Particle Vaccines: A Prospective Panacea Against an Avian Influenza Panzootic. *Vaccines* **8**, (2020).

17. Rockman, S., Laurie, K. L., Parkes, S., Wheatley, A. & Barr, I. G. New Technologies for Influenza Vaccines. *Microorganisms* **8**, (2020).

18. Anderson, E. J. *et al.* Safety and Immunogenicity of SARS-CoV-2 mRNA-1273 Vaccine in Older Adults. *N. Engl. J. Med.* (2020) doi:10.1056/NEJMoa2028436.

19. Ura, T., Yamashita, A., Mizuki, N., Okuda, K. & Shimada, M. New vaccine production platforms used in developing SARS-CoV-2 vaccine candidates. *Vaccine* (2020) doi:10.1016/j.vaccine.2020.11.054.

20. Sahin, U. *et al.* COVID-19 vaccine BNT162b1 elicits human antibody and T H 1 T cell responses. *Nature* **586**, 594–599 (2020).

21. Nayak, D. P., Balogun, R. A., Yamada, H., Zhou, Z. H. & Barman, S. Influenza virus morphogenesis and budding. *Virus Res.* **143**, 147–161 (2009).

22. Latham, T. & Galarza, J. M. Formation of Wild-Type and Chimeric Influenza Virus-Like Particles following Simultaneous Expression of Only Four Structural Proteins. *J. Virol.* **75**, 6154–6165 (2001).

23. Chen, B. J., Leser, G. P., Morita, E. & Lamb, R. A. Influenza Virus Hemagglutinin and Neuraminidase, but Not the Matrix Protein, Are Required for Assembly and Budding of Plasmid-Derived Virus-Like Particles. *J. Virol.* **81**, 7111–7123 (2007).

24. Durous, L., Rosa-Calatrava, M. & Petiot, E. Advances in influenza virus-like particles bioprocesses. *Expert Rev. Vaccines* **18**, 1285–1300 (2019).

25. Dai, S., Wang, H. & Deng, F. Advances and challenges in enveloped virus-like particle (VLP)-based vaccines. *J. Immunol. Sci.* **2**, (2018).

26. Sarkar*, B., Islam, S. S., Zohora, U. S. & Ullah, and M. A. Virus like particles- A recent advancement in vaccine development. *Microbiol. Soc. Korea* **55**, 327–343 (2019).

27. Thompson, C. M. *et al.* Critical assessment of influenza VLP production in Sf9 and HEK293 expression systems. *BMC Biotechnol.* **15**, 31 (2015).

28. Pushko, P. & Tretyakova, I. Influenza Virus Like Particles (VLPs): Opportunities for H7N9 Vaccine Development. *Viruses* **12**, 518 (2020).

29. Sokolenko, S. *et al.* Co-expression vs. co-infection using baculovirus expression vectors in insect cell culture: Benefits and drawbacks. *Biotechnol. Adv.* **30**, 766–781 (2012).

30. Fernandes, F., Teixeira, A. P., Carinhas, N., Carrondo, M. J. T. & Alves, P. M. Insect cells as a production platform of complex virus-like particles. *Expert Rev. Vaccines* **12**, 225–236 (2013).

31. Kost, T. A., Condreay, J. P. & Jarvis, D. L. Baculovirus as versatile vectors for protein expression in insect and mammalian cells. *Nat. Biotechnol.* **23**, 567–575 (2005).

32. Crisci, E., Bárcena, J. & Montoya, M. Virus-like particle-based vaccines for animal viral infections. *Inmunología* **32**, 102–116 (2013).

33. Buffin, S. *et al.* Influenza A and B virus-like particles produced in mammalian cells are highly immunogenic and induce functional antibodies. *Vaccine* **37**, 6857–6867 (2019).

34. Venereo-Sanchez, A. *et al.* Hemagglutinin and neuraminidase containing virus-like particles produced in HEK-293 suspension culture: An effective influenza vaccine candidate. *Vaccine* **34**, 3371–3380 (2016).

35. Venereo-Sánchez, A. *et al.* Characterization of influenza H1N1 Gag virus-like particles and extracellular vesicles co-produced in HEK-293SF. *Vaccine* **37**, 7100–7107 (2019).

36. Venereo-Sanchez, A. *et al.* Process intensification for high yield production of influenza H1N1 Gag virus-like particles using an inducible HEK-293 stable cell line. *Vaccine* **35**, 4220–4228 (2017).

37. Abbe, E. Beiträge zur Theorie des Mikroskops und der mikroskopischen Wahrnehmung. *Arch. Für Mikrosk. Anat.* **9**, 413–468 (1873).

38. Masters, B. R. Abbe Theory of Image Formation and Diffraction of Light in Transmitted Light Microscopes. 37–49 (2006) doi:10.1117/3.660403.ch3.

39. Laine, R. F. *et al.* Structural analysis of herpes simplex virus by optical super-resolution imaging. *Nat. Commun.* **6**, 5980 (2015).

40. Dahmane, S. *et al.* Nanoscale organization of tetraspanins during HIV-1 budding by correlative dSTORM/AFM. *Nanoscale* **11**, 6036–6044 (2019).

41. Muranyi, W., Malkusch, S., Müller, B., Heilemann, M. & Kräusslich, H.-G. Super-Resolution Microscopy Reveals Specific Recruitment of HIV-1 Envelope Proteins to Viral Assembly Sites Dependent on the Envelope C-Terminal Tail. *PLOS Pathog.* **9**, e1003198 (2013).

42. Sieben, C., Sezgin, E., Eggeling, C. & Manley, S. Influenza A viruses use multivalent sialic acid clusters for cell binding and receptor activation. *bioRxiv* 264713 (2018) doi:10.1101/264713.

43. Jungmann, R. *et al.* Single-Molecule Kinetics and Super-Resolution Microscopy by Fluorescence Imaging of Transient Binding on DNA Origami. *Nano Lett.* **10**, 4756–4761 (2010).

44. Schnitzbauer, J., Strauss, M. T., Schlichthaerle, T., Schueder, F. & Jungmann, R. Super-resolution microscopy with DNA-PAINT. *Nat. Protoc.* **12**, 1198–1228 (2017).

45. Pageon, S. V., Nicovich, P. R., Mollazade, M., Tabarin, T. & Gaus, K. Clus-DoC: a combined cluster detection and colocalization analysis for single-molecule localization microscopy data. *Mol. Biol. Cell* **27**, 3627–3636 (2016).

46. Delcanale, P., Miret-Ontiveros, B., Arista-Romero, M., Pujals, S. & Albertazzi, L. Nanoscale Mapping Functional Sites on Nanoparticles by Points Accumulation for Imaging in Nanoscale Topography (PAINT). *ACS Nano* **12**, 7629–7637 (2018).

47. Chen, C. *et al.* Profiling of Exosomal Biomarkers for Accurate Cancer Identification: Combining DNA-PAINT with Machine- Learning-Based Classification. *Small* **15**, 1901014 (2019).

48. Rohovie, M. J., Nagasawa, M. & Swartz, J. R. Virus-like particles: Next-generation nanoparticles for targeted therapeutic delivery. *Bioeng. Transl. Med.* **2**, 43–57 (2017).

49. Qian, C. *et al.* Recent Progress on the Versatility of Virus-Like Particles. *Vaccines* **8**, (2020).

50. Sun, Y., Sun, Y., Zhao, R. & Gao, K. Intracellular delivery of messenger RNA by recombinant PP7 virus-like particles carrying low molecular weight protamine. *BMC Biotechnol.* **16**, (2016).

51. Hoffmann, D. B. *et al.* In Vivo siRNA Delivery Using JC Virus-like Particles Decreases the Expression of RANKL in Rats. *Mol. Ther. Nucleic Acids* **5**, e298 (2016).

52. Sinn, P. L., Burnight, E. R. & McCray, P. B. Progress and Prospects: prospects of repeated pulmonary administration of viral vectors. *Gene Ther.* **16**, 1059–1065 (2009).

53. Jain, A. & Jain, S. K. PEGylation: An Approach for Drug Delivery. A Review. *Crit. Rev. Ther. Drug Carr. Syst.* **25**, (2008).

54. Peyret, H. *et al.* Tandem Fusion of Hepatitis B Core Antigen Allows Assembly of Virus-Like Particles in Bacteria and Plants with Enhanced Capacity to Accommodate Foreign Proteins. *PLOS ONE* **10**, e0120751 (2015).

55. Galaway, F. A. & Stockley, P. G. MS2 Viruslike Particles: A Robust, Semisynthetic Targeted Drug Delivery Platform. *Mol. Pharm.* **10**, 59–68 (2013).

56. Stephanopoulos, N., Tong, G. J., Hsiao, S. C. & Francis, M. B. Dual-surface modified virus capsids for targeted delivery of photodynamic agents to cancer cells. *ACS Nano* **4**, 6014–6020 (2010).

57. Gillitzer, E., Suci, P., Young, M. & Douglas, T. Controlled ligand display on a symmetrical protein-cage architecture through mixed assembly. *Small Weinh. Bergstr. Ger.* **2**, 962–966 (2006).

58. Hoffmann, E., Neumann, G., Kawaoka, Y., Hobom, G. & Webster, R. G. A DNA transfection system for generation of influenza A virus from eight plasmids. *Proc. Natl. Acad. Sci.* **97**, 6108–6113 (2000).

59. Czudai-Matwich, V., Schnare, M. & Pinkenburg, O. A simple and fast system for cloning influenza A virus gene segments into pHW2000- and pCAGGS-based vectors. *Arch. Virol.* **158**, 2049–2058 (2013).

60. Bouback, T. a. F. & Redwan, N. A. Approaches toward the development of DNA vaccine for influenza virus. *Afr. J. Biotechnol.* **10**, 5209–5218 (2011).

61. Mostafa, A., Kanrai, P., Ziebuhr, J. & Pleschka, S. Improved dual promotor-driven reverse genetics system for influenza viruses. *J. Virol. Methods* **193**, 603–610 (2013).

62. Yu, J. *et al.* Development and Characterization of a Reverse-Genetics System for Influenza D Virus. *J. Virol.* **93**, (2019).

63. Delcanale, P. & Albertazzi, L. DNA-PAINT super-resolution imaging data of surface exposed active sites on particles. *Data Brief* **30**, 105468 (2020).

Chapter 5: Super-resolution microscopy identification of hepatitis virus on paraffin embedded liver tissues from patients

This chapter explains the work performed in collaboration with Dr. Ester Garcia Pras, from the group of MD. Dr. Xavier Forns from the Hospital Clinic of Barcelona and IDIBAPS.

5.1 Introduction

In previous chapters we described the study of the effects of different influenza antivirals and the production of viral recombinant proteins using *in vitro* mammalian cell culture. This approach is the most commonly used due to the manageability of cell culture and the experimental conditions. However, although *in vitro* experiments are very useful, sometimes the virus strain has adapted to grow in lab conditions, masking the real behaviour of the virus on target cells in infected tissues. In other cases, in order to characterize the viral mechanism in patients and the viral behaviour on tissues it is not possible to use cell cultures, especially due to their lack of differentiation and 3D organization.

In those cases where the biological inquiry needs the infected tissue to resolve the incognita behind viral infections, studies using formaldehyde fixed paraffin embedded (FFPE) tissues could satisfy that gap of knowledge. FFPE tissues are obtained from biopsies or explant of patients and are preserved in paraffin blocks that are cut in thin sections to be stained and observed with conventional microscopies[1,2].

The huge amount of FFPE tissues in biorepositories[3] and the longevity of these preparations[4] opens the possibility to improve our knowledge of diseases impossible to achieve using cell culture. Since the patient tissue is preserved in the same state as when it was removed, FFPE had been used to study different pathologies such as cancer[5], the detection of human papillomavirus[6] and enterovirus[7] or skin infections[8] using either conventional staining of the FFPE (alkaline fast red, haematoxylin and eosin)[9,10], PCR measurements[11,12] or immunohistochemistry[13]. With the right deparaffination and rehydration, tissue samples can be immunostained to observe certain epitopes after the antigen retrieval[14] (unmasking the antigen epitopes that were cross-linked by methylene bridges due to the action of the formaldehyde[15]), allowing the study of these sections with confocal microscopy[16,17] or novel methods such as the

implementation of Föster resonance energy transfer (FRET) as labelling method to observe the proximity of two proteins[18] as well as light sheet microscopy[19].

Recently it has been suggested the use of single-molecule localization microscopy (SMLM) on FFPE tissues to increase the resolution in immunostained tissues[20-23]. With this approach it is expected to resolve certain structures inside the cells of the tissue and besides, with the single localization of fluorophores, it is suggested an increased of the sensitivity, recognizing signals impossible to be appreciated with confocal microscopy. In virology this increment of resolution could help elucidating the presence and mechanisms of actions of certain viruses in real patients, to small to be studied with fluorescence microscopy.

The main drawback of this approximation is the sample characteristics and idiosyncrasies. Paraffin tissues are thick layers (2-4 μm thickness) of dense but delicate tissue that possess strong auto-fluorescence and lack of transparency. However, there are several methods to remove the auto-fluorescence given by the fixation methods[24,25], which in combination with the usage of total internal reflection fluorescence (TIFR) microscopy associated to dSTORM and with a great deal of practice these drawbacks could be overcome[26].

Altogether, in this chapter we optimized the super-resolution image acquisition of liver tissues to characterize the presence of hepatitis B and hepatitis Delta in cirrhotic patients from the Hospital Clinic of Barcelona.

Hepatitis B virus (HBV) is an enveloped circular dsDNA virus that infects the liver and produces severe liver diseases such as cirrhosis or cancer[27,28]. Its structure is quite simple (Figure 5.1), consisting of an lipid membrane envelope with three surface proteins (S, M and L, entitled HBsAg), a capsule formed by a core antigen, the partially double strain DNA, the viral polymerase and small e antigens around[29,30]. Highly contagious through blood and perinatal transmission, the World Health Organization (WHO) estimates that in 2015 up to 257 million people were living with the disease, estimating that 887,000 people died that year because of cirrhosis or liver cancer derivate from HBV[31].

On the other hand, hepatitis Delta virus (HDV), discovered in 1977[32] , is a small circular RNA satellite virus with a unique genome, the smallest among mammalian viruses, more similar to viroids of plants than to any other animal virus[33,34]. HDV only contains a circular RNA sequence

of 1700 nucleotides and two proteins that conform the virus (S-HDAg and L-HDAg)(Figure 5.1).

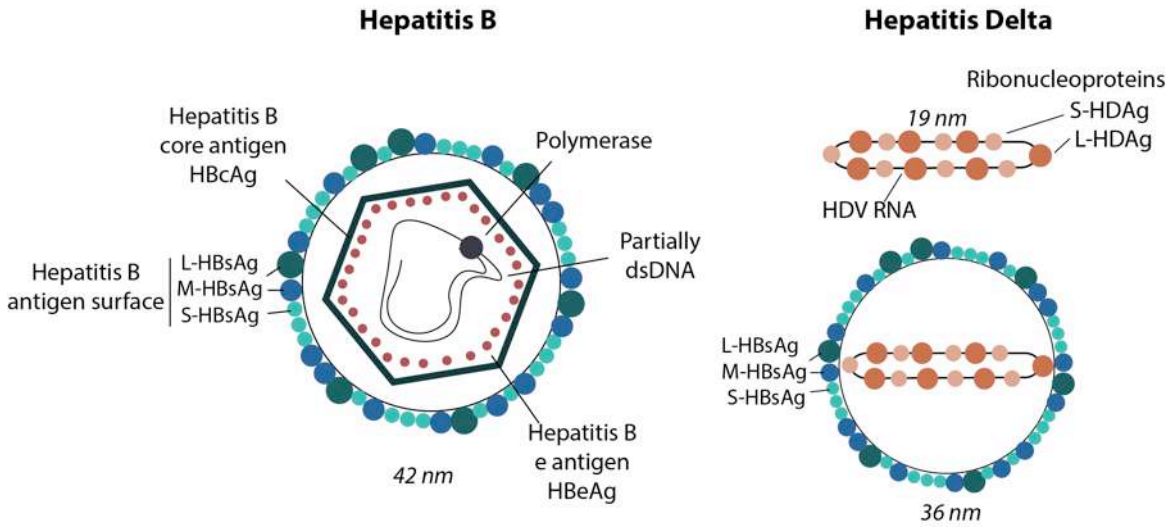

Figure 5.1: Schematic representation of hepatitis B and hepatitis Delta structure. Hepatitis B is a DNA virus composed by an envelope with a lipid membrane and three antigen surface proteins (L, M and S), a core and antigen e with a polymerase inside. Hepatitis delta is a small satellite RNA virus consisting on a circular RNA sequence and two proteins (S and L) that combined form the ribonucleoprotein complex. To be released and fully infective it need the envelope and the three proteins of hepatitis B (L, M and S).

One of the most outstanding features of HDV is its lack of any core, envelope protein nor viral polymerase, thus to fulfil its viral cycle it relies on the host cells and HBV[35]. Both HBV and HDV share the same pathways of transmission, where HDV, as an obligate satellite, depends on the surface proteins of the envelope of HBV (HBsAg) to finish its viral replication cycle, release and infect other cells (Figure 5.1). Consequently, HDV infection is completely dependent on the presence of HBV on liver cells; thus co-infection HBV/HDV is quite common in geographic areas with high level of endemicity[36,37]. Additionally, HDV is associated with aggressive forms of hepatitis[38,39], infecting up to 70 million people worldwide[40,41].

Given the co-dependency of HDV with HBV to develop the disease and spread the virus, it is expected to find both viruses in the same hepatocyte in patients HDV positive, or at least find the surface antigen of HBV (HBsAg) in HDV infected cells, however this phenomenon is hard to visualized due to the low expression of HBV in co-infected cells with HDV[42].

Hence, in this chapter we optimized the image acquisition of FFPE tissues of patients using dSTORM. The main objective was to visualize the co-infection of HBV with HDV in hepatocytes using two different antigens: surface HBsAg and general HDAg. With super-resolution microscopy it was possible to visualize HDV infected cells with low or big expression of HBV, proving how super-resolution microscopy could be implemented in the study of FFPE tissues with the right selection of buffer, angle of the laser, exposure time and selections of dyes. With this optimization we could validate this approach for future studies.

5.2 Results and discussion

5.2.1 Validation of the methodology: positive and negative control

Firstly, in order to validate the usage of dSTORM on tissues, we tested a highly infected tissue with hepatitis B as a positive control and a tissue infected with hepatitis C as a negative control. This way we could observe how dSTORM behaves on paraffin tissues with either high amount of targets or without any target, so we could identify the amount of auto-fluorescence and the signal-to-noise after the super-resolution acquisition and reconstruction. Hence, positive and negative controls were immunostained with primary antibody against hepatitis B (anti-HBsAg) and secondary Alexa647.

Next, we focused on the selection of the STORM buffer, crucial to optimize the super-resolution acquisition. As explained in chapter 1, dSTORM is a SMLM technique that relies in the photoactivation of photoswitchable dyes in order to reconstruct the super-resolution image. For this purpose, it is essential the selection of a buffer that would create the “blinking” of the dyes with high signal-to-noise and no quenching. Several researchers had reported the usage of the mounting medium Vectashield (Vectorlabs) as buffer for STORM and other super-resolution techniques using Alexa647 among other dyes[43-46]. However, this information contradicts other studies, specially the work of Arsic et al.[47,48], which confirmed the Vectashield incompatibility with Alexa647 and the capacity of Vectashield to quench this dye. For this purpose, we tested first the capacity of Vectashield freshly added to perform super-resolution images with dSTORM.

Figure 5.2 A shows how the positive control behaved with Vectashield. DAPI was used to identify the centre of the cell. In general we experienced a bad super-resolution acquisition; the fluorophore was not properly activated so the sample did not suffer a proper cycle “on-off”, instead dyes were displaying a ripple effect or fluctuation where the signal-to-noise was quite

low in the highly stained area. The reconstruction (Figure 5.2 A dSTORM) did not retrieve the characteristic single-molecule aggregation of dyes but a saturated image without proper single-localization identification.

In contrast, the negative control (Figure 5.2 B) did not display any signal despite the presence of auto-fluorescence in the sample, due to a lack of blinking during the acquisition. Naked eye, this could be an excellent negative control if we did not consider how badly the dye behaved in our experiment with Vectashield and the lack of single blinking in the positive control.

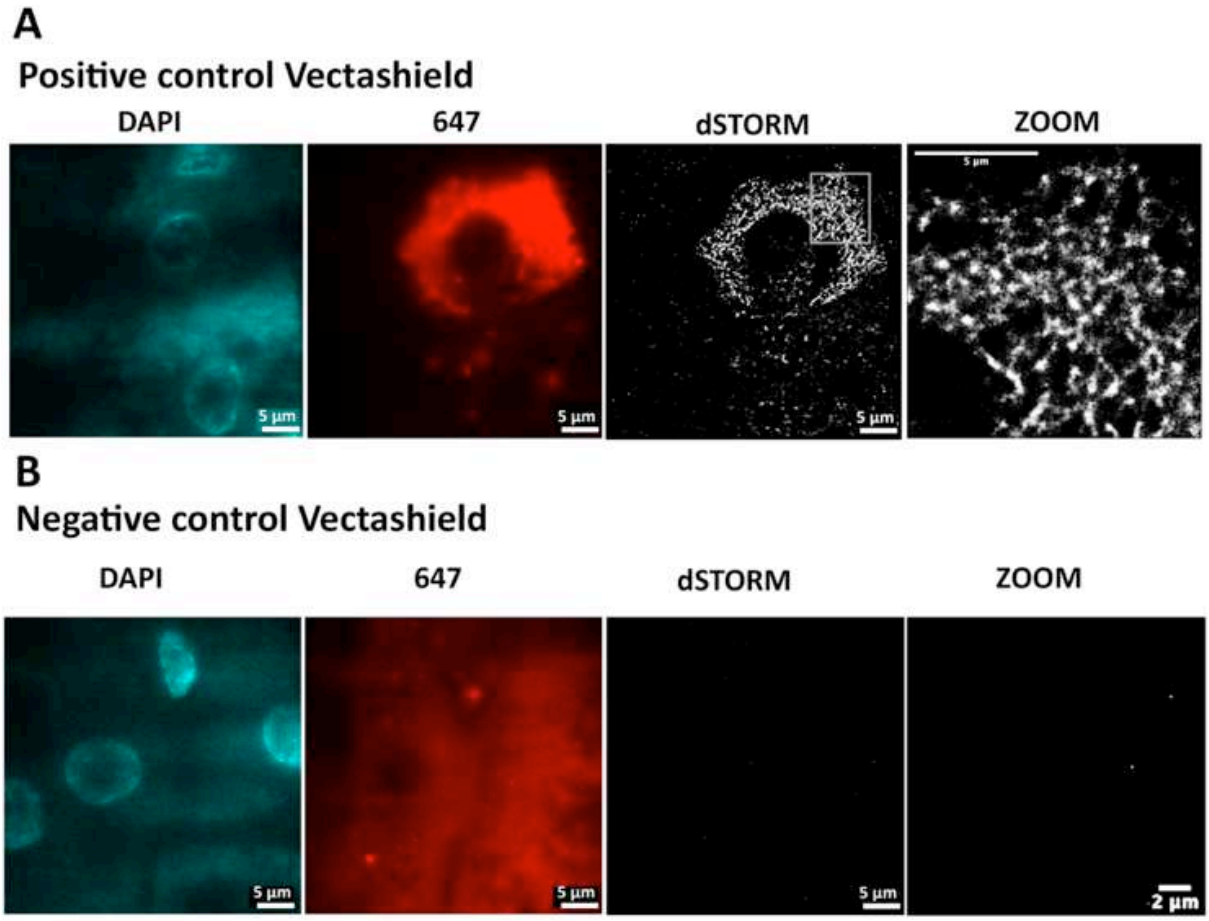

Figure 5.2: dSTORM images of formaldehyde fixed paraffin tissue with Vectashield as STORM buffer freshly added. A) Positive control consisting on tissues of a patient highly infected with hepatitis B. DAPI was observed in channel 405. On the channel 647 it can be observed the immunostaining against the surface antigen of hepatitis B (HBsAg). dSTORM image was obtained and zoomed in (square). One size was imaged: 256 x 256 pixels. B) Negative control consisting on tissues of a patient highly infected with hepatitis C. DAPI was observed in channel 405. On the channel 647 it can be observed the immunostaining against the surface antigen of hepatitis B (HBsAg). dSTORM image was obtained and zoomed in (square). One size was imaged: 256 x 256 pixels.

All in all, we decided to use conventional STORM buffer as reported by Creech et al.[20]. Accordingly, to perform super-resolution images in our FFPE set of samples, we used STORM buffer with the addition of Glycerol (PBS-Glycerol 1:1) to thicken it, so the coverslip on top of the tissue could not move and made sure that the buffer stayed in place during the whole acquisition time.

To explore the imaging possibilities, a bigger image size was performed (512 x 512 pixels). Exposure time was then set accordingly, so for the smallest size exposure time was set at 10 msec., while the bigger size had an exposure time of 30 msec. An important appreciation is the need to focus perfectly and play with the angle of the laser, since the tissue possess strong signal of auto-fluorescence, especially in 488.

Positive control images with freshly added STORM buffers are displayed in Figure 5.3. Surprisingly the STORM buffer with glycerol worked perfectly, not needed to set the laser power at 100% to see the characteristic “blinking” expected in dSTORM and with a decent signal-to-noise. In comparison with Vectashield, the reconstruction of the super-resolution image (Figure 5.3 dSTORM and zoom in) retrieved single-molecules on the areas with HBV. In general, bigger fields would allow us to identify more cell infection and co-infections, including around 6-7 nuclei of different cells in the tissue.

Observing in detail the dSTORM images of the Figure 5.3, HBV was observed forming a net structure along the whole cytoplasm, probably in the reticulum, similar than the structure observed in Figure 5.2 A. The image in the bottom displayed better resolution in general, maybe due to the localized dye presence inside the highly infected cell. It must be highlighted how much signal was found around the positive HBV cell, due to the residues of the virus in the tissue and the surroundings.

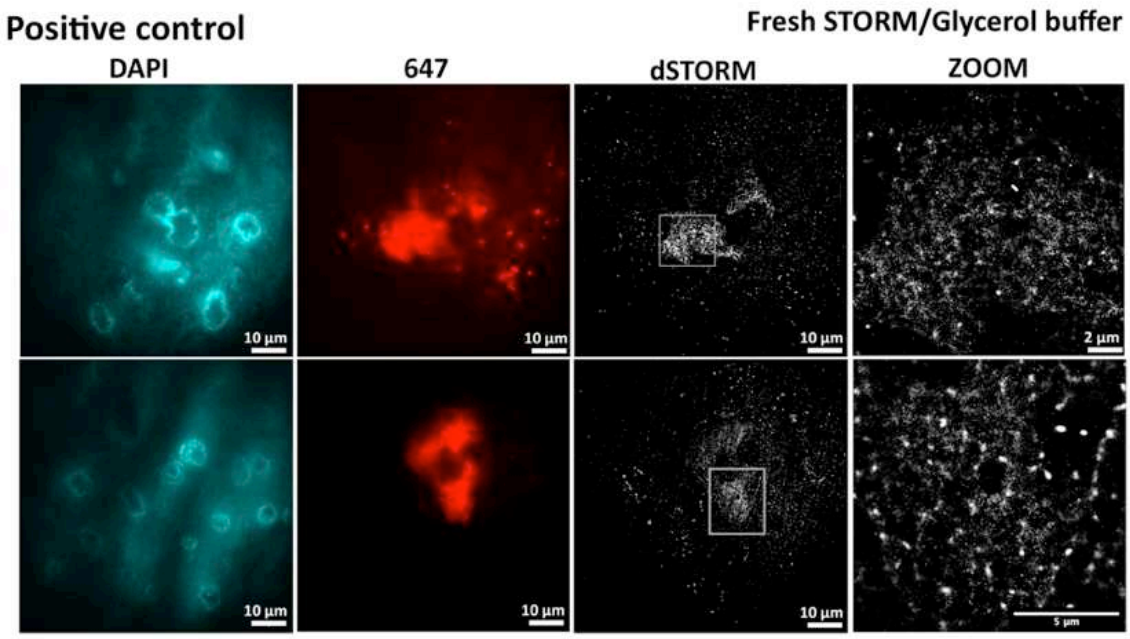

Figure 5.3: Positive control consisting in tissues of a patient highly infected with hepatitis B freshly prepared. The STORM-Glycerol buffer was added right before the image acquisition. DAPI was observed in channel 405. On the channel 647 it can be observed the immunostaining against the surface antigen of hepatitis B (HBsAg). dSTORM image was obtained and zoomed in (square). One size was imaged: 512 x 512 pixels.

Next, we observed how the negative control displayed the signal in the channel 647, related mostly to the auto-fluorescence (Figure 5.4). Again, nuclei was observed in the channel 405, while in the channel 647 a general a homogeneous signal was observed, belonging to the auto-fluorescence of the tissue. This signal seen in low-resolution did not affect in excess the super-resolution acquisition and the reconstruction of the image, but single isolated blinking were found in certain areas (Figure 5.4 Zoom), maybe due to unbound secondary antibody. In general there is a strong auto-fluorescence in the channel 647 but did not affect the super-resolution reconstruction.

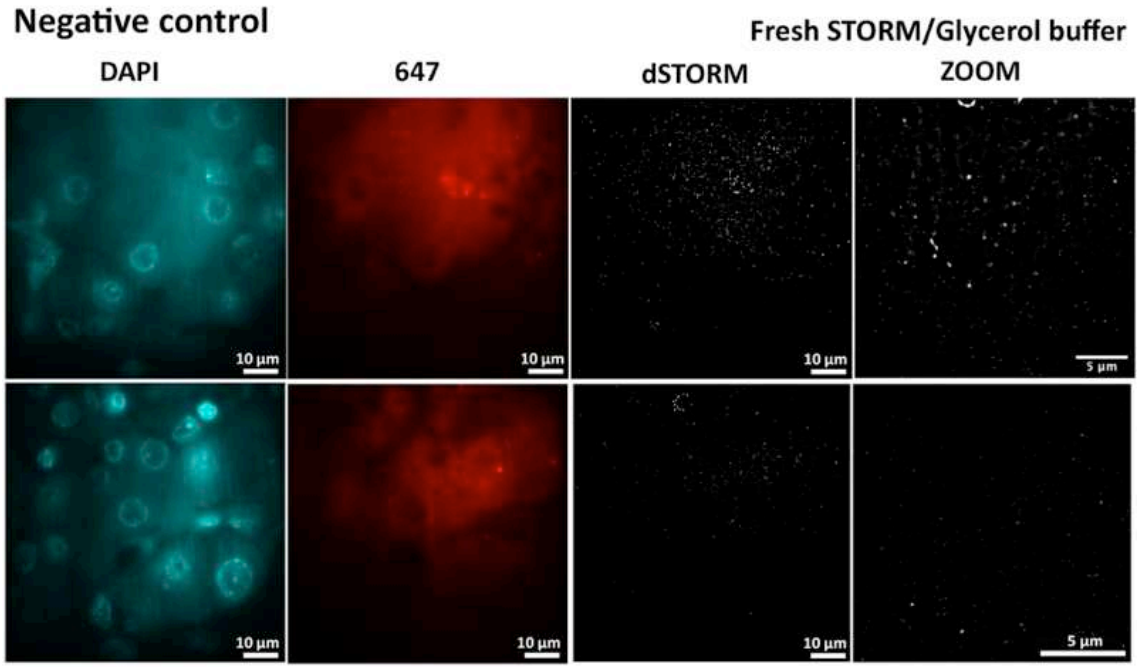

Figure 5.4: Negative control consisting in tissues of a patient highly infected with hepatitis C freshly prepared. The STORM-Glycerol buffer was added right before the image acquisition. DAPI was observed in channel 405. On the channel 647 it can be observed the immunostaining against the surface antigen of hepatitis B (HBsAg). dSTORM image was obtained and zoomed in (square). One size was imaged: 512 x 512 pixels.

In addition, we wanted to test how long STORM buffer could last on the tissue samples. Generally, FFPE tissues are covered with a mounting medium such as Vectashield or Fluoromont (Invitrogene) that would protect the tissue and allow the sample to be studied during an extended period of time. In this case, instead of removing the STORM-Glycerol buffer and changed with Vectashield, we sealed with clear nail polish the corners and the edges of the coverslip located on top of the tissue, allowing it to rest at 4ºC in the dark for 5 days. Following this time we took the sample and image it with the same conditions and set-up as previously explained.

In Figure 5.5 is shown the positive control images after 5 days of the addition of STORM-Glycerol buffer. As observed in the images, the STORM-Glycerol buffer performed similarly as when it was added fresh and the super-resolution image was successfully reconstructed without problems. The dye Alea647 was still quite intact and the blinking observed during the acquisition had the quality enough to be reconstructed by a Gaussian fitting.

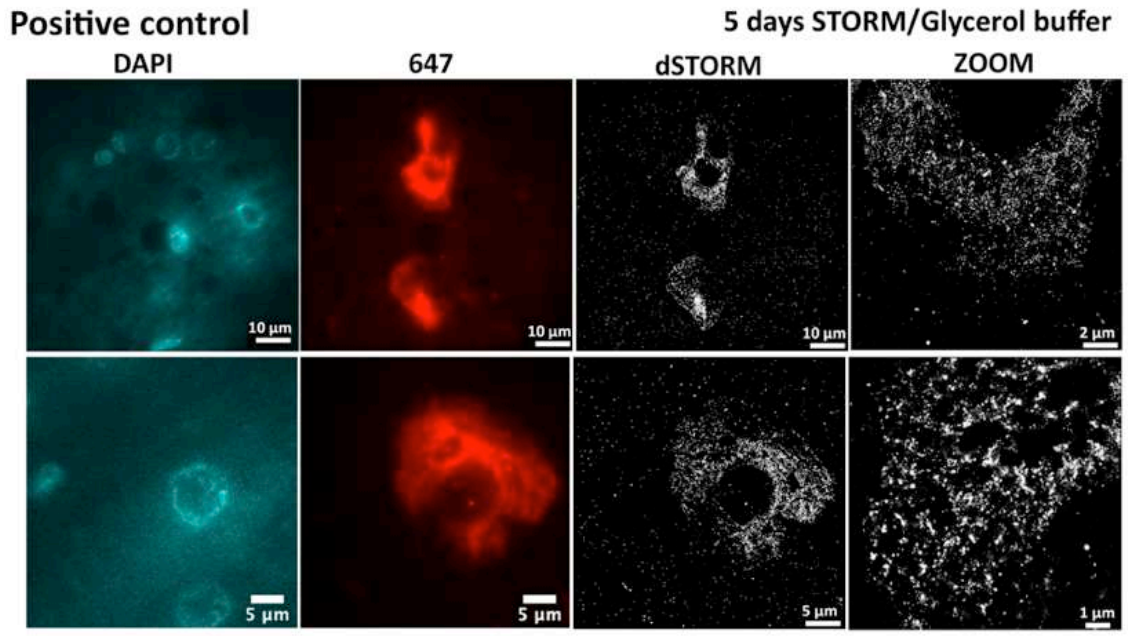

Figure 5.5: Positive control consisting in tissues of a patient highly infected with hepatitis B 5 days after initial preparation. The STORM buffer/Glycerol was added 5 days before the image acquisition. DAPI was observed in channel 405. On the channel 647 it can be observed the immunostaining against the surface antigen of hepatitis B (HBsAg). dSTORM image was obtained and zoomed in (square). Two different sizes were imaged: top 512 x 512 pixels; bottom 256 x 256 pixels.

However, despite the good blinking of the dye, dSTORM images were not as defined as before. The zoom-in of the dSTORM images (Figure 5.5 dSTORM and zoom) showed how less precise and less defined were the reticular structures, maybe due to the degradation of the dye due to a lack of conservation. Also the signal is slightly lower than before, due to the action of the old buffer. The negative control (Figure 5.6) remained similarly. The auto-fluorescence in 647 nm was still quite present and super-resolution images were displaying small signals from rests of unbound antibodies and from the auto-fluorescence itself, similar than observed before.

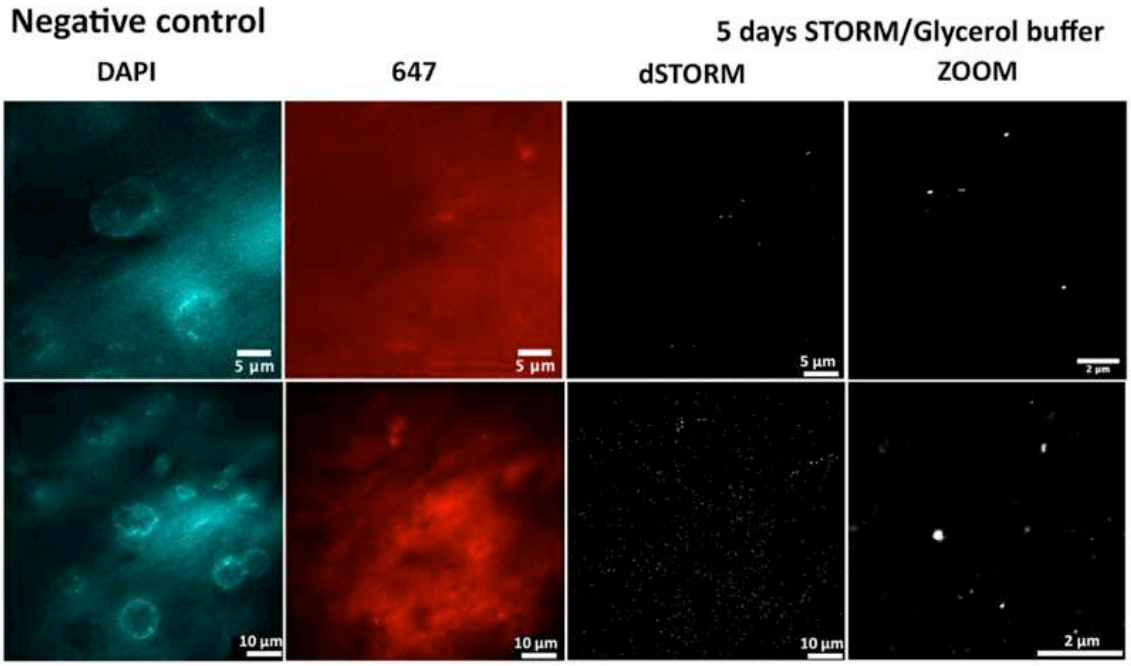

Figure 5.6: Negative control consisting in tissues of a patient highly infected with hepatitis C 5 days after initial preparation. The STORM-Glycerol buffer was added 5 days before the image acquisition. DAPI was observed in channel 405. On the channel 647 it can be observed the immunostaining against the surface antigen of hepatitis B (HBsAg). dSTORM image was obtained and zoomed in (square). Two different sizes were imaged: bottom 512 x 512 pixels; top 256 x 256 pixels.

In brief, the STORM-Glycerol buffer in combination with a setup of the angle and power of the laser was a good approach to obtain super-resolution images on liver tissues. The intensity of the infected cells was strong enough to reconstruct the reticular structure of HBV on hepatocytes, while the signal originated from the tissue fixation was not a strong obstacle to reconstruct the super-resolution image. Negative controls only contained small signals, individually distributed along the image, mainly due to the formaldehyde and rest of unbound secondary antibody. We expected that cells with both HDV and HBV could be imaged with this setup and buffer selection.

5.2.2 Super-resolution imaging of HBV using HDV as a reference

After the setup for imaging acquisition using FFPE tissues, we immunostained explants and biopsies of patients with two different primary antibodies: anti-HDAg and anti-HBsAg. The aim of this approach is to identify the presence of the HBsAg inside co-infected cells with HDV, impossible to found using confocal microscopy, to characterize with great sensitivity and resolution the co-infection of both viruses inside hepatocytes. Hence, in order to select cells infected with both viruses, hepatitis D was immunostained with a secondary antibody Alexa568 and hepatitis B with Alexa647.

Some of the images obtained are displayed in Figure 5.7 and in Figure 5.8. In both cases, Delta virus was search using conventional fluorescence microscopy in the channel 561 nm. Once one or two cells in the field contained HDV, super-resolution of the channel 647 nm was performed to identify the distribution of HBsAg inside those positive cells. In most cases, HDV was mostly concentrated in the nuclei of the cells (confirmed with DAPI). In those cells, however, the presence of HBsAg was very low or even not present. In Figure 5.7, HBsAg was absent in the cell infected with HDV, although it was quite present in the cells surroundings (Zoom in Right).

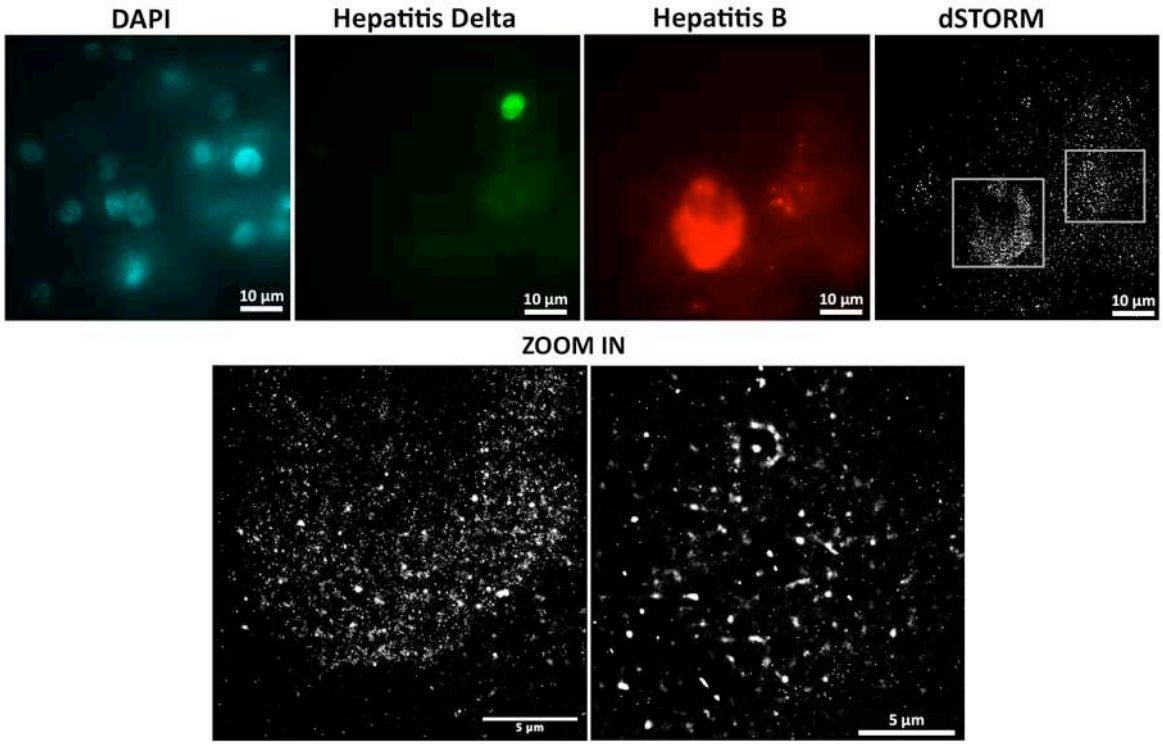

Figure 5.7: Super-resolution images of hepatitis B in tissue with both hepatitis B and hepatitis Delta. The cell positive for hepatitis D showed low amounts of hepatitis B. The STORM-Glycerol buffer was added right before the image acquisition. DAPI was observed in channel 405. Hepatitis Delta was stained with anti-HDAg and secondary

Alexa568, observed in channel 568 and used as a reference to select the cell. On the channel 647 it can be observed the immunostaining against the surface antigen of hepatitis B (HBsAg). dSTORM image was obtained and zoomed in (square).

On the other hand, in other cases HDV was present both in the nucleus of the positive cell and spread in the cytoplasm of nearby cells (Figure 5.8). Focusing attention on the cell with HDV in the nucleus, we observed that the amount of signal of HBsAg around the cytoplasm was very weak but clear, displaying the protein in single dense dots along the membrane (Figure 5.8 Zoom left). Moreover, a dense distribution of HBsAg was found in cells with lower content of HDV (Figure 5.8 Zoom left), exhibiting a soft co-infection in that single cell in the area.

Interestingly, if we compare the fluorescence microscopy image obtained in the channel 647 (Figure 5.7 and Figure 5.8 Hepatitis B) with the dSTORM images acquired, these super-resolved distributions of HBsAg were almost impossible to be distinguished, proving the power of dSTORM to identify single fluorophores in cells with low amount of viral content.

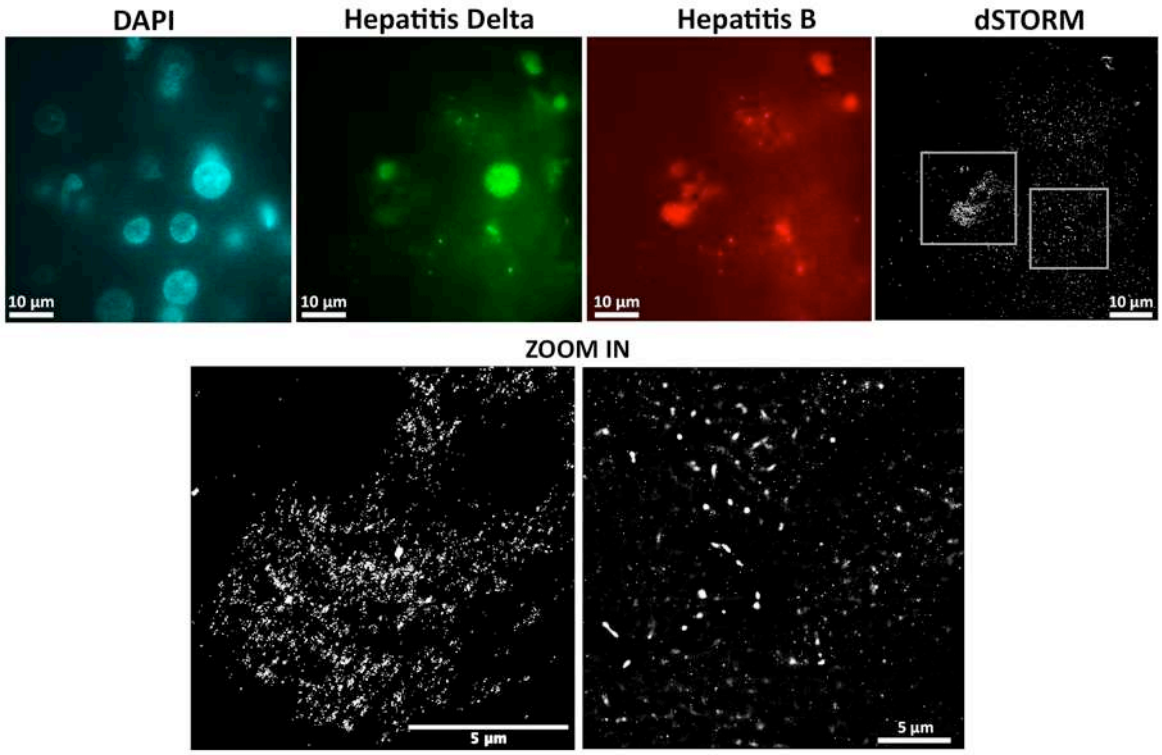

Figure 5.8: Super-resolution images of hepatitis B in tissue with both hepatitis B and hepatitis Delta. The cell positive for hepatitis D showed low amounts of hepatitis B. The STORM-Glycerol buffer was added right before the image acquisition. DAPI was observed in channel 405. Hepatitis Delta was stained with anti-HDAg and secondary Alexa568, observed in channel 568 and used as a reference to select the cell. On the channel 647 it can be observed

the immunostaining against the surface antigen of hepatitis B (HBsAg). dSTORM image was obtained and zoomed in (square).

In general, in most cases HDV infected cells did not contain highly express amounts of HBsAg, but this antigen was found organized in small clusters, not only in HDV cells but also in surrounding cells. With the increased sensitivity of dSTORM it was possible to identify the small clusters of HBsAg on the cytoplasm, almost impossible to differentiate with confocal or conventional fluorescence microscopy. However, the presence of HBsAg was not homogeneous and constant in all HDV infected cells, confirming that there are biological questions that we could not answer with super-resolution microscopy, where HDV and HBV are co-infecting but not easily found in cirrhotic patients.

5.2.3 Super-resolution imaging of HDV using HBV as a reference

Finally, to had a better understanding of the co-infection of HBV and HDV, we immunostained explants and biopsies with primary antibodies anti-HDV and anti-HBsAg but changing the secondary antibody combination. In this case we wanted to find cells positive with HBV in the channel 488 (using Alexa488) and perform super-resolution microscopy images of the proteins HDV with the channel 647 (using Alexa647). This way we would search for cells infected with HBV and try to identify with high-resolution if HDV was present co-infecting inside the cells and in which areas of the cell HDV could be found.

First, we imaged a cell with both hepatitis B and hepatitis Delta in the cytoplasm (Figure 5.9). In this case, the cell displayed a soft presence of both viruses along the cytoplasm, although the signal observed in channel 647 (Hepatitis D) was so weak that it could possible be mistaken as noise from the sample. Examining the super-resolution image of hepatitis Delta (Figure 5.9 dSTORM), we could confirm that the expression of HDV was weak, but it was recognized by single-molecule localization, displaying single proteins on the membrane. Thus, in this cell in concrete we could observe the co-infection of both viruses when they were present on the membrane expressing low amount of proteins.

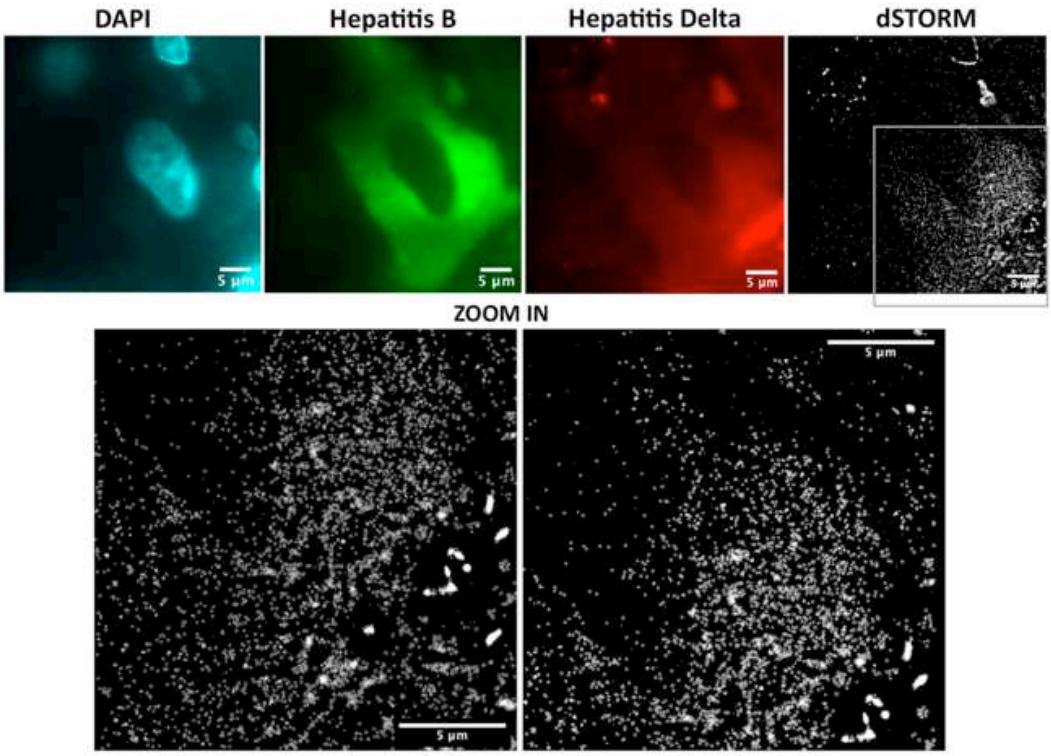

Figure 5.9: Super-resolution image of hepatitis D in a tissue with both hepatitis B and hepatitis Delta. The cell positive for hepatitis B showed medium amount of hepatitis D around the cytoplasm. The STORM-Glycerol buffer was added right before the image acquisition. DAPI was observed in channel 405. Hepatitis B was stained with anti-HBsAg and secondary Alexa488, observed in channel 488 and used as a reference to select the cell. On the channel 647 it can be observed the immunostaining against the surface antigen of hepatitis D (HDAg). dSTORM image was obtained and zoomed in (square).

Further, in order to distinguish more the co-infection profiles, we imaged several cells infected with HBV and HDV where HDV was highly concentrated inside the nuclei of the cells. This is the case of the cells displayed in Figure 5.10, where dSTORM images allowed the study of the distribution of the virus HDV inside the nuclei of adjoining cells and its absence in the cytoplasm, the areas where HBV was found.

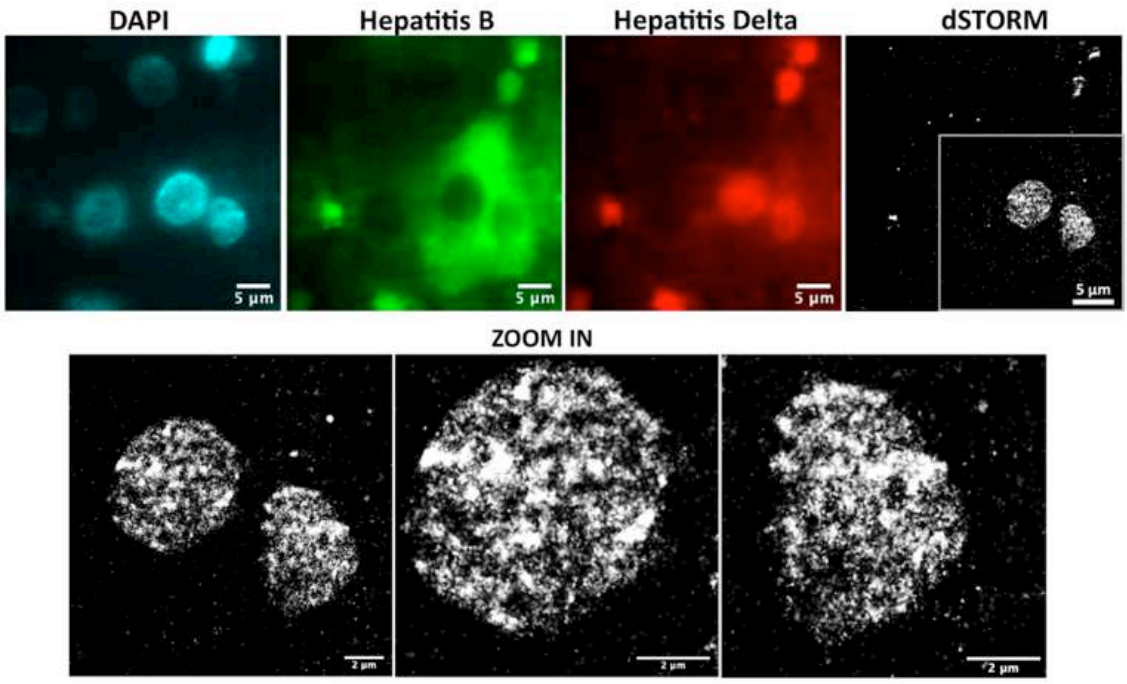

Figure 5.10: Super-resolution image of hepatitis D in a tissue with both hepatitis B and hepatitis Delta. The cell positive for hepatitis B showed hepatitis D only inside the nucleus and barely on the cytoplasm. The STORM-Glycerol buffer was added right before the image acquisition. DAPI was observed in channel 405. Hepatitis B was stained with anti-HBsAg and secondary Alexa488, observed in channel 488 and used as a reference to select the cell. On the channel 647 it can be observed the immunostaining against the surface antigen of hepatitis D (HDAg). dSTORM image was obtained and zoomed in (square).

Finally, we found a field where three different HBV positive cells displayed different profiles of co-infection with HDV (Figure 5.11). First, the biggest cell with HBV (Figure 5.11 cell 1) did not present any type of co-infection with HDV; secondly, the two cells located in the bottom of the image displayed co-infection with HDV but with different distributions: while one of them contained HDV highly concentrated inside the nucleus only (Figure 5.11 cell 2), the other cell only displayed signal of HDV along the cytoplasm (Figure 5.11 cell 3).

This figure could be a great representation of our main assessment of the co-infection of HBV and HDV: each cell contains different amounts of both viruses and there is not an obvious pattern of behaviour of the co-infection, presumably because the biological question could not be answer only with super-resolution microscopy.

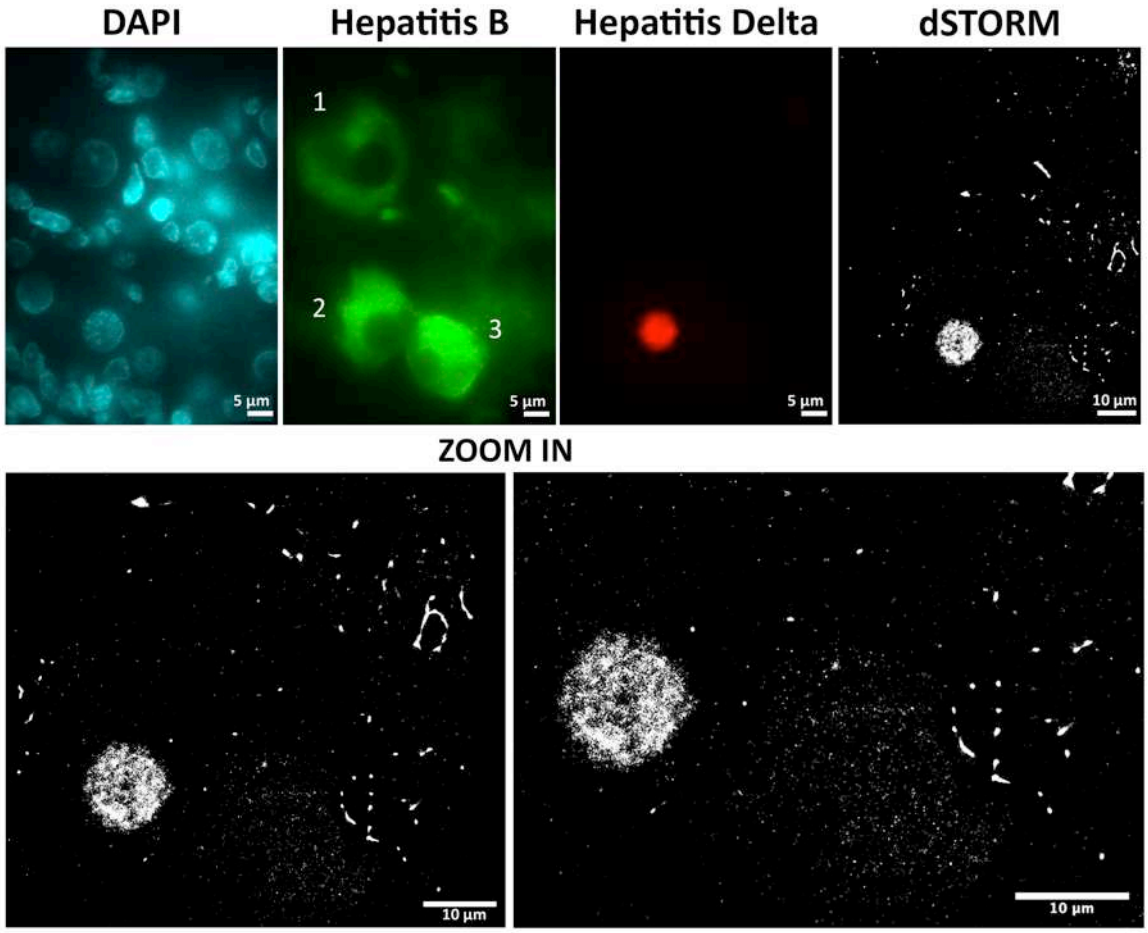

Figure 5.11: Super-resolution image of hepatitis D in a tissue with both hepatitis B and hepatitis Delta. The cell positive for hepatitis B showed diverse amounts of hepatitis D, mainly in the nucleus. The STORM-Glycerol buffer was added right before the image acquisition. DAPI was observed in channel 405. Hepatitis B was stained with anti-HBsAg and secondary Alexa488, observed in channel 488 and used as a reference to select the cell. On the channel 647 it can be observed the immunostaining against the surface antigen of hepatitis D (HDAg). dSTORM image was obtained and zoomed in (square). Numbers indicated different cells expressing HBV.

Overall, with this new approach to search for co-infected cells, HDV was not only found in the nuclei, where it is highly concentrated and visible with fluorescence microscopy, but was also found very spread and weak inside the cytoplasm, impossible to differentiate using conventional microscopy but clearly recognized with dSTORM.

All in all, with dSTORM we could have a better understanding of the different profiles of co-infection of these two viruses: HDV was found either in the nucleus of the cell, highly concentrated, or was weakly expressed inside the cytoplasm. On the other hand, HBV was only found dispersed in the cytoplasm and never concentrated inside the nuclei. These

approximations could not be hypothesized and observed with conventional fluorescence microscopy due to the low signal of spread viruses inside the cytoplasm, therefore dSTORM proved to be a sensitive and strong technique to observe viral structures inside FFPE tissues, even when the virus is not highly expressed. Even so, with dSTORM we could not resolver the unknown behind the behaviour of the co-infection of HDV and HBV but we could confirm that there are more biological questions to be addressed.

5.3 Conclusions and perspectives

In this chapter we verified and validated the application of dSTORM in the image acquisition of FFPE tissues, in concrete to observe the distribution and presence of two hepatitis viruses in the same cell.

We tested different settings to perform super-resolution microscopy on tissues such as the field size, buffer and combinations of dyes. We could confirm that Vectashield did not work properly in our system, hence we used STORM-Glycerol buffer instead with a good signal emission for SMLM. On the other hand, different dyes (e.g. Alexa 488 or Alexa568) were successfully applied to use as a marking for other viral structures in fluorescence microscopy, while Alexa647 was still in use for performing super-resolution images with dSTORM. In general, although tissues possessed strong auto-fluorescence, with the correct focus, angle of the laser and practice, super-resolution images could be performed on hepatocytes with different virus content.

From then on, we imaged the virus HBV on infected cells with the virus HDV located inside the nuclei, in order to identify the co-infection of both viruses. While HBV was not found strongly on HDV infected cells, it was strongly present on adjoining cells describing a reticular distribution along the cytoplasm. On the contrary, HDV was imaged on cells containing big amounts of HBV, observing that HDV was distributed either inside the nucleus or spread on the cytoplasm, with different levels of viral content. The cytoplasmic distribution of HDV could not be visualized using conventional fluorescence microscopy, proving how powerful and sensitive dSTORM is.

In general, we could not develop a model of co-infection of HBV and HDV with super-resolution microscopy. Both viruses distributed differently on all the hepatocytes observed, concluding that the biological mechanism that these two viruses employ to infect and spread on

cirrhotic patients is still quite unknown and could not be acknowledge using this approach. However, dSTORM could fulfil our knowledge increasing the sensitivity of the HDV recognition, confirming the possibility to use SMLM techniques on FFPE studies.

Altogether, SMLM proved to be an interesting tool to study the hepatitis viral distribution on FFPE tissues with the right optimization, setup and buffer. However, technically FFPE tissues are still a challenge due to their thickness and the lack of control during the sectioning with the microtomy, which could create tissues without an homogeneous thickness or even chunky. Also, the auto-fluorescence is still an issue that needs to be solved and manage in order to perform multi-colour images or use a different dye (specially in the wavelength of 488 nm) to visualize them with high signal-to-noise.

5.4 Materials and methods

5.4.1 Tissues explants and biopsies

All tissues samples were collected from explants and biopsies from liver in cirrhosis extracted from patients from the Hospital Clinic of Barcelona within the last 5 years and preserved in paraffin blocks. The tissues were given by the IDIBAPS centre, the group of Dr. MD. Xavier Forns, and cut in the Hospital Clinic facility in sections of 1.5 µm-2 µm thickness.

5.4.2 Immunostaining of paraffin tissues

To perform the immunostaining on paraffin tissues, freshly sectioned tissues were placed on glass slides coated with poly-lysine. To perform a deparaffination of the tissues, the sample were rinsed 3 times in a Xylene bath for 10 minutes each, changing the Xylene after each rinse. The samples were further hydrated using decreased alcohol solutions: the slides were first immerse in a bath with 100% ethanol for 10 minutes twice, followed by 5 minutes in 95% alcohol, 5 minutes in 70% alcohol, 5 minutes in 40% alcohol and finishing with a rinse with H_2Omq.

Further, rehydrated samples were treated to allow the antigen retrieval, a mechanism to release the methylene bridges formed during fixation that masked the antigenic sites. The samples were placed on a streamer with Tris-EDTA buffer, consisted on 10 mM Tris base, 1 mM EDTA, 0.05% Tween 20 diluted on distilled H_2O at pH 9. The samples were steamed for 30 minutes and left for extra 30 minutes with the residual heat. Right after, the samples attached on the slides were kept in PBS.

To perform the immunostaining, samples were blocked during 1 hour with 5% BSA at room temperature followed by 3 rinses with PBS for 5 minutes each and the incubation with the two primary antibodies (mouse anti-HBsAg at 2.5 µg/ml and human anti-HDAg at 2 µg/ml (donated from collaborators)) diluted in 5% BSA overnight at 4ºC. After the incubation time, samples were rinsed with PBS for 5 minutes 3 times and followed by the secondary antibody incubation (anti-mouse Alexa Fluor 647, anti-mouse Alexa Fluor 488, anti-human Alexa Fluor 568 or anti-human Alexa Fluor 647 at 1/500 (Invitrogen)) in 5% BSA in PBS for 1 hour at room temperature and covered from the light with DAPI diluted at 1/1000 (1µg/ml). Following the incubation with secondary antibodies and DAPI, samples were rinsed with PBS for 5 minutes and kept in PBS prior observation with the dSTORM microscope.

5.4.3 dSTORM

Immunostained samples were used to acquire dSTORM images. Immunostained tissues on slide were washed once with PBS and 40 µl of STORM buffer was added on top. The STORM buffer consists of an oxygen scavenging system (0.5 mg/ml glucose oxidase, 40 µg/ml Catalase), 5% w/v glucose and cysteamine 100 mM in PBS-Glycerol (Sigma) 1:1. Once the STORM buffer was added, a coverslip was placed on top avoiding bubbles and sealed with clear nail polish.

Images were acquired using a Nikon N-STORM 4.0 system configured for total internal reflection fluorescence imaging. Excitation inclination was tuned to adjust focus and to maximize the signal-to-noise ratio. Alexa-647 was excited by illuminating the sample with a 647 nm (160 mW) laser built into the microscope. During acquisition the integration time was 10ms for 256 x 256 pixel region or 30 ms for 512 x 512 pixel region. For the measurements with Alexa-647 20,000 frames were acquired in the 647 channel. The total time required to acquire one image was about 5 min.

Fluorescence was collected by means of a Nikon x100, 1.4 NA oil immersion objective and passed through a quad-band-pass dichroic filter (97335 Nikon). Images were recorded onto a 256 x 256 pixel region or 512 x 512 pixel region (pixel size 160 nm) of a sCMOS camera (Hamamatsu). Single-molecule localization sequences were analysed with the STORM plug-in of NIS element Nikon software.

Images were artificially coloured with ImageJ Fiji software.

5.5 References

1. Sadeghipour, A. & Babaheidarian, P. Making Formalin-Fixed, Paraffin Embedded Blocks. *Methods Mol. Biol. Clifton NJ* **1897**, 253–268 (2019).

2. Sy, J. & Ang, L.-C. Microtomy: Cutting Formalin-Fixed, Paraffin-Embedded Sections. *Methods Mol. Biol. Clifton NJ* **1897**, 269–278 (2019).

3. Baker, M. Building better biobanks. *Nature* **486**, 141–146 (2012).

4. Kokkat, T. J., Patel, M. S., McGarvey, D., LiVolsi, V. A. & Baloch, Z. W. Archived Formalin-Fixed Paraffin-Embedded (FFPE) Blocks: A Valuable Underexploited Resource for Extraction of DNA, RNA, and Protein. *Biopreservation Biobanking* **11**, 101–106 (2013).

5. Gaffney, E. F., Riegman, P. H., Grizzle, W. E. & Watson, P. H. Factors that drive the increasing use of FFPE tissue in basic and translational cancer research. *Biotech. Histochem. Off. Publ. Biol. Stain Comm.* **93**, 373–386 (2018).

6. Kocjan, B. J., Hošnjak, L. & Poljak, M. Detection of alpha human papillomaviruses in archival formalin-fixed, paraffin-embedded (FFPE) tissue specimens. *J. Clin. Virol. Off. Publ. Pan Am. Soc. Clin. Virol.* **76 Suppl 1**, S88–S97 (2016).

7. Muehlenbachs, A., Bhatnagar, J. & Zaki, S. R. Tissue tropism, pathology and pathogenesis of enterovirus infection. *J. Pathol.* **235**, 217–228 (2015).

8. Sunderkötter, C. *et al.* Molecular diagnosis of skin infections using paraffin-embedded tissue - review and interdisciplinary consensus. *J. Dtsch. Dermatol. Ges. J. Ger. Soc. Dermatol. JDDG* **16**, 139–147 (2018).

9. Bancroft, J. D. & Layton, C. 10 - The hematoxylins and eosin. in *Bancroft's Theory and Practice of Histological Techniques (Seventh Edition)* (eds. Suvarna, S. K., Layton, C. & Bancroft, J. D.) 173–186 (Churchill Livingstone, 2013). doi:10.1016/B978-0-7020-4226-3.00010-X.

10. Slide Preparation. in *Diagnostic Pathology: Intraoperative Consultation (Second Edition)* (ed. Lester, S. C.) 68–73 (Elsevier, 2018). doi:10.1016/B978-0-323-57019-0.50016-9.

11. Greer, C. E., Lund, J. K. & Manos, M. M. PCR amplification from paraffin-embedded tissues: recommendations on fixatives for long-term storage and prospective studies. *PCR Methods Appl.* **1**, 46–50 (1991).

12. Dietrich, D. *et al.* Improved PCR performance using template DNA from formalin-fixed and paraffin-embedded tissues by overcoming PCR inhibition. *PloS One* **8**, e77771 (2013).

13. Magaki, S., Hojat, S. A., Wei, B., So, A. & Yong, W. H. An Introduction to the Performance of Immunohistochemistry. *Methods Mol. Biol. Clifton NJ* **1897**, 289–298 (2019).

14. Ezaki, T. Antigen retrieval on formaldehyde-fixed paraffin sections: its potential drawbacks and optimization for double immunostaining. *Micron Oxf. Engl. 1993* **31**, 639–649 (2000).

15. Thavarajah, R., Mudimbaimannar, V. K., Elizabeth, J., Rao, U. K. & Ranganathan, K. Chemical and physical basics of routine formaldehyde fixation. *J. Oral Maxillofac. Pathol. JOMFP* **16**, 400–405 (2012).

16. Almuhanna, A. H. *et al.* Optimisation and validation of immunohistochemical axonal markers for morphological and functional characterisation of equine peripheral nerves. *Equine Vet. J.* **n/a**,.

17. Robertson, D., Savage, K., Reis-Filho, J. S. & Isacke, C. M. Multiple immunofluorescence labelling of formalin-fixed paraffin-embedded (FFPE) tissue. *BMC Cell Biol.* **9**, 13 (2008).

18. Kelleher, M. T. *et al.* The potential of optical proteomic technologies to individualize prognosis and guide rational treatment for cancer patients. *Target. Oncol.* **4**, 235–252 (2009).

19. Blutke, A. *et al.* Light sheet fluorescence microscopy guided MALDI-imaging mass spectrometry of cleared tissue samples. *Sci. Rep.* **10**, 14461 (2020).

20. Creech, M. K., Wang, J., Nan, X. & Gibbs, S. L. Superresolution Imaging of Clinical Formalin Fixed Paraffin Embedded Breast Cancer with Single Molecule Localization Microscopy. *Sci. Rep.* **7**, (2017).

21. Øie, C. I. *et al.* New ways of looking at very small holes – using optical nanoscopy to visualize liver sinusoidal endothelial cell fenestrations. *Nanophotonics* **7**, 575–596 (2018).

22. Wang, Y. *et al.* Rapid Sequential In Situ Multiplexing With DNA-Exchange-Imaging. *bioRxiv* 112227 (2017) doi:10.1101/112227.

23. Baddeley, D. *et al.* 4D Super-Resolution Microscopy with Conventional Fluorophores and Single Wavelength Excitation in Optically Thick Cells and Tissues. *PLOS ONE* **6**, e20645 (2011).

24. Viegas, M. S., Martins, T. C., Seco, F. & do Carmo, A. An improved and cost-effective methodology for the reduction of autofluorescence in direct immunofluorescence studies on formalin-fixed paraffin-embedded tissues. *Eur. J. Histochem. EJH* **51**, 59–66 (2007).

25. Davis, A. S. *et al.* Characterizing and Diminishing Autofluorescence in Formalin-fixed Paraffin-embedded Human Respiratory Tissue. *J. Histochem. Cytochem. Off. J. Histochem. Soc.* **62**, 405–423 (2014).

26. Hernandez, V. & Enrique, L. Optical nanoscopy of tissue sections. (2018).

27. Tsukuda, S. & Watashi, K. Hepatitis B virus biology and life cycle. *Antiviral Res.* **182**, 104925 (2020).

28. Aspinall, E. J., Hawkins, G., Fraser, A., Hutchinson, S. J. & Goldberg, D. Hepatitis B prevention, diagnosis, treatment and care: a review. *Occup. Med. Oxf. Engl.* **61**, 531–540 (2011).

29. Chisari, F. V., Ferrari, C. & Mondelli, M. U. Hepatitis B virus structure and biology. *Microb. Pathog.* **6**, 311–325 (1989).

30. Venkatakrishnan, B. & Zlotnick, A. The Structural Biology of Hepatitis B Virus: Form and Function. *Annu. Rev. Virol.* **3**, 429–451 (2016).

31. Hepatitis B. https://www.who.int/news-room/fact-sheets/detail/hepatitis-b.

32. Rizzetto, M. *et al.* Immunofluorescence detection of new antigen-antibody system (delta/anti-delta) associated to hepatitis B virus in liver and in serum of HBsAg carriers. *Gut* **18**, 997–1003 (1977).

33. Denniston, K. J. *et al.* Cloned fragment of the hepatitis delta virus RNA genome: sequence and diagnostic application. *Science* **232**, 873–875 (1986).

34. Wang, K.-S. *et al.* Structure, sequence and expression of the hepatitis delta (δ) viral genome. *Nature* **323**, 508–514 (1986).

35. Sureau, C. & Negro, F. The hepatitis delta virus: Replication and pathogenesis. *J. Hepatol.* **64**, S102–S116 (2016).

36. Liaw, Y. F. Role of hepatitis C virus in dual and triple hepatitis virus infection. *Hepatol. Baltim. Md* **22**, 1101–1108 (1995).

37. Sagnelli, E. *et al.* Advances in the treatment of hepatitis B virus/hepatitis C virus coinfection. *Expert Opin. Pharmacother.* **15**, 1337–1349 (2014).

38. Smedile, A. *et al.* INFLUENCE OF DELTA INFECTION ON SEVERITY OF HEPATITIS B. *The Lancet* **320**, 945–947 (1982).

39. Zamor, P. J., deLemos, A. S. & Russo, M. W. Viral hepatitis and hepatocellular carcinoma: etiology and management. *J. Gastrointest. Oncol.* **8**, 229–242 (2017).

40. Mentha, N., Clément, S., Negro, F. & Alfaiate, D. A review on hepatitis D: From virology to new therapies. *J. Adv. Res.* **17**, 3–15 (2019).

41. Stockdale, A. J. *et al.* The global prevalence of hepatitis D virus infection: Systematic review and meta-analysis. *J. Hepatol.* **73**, 523–532 (2020).

42. Giersch, K. & Dandri, M. Hepatitis B and Delta Virus: Advances on Studies about Interactions between the Two Viruses and the Infected Hepatocyte. *J. Clin. Transl. Hepatol.* **3**, 220–229 (2015).

43. Olivier, N., Keller, D., Rajan, V. S., Gönczy, P. & Manley, S. Simple buffers for 3D STORM microscopy. *Biomed. Opt. Express* **4**, 885–899 (2013).

44. Mönkemöller, V., Øie, C., Hübner, W., Huser, T. & McCourt, P. Multimodal super-resolution optical microscopy visualizes the close connection between membrane and the cytoskeleton in liver sinusoidal endothelial cell fenestrations. *Sci. Rep.* **5**, 16279 (2015).

45. Kwakwa, K. *et al.* easySTORM: a robust, lower-cost approach to localisation and TIRF microscopy. *J. Biophotonics* **9**, 948–957 (2016).

46. Bon, P. *et al.* Three-dimensional nanometre localization of nanoparticles to enhance

super-resolution microscopy. *Nat. Commun.* **6**, 7764 (2015).

47. Cordes, T., Maiser, A., Steinhauer, C., Schermelleh, L. & Tinnefeld, P. Mechanisms and advancement of antifading agents for fluorescence microscopy and single-molecule spectroscopy. *Phys. Chem. Chem. Phys. PCCP* **13**, 6699–6709 (2011).

48. Arsić, A., Stajković, N., Spiegel, R. & Nikić-Spiegel, I. Effect of Vectashield-induced fluorescence quenching on conventional and super-resolution microscopy. *Sci. Rep.* **10**, 6441 (2020).

Chapter 6: Characterization of the inhibition of influenza viral infection by 6'-sialyllactose conjugated dendritic polymer

This chapter explains the work accomplished at VIB-UGENT center for medical biotechnology, performed during a three-months internship at the group of Dr. Xavier Saelens, located in Gent (Belgium).

6.1 Introduction

Influenza virus (IAV) mutates so fast that antivirals are always in need of development. As explained in detail in chapter 1, there are different novel approaches to target efficiently IAV. One of them is developing antivirals against the protein hemagglutinin (HA), since plays a crucial role in viral binding, fusion and entry process[1,2]. This essential role is lead by the affinity of HA towards the cell membrane, where human IAV binds to the terminal sialic acid (SA) residues in a α2-6 linkage (SA α2.6Gal)[3].

The usage of SA analogues is an interesting approach that consist on developing sugars that could interact with HA at a lower K_D than SA[4-7]. Interestingly, the K_D of the monovalent interaction of HA-SA is very high, in the millimolar range, thus it has been suggested the need to follow a multivalent approach in order to obtain high stability bindings of the analogue sugar and HA, since monovalent approached resulted in increasing the concentration of the antiviral up to toxic and non-physiological quantities[8,9]. Multivalency antiviral approach mainly focus on using small particles conjugated with high number of SA analogues, in order to cover the whole surface of the virus[10,11]. The sugar analogues must be displaced along the structure with controlled valency and with certain spacing between ligands to improve the attachment, thus the particle must be small and charged with enough sugars to interact with viruses in multiple areas.

The design of polymers with multivalent conjugation of sugars like 6'-sialyllactose or 3'-sialyllactose had been tested and proved to be a good candidate for in vitro inhibition of influenza[12-16]. One of the most promising particles to use is polyamidoamine (PAMAM) dendrimer. PAMAM dendrimers are commercially available in multiple shapes and generations and are wildly used in the literature to block viruses, including influenza[17-20]. The main

advantage of dendrimers is its small structure, with a width around 3-5 nm, small enough to block influenza receptors by strong interactions, besides its capacity to be labelled due to the high amount of branches with numerous amines, perfect for high contents of SA analogues.

To explore the potential use of PAMAM dendrimers as scaffolds for SA analogues, in this chapter we synthesized PAMAM dendrimers with an analogue of SA, 6'-sialyllactose (6SL), in order to test the in vitro inhibition of the antiviral against 4 different strains of influenza, each of them with a different type of HA. By performing plaque assays and hemagglutination inhibition assays we could study the importance of the valency and distribution of the sugars to produce a successful inhibition of the infection, since we could prove that our dendrimers could bind to most of the strains tested but without inhibiting the infection of the virus.

Thus, using two-colour super-resolution microscopy we could study how dendrimers behaved in the presence of infected cells and how it aggregates in small groups, not covering the whole virus expressed on cells. Therefore, dSTORM could also contribute to the study of antivirals, understanding the behaviour of the particle with influenza virus and infected cells, an approach not fully exploited yet in the field.

6.2 Results and discussion

6.2.1 Synthesis of 6SL and lactose PAMAM dendrimer

Our first approach was to label the PAMAM dendrimers with sugars that could block influenza virus. In our case we selected 6-sialyllactose (6SL) for the promising results shown in different literature references (17,19), while lactose was selected as the negative control, since is a sugar that could not interact with HA. The protocol for labelling PAMAM dendrimers with sugars is well established, consisting on a reductive amination of an aldehyde. Here, we adapted the synthesis protocol from Kwon S-J. et al.[19], where they tested several generations of PAMAM dendrimer attached to different ratios of 6SL, concluding that the generation 4 (G4) with 20-24 6SL per dendrimer had the best blocking effect against H1N1 (NWS) *in vitro* and *in vivo*.

Following these results, we labelled Generation 4 PAMAM dendrimers with 24 6-sialyllactose by a reductive amination driven by $NaBH_3CN$ followed by a purification and MALDI-TOF characterization (Figure 6.1). Our final goal was not only to test in vitro the inhibition effects of 6SL PAMAM dendrimers but also to characterized by super-resolution microscopy the

interaction between influenza particles and the dendrimer, hence we also labelled the structure with 2-3 molecules of Cy3, a super-resolution adequate dye, to identify the final interaction between the virus and the antiviral structure. In this case we used a spectrophotometer to test the amount of Cy3 per molecule, instead of MALDI-TOF, to avoid noise and have a more precise measurement of the amount of dye per particle.

Thanks to the MALDI-TOF and spectrophotometer analyses we could conclude that out final dendrimers contained 24 molecules of 6SL per dendrimer with an average of 2.4 Cy3 per structure (Figure 6.1). In the case of the negative control with lactose, the molecular ratio was higher, containing 40 lactoses per dendrimer. Lactose dendrimer also had 3 Cy3 in the structure, in order to visualize the interaction of the negative control dendrimer on viral particles.

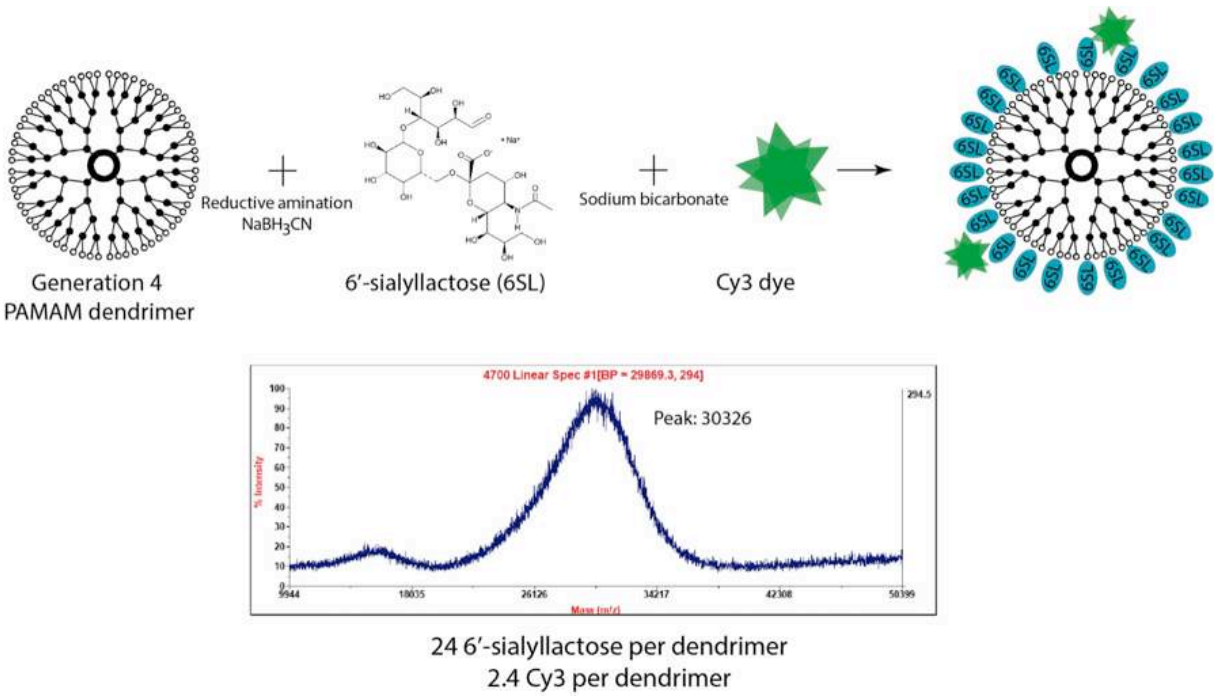

Figure 6.1: Diagram of 6SL PAMAM-dendrimer synthesis. The generation 4 of PAMAM dendrimer was subjected to a reductive amination with $NaBH_3CN$ with 6'-sialyllactose (6SL) or lactose for the negative control. After the reductive amination the sample was measured by MALDI-TOF MS and it was characterized the ratio 6SL-PAMAM (24:1) and lactose-PAMAM (40:1). Following a labelling of 2-3 Cy3 per PAMAM dendrimer was performed by incubation with Sodium bicarbonate.

6.2.2 Testing the inhibition of influenza induced by 6SL PAMAM dendrimer by plaque assay

The theoretical ability of these 6SL dendrimers is to interact with HA through which they avoid the recognition of the receptor to the target cell, thus not attaching and infecting. Accordingly, the first approach that we took in order to test the ability of our dendrimers to block influenza infection was to perform a plaque assay. This type of assay would let us identify the capability of the dendrimers to avoid the interaction of the viral particle and the cell.

The main assay consists on incubating a mixture of the dendrimer and the virus on top of a monolayer of cells for 1 hour. After this time, a layer of dense cellulose is applied on top, with the influenza-dendrimer interacting on the cells, for 48 hours. The main role of the cellulose is to avoid the spread of the newly formed viruses, thus viruses that infected cells would only be spreading and growing in the surrounding cells and therefore they would be forming a plaque of dead cells due to the infection, visible by eye after immunostaining. The number and size of the plaque work as an indicator of the amount of infection produced by the virus: the smaller the plaque and the lower the number of plaques the higher inhibition of infection by the interaction of the 6SL dendrimer.

In order to have a broad study of the effects of 6SL PAMAM dendrimer on different influenza strains, we tested the inhibition of infectivity in four different strains of influenza (in Table 6.1), with different subtypes of HA, in order to identify the biggest and lowest affinity towards HA.

Common name of strain	Type
Udorn	A/Udorn/72/H3N2
PR8	A/Puerto Rico/8/34/H1N1
X31	A/X-31/H3N2
Pdm09	A/Pdm09/H1N1

Table 6.1: Types of influenza strains used in this work. The common name is the abbreviation used to identify the strain. The type of influenza is the full name with the type of HA and NA of the strain.

According to the literature[19] the IC_{50} of the 6SL dendrimer is 3.4 μM, thus we tested 5 different concentrations of the PAMAM dendrimer to study the spectrum of action at different concentrations: 5 μM, 1 μM, 500 nM and 100 nM.

First we tested the inhibitory effect on the Udorn strain, performing a plaque assay and measuring the area of the resulting plaques. Due to the big size of the plaques in Udorn, the size is a good indicator of the infectivity of the virus. As shown in Figure 6.2 A, the treatment of lactose dendrimers did not produce any decrease in the area of the formed plaques. If we compare the different concentrations of lactose dendrimer with the negative control (influenza virus alone), we could see how the areas are quite similar, very broad and with a similar variability. On the other hand, if we compare the lactose dendrimer results with the 6SL dendrimer treatment (Figure 6.2 B) we could identify a soft tendency to produce smaller plaques. Although is a very visual tendency, the treatment with 6SL dendrimer led to very heterogeneous plaques, where some of them were smaller but some of them had the same size of the ones produced in the negative control, not giving concluding statistics differences. With this first assay we could not determine if 6SL dendrimers produced a good inhibition of influenza infection, but initially did not seem to block strongly the interaction of influenza with the cell during a long incubation time.

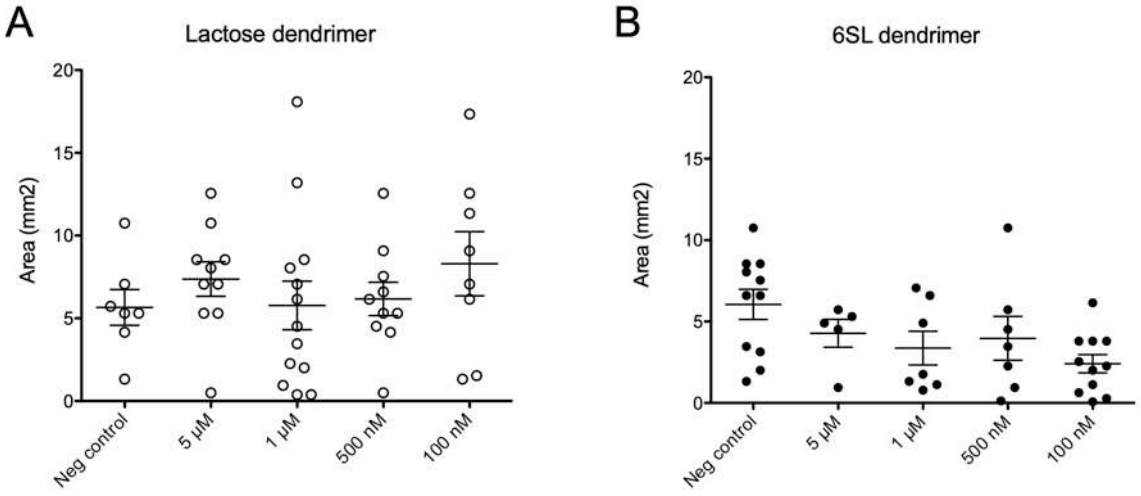

Figure 6.2: Udorn plaque areas (mm^2) of plaque assay. Four different concentrations of dendrimer were tested (5µM, 1 µM, 500 nM and 100 nM) in duplicates. The negative controls in both graphs consist on influenza virus alone. A) Area (mm^2) of plaques formed on a monolayer of cells treated with different concentrations of lactose dendrimers. B) Area (mm^2) of plaques formed on a monolayer of cells treated with different concentrations of 6'-sialyllactose (6SL) dendrimers. Quantification of the plaque size was based on ImageJ analysis. The graph shows the area of each plaque and the bars represent the mean area ± SEM.

Since we could not have a clear conclusion measuring the areas of the plaques, we decided to compare the resulting number of plaques as well (Figure 6.3 A). Again we could see a huge variability in terms of number of plaques. Virus incubated with lactose dendrimer did not

decreased the number of plaques, oscillating between 4 and 6 plaques, but again we could see a tendency of the 6SL dendrimer to inhibit slightly the plaque formation, where the incubation of Udorn with increasing concentrations of 6SL dendrimer decreased the number of plaques formed in the monolayer of cells: 100 nM did not produce any different compared to the negative control, 500 nm and 1 µM produced less plaques (3-4) and 5 µM decreased by half the number of plaques forms (2 plaques). Unfortunately, again the heterogeneity of the results did not produced conclusive statistics analysis.

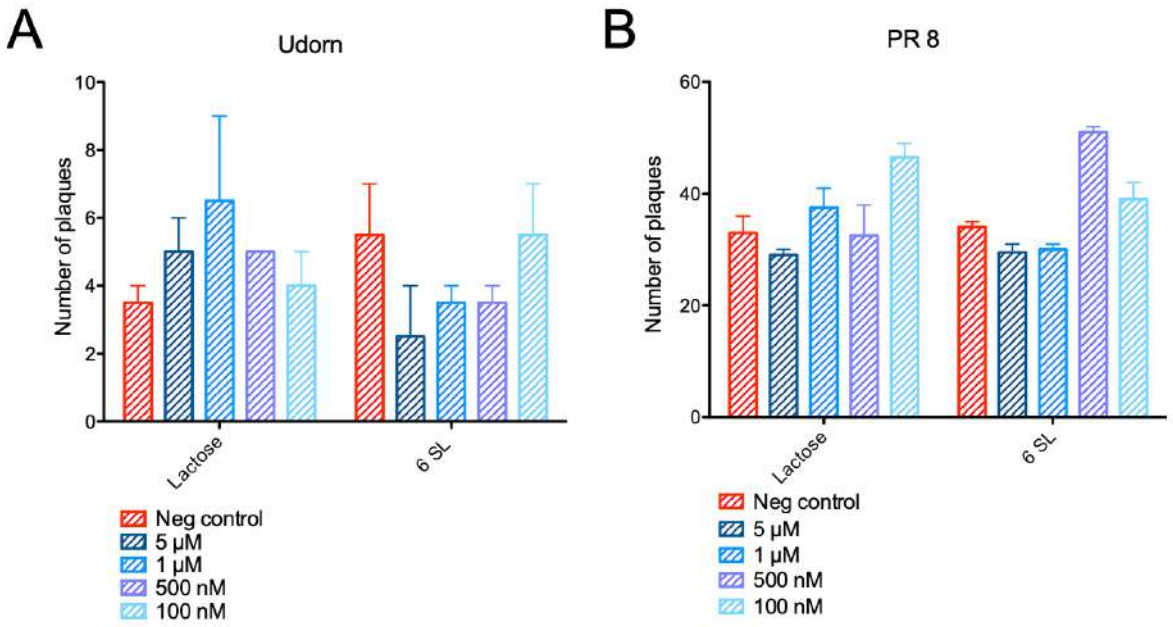

Figure 6.3: Number of plaques formed in the plaque assay. A) Udorn virus was treated with different concentrations (5 µM, 1 µM, 500 nM and 100 nM) of lactose or 6'-sialyllactose (6SL) dendrimer for 48 hours in duplicates. Plaques of the biological replicates were counted by hand and plotted. B) PR8 virus was treated with different concentrations (5 µM, 1 µM, 500 nM and 100 nM) of lactose or 6'-sialyllactose (6SL) dendrimer for 48 hours. Plaques of the biological replicates were counted by hand and plotted. Negative control was influenza virus alone.

Secondly, we also performed plaque assay on the strain PR8. The size of the plaques are small, thus hard to measure, so we compared the total number of plaque formed. As shown in the graph in Figure 6.3 B, lactose dendrimers and 6SL dendrimers produced an even number of plaques, independently the concentration of the dendrimer, being most of them around 30 plaques per well. With this numbers of plaques we could determine that in this conditions dendrimers did not block the interaction of the influenza virus with the cell in the strain PR8.

Comparable results were obtained when the strains X31 and Pdm09 were tested (Figure 6.4 A and B respectively). Similar total number of plaques formed were observed independently the

concentration of the dendrimer in both strains, meaning that 6SL dendrimer incubated with the influenza strain for the 48 hours that the infection lasted did not produced any inhibition of entrance or infection of any kind.

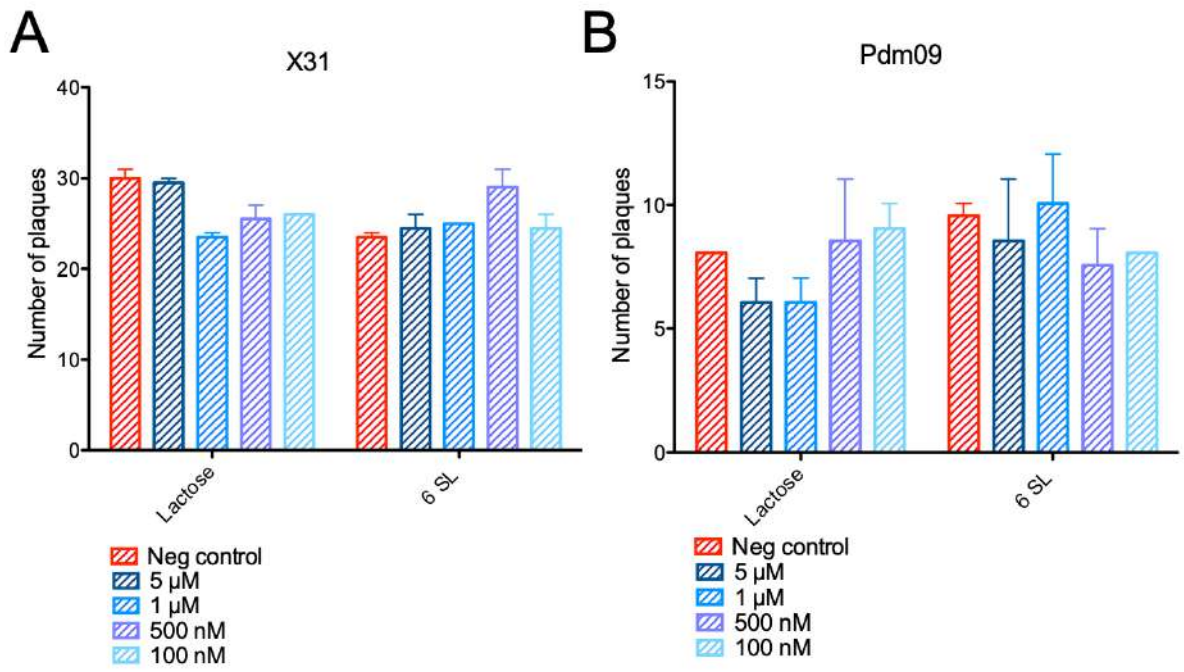

Figure 6.4: Number of plaques formed in the plaque assay. A) X31 virus was treated with different concentrations (5 µM, 1 µM, 500 nM and 100 nM) of lactose or 6'-sialyllactose (6SL) dendrimer for 48 hours in duplicates. Plaques of the biological replicates were counted by hand and plotted. B) Pdm09 virus was treated with different concentrations (5 µM, 1 µM, 500 nM and 100 nM) of lactose or 6'-sialyllactose (6SL) dendrimer for 48 hours. Plaques of the biological replicates were counted by hand and plotted. Negative control was influenza virus alone.

As a conclusion, the mixture of 6SL dendrimer and influenza incubated during the whole cycle of infection did not produce any inhibition of the plaque formation in 3 of the 4 strains tested. Only the strain Udorn showed a small decrease in the number of plaques formed, where the resulting plaques were smaller than the ones produced in the negatives controls, specially with a high concentration of 6 SL dendrimer, but the data was so heterogeneous that did not give any statistical conclusion. These results could be due to different factors that needed to be further tested, like the concentration of the dendrimer, incubation times or the inhibition of the protein NA due to its capacity to hydrolase 6SL.

6.2.3 Testing the interaction of HA and dendrimers by hemagglutinin inhibition assay

As previously seen, long incubation times of the dendrimer did not produce inhibition of influenza infection at those concentrations. One possible explanation of these results is that the interaction between the influenza strain and the 6SL dendrimer was not strong enough to be maintained with time, thus long incubations with the cells led to an eventually dispatched of the virus from the dendrimer and the ability of the virus to infect. Further, to explore the possibility than 6SL dendrimer attach with low affinity to the HA proteins of the influenza virus we performed hemagglutination inhibition assays.

Influenza protein HA has the ability to bind to red blood cells, producing an interaction that results in a lattice of agglutinated cells that set irregularly in the bottom of a U-shape 96 well plate if the virus is present in sufficient quantity, called hemagglutination[21]. If the virus is incubated with antibodies or antivirals with enough concentration for blocking the protein HA, influenza will not interact with the erythrocytes and thus will not produce the hemagglutination of red blood cells (Figure 6.5)[22].

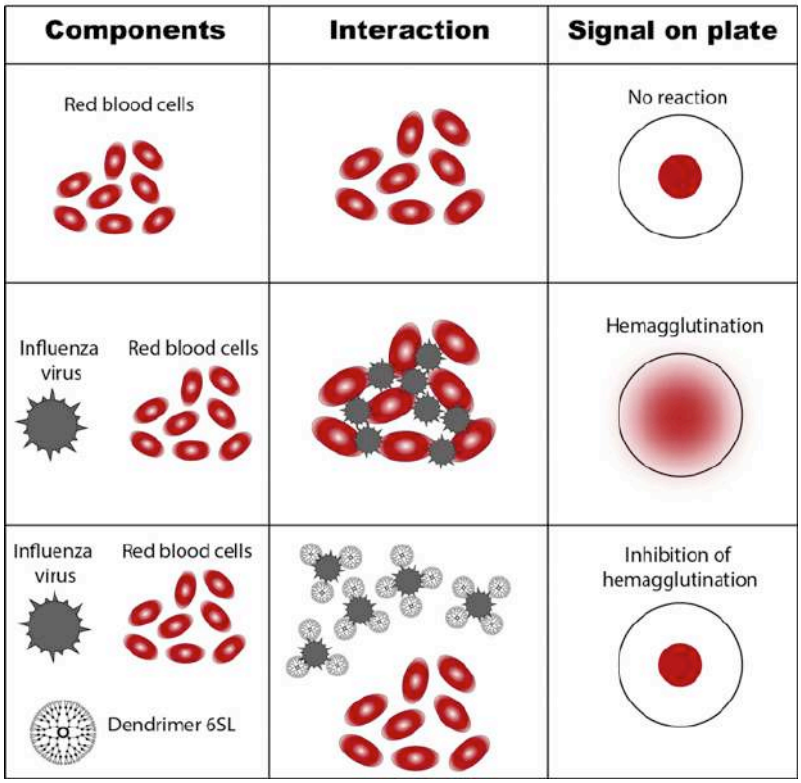

Figure 6.5: Diagram of the principle of hemagglutination inhibition assay. Red blood cells precipitate in the bottom of a 96 well plate when does not interact with the virus. When the virus is present in the right concentration, influenza

HA interacts with the red blood cells and produces lattice of agglutinated cells, showing a blur signal in the plate. When dendrimers that binds against HA are present in the right concentration, they block the protein HA avoiding the hemagglutination and leaving the red blood cells to precipitate at the bottom of the well.

Accordingly, we tested the affinity of 6SL and lactose dendrimers towards HA at different concentrations against different dilutions of each strain of influenza. This time we increased the concentration of the dendrimers to up to 10 μM, in order to test the hypothesis that it is needed higher amount of 6SL dendrimers to block the virus. Moreover, since there is strong evidence that NA can hydrolyse 6SL ligands, resulting in a lack of efficiency of the 6SL-PAMAM dendrimers, we also tested the affinity of the PAMAM dendrimers in the presence of oseltamivir (OC) a common antiviral drug called Tamiflu that blocks the hydrolase activity of the protein NA[23]. Finally, as a new positive control, we also tested if each strain could suffer under these conditions a normal inhibition of hemagglutination by using 2 different concentrations of specific serum against each strain. Those serums were obtained from mouse infected with each strains and are known to be very efficient against the infection[24].

First, we tested the affinity towards HA of the strain Udorn, since it was the only strain that showed a slightly effect of diminution of plaque areas and number in the plaque assay previously performed (Figure 6.2). In Figure 6.6 A, we could see how a hemagglutination inhibition assay looks like. The positive control (Udorn +) showed us at which dilution the virus could produce agglutination of the erythrocytes, indicated with a blue line. Lower dilutions of the virus produced hemagglutination (1, 1/2) and bigger dilutions of the virus (1/4 and 1/8 in this case) did not produce hemagglutination, indicating that at this concentration the amount of virus is not enough to agglutinate the red blood cells, producing bright red dots of precipitated erythrocytes. When the incubation with 6SL dendrimers produced bright and rounded dots at higher dilutions of the indicated with blue line (1/4), it is a signal of the inhibition of hemagglutination (indicated here with an asterisk (*)), thus meaning that 6SL dendrimer would interact with HA.

In this case, Udorn did inhibit the agglutination of the red blood cells with most of the concentration of the dendrimers without the effect of the oseltamivir. With the inhibition of NA by OC 1 μM, the smallest concentration of dendrimer tested (0.31 μM) produced also an effect on the hemagglutination inhibition, meaning that by blocking the hydrolysis the 6SL dendrimer gained sensitivity, being able to bind to HA at a very low concentration. However, the affinity

of 6SL dendrimer towards the strain Udorn is not strong enough to block the virus at its bigger concentration (dilution 1), even in the presence of OC.

In comparison, the serum against Udorn could indeed block HA at the biggest dilution, indicating that the effect of 6SL dendrimer is a consequence of the interaction towards the strain and not the inability of the virus to be blocked.

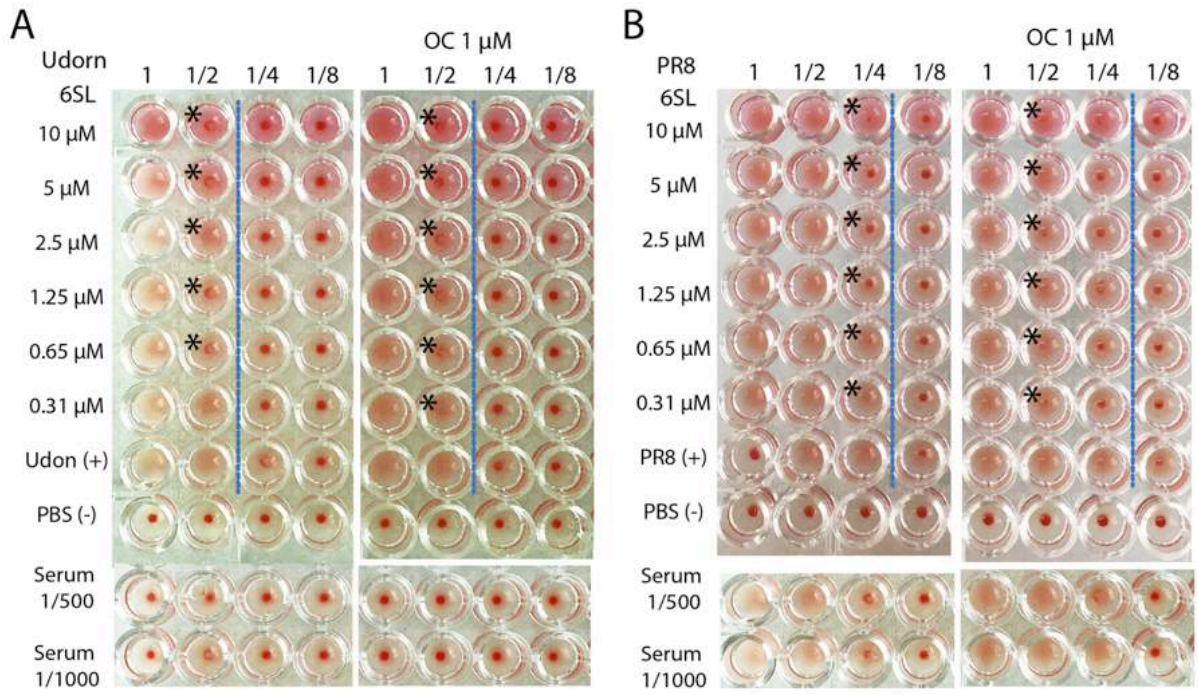

Figure 6.6: Hemagglutination inhibition assay of A) Udorn and B) PR8 testing the affinity of 6SL dendrimer at different concentrations (10 µM, 5 µM, 2.5 µM, 1.25 µM, 0.65 µM and 0.31 µ) against decreasing concentrations of the virus with and without the antiviral drug Oseltamivir 1 µM (OC 1 µM). The positive control is the virus alone. A) Udorn, B) PR8) incubated with PBS and the negative control consist only on PBS. To test the ability of the strain to be inhibited, it was tested the hemagglutination inhibition using serum against the strain at 1/500 and 1/1000 dilution. The line represents the maximum dilution of the virus that produced hemagglutination of erythrocytes, while the asterisk mark the wells that produced inhibition of hemagglutination due to the action of the dendrimer.

Further, we analysed the interaction of 6SL and the strain PR8 (Figure 6.6B) the same way. Here we could observe that without OC, PR8 was inhibited at a dilution of 1/4, in a similar way that we observed in Udorn, but in this case, the effect of OC produced a high increase of affinity of the 6SL dendrimer to the HA, since the inhibition of the hemagglutination was done in this case at double concentration of the virus (1/2). Therefore, blocking the activity of NA in PR8 increased strongly the affinity of the 6SL dendrimer. Also the inhibition of the virus done by the

serum against PR8 is less strong that the inhibition produced by the 6SL dendrimer in the presence of OC, while without OC 6SL showed similar levels of inhibition that a serum from mouse anti-PR8.

When we compare both results with the effects of the incubation of lactose dendrimers we could observe than in both strains, Udorn (Figure 6.7A) and PR8 (Figure 6.7B), lactose dendrimers did not produce any inhibition of the hemagglutination, since there is not presence of bright erythrocytes precipitates at the bottom of the well above the blue line.

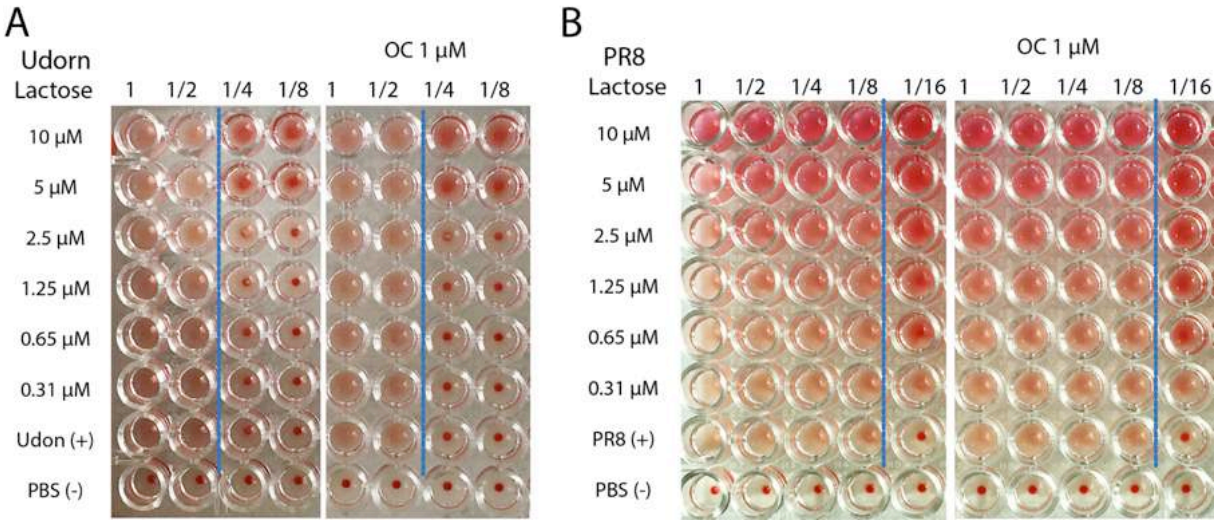

Figure 6.7: Hemagglutination inhibition assay of A) Udorn and B) PR8 testing the affinity of lactose dendrimer at different concentrations (10 µM, 5 µM, 2.5 µM, 1.25 µM, 0.65 µM and 0.31 µ) against decreasing concentrations of the virus with and without the antiviral drug Oseltamivir 1 µM (OC 1 µM). The positive control is the virus alone. A) Udorn, B) PR8) incubated with PBS and the negative control consist only on PBS. The line represents the maximum dilution of the virus that produced hemagglutination of erythrocytes.

In brief, in these two strains we could observe how important is the inhibition of the hydrolase activity of NA, since the degradation of 6SL dendrimers affected strongly the affinity of the dendrimer, especially against the strain PR8, which showed a strong interaction.

Next we also tested the strain X31, one of the strains that did not show any inhibition of the plaque formation in the past experiment (Figure 6.4 A). As seen in the assay in Figure 6.8 A, X31 did produce hemagglutination at dilution 1/8. The incubation with 6SL dendrimers inhibited the hemagglutination produced at 1/8 in all concentrations of the dendrimer but not at higher amounts of the virus. Also, the presence of OC 1µM did not increase the sensitivity of

6SL dendrimer against the strain X31, indicating that for in this strain the soft hydrolysis suffered on the dendrimer did not affect the binding capacities towards HA. If we compare the inhibition performed with the serum against X31, we could observe that the strain was blocked successfully up to a dilution of 1/2, thus indicating that 6SL dendrimer could only block the strain softly.

Lastly, we tested the inhibition of hemagglutination against the strain Pdm09, a strain that historically is hard to block since it belong to the pandemic influenza of 2009. As seen in Figure 6.8 B, the strain could not be blocked by 6SL dendrimer, since the hemagglutination was produced even in present of 10 μM of 6SL dendrimer. The serum though, could block perfectly the strain up to a dilution of 1, meaning that 6SL dendrimer did not produce any effect against the strain Pdm09 even in the presence of OC 1 μM.

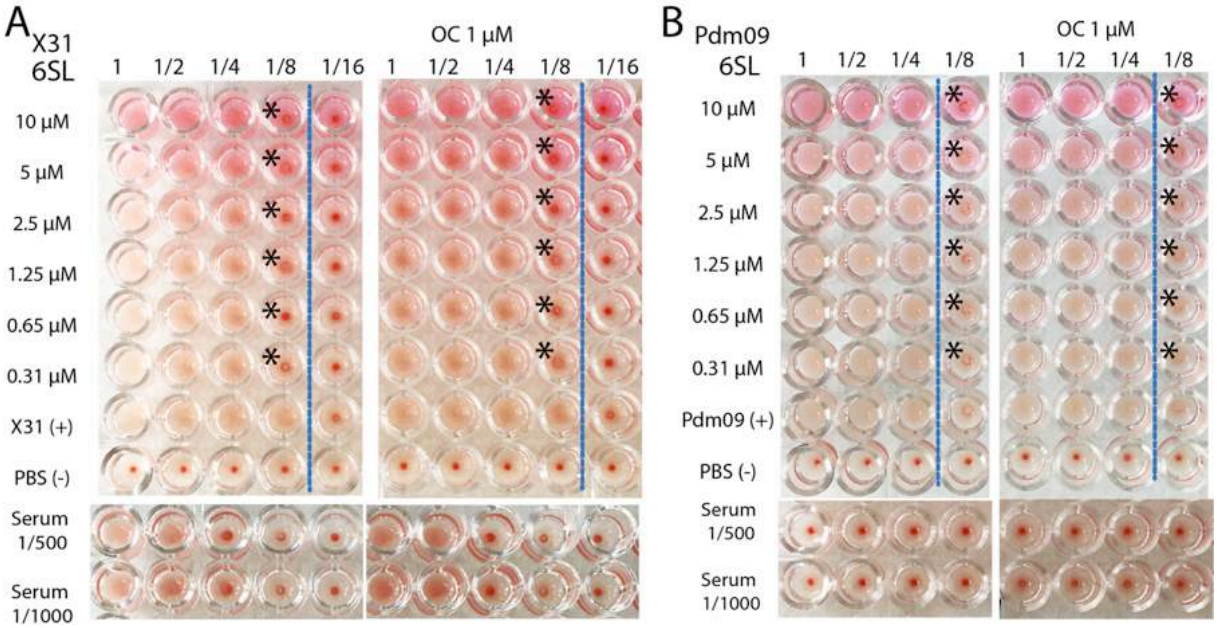

Figure 6.8: Hemagglutination inhibition assay of A) X31 and B) Pdm09 testing the affinity of 6SL dendrimer at different concentrations (10 μM, 5 μM, 2.5 μM, 1.25 μM, 0.65 μM and 0.31 μ) against decreasing concentrations of the virus with and without the antiviral drug Oseltamivir 1 μM (OC 1 μM). The positive control is the virus alone. A) Udorn, B) PR8) incubated with PBS and the negative control consist only on PBS. To test the ability of the strain to be inhibited, it was tested the hemagglutination inhibition using serum against the strain at 1/500 and 1/1000 dilution. The line represents the maximum dilution of the virus that produced hemagglutination of erythrocytes, while the asterisk mark the wells that produced inhibition of hemagglutination due to the action of the dendrimer.

The controls using lactose dendrimers in both strains (Figure 6.9 A and B) showed that there was not interaction with these dendrimers, since did not produce any inhibition of the hemagglutination as expected.

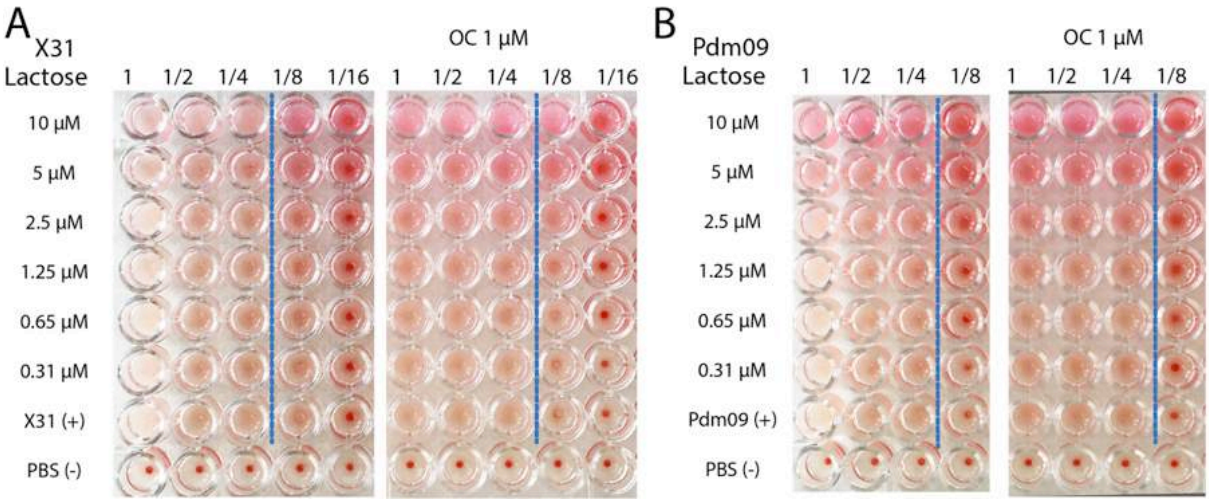

Figure 6.9: Hemagglutination inhibition assay of A) X31 and B) Pdm09 testing the affinity of lactose dendrimer at different concentrations (10 µM, 5 µM, 2.5 µM, 1.25 µM, 0.65 µM and 0.31 µ) against decreasing concentrations of the virus with and without the antiviral drug Oseltamivir 1 µM (OC 1 µM). The positive control is the virus alone. A) Udorn, B) PR8) incubated with PBS and the negative control consist only on PBS. The line represents the maximum dilution of the virus that produced hemagglutination of erythrocytes.

In general this test unveiled the interaction of the 6SL dendrimer toward the HA protein of the four strains tested, giving us information about the effect of Tamiflu (OC) on the interaction.

6SL dendrimers previously showed us some interaction against Udorn by the plaque assay, but with the hemagglutination inhibition assay we could confirm that dendrimers could attach slightly to HA at most concentrations tested (10 µM-0.65 µM); however the interaction was not strong enough to be able to attach to HA efficiently at higher concentrations of the virus, something that indeed happened with the strain PR8. Even though PR8 was not inhibited by 6SL in plaque assay, the hemagglutination assay showed that this strain had interaction with 6SL, especially once was treated with Tamiflu, being able to block HA more efficiently than the serum against PR8.

Despite these promising results, the strain Pdm09 did not show any interaction against 6SL with or without Tamiflu; X31 had some interaction but was not as promising as the interaction

studied with PR8 and Udorn, since the interaction was much lower that the one showed with the serum against X31 and did not increase with Tamiflu.
Taking into consideration these results, we decided to stop testing with X31 and Pdm09 due to the lack of successful binding towards 6SL dendrimers, but we decided to keep testing PR8 and Udorn in vitro, since these two strains are the ones that had more effect with 6SL dendrimers.

6.2.4 Shorts incubations plaque assay of dendrimers with PR8 and Udorn strain

Despite the lack of concluding results obtained from the first plaque assay performed, we decided to continue testing in vitro the effects of the 6SL dendrimers using the information obtained from the hemagglutination inhibition assay. We now know that Tamiflu played an important role in the increasing sensitivity of 6SL dendrimers, especially in the strain PR8 where there was indeed an interaction between the HA of the virus and the dendrimer.

Taking into account this information, we performed a new plaque assay with only the strains PR8 and Udorn. In this case, we also incubated the influenza strains with Oseltamivir (OC) for 30 minutes prior the incubation with 6SL or lactose dendrimers. Right after the incubation of the virus and the dendrimers, the mixture was incubated for 1 hour on top of the monolayer of MDCK cells. Since we hypothesized that the interaction dendrimer-virus was not long lasting, we washed the cells right after, this way we could observe the plaque formed from the virus that interacted only during the initial contact, when presumably the virus was still blocked by 6SL dendrimer.

First, we tested the effect of 6SL and lactose on the strain Udorn (Figure 6.10). The negative control consisted on influenza particles without any dendrimer but in the case of the OC sample, they were also incubated with Tamiflu. If we observe the results obtained in the sample incubated with lactose dendrimer (Figure 6.10 A), it was remarkable that the incubation with OC seemed to affect the general infectivity of the virus. All samples treated with OC showed lower number of plaques than those without OC. Even though NA is not crucial for the interaction of the cell and the virus, Udorn seemed sensitive to the action of OC for the general infectivity, decreasing the total number of plaques independently the effect of the lactose dendrimer. A similar feature was observed in the sample treated with OC 6SL (Figure 6.10 B), where the total number of plaques formed was smaller compared to the sample without OC, even inhibiting the total infection in the case of 5 μM, presumably an effect of OC and not the

dendrimer. Thus, at this point it was hard to identify the real role of 6SL dendrimers in the presence of OC.

Observing the samples without OC, in general we could see that 6SL dendrimer did not produce a dramatic decrease of plaque formation at short incubation times, concluding that 6SL dendrimer was not able to block in vitro infection of the strain Udorn even though it could bind to HA at different concentrations.

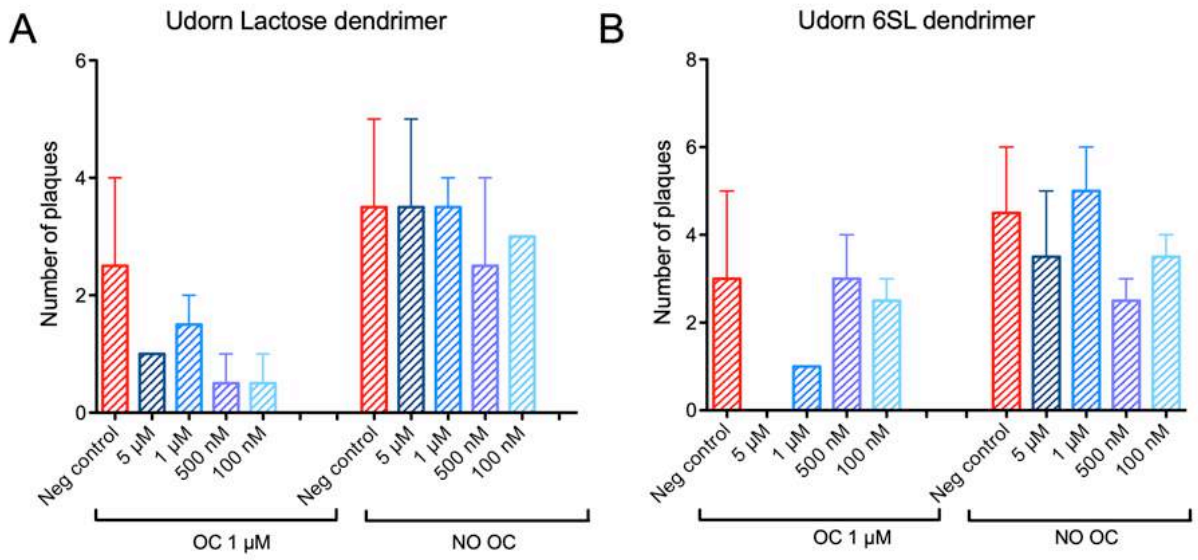

Figure 6.10: Number of plaques formed in the plaque assay. A) Udorn virus was treated with different concentrations (5 µM, 1 µM, 500 nM and 100 nM) of lactose dendrimer for 48 hour with Oseltamivir (OC) or without oseltamivir (NO OC). Plaques of the biological replicates were counted by hand and plotted. B) Udorn virus was treated with different concentrations (5 µM, 1 µM, 500 nM and 100 nM) of 6'-sialyllactose (6SL) dendrimer for 48 hours with Oseltamivir (OC) or without oseltamivir (NO OC). Plaques of the biological replicates were counted by hand and plotted. Negative control was influenza virus alone.

In the case of the strain PR8 (Figure 6.11 A), we could not observe a special sensitivity of the strain towards OC. The lactose control treated with OC did not show a strong decrease in the amount of plaque formation, but either with 6SL dendrimers (Figure 6.11 B). Although 6SL dendrimer could bind to HA, especially in the presence of OC, that binding studied in the hemagglutination assays did not translate into a decrease in the infectivity of the virus. The amount of plaques formed with 6SL (Figure 6.11 B) was not decreased strongly enough to determined that 6SL could block the infection at small incubation times.

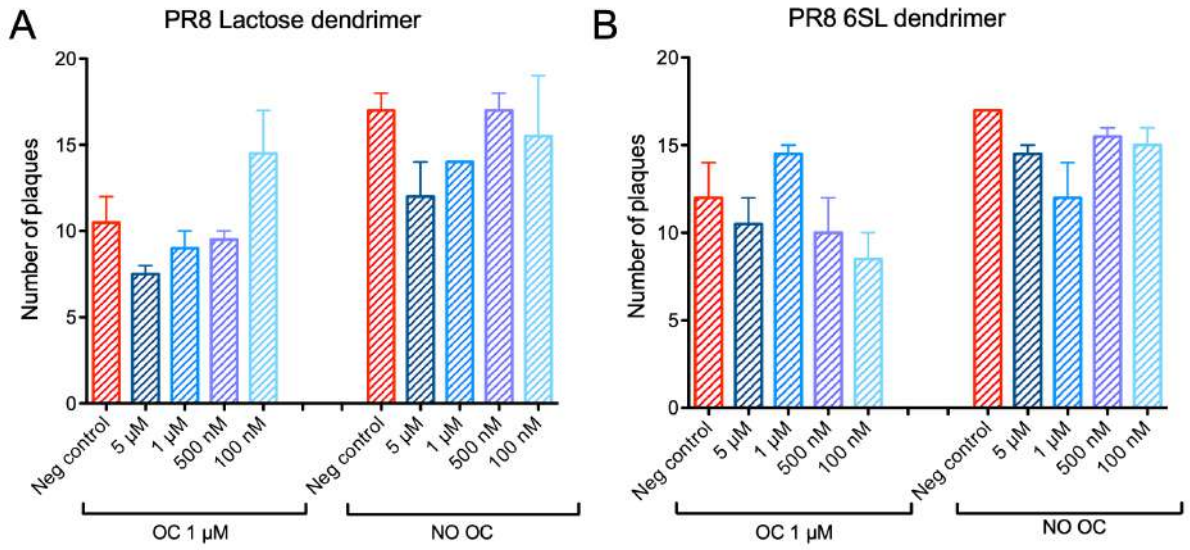

Figure 6.11: Number of plaques formed in the plaque assay. A) PR8 virus was treated with different concentrations (5 µM, 1 µM, 500 nM and 100 nM) of lactose dendrimer for 48 hour with Oseltamivir (OC) or without oseltamivir (NO OC). Plaques of the biological replicates were counted by hand and plotted. B) PR8 virus was treated with different concentrations (5 µM, 1 µM, 500 nM and 100 nM) of 6'-sialyllactose (6SL) dendrimer for 48 hours with Oseltamivir (OC) or without oseltamivir (NO OC). Plaques of the biological replicates were counted by hand and plotted. Negative control was influenza virus alone.

Taking into account these results, we could conclude that the 6SL dendrimers could not block the infection of influenza in the absence or presence of OC in both strains. The lack of inhibition is not due to a lack of binding to HA though, since the hemagglutination assays showed certain binding and blockage of HA (Figure 6.6) in short times of incubation. 6SL proved to be somehow interacting with HA in order to avoid the agglutination of erythrocytes but that interaction was not enough to block the infectivity of influenza in short incubation times.

We hypothesized that this lack of strong interaction could be due to a deficiency of homogeneity in the 6SL dendrimers synthetized. The IC50 of the dendrimers described by Kwon et al[19] varies dramatically with the number of 6SL molecules attached. When dendrimers had 20 molecules of 6SL the IC50 set around 3.4 µM but increasing the amount to 26 molecules per dendrimer, the IC50 increases up to 12 µM. This huge increase by a slightly modification of molecules of 6SL per dendrimer is due to the need of a certain distance of the sugars to obtain a successful multivalency effect, so they could match efficiently with each of the monomers of the HA trimer. A similar conclusion was obtained recently by Günther S.C et al[17], where they synthetized 6SL PAMAM dendrimers of generation 0 and 1 with only 8 6SL per dendrimer, proving that 6SL dendrimers could bind to HA by hemagglutination assay but having difficulties

in inhibiting in vitro infections, requiring high concentrations of PAMAM dendrimers (500 µM). Taking into account this information, we could assume that our dendrimers should have slightly less amount of 6SL and more evenly distributed to inhibit in vitro infections.

6.2.5 Super-resolution microscopy of interaction of influenza and dendrimers

Finally, we wanted to have an idea of how dendrimers and influenza virus binds to characterize the interaction seen in the hemagglutination inhibition assay. We knew that the protein HA from the strain PR8 interacted efficiently with 6SL dendrimers, but this interaction was not efficient enough to inhibit the infectivity of the virus, thus we decided to take advantage of the resolution obtained with super-resolution microscopy to visualize how dendrimers attach on infected cells to understand how efficiently 6SL dendrimers bind to the virus.

We selected dSTORM as super-resolution microscopy technique. As explained in chapter 1 and tested in chapter 2, Stochastic Optical Reconstruction Microscopy (dSTORM)[12] is a potent super-resolution microscopy technique that would allow us to analyse the spatial arrangements of 6SL dendrimers by using a total internal reflexion fluorescence microscopy (TIRF) and an oxide-reductive buffer to make dies blink.

For this purpose we incubated PR8 influenza particles with 300 nM of 6SL dendrimer for 30 minutes and then added to MDCK cells for 24 hours, leaving the influenza particles to infect the cell and the dendrimers interact with the newly synthetized virus. Further we fixed and immunostained the cells labelling influenza PR8 using serum against PR8 and alexa647 to have a view of where the virus is spread on the cell. Then we performed 2-colour dSTORM to identify the distribution of 6SL dendrimers that were labelled with Cy3.

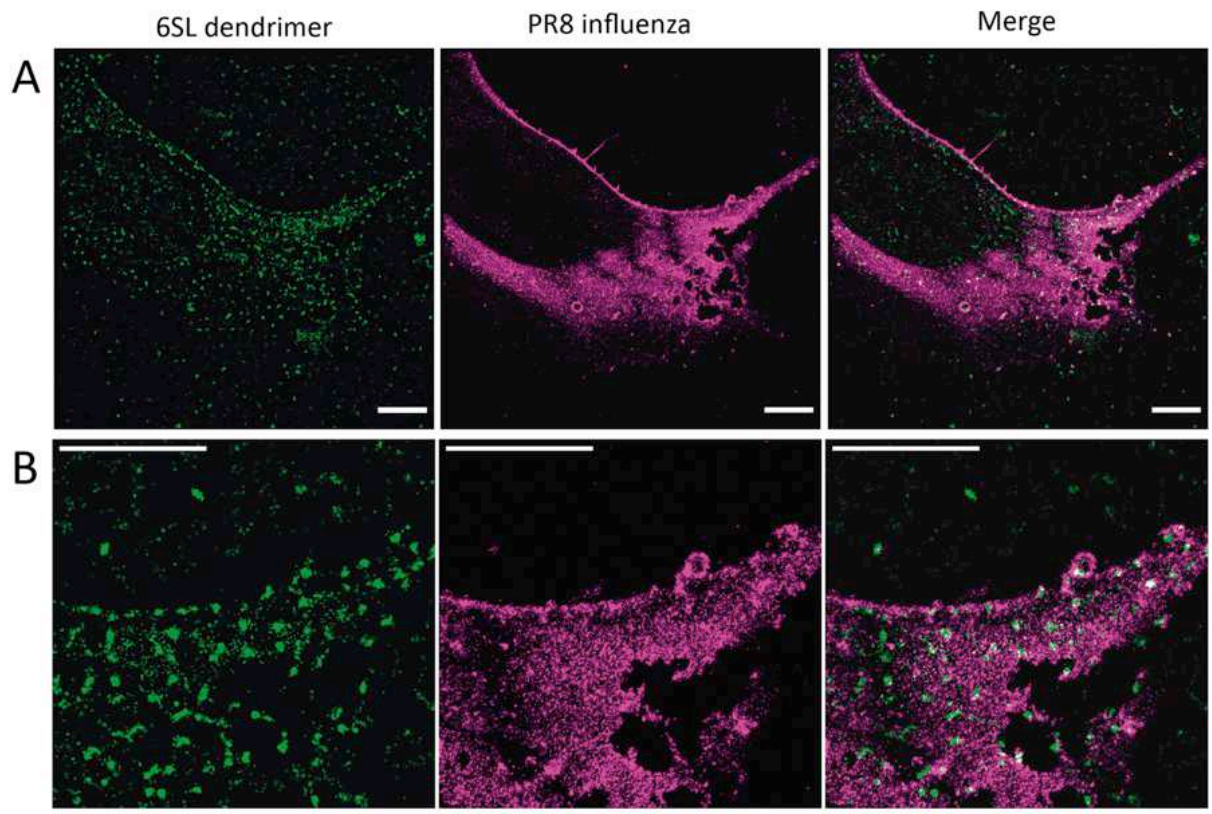

Figure 6.12: dSTORM microscopy image. MDCK cells infected with PR8 influenza and treated with 300 nM of 6SL dendrimer for 24 hours. A) Full cell. In green 6SL dendrimer, in magenta PR8 strain (serum). B) Close up of the membrane. In green 6SL dendrimer, in magenta PR8 strain (serum). Scale bar 5 μm.

In Figure 6.12 A, we could observe the molecular distribution of the dendrimers (green) on top of the cell infected with PR8 (magenta). Dendrimers were distributed evenly on top of infected areas, in small groups of small size (around 250 nm) but not covering all the influenza infection. These small agglomerates were bigger than the particle of influenza, which could explain why the interaction virus-dendrimer is not the expected. In the close-up image of the membrane area (Figure 6.12 B) it could be seen that on the slide there are some small aggregates of dendrimer but most of them are on the cell.

As a conclusion, thanks to these super-resolution images we could observe that even though 6SL dendrimer attached to the influenza on the cell, dendrimers did not cover all of it; instead, it aggregated in areas homogeneously on top of the cell. This could solve the doubt of why we could not inhibit influenza infection, since dendrimer did not attach properly to all HA available on the infected cell. At this concentration of the dendrimer (300 nM), influenza virus could infect the cell even though it interacts with 6SL dendrimer, since the dendrimer seems to aggregate in small cluster of around 250 nm, bigger than the influenza particle.

6.3 Conclusions and perspectives

In this chapter we studied the antiviral effect of 24-6SL dendrimer on 4 types of influenza virus strains, in order to characterize the affinity of the dendrimer towards different types of HA. The techniques applied to study the antiviral effects comprised several *in vitro* assays on infected cells with influenza and super-resolution image acquisition to describe the interaction of the dendrimer with the membrane on infected cells.

By performing plaque assays on MDCK cells we could observe that, in general, the infection of most influenza strains was not block by 6SL dendrimers. Likewise, 6SL dendrimers could not block the release of newly synthetized virus from infected cells, given by the formation of plaques with the same size in the control and the treated cells.

Udorn strain was the only strain that showed a small inhibition effect in the plaque formation, where the size of the plaques resulted was smaller than the negative control. Even though, using the hemagglutination inhibition assay we could observe that indeed 6SL dendrimers could successfully attach to the protein HA of PR8 and Udorn at low concentrations of dendrimers, especially in the presence of Tamiflu, a drug that inhibit the hydrolase activity of the protein NA.

Finally, thanks to super-resolution microscopy we could characterize that this binding was done in clusters of 250 nm of diameter, not covering the whole virus and attaching to infected cells in patches.

To sum up, 6SL dendrimers displayed a soft interaction towards Udorn and PR8, so we hypothesized that this soft interaction towards HA is not strong enough to block the viral interaction with the host, thus inhibiting the infectivity of the virus. We concluded that our dendrimers were not homogeneously synthesized enough to obtain the right distribution of 6SL among the dendrimer so it could not have a perfect interaction with the trimer HA, an essential parameter to fulfil the multivalency interaction. This synthesis must be optimized and control in order to develop better 6SL dendrimers, with the right ratio of sugars evenly distributed along the surface of the PAMAM dendrimers.

6.4 Materials and methods

6.4.1 Synthesis of 6SL PAMAM-dendrimer and Lactose PAMAM-dendrimer with Cy3

6.4.1.1 Synthesis of 6S and Lactose PAMAM-dendrimer

6'-Sialyllactose-PAMAM conjugate and lactose-PAMAM conjugate were prepared by a reductive amination of the aldehyde group of the reducing sugar in 6S (Carbosynth OS04396) or lactose (Sigma-Aldrich) with the amino groups of PAMAM dendrimers generation 4 (Sigma-Aldrich 412449). To produce this controlled reaction the protocol was adapted from reference[19]; 20 mg of PAMAM dendrimer G4 was mixed with 6SL or lactose in a molar ratio of 1:32 (PAMAM:sugar) in 0.1 M sodium borate buffer (50 mM NaCNBH pH 9.5) for 5 days in the dark with gentle shaking at RT. After the incubation time the dendrimers were filtrated using Amicon Ultra-0.5 centrifugal filters with molecular cutoff MWCO 3K (Milipore) at 14.000 g for 20 min 3 times to remove the unreacted reagents and to change the solvent to H_2Omq. After filtration, the solutions were freeze-dried and stored in the dark at -20ºC.

6.4.1.2 Analysis of ligands in 6S and Lactose PAMAM-dendrimer

The number of lactose and 6SL ligands attached to PAMAM dendrimer was determined using matrix-assisted laser desorption (ionization time-of-flight mass spectrometry (MALDI-TOF MS). MALDI-TOF MS was carried out using a 337 nm nitrogen laser. 2,5-Dihydroxybenzoic acid (10 mg/ml) in 50 % Acetonitrile was used as a matrix. The analyte-matrix solution (alpha-Cyano-4-hydroxycinnamic acid) was prepared at a ratio of 1:1 (analyte:matrix, v/v) in Water:ACN 1:1 and 0.1% Trifluoacetic acid (TFA) at 10 µg/ml. The analyte-matrix solution (1 µl) was deposited onto the sample plate and dried by vacuum evaporation. At lest 100 shots per spectrum were acquire using a linear positive-ion mode.

6.4.1.3 Ligation of Cy3 onto 6SL and lactose dendrimer

In order to visualize with super-resolution microscopy the dendrimer-virus interaction, PAMAM dendrimers were ligated with the dye Cy3 by adding 2.5 equivalents of Cy3 to a dilution of PAMAM dendrimer into a Sodium Bicarbonate buffer (pH 8.5) for 2 hours in the dark with soft stirring. After the incubation, the sample was purified by dialysis in PBS for 24 hours. To characterize the amount of Cy3 bound to the PAMAM dendrimers, we diluted the sample at 0.115 mM in H_2Omq and measured the Cy3 content with the Nanodrop ND-1000 Spectophotometer at 552 nm wavelength obtaining an average of 2.4-3 Cy3/Dendrimer.

6.4.2 Cell culture

For all the in vitro assays Madin-Darby Canine Kidney Cells (MDCK) cells were used. Cells were grown in Dulbecco's Modified Eagle medium (DMEM) medium supplemented with non-essential amino acids, 2 mM L-glutamine and 0.4 mM sodium pyruvate, 10% of fetal bovine serum (FCS) and 5% of antibiotics mix (ampicillin/streptavidin). Cells were seeded in a T-75 flask in order to keep cells growing at 37ºC in 5% CO_2. Once cells achieved 80-90% confluence, cells were washed with warm PBS 1x and treated with 1.5 ml 0.5% Trypsin-EDTA 10x (Gibco) for 10-15 min at 37ºC. After the detachment of cells, Trypsin was deactivated by adding 20 ml of DMEM with all the supplements. Cells were split at 1/60 dilution on a new T-75 flask for 4-5 days and kept at 37ºC in 5% CO_2.

6.4.3 Influenza culture

Influenza strains used in this work: Udorn: A/Udorn/72/H3N2; PR8: A/Puerto Rico/8/34/H1N1; Pdm09: A/Pdm09/H1N1; X31: A/X-31/H3N2. Virus strains were amplified on Madin-Darby canine kidney (MDCK) cells in serum-free DMEM supplemented with non-essential amino acids, 2 mM L-glutamine and 0.4 mM sodium pyruvate in presence of 2 µg/ml TPCK-treated trypsin (Sigma) at 37ºC in 5% CO_2. 96 hours after virus inoculation, the culture medium was collected and cell debris was removed by centrifugation for 10 min at 2,500 g at 4ºC, and the virus was pelleted from the supernatants by overnight centrifugation at 30,000 g at 4ºC. The pellet was resuspended in sterile 20% glycerol in PBS, aliquoted and stored at -80ºC until used.

6.4.4 Plaque assay

For plaque assay, MDCK cells must be fully confluent in a monolayer. For this reason, cells were seeded in high number the day before the assay. For 6 well plates, 500,000 cells were seeded, for 12 well plate 250,000 cells per well and for 24 well plate 120,000-150,000 cells per well.

For the experiments in Figure 6.10-11, prior the incubation of the dendrimer and the virus, the samples treated with oseltamivir (OC), virus dilution was incubated with 1 µM of oseltamivir for 30 min at 37ºC. Then, serial dilutions of dendrimer were incubated with the virus at a dilution of 20-50 plaque-forming units (PFU) for 30 min at 37ºC. For the positive control, serum against influenza (pure mouse serum) at 1/1000 dilution was incubated with the virus dilution. For the negative control free serum DMEM was used. After the incubation time, the mixture with the virus diluted was incubated with the monolayer of cells for 1 h at 37ºC in 5% CO_2.

Right after, for Figure 6.10-11 cells were washed thoroughly and for Figure 6.2-4 influenza-dendrimer mixture was kept; in each well it was added an overlay with Avicel RC-591 (FMC Biopolymer), serum free DMEM and Trypsin at final concentration of 0.6% of Avicel and 2 µg/ml of Trypsin. Cells were then incubated for 48 h at 37ºC in 5% CO_2 for 6 well plate. Avicel was subsequently removed and the cells were washed with 1x PBS and fixed with 4% PFA for 30 min at RT. After, permeabilization was performed incubating 0.5% TritonX-100 20 mM glycine in PBS for 5 min at RT and blocked with 1% BSA 0.05% Tween20 in BPS for 1h at RT.
Further the cells were stained with 1/5000 diluted convalescent serum anti-X47 (for Udorn and X31), anti-PR8 and anti-Pdm09 for 1 h at RT followed by donkey-anti-mouse IgG HRP-linked antibody (Santa Cruz Biotechnology, cat no. SC2020) for 1 h at RT with a gentle shaking. After washing with BSA-Tween mixture and 1x PBS, TrueBlue peroxidase substrate (KPL) was used for 30 min to visualize the plaques. The wells were photographed and the plaque size was determined using Image J Analysis Software.

6.4.5 Hemagglutination inhibition assay

For performing hemagglutination assays we prepared a ½ sequential dilution of the dendrimer, starting from 10 µM up to 0.312 µM in a U-bottom 96 well plate. In a new U-bottom well plate we prepared a ½ sequential dilution of each virus, starting from the stock of the virus up to 1/32 dilution. In the samples treated with oseltamivir (OC), virus dilution were incubated with 1 µM of oseltamivir for 30 min at 37ºC. Right after, in the plate, we added the dendrimer dilution in order into the influenza dilution in a ratio 1:1 to a final volume of 50 µl and we led incubate the mixture for 30 min at 37ºC. For the positive control, the virus was incubated only with PBS 1x. The negative control consisted only in PBS. In parallel it was tested the capacity of serums (pure mouse serum) against each strain at two different dilutions (1/500 and 1/1000) incubated for 30 min at 37ºC before the interaction with the erythrocytes.
After the incubation time, 50 µl of 1% red blood cell suspension was added to each well and led incubate for 15-20 minutes. Right after, a picture was taken to each plate.

6.4.6 Super-resolution images

6.4.6.1 Cell preparation and staining

MDCK cells were seeded at 3×10^3 cells per well in an 8 well µ-Slide (Cat. No. 80826, ibidi GmbH, Germany). Influenza at different PFU were incubated with either 6SL PAMAM dendrimer or lactose PAMAM dendrimer at concentration of 300 mM for 30 minutes prior to

the incubation with cells. 24 hours after infection, cells were then washed with PBS 1x and fixed with 4% paraformaldehyde (PFA) at room temperature for 20 min. The cells were blocked with 1% bovine serum albumin (BSA) solution in PBS for 1 hour at room temperature and stained at room temperature for 1 hour with 1/500 diluted convalescent mouse serum against A/Udorn/72. An Alexa Fluor 647 Donkey anti-Mouse IgG (1/600; Invitrogen) was used as fluorescently labeled secondary antibody. Then the cells were washed 3 times for 5 minutes with PBS. Subsequently, the cells were visualized under the super-resolution microscope.

6.4.6.2 dSTORM images acquisition

Immuno-stained samples were used to acquire dSTORM images. Cells that had been fixed and stained in ibidi® labteck slides were washed once with PBS, after which 300 µl of STORM buffer was added. The STORM buffer consists of an oxygen scavenging system (0.5 mg/ml glucose oxidase, 40 µg/ml Catalase), 5% w/v glucose and cysteamine 100 mM in PBS.

Images were acquired using a Nikon N-STORM 4.0 system configured for total internal reflection fluorescence imaging. Excitation inclination was tuned to adjust focus and to maximize the signal-to-noise ratio. Alexa-647 and WGA-568 fluorophores were excited by illuminating the sample with a 647 nm (160 mW) and 561 (80 mW) laser, respectively, built into the microscope. During acquisition the integration time was 10ms. For the measurements with Alexa-647 20,000 frames were acquired in the 647 channel. The total time required to acquire one image was about 5 min. For the measurements with WGA-568 40,000 frames were acquired in the 561 channel. The total time required to acquire one image was about 10 minutes. Fluorescence was collected by means of a Nikon x100, 1.4 NA oil immersion objective and passed through a quad-band-pass dichroic filter (97335 Nikon). Images were recorded onto a 256 x 256 pixel region (pixel size 160 nm) of a sCMOS camera (Hamamatsu). Single-molecule localization sequences were analyzed with the STORM plug-in of NIS element Nikon software.

6.5 References

1. Shen, X., Zhang, X. & Liu, S. Novel hemagglutinin-based influenza virus inhibitors. *J Thorac Dis* **5**, S149–S159 (2013).

2. Shi, Y., Wu, Y., Zhang, W., Qi, J. & Gao, G. F. Enabling the 'host jump': structural determinants of receptor-binding specificity in influenza A viruses. *Nature Reviews Microbiology* **12**, 822–831 (2014).

3. Rogers, G. N., Pritchett, T. J., Lane, J. L. & Paulson, J. C. Differential sensitivity of human, avian, and equine influenza A viruses to a glycoprotein inhibitor of infection: selection of

receptor specific variants. *Virology* **131**, 394–408 (1983).

4. Jeyaram, R. A., Radha, C. A., Gromiha, M. M. & Veluraja, K. Design of fluorinated sialic acid analog inhibitor to H5 hemagglutinin of H5N1 influenza virus through molecular dynamics simulation study. *J. Biomol. Struct. Dyn.* **38**, 3504–3513 (2020).

5. Yamabe, M., Kaihatsu, K. & Ebara, Y. Binding inhibition of various influenza viruses by sialyllactose-modified trimer DNAs. *Bioorg. Med. Chem. Lett.* **29**, 744–748 (2019).

6. Vanderlinden, E. & Naesens, L. Emerging antiviral strategies to interfere with influenza virus entry. *Med Res Rev* **34**, 301–339 (2014).

7. Sauter, N. K. *et al.* Hemagglutinins from two influenza virus variants bind to sialic acid derivatives with millimolar dissociation constants: a 500-MHz proton nuclear magnetic resonance study. *Biochemistry* **28**, 8388–8396 (1989).

8. Tj, P., R, B., U, R. & Jc, P. Recognition of monovalent sialosides by influenza virus H3 hemagglutinin. *Virology (Lond)* **160**, 502–506 (1987).

9. Reuter, J. D. *et al.* Inhibition of Viral Adhesion and Infection by Sialic-Acid-Conjugated Dendritic Polymers. *Bioconjugate Chem.* **10**, 271–278 (1999).

10. Lauster, D. *et al.* Multivalent Peptide–Nanoparticle Conjugates for Influenza-Virus Inhibition. *Angew Chem Int Ed Engl* **56**, 5931–5936 (2017).

11. Ogata, M. *et al.* Synthesis of multivalent sialyllactosamine-carrying glyco-nanoparticles with high affinity to the human influenza virus hemagglutinin. *Carbohydr Polym* **153**, 96–104 (2016).

12. Zhang, Z. *et al.* Influenza-binding sialylated polymer coated gold nanoparticles prepared via RAFT polymerization and reductive amination. *Chem. Commun.* **52**, 3352–3355 (2016).

13. Hendricks, G. L. *et al.* Sialylneolacto-N-tetraose c (LSTc)-bearing liposomal decoys capture influenza A virus. *J. Biol. Chem.* **288**, 8061–8073 (2013).

14. Terabayashi, T., Morita, M., Ueno, M., Nakamura, T. & Urashima, T. Inhibition of influenza-virus-induced cytopathy by sialylglycoconjugates. *Carbohydrate Research* **341**, 2246–2253 (2006).

15. Gambaryan, A. S. *et al.* Polymeric inhibitor of influenza virus attachment protects mice from experimental influenza infection. *Antiviral Research* **55**, 201–205 (2002).

16. Bandlow, V. *et al.* Sialyl-LacNAc-PNA·DNA concatamers by rolling circle amplification as multivalent inhibitors for Influenza A virus particles. *Chembiochem* (2018) doi:10.1002/cbic.201800643.

17. Günther, S. C. *et al.* Antiviral potential of 3'-sialyllactose- and 6'-sialyllactose-conjugated dendritic polymers against human and avian influenza viruses. *Sci Rep* **10**, 768 (2020).

18. Mhlwatika, Z. & Aderibigbe, B. A. Application of Dendrimers for the Treatment of

Infectious Diseases. *Molecules* **23**, (2018).

19. Kwon, S.-J. *et al.* Nanostructured glycan architecture is important in the inhibition of influenza A virus infection. *Nat Nano* **advance online publication**, (2016).

20. Esfand, R. & Tomalia, D. A. Poly(amidoamine) (PAMAM) dendrimers: from biomimicry to drug delivery and biomedical applications. *Drug Discovery Today* **6**, 427–436 (2001).

21. Pedersen, J. C. Hemagglutination-Inhibition Assay for Influenza Virus Subtype Identification and the Detection and Quantitation of Serum Antibodies to Influenza Virus. in *Animal Influenza Virus* 11–25 (Humana Press, New York, NY, 2014). doi:10.1007/978-1-4939-0758-8_2.

22. Klimov, A. *et al.* Influenza Virus Titration, Antigenic Characterization, and Serological Methods for Antibody Detection. in *Influenza Virus: Methods and Protocols* (eds. Kawaoka, Y. & Neumann, G.) 25–51 (Humana Press, 2012). doi:10.1007/978-1-61779-621-0_3.

23. Ranadheera, C. *et al.* Reduction of Neuraminidase Activity Exacerbates Disease in 2009 Pandemic Influenza Virus-Infected Mice. *J Virol* **90**, 9931–9941 (2016).

24. Anders, E. M., Hartley, C. A. & Jackson, D. C. Bovine and mouse serum beta inhibitors of influenza A viruses are mannose-binding lectins. *Proc. Natl. Acad. Sci. U.S.A.* **87**, 4485–4489 (1990).

Chapter 7: Super-resolution imaging of antigen-nanoparticle uptake by dendritic cells for immunization

This chapter exposes the work performed in collaboration with Dr. Maruthi Prasanna from the group of "Natural polymers and biomimetics group" directed by Dr. Noemí Csaba from the Center for Research in molecular medicine and chronic disease (CiMUS) and Universidad de Santiago de Compostela. Dr. Prasanna developed the antigen-nanoparticles and my work consisted on perform the imaging of the internalization of the antigen-nanoparticles by dendritic cells using super-resolution microscopy. This work was part of the PhD thesis of Dr. Maruthi Prasanna, entitled "Preparation and characterization of antigen loaded chitosan nanoparticles for immunization" by the Universidad de Santiago de Compostela (2020).

7.1 Introduction

Chapter 1 exposed the main strategies for vaccine development against influenza virus. The inactivation of the viral particle or the split of the envelope are the main strategies for viral vaccine production[1,2] and in terms of vaccine development against bacteria, the industry follows similar strategies including other elements e.g. toxoids (bacterial toxics inactivated) or sugars in the vaccine formulation among other adjuvants[3].

In the development of full protection against bacteria we can find the same drawback that we found in the viral vaccine development: lack of full protection against all bacterial serotypes, which usually is translated in the increase of the amount of antibiotic-resistant non-vaccinate variants[4], due to the selective pressure the non-vaccinate variants receive. This problematic contributes in the difficulty of the development of protection against some bacteria such as *Streptococcus pneumoniae*[5,6], cause of an estimated 2.6 million deaths worldwide in 2017[7].

An interesting approach for vaccine improvement is the development of polysaccharides vaccines, consisting on using the same sugars that cover the bacteria to boost the immune system acting as bacterial antigen[8,9]. These sugars would be internalized by dendritic cells (DCs) in order to create immune response in the system. DCs are antigen-presenting cells and their main role is to uptake and process antigenic materials to present them on their surface (using

their major histocompatibility complex MHC) so they could be identify by T-cells, generating cellular and humoral responses[10].

The most promising polysaccharide vaccines are glycoconjugate (GC) vaccines, prepared by coupling different polysaccharides moieties into a carrier made of proteins[11]. Despite their main advantages, these GC vaccines are always in need of development and improvement[12], specially regarding the coupling of the polysaccharides and the carrier, since the uptake of these sugar moieties by DCs is essential to create a successful immune response[13].

Given the current trends in drug delivery and nanotechnology, novel carriers are under development to improve the internalization of GC moieties. In this field, chitosan nanoparticles have been proposed as drug delivery cargo, vaccines adjuvant and insulin delivery system[14-16]. Chitosan is an abundant non-toxic, biocompatible and biodegradable polysaccharide with antimicrobial activity and non-soluble in water[17], easily mouldable to produce nanoparticles by different methods[18]. Taking this into account, chitosan nanoparticles are easily conjugated covalently with different antigens and semisynthetic GCs that could boost the DCs uptake and antigen presentation[16,18,]. Thus, the use of chitosan as cargo for GCs could protect the antigen from degradation and promote the uptake by DCs to activate the humoral and cellular response by T-cells.

In theory these chitosan nanoparticles with semisynthetic GC (GC-CNPs) should interact with the cells and enter DCs in a regular drug delivery pathway, but due to the small size of the particles is almost impossible to track the nanoparticle pathway inside the cells, to make sure that the GC-CNPs and the DCs are interacting properly and the antigen is being exposed on MHC. As explained in detail in previous chapters, super-resolution microscopy is a powerful microscopy technique that could overcome the diffraction limit and study nanoparticle distribution inside cells[19,20], thus could be a great implementation in the study of the interaction and internalization of these “nanovaccines” by dendritic cells.

For this purpose, in this chapter we used dSTORM imaging to characterize the uptake of GC-CNPs bound to the dye Cy5 by dendritic cells, using both DC 2.4 or human monocyte-derived dendritic cells (MoDCs) at different conditions and time points. By this super-resolution approach we could image the interaction and internalization of GC-CNPs in different layers of the dendritic cells, in order to identify the pathway that they follow prior internalization at different time points and under several incubation parameters.

7.2 Results and discussion

7.2.1 Internalization of Cy5-GC-CNPs in MoDCs

Firstly, we studied the internalization of GC-CNPs labelled with Cy5 by human monocytes-derived dendritic cells (MoDCs) at different time points. Right after all the incubation time of all the time points (0.5, 1, 2 and 4 hours), cells were fixed and the membrane of the cells was stained using Alexa488- Wheat Germ Agglutinin (WGA) to identify if the GC-CNPs crossed the membrane or not. Further, 2 colour super-resolution images were acquire, using the dye Cy5 for locating the GC-CNPs.

Figure 7.1 displays the 2 colour-images obtained, showing the internalization of the GC-CNPs by MoDCs with time. As observed in the figure, each cell was imaged at two different planes: middle and top (0.5 µm thick), with the purpose of recognize whether GC-CNPs stayed attached to the membrane (top) or internalized (middle). In green we can observe the cell membrane and the red dots represent the nanoparticles presented inside or outside MoDCs. Observing the images from 0.5 h to 4 h, we could detect a slight gradual increase in the uptake of nanoparticles with time, however, the internalization was not very strong, noticing lots of presence of nanoparticles on top of the cells and on the outside of the membrane at each time point, leading us to believe that internalization is a slow process that requires more incubation time.

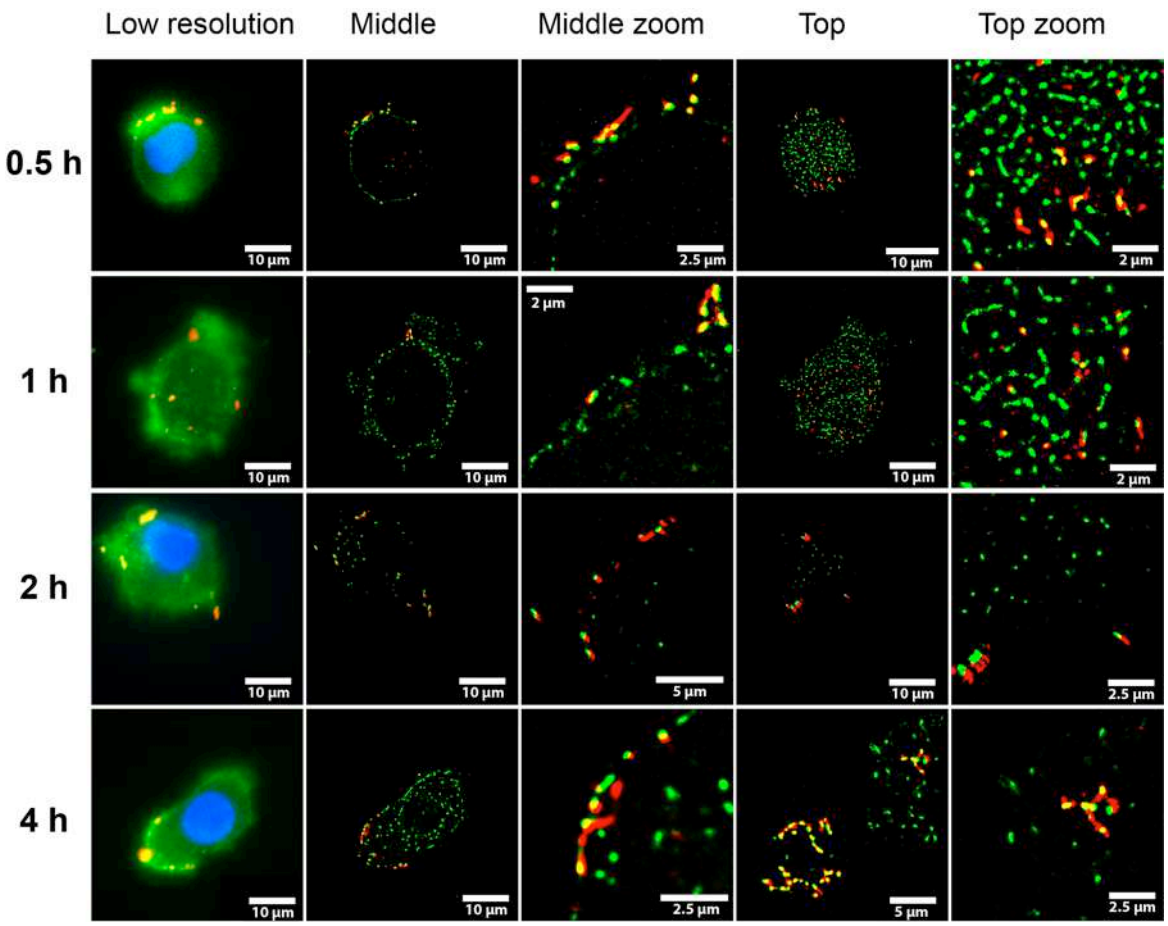

Figure 7.1: Super-resolution images of the internalization of Cy5-GC-CNPs (50 µg/million cells) by MoDCs cells at different time points (0.5h, 1h, 2h and 4h). Low-resolution image displayed the fluorescence microscopy images from the nucleus (DAPI, blue), the cell membrane (WGA-488, green) and the Cy5-GC-CNPs (Cy5, red). Super-resolution images displayed two cell fields: middle and top.

Then, to test this possibility we incubated the GC-CNPs at 24 h on MoDCs and we also performed two different controls. One control consisted on incubating the nanoparticles during 24h but at 4ºC, in order to inhibit the endocytosis, and the second control without any nanoparticle. In Figure 7.2 we could observe that after long incubation times (24h) the nanoparticle uptake was significantly higher, with MoDCs cells full of GC-CNPs on the inside.

On the other hand, the control consisting on 24h incubation at 4ºC displayed a lack of nanoparticles both on the inside and on the outside, indicating that NPs internalized by the endocytic pathway, since low temperatures did not permitted the uptake of NPs by the cell. The lack of nanoparticles attachment on the membrane could be due to the long incubation time, which revealed a lack of strong and durable interaction between the membrane and the GC-CNPs.

Finally, the negative control did not display any signal, demonstrating that the signal observed in the channel 647 in the samples prepared with GC-CNPs was given by the Cy5 of the GC-CNPs and not due to auto-fluorescence or residual noise from the fixation method.

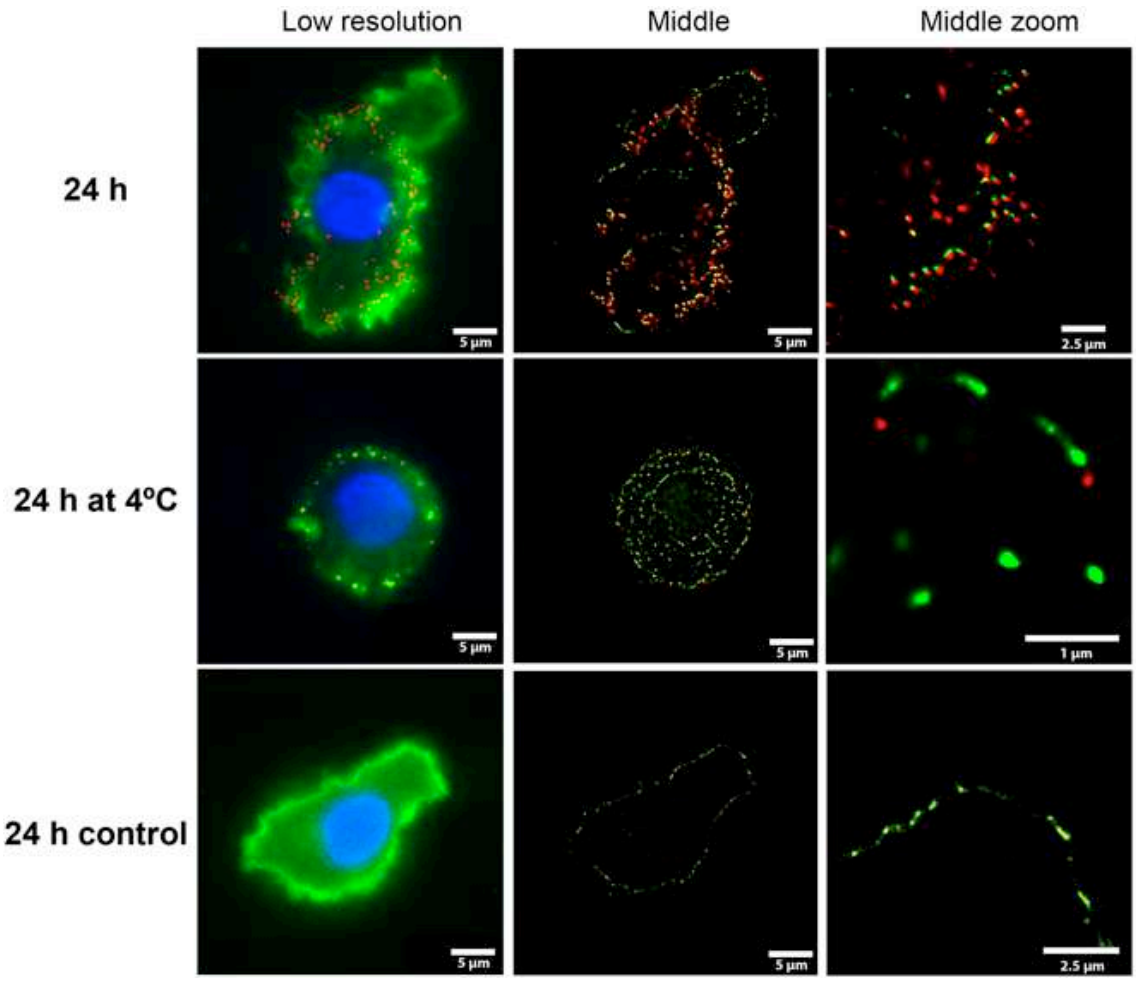

Figure 7.2: Super-resolution images of the internalization of Cy5-GC-CNPs (50 µg/million cells) by MoDCs cells at different time points and conditions (24h at 37ºC, 24h at 4ºC) as well as a negative control without Cy5-GC-CNPs. Low-resolution image displayed the fluorescence microscopy images from the nucleus (DAPI, blue), the cell membrane (WGA-488, green) and the Cy5-GC-CNPs (Cy5, red).

Altogether, we could conclude that these GC-CNPs could interact successfully with human DCs. The uptake of chitosan nanoparticles by MoDCs was dependent on the temperature and time, where the strongest internalization of NPs was performed after continuous incubation for 24h and at 37ºC, since is dependent on endocytosis.

7.2.2 Internalization of GC-CNPs on DC2.4 cell line at different time points

Next, we wanted to test if the internalization could be successfully performed with different incubation conditions. For this purpose, we perform internalization assays using the immortal DC2.4 cell line. DC 2.4 is a dendritic cell line obtained from mouse and easily cultured in the lab, which would allow us to play more with the conditions of the incubation with GC-CNPs without artefacts in the cell culture.

Firstly, we followed a similar approach as before, incubating the cells with a constant concentration of GC-CNPs (0.5 µg/ml) and fixing them after different incubation times (0.5 h, 1 h, 2 h and 24). The Figure 7.3 displays the cells incubated with short incubation times (0.5, 1h and 2h), exhibiting a rapid and strong internalization of the GC-CNPs, faster than the internalization observed in MoDCs. After just 0.5 h of incubation a robust presence of nanoparticles was observed perfectly in the middle plane of the cell, so strong that it was even easily observed in low resolution.

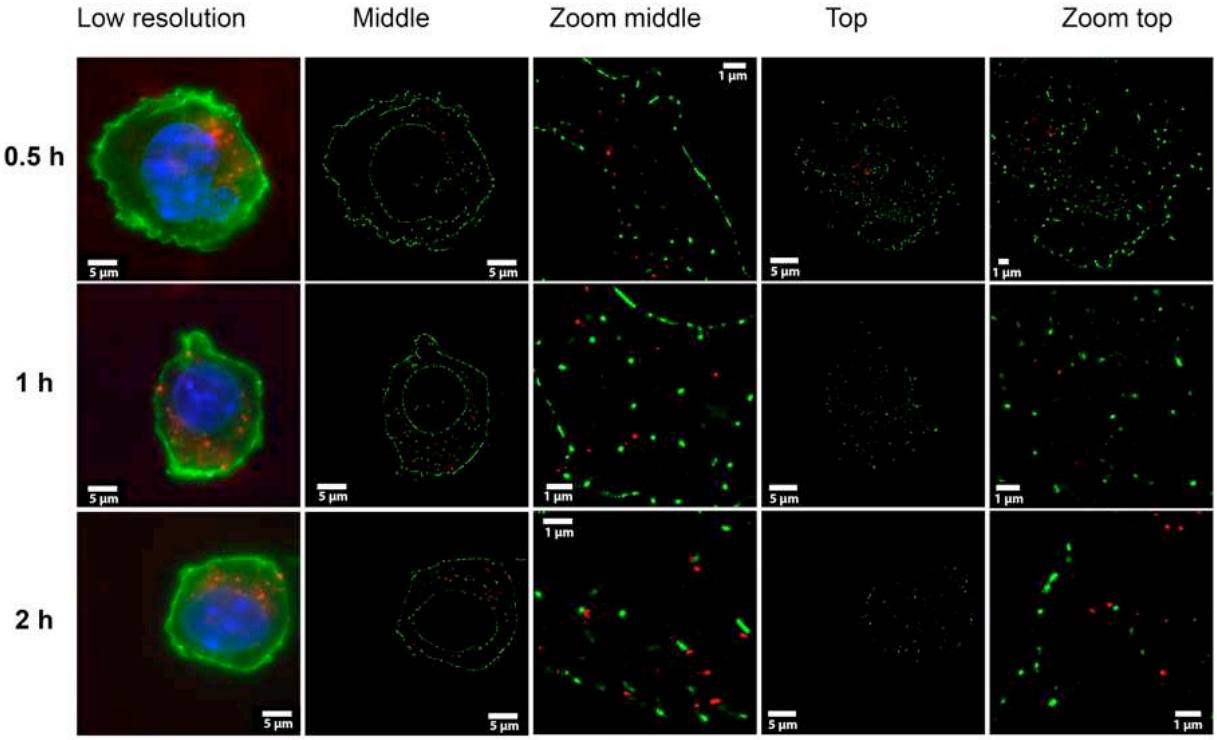

Figure 7.3: Super-resolution images of the internalization of Cy5-GC-CNPs (0.5 µg/ml) by DC2.4 cells at different time points (0.5h, 1h and 2h). Low-resolution image displayed the fluorescence microscopy images from the nucleus (DAPI, blue), the cell membrane (WGA-488, green) and the Cy5-GC-CNPs (Cy5, red). Super-resolution images displayed two cell fields: middle and top.

In this case, the amount of NPs inside the cell increased with time, not observing any rest of NPs on the outside of the cell membrane after just 2 hours of incubation. Studying the internalization with longer incubation times (Figure 7.4), we could confirm how strongly DC 2.4 cells internalized these GC-CNPs with long incubation periods. After 24 hours of continuous incubation the cell was fully filled with NPs that kept internalizing during the whole 24 hours of incubation.

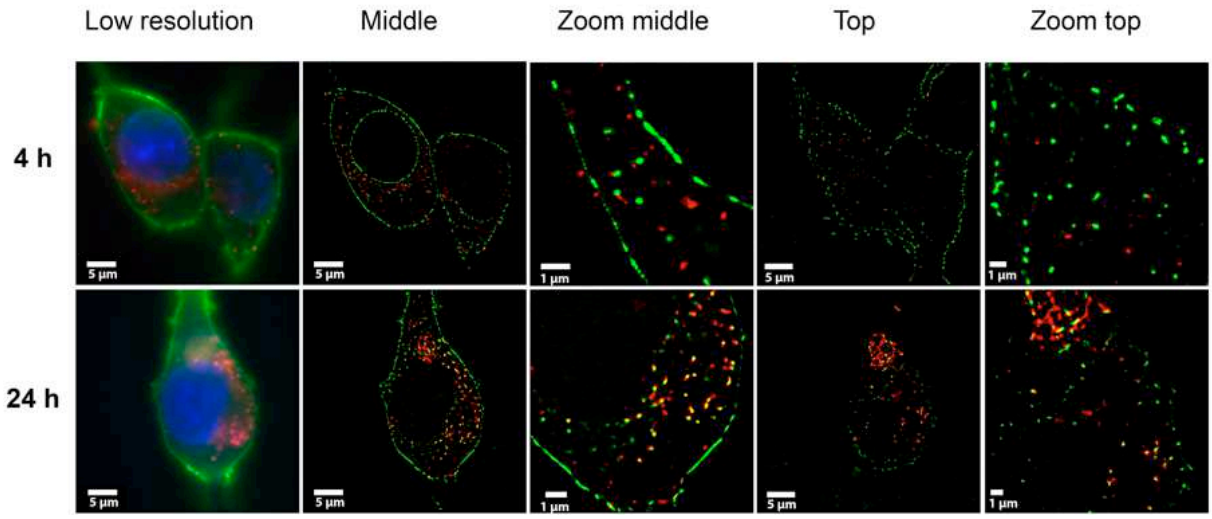

Figure 7.4: Super-resolution images of the internalization of Cy5-GC-CNPs (0.5 µg/ml) by DC2.4 cells at different time points (4h and 24h). Low-resolution image displayed the fluorescence microscopy images from the nucleus (DAPI, blue), the cell membrane (WGA-488, green) and the Cy5-GC-CNPs (Cy5, red). Super-resolution images displayed two cell fields: middle and top.

After long incubation times it was not possible to observe any rest of NPs on the membrane, concluding that GC-CNPs internalized very fast in DC 2.4 cells and that a continuous incubation led to an increased in the internalization of NPs. All in all, although DC 2.4 behaved similarly to MoDCs, it showed a better uptake efficiency of NPs.

In general, the increased presence of NPs in the cytoplasmic was due a continuous incubation of the nanoparticles with the DC 2.4 cells, so to unveil the fate of the NPs once were internalized, we incubated the DC 2.4 cells with GC-CNPs only for 1 hour, to be further fixed (1h) or washed and incubated at 37ºC at two time points: 4 h and 24 h. Also we tested the internalization of the nanoparticles at higher concentrations (0.5 µg/ml and 2.5 µg/ml).

In Figure 7.5 we could observe how cells internalized the NPs after just 1 hour of incubation (1h), containing several NPs in the cytoplasm and few of them on the membrane. After 4 hours, the NPs that were internalized prior that first hour of incubation were mainly present inside the cell, demonstrating that the NPs that remained on the cell surface were internalized completely. Surprisingly, an increased in the NPs concentration (2.5 µg/ml) did not result in a strong increment in the nanoparticle internalization.

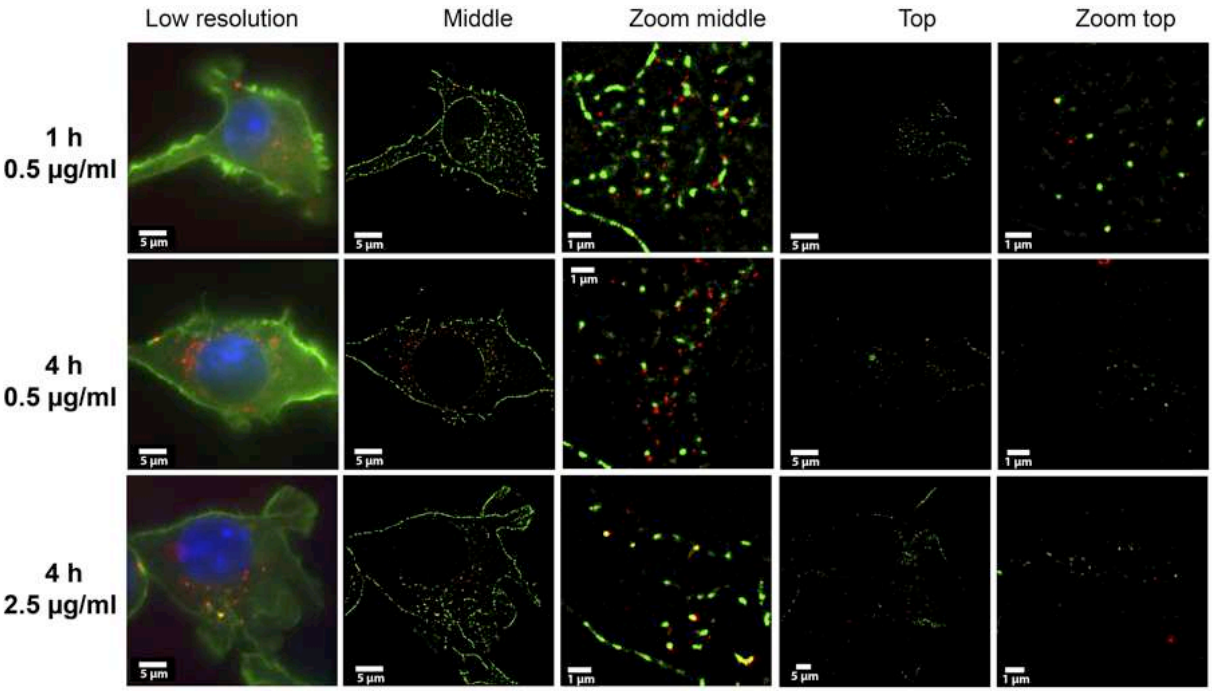

Figure 7.5: Super-resolution images of the internalization of Cy5-GC-CNPs at two different concentrations (0.5-2.5 µg/25.000 cells) by DC2.4 cells incubated for 1h and then washed, followed by a final incubation time (4 h). Low-resolution image displayed the fluorescence microscopy images from the nucleus (DAPI, blue), the cell membrane (WGA-488, green) and the Cy5-GC-CNPs (Cy5, red). Super-resolution images displayed two cell fields: middle and top.

However, at 24 h (Figure 7.6) the concentration of NPs inside the cytoplasm of the cells had decreased dramatically, suggesting that the internalized NPs were processed by the cell machinery between 4h and 24h post incubation. As observed before, in this case the increased of concentration of NPs did not produce an sensitive increased in the uptake of GC-CNPs by DC 2.4 cells, confirming that the increased in the concentration of the NPs did not produce an increased in the internalization.

Overall, we could conclude that GC-CNPs were internalized after just 1 hour of incubation with the cells. Right after, between 4h and 24h after the uptake, NPs started to being processed, releasing their glycoconjugates, presumably to be exposed on the MHC of the dendritic cells.

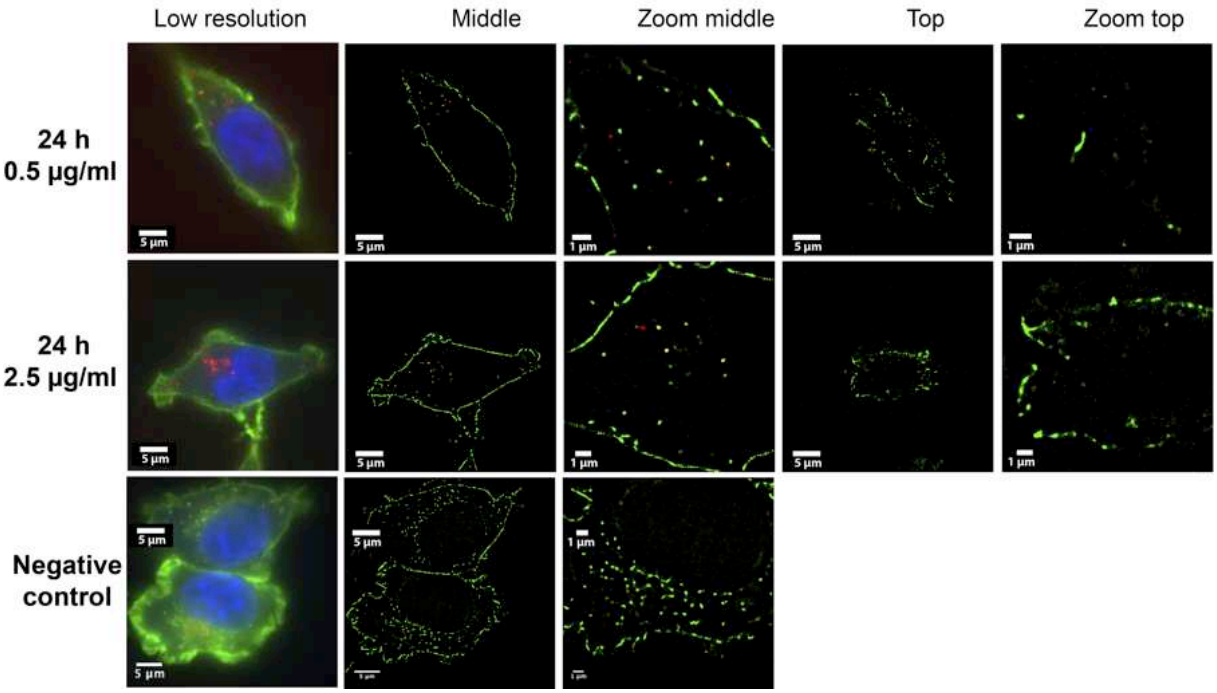

Figure 7.6: Super-resolution images of the internalization of Cy5-GC-CNPs at two different concentrations (0.5-2.5 µg/25.000 cells) by DC2.4 cells incubated for 1h and then washed, followed by a final incubation time (24 h). The negative control was performed without any incubation with GC-CNPs. Low-resolution image displayed the fluorescence microscopy images from the nucleus (DAPI, blue), the cell membrane (WGA-488, green) and the Cy5-GC-CNPs (Cy5, red). Super-resolution images displayed two cell fields: middle and top.

7.2.3 Characterization of GC-CNPs endosomal pathway on DC2.4 cell line

Finally, to study in detail the endosomal uptake of the NPs observed in the previous experiment, we performed an immunostaining against the lysosome glycoprotein (Lamp2) in order to co-localize the presence of GC-CNPs (labelled with Cy5) and the lysosomes (labelled with Alexa-488). In this case, we incubated the DC 2.4 cells with the higher concentration of NPs (2.5 µg/ml) for 1 hour, and then we washed the cells and fixed them after 3 hours.

Figure 7.7 displays the images obtained of the negative control (untreated) and the treated cells. The untreated cells verified the immunostaining against Lamp2 and showed how the lysosomes are displayed along the cell (green dots). Paying attention to the two cells treated, we could

observe a lack of co-localization between the NPs and Lamp2. In concrete, the NPs internalized were not located on top of the late endosomes, illustrating a lack of interaction between both structures. These data opposes to the literature, which showed that chitosan coated nanoparticles were delivered thought the endocytic pathway, from early to late endosomes[21,22].

Hence, observing the results obtained and displayed in Figure 7.7 we hypothesized that GC-CNPs were escaping the endosomes in an early stage by endosomal scape. Taking into consideration the lack of replicates in this experiment, we could not conclude that chitosan NPs were not following the endocytic pathway as it was suggested in the literature and in our prior experiment, where we proved that inhibiting the active internalization of NPs at 4ºC led to a decreased presence of NPs inside the cytoplasm (Figure 7.2).

On the other hand, could be interesting, as a perspective of this study, to track the internalization of NPs with dSTORM in combination with different blockers of the endosomal pathway, to further confirm the pathways involved in the internalization and degradation of GC-CNPs.

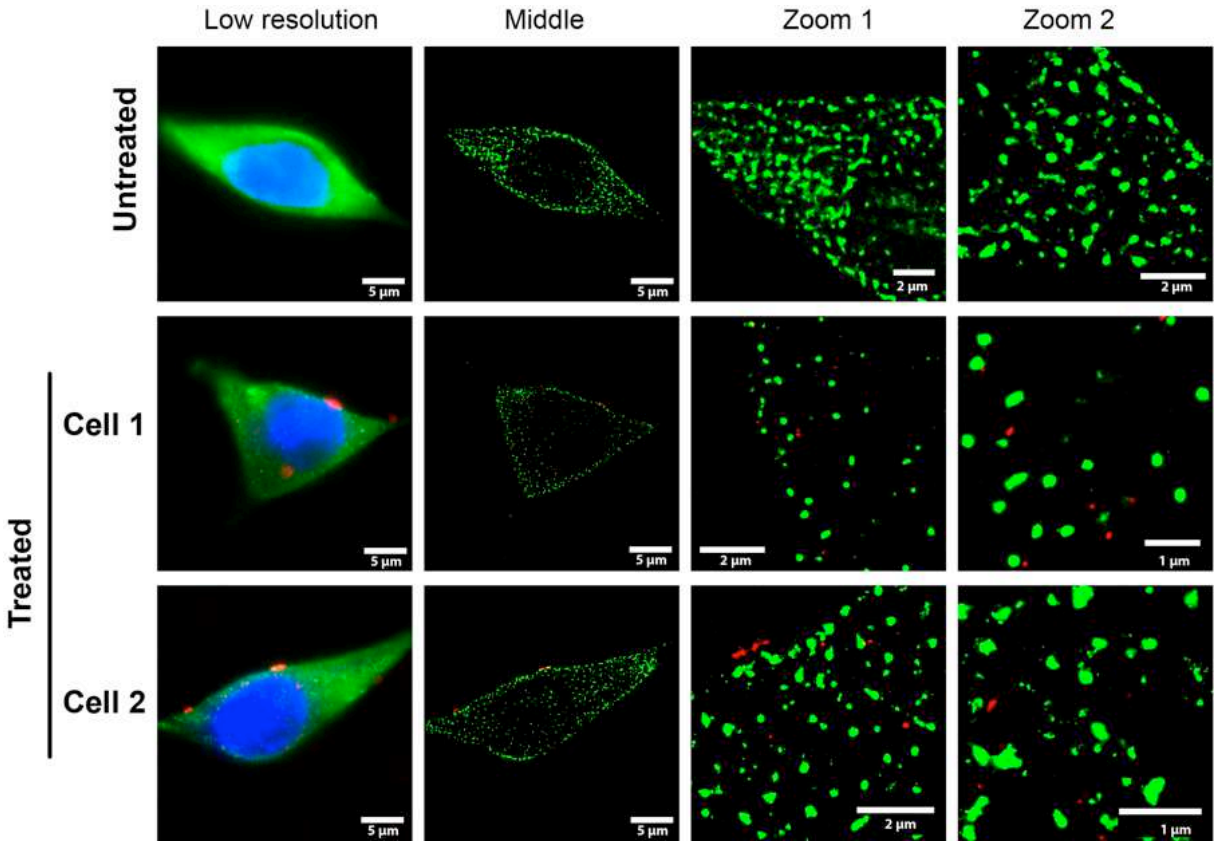

Figure 7.7: Super-resolution images of the endosomal uptake of Cy5-GC-CNPs by DC2.4 after 1h of pulse incubation (2.5 µg/ml) and 3h of post-incubation at 37ºC. The endosomes were stained with anti-Lamp2 (Alexa-488, green), the nucleus with DAPI (blue) and the nanoparticles with Cy5 (red).

To sum up, in this preliminary experiment we could not co-localize late endosomes or lysosomes with the GC-CNPs internalized by DC 2.4 cells. This deficiency in co-localization could not be an indication of a lack of endocytic uptake of the nanoparticles, due to the absence of replicates performed in this experiment. All in all, combining the immunostaining against components of the endocytic pathway and the labelling of NPs was an interesting approach to research the mechanisms of uptake and degradation of the GC-CNPs once are internalized by dendritic cells.

7.3 Conclusions

In this chapter we applied super-resolution imaging with dSTORM to study the internalization mechanism of nanovaccines by dendritic cells. By testing different conditions, incubation time points and approaches we could obtain a general picture of how chitosan nanoparticles are interacting with dendritic cells and how long did they take to internalized and degraded inside the cytoplasm.

In general, NPs interacted rapidly with the DCs, which led to their internalization after just 30 min-1 hour of interaction. This internalization continued in time, increasing enormously the amount of NPs inside the cytoplasm after 24 hours of continue incubation. In addition, between 4 hours and 24 hours post internalization, chitosan nanoparticles were starting to be degraded in the cytoplasm, presumably to expose their glycoconjugates to the MHC of the dendritic cells. When we tried to observe the co-localization of late endosomes and GC-CNPs we could not conclude if the NPs tested followed an endocytic pathway or not, presumably due to a lack of replicas of the experiment. All in all, the inhibition of the active uptake of nanoparticles at 4ºC displayed a lack of internalization of nanoparticles, proving that NPs were initially entering the cells by endocytic mechanisms.

Overall, dSTORM images were effectively used to examine the interaction of the GC-CNPs with DCs, proving how the increased in resolution could lead into a better understanding of the nanoparticle journey inside dendritic cells. With this new approach we could further continue inquire in the utility of chitosan nanoparticles as nanovaccine to reinforce the immune system against bacteria.

7.4 Materials and methods

7.4.1 Cell line preparation

Dendritic cells (DC2.4 cells) were cultured in RPMI 1640 medium that was supplemented with 10% fetal bovine serum (FBS) and 1/100 dilution of 5,000 U/ml of penicillin/streptomycin (Sigma) antibiotics.

Monocyte-derived dendritic cells (MoDCs) were prepared by Dr. Maruthi Prasanna at CiMUS.

7.4.2 Labelling of chitosan nanoparticles

The development, synthesis and purification of the glycoconjugate encapsulated on chitosan nanoparticles (GC-CNPs) were performed by Dr. Maruthi Prasanna.

The preparation of the GC-CNPs was performed following the work of Calvo P. et al.[23], using the ionic gelation technique. After the synthesis and purification of chitosan, 50 mg of Chitosan was dissolved in 5 ml of H_2Omq. Following, 1 mg of Cyanine (Cy5) was dissolved in 0.3 ml of dimethyl sulfoxide (DMSO) and added to the chitosan solution and stirred for 16h at RT in the dark.
Subsequent the incubation time, the labelled chitosan was purified with PD10 columns (Centri Pure P10, Zetadex Gel Filtration), measuring the final yield of the reaction by freeze-dried the product. The final labelling of GC-CNPs was performed by adding 2% of Cy5-labelled chitosan to the final mixture during the synthesis of the CNPs.

7.4.3 Internalization studies of GC-CNPs on dendritic cells (MoDCs and DC 2.4)

7.4.3.1 Internalization of GC-CNPs in MoDCs

MoDCs were plated at $5x10^5$ cells per well into a 24 well plate with 0.5 ml of R10 medium. Right after, cells were incubated with the Cy5 labelled GC-CNPs at a concentration of 50 µg/million cells for different periods of time: half an hour (0.5 h), 1 h, 2h, 4h and 24h. Following each incubation time, the DCs were washed once with warm PBS and fixed with paraformaldehyde (PFA) 4% for 15 min.

To performed super-resolution images of the cells, cells were placed in 8-well glass-bottom Nunc lab-tek (Thermofisher 155411PK). Firstly, the membrane of the treated DCs was stained with Wheat Germ Agglutinin (WGA) labelled with Alexa 488 at 0.2 µg/ml, while the nucleus was stained with DAPI 1 µg/ml for 5-10 minutes. Once the DCs were washed twice with PBS, cells were suspended in 30 µl of STORM buffer. The STORM buffer consists of an oxygen scavenging system (0.5 mg/ml glucose oxidase, 40 µg/ml Catalase), 5% w/v glucose and cysteamine 100 mM in PBS just before imaging with dSTORM.

7.4.3.2 Internalization of GC-CNPs in DC2.4 cell line

DC2.4 cells were seeded at 25,000 cells/well on Nunc Lab-Tek plates with 0.2 mL of RPMI media. Following, cells were incubated with the Cy5 labelled GC-CNPs (0.5 µg of NPs) at

different time periods (0.5, 1, 2, 4 and 24h). After the incubation time, the DCs were washed with PBS and fixed with 4% PFA for 15 min.

For imaging, cells were stained with DAPI (1 μg/ml) and WGA Alexa-488 (0.2 μg/ml) for 10 min, washed twice with PBS and resuspended in STORM buffer prior imaging.

7.4.3.3 Pulse incubation of GC-CNPs in DC2.4 cell lines

DC2.4 cells were seeded at 25,000 cells/well on Nunc Lab-Tek plates with 0.2 mL of RPMI medium. Following, cells were incubated with the Cy5 labelled GC-CNPs (0.5 and 2.5 μg of NPs) and incubated at 37ºC for 1h. After the incubation time, the DCs were washed with PBS and replaced with RPIM medium and incubated at 37ºC. Following, at different time points (1, 4 and 24h), cells were fixed with 4% PFA for 15 min.

For imaging, cells were stained with DAPI (1 μg/ml) and WGA Alexa-488 (0.2 μg/ml) for 10 min, washed twice with PBS and resuspended in STORM buffer prior imaging.

7.4.3.4 Endosomal tracking of GC-CNPs in DC2.4 cell lines

DC2.4 cells were seeded at 25,000 cells/well on Nunc Lab-Tek plates with 0.2 mL of RPMI medium. Following, cells were incubated with the Cy5 labelled GC-CNPs (2.5 μg of NPs) and incubated at 37ºC for 1h. After the incubation time, the DCs were washed with PBS and replaced with RPIM medium and incubated at 37ºC. 4h post-incubation cells were fixed with 4% PFA for 15 min.

For imaging, cells were stained with DAPI (1 μg/ml) and rabbit anti-lamp2 primary antibody (1/1000 on BSA 1% for 1h) followed by secondary anti-rabbit Alexa-488 (Sigma; 1/500 on BSA 1% for 1h). Further immunostaining, cells were washed twice with PBS and resuspended in STORM buffer prior imaging.

7.4.4 Super-resolution imaging with dSTORM

Images were acquired using a Nikon N-STORM 4.0 system configured for total internal reflection fluorescence imaging. Excitation inclination was tuned to adjust focus and to maximize the signal-to-noise ratio. Alexa-647, WGA-488 and Alexa-488 fluorophores were excited by illuminating the sample with a 647 nm (160 mW) and 488 (80 mW) lasers,

respectively, built into the microscope. During acquisition the integration time was 10ms. For the measurements with Alexa-647 20,000 frames were acquired in the 647 channel. The total time required to acquire one image was about 3 min. For the measurements with WGA-488 20,000 frames were acquired in the 488 channel. The total time required to acquire one image was about 3 minutes.

Fluorescence was collected by means of a Nikon x100, 1.4 NA oil immersion objective and passed through a quad-band-pass dichroic filter (97335 Nikon). Images were recorded onto a 256 x 256 pixel region (pixel size 160 nm) of a sCMOS camera (Hamamatsu). Single-molecule localization sequences were analysed with the STORM plug-in of NIS element Nikon software.

7.4.5 Image procesing

Images retrieved from the analysis with STORM plug-in were artificially coloured using ImageJ software.

7.5 References

1. Demicheli, V., Jefferson, T., Ferroni, E., Rivetti, A. & Di Pietrantonj, C. Vaccines for preventing influenza in healthy adults. *Cochrane Database Syst. Rev.* **2**, CD001269 (2018).
2. Sridhar, S., Brokstad, K. A. & Cox, R. J. Influenza Vaccination Strategies: Comparing Inactivated and Live Attenuated Influenza Vaccines. *Vaccines* **3**, 373–389 (2015).
3. Giesker, K. & Hensel, M. Bacterial Vaccines. in *Reference Module in Biomedical Sciences* (Elsevier, 2014). doi:10.1016/B978-0-12-801238-3.00141-0.
4. Masomian, M., Ahmad, Z., Gew, L. T. & Poh, C. L. Development of Next Generation Streptococcus pneumoniae Vaccines Conferring Broad Protection. *Vaccines* **8**, (2020).
5. Wyres, K. L. *et al.* Pneumococcal capsular switching: a historical perspective. *J. Infect. Dis.* **207**, 439–449 (2013).
6. Brueggemann, A. B., Pai, R., Crook, D. W. & Beall, B. Vaccine escape recombinants emerge after pneumococcal vaccination in the United States. *PLoS Pathog.* **3**, e168 (2007).
7. Global Burden of Disease (GBD 2019). *Institute for Health Metrics and Evaluation* http://www.healthdata.org/gbd/2019.
8. Astronomo, R. D. & Burton, D. R. Carbohydrate vaccines: developing sweet solutions to sticky situations? *Nat. Rev. Drug Discov.* **9**, 308–324 (2010).
9. Pozsgay, V. Recent developments in synthetic oligosaccharide-based bacterial vaccines. *Curr. Top. Med. Chem.* **8**, 126–140 (2008).
10. Patente, T. A. *et al.* Human Dendritic Cells: Their Heterogeneity and Clinical Application

Potential in Cancer Immunotherapy. *Front. Immunol.* **9**, (2019).

11. Rappuoli, R. Glycoconjugate vaccines: Principles and mechanisms. *Sci. Transl. Med.* **10**, (2018).

12. Micoli, F. *et al.* Glycoconjugate vaccines: current approaches towards faster vaccine design. *Expert Rev. Vaccines* **18**, 881–895 (2019).

13. MacCalman, T. E., Phillips-Jones, M. K. & Harding, S. E. Glycoconjugate vaccines: some observations on carrier and production methods. *Biotechnol. Genet. Eng. Rev.* **35**, 93–125 (2019).

14. Mukhopadhyay, P., Mishra, R., Rana, D. & Kundu, P. P. Strategies for effective oral insulin delivery with modified chitosan nanoparticles: A review. *Prog. Polym. Sci.* **37**, 1457–1475 (2012).

15. Lopes, P. P., Tanabe, E. H. & Bertuol, D. A. Chapter 13 - Chitosan as biomaterial in drug delivery and tissue engineering. in *Handbook of Chitin and Chitosan* (eds. Gopi, S., Thomas, S. & Pius, A.) 407–431 (Elsevier, 2020). doi:10.1016/B978-0-12-817966-6.00013-3.

16. Shi, L. E. S., Chen, M., Xinf, L. Y., Guo, X. F. & Zhao, L. M. Chitosan nanoparticles as drug delivery carriers for biomedical engineering. *J. Chem. Soc. Pak.* **33**, 929–934 (2011).

17. Xing, K. *et al.* Antifungal and eliciting properties of chitosan against Ceratocystis fimbriata in sweet potato. *Food Chem.* **268**, 188–195 (2018).

18. Grenha, A. Chitosan nanoparticles: a survey of preparation methods. *J. Drug Target.* **20**, 291–300 (2012).

19. Pujals, S., Feiner-Gracia, N., Delcanale, P., Voets, I. & Albertazzi, L. Super-resolution microscopy as a powerful tool to study complex synthetic materials. *Nat. Rev. Chem.* **3**, 68–84 (2019).

20. van der Zwaag, D. *et al.* Super Resolution Imaging of Nanoparticles Cellular Uptake and Trafficking. *ACS Appl. Mater. Interfaces* **8**, 6391–6399 (2016).

21. Durán, V. *et al.* Preferential uptake of chitosan-coated PLGA nanoparticles by primary human antigen presenting cells. *Nanomedicine Nanotechnol. Biol. Med.* **21**, 102073 (2019).

22. Han, Y., Zhao, L., Yu, Z., Feng, J. & Yu, Q. Role of mannose receptor in oligochitosan-mediated stimulation of macrophage function. *Int. Immunopharmacol.* **5**, 1533–1542 (2005).

23. Calvo, P., Remuñan-López, C., Vila-Jato, J. L. & Alonso, M. J. Chitosan and chitosan/ethylene oxide-propylene oxide block copolymer nanoparticles as novel carriers for proteins and vaccines. *Pharm. Res.* **14**, 1431–1436 (1997).

Conclusions and future perspectives

In this thesis we have optimized and implemented single-molecule localization microscopy (SMLM) techniques for the study of influenza viral structures. Specifically, we have characterized the interaction and effects of several antivirals at the nanoscale, as well as described the viral compositions of vaccines constructs such as virus-like particles and recombinant vaccines at single-particle level.

In this context, we have focused each chapter in the nanostructural characterization of a different viral component, antiviral and vaccine using optimized super-resolution techniques such as dSTORM and DNA-PAINT, proving how robust, powerful and sensitive is SMLM in the study of viral features, independently of their nature, environment, fixation agent or shape and size.

Taking this general outcome into account, the conclusions retrieved from this thesis are the following:

Firstly, using dSTORM imaging we could characterize the morphology of the filaments of A/Udorn/72 influenza strain and their different features, such as Archetti bodies and filament distribution. We could further study how M2e-specific monoclonal antibodies (MAb) mediated the inhibition of the filament formation, discovering that not only MAbs depleted the formation of the filaments from the initial stages of the infection, but also interfered in the integrity of pre-existing filaments produced on the host-infected cell. Thanks to the gained resolution, we could measure structural details such as the width, the length and the aspect ratio of the filaments, confirming that depleted filaments resulted to be shorted and wider compared to untreated ones. Overall, our data could determine that the protein M2 plays a crucial role in the filament formation and its blockage would lead in a decrease of the infectivity of the virus.

Secondly, to later perform multiplexing quantitative super-resolution microscopy on viral samples, we demonstrated that DNA-PAINT is a sensitive technique for functional characterization of nanomaterials, quantifying the number of available targets on the surface of nanoparticles with a highly selective recognition. Besides, we mapped the inter- and intraparticle distributions of several targets at single-particle level, validating this method for further characterize virus-like particles and virus isolates.

Subsequently, taking into account the previous optimization and setup, using DNA-PAINT we imaged and quantified the expression and distribution of three recombinant viral proteins of influenza both on transfected cells and on the isolated virus-like particles. First, studying the expression on the membrane of transfected cells we demonstrated that the recombinant proteins were produced heterogeneously within the population of cells, revealing that the three proteins were organized in small clusters along the membrane that co-localize with time. Successively, we characterized the distribution of the proteins on virus-like particles at single-particle level, showing a higher expression of HA compared to NA and M2, while displaying a soft heterogeneity inter- and intra-particle. This characterization at single-molecule level proved that DNA-PAINT is a powerful tool to study and describe new vaccines systems, monitoring the recombinant expression of protein on cells and the budding and released of virus-like particles, to help in the development of recombinant vaccines.

Thirdly, we kept proving the potential of using dSTORM to identify antivirals and the presence of different viruses in other preparations. In this context, we optimized the imaging acquisition on formaldehyde fixed paraffin embedded tissues (FFPE), for the characterization of the presence of hepatitis B and delta. Thanks to the resolution and sensitivity gained with dSTORM we could identify the presence and the distribution of hepatitis B and Delta on FFPE tissues of cirrhotic patients, even in thick preparations with strong auto-fluorescence. We could identify different co-infection patterns in some hepatocytes thanks to the gaining in sensitivity, specially recognizing the distribution of both viruses when they are infecting the same hepatocyte. In Brief, these results open the possibility to implement dSTORM in the study of FFPE tissues to further describe the viral cycle in patients.

On the other hand, dSTORM was implemented in the study of the antiviral activity of analogues of sialic acid bound to dendrimers (6SL dendrimers). The main aim of the study consisted in performing *in vitro* assays on four different strains of influenza, concluding that our 6SL dendrimers displayed a soft interaction towards two of the strains of influenza (Udorn and PR8) and no interaction to the other two strains (Pdm09 and X31). This weak interaction towards Udorn and PR8 was not strong enough to block influenza virus and thus did not inhibit the infectivity. Using dSTORM it was possible to discern how 6SL dendrimers distributed in aggregates on top of host-infected cells, concluding that the virus did not inactivate by the action of 6SL dendrimers due to a lack of homogeneity in the dendrimer preparation.

Finally, dSTORM was used to study the intracellular trafficking of antigen-nanoparticles (nanovaccines) inside dendritic cells. Thanks to the super-resolution images obtained by dSTORM of different time points and sections of the cells it was possible to investigate the mechanism of uptake, distribution and exposure of the antigen on the surface of dendritic cells. dSTORM images showed that dendritic cells successfully internalized the nanovaccines after 1 hour of incubation, increasing the uptake with time. With the implementation of super-resolution microscopy in nanovaccine development a rational design of the nanoparticle could be performed.

In general, SMLM has demonstrated to be an ideal approach to characterize viruses and antiviral systems, fitting perfectly the requirements for new viral studies and antiviral development.

Taking into consideration the conclusions explained above, our first perspective is the application of SMLM in the description of other viral proteins and structures e.g. influenza filament formation. While in chapter 2 we studied the presence on the viral filament of the protein M2 and HA, separately, in chapter 3 we could perform multicolour imaging of HA and RNPs in the same filaments, observing different protein content within the population of filaments. Accordingly, multicolour SMLM would play an important role in discerning the filament distribution of influenza proteins (NA and M1), as well as other crucial influenza elements such as genetic material or lipid composition. Hence, we could be able to analyse the viral arrangement of several filaments to disclose their composition, in order to unveil the final role of the filament formation and its implication in the spread of newly synthesized viral particles.
In the same line, we propose the use of SMLM to distinguish the distribution of proteins of other viruses such as SARS-CoV-2, in order to describe its mechanism of action and to unveil the correct antivirals mechanisms against it.

Next, we propose the implementation of SMLM in the rational design of antivirals and vaccines. The increased resolution gained with dSTORM and DNA-PAINT allowed us to identify the mechanism of action of antivirals as well as characterize the structure of vaccines candidates. Hence, these techniques could be employed as an ordinary step in the smart design and industrial production of vaccines and antivirals, which would faster the development of these treatments and get ahead of the appearance of new variants or strains of viruses.

Furthermore, we believe that the next step towards the smart design of vaccines would be the implementation of a high-throughput system to analyse several virus-like particles and vaccine candidates at the same time, using SMLM and machine learning. Implementing the optimization performed in this thesis for acquiring SMLM images on viruses and vaccines, in combination with the automation of several crucial steps and machine learning, would allow the characterization of numerous structures at the same time. Hence, with this method it could be discerned the best vaccine candidate with the right protein content and distribution at single-particle level.
Specifically, we would automatized all the washing steps for the exchange of the imagers, to perform a multiplexed image acquisition with DNA-PAINT, we could be able to use a multi-well plate arrangement for allocating different VLP candidates and finally, we would study the protein distribution by performing single-particle analysis with machine learning. Further, we expect to be able to automatize the purification of VLPs, and the identification of the relationship between the expressions of recombinant proteins from cells with the protein content of the retrieved VLPs, to step up the analysis. In brief, by combining high-throughput methods with an increased resolution the vaccine development could be refined.

Moreover, this high-throughput system could be potentially applied in the development of a sensitive, rapid and unequivocal system for the identification and detection of viral presence in different samples for diagnosis. In particular, the usage of SMLM in combination with machine learning is proposed to identify and classify groups of viruses from non-purified samples such as contaminant water and supernatant of cells.

Finally, a future prospect would be enhancing the application of DNA-PAINT in broader viral studies and samples. In the present thesis we showed how important is selecting the concrete SMLM technique for each sample type. In this context, DNA-PAINT was better applied on fixed cells and small biological samples that could be immunostained, while dSTORM displayed more flexibility and was suitable for more sample types such as paraffin tissues, fixed cells and nanoparticle identification that could be labelled with both dyes and antibodies. As commented in Chapter 3 and 4, DNA-PAINT poses several advantages over dSTORM, such as the ability of observing different targets on the sample avoiding chromatic aberration, and the capacity to quantify the number of proteins.
However, DNA-PAINT possesses several drawbacks including long imaging acquisition times and time-consuming washing steps, the need of an optimization of the probe labelling, and the high amount of background noise. All this disadvantages makes its application challenging in

different conditions, needing a great deal of optimization and validation. Hence, we would want to keep upgrading DNA-PAINT for its further utilization in broader sample types and viral studies. This could be done by the selection of newly proposed small docking sequences, by the application of non-sticky dyes for imaging (e.g. Cy3b) or the automation of the washing steps by a microfluidic chamber organization in combination with a NanoJ-Fluidics system. Therefore, we would make DNA-PAINT more accessible for future assays that would widen viral studies.

List of publications and congress presentations

The list of publications and congress presentations derived from this thesis are presented here:

Publications

Pietro Delcanale, Bernat Miret-Ontiveros, **Maria Arista-Romero**, Silvia Pujals, and Lorenzo Albertazzi. Nanoscale Mapping Functional Sites on Nanoparticles by Points Accumulation for Imaging in Nanoscale Topography (PAINT).*ACS Nano 12* (8), 7629-7637 (**2018**)

Annasaheb Kolpe*, **Maria Arista-Romero***, Bert Schepens, Silvia Pujals, Xavier Saelens, and Lorenzo Albertazzi. Super-resolution microscopy reveals significant impact of M2e-specific monoclonal antibodies on influenza A virus filament formation at the host cell surface. *Sci Rep* **9,** 4450 (**2019**).

Ruben De Coen, Lutz Nuhn, Chamani Perera, **Maria Arista-Romero**, Martijn D. P. Risseeuw, Alec Freyn, Raffael Nachbagauer, Lorenzo Albertazzi, Serge Van Calenbergh, David A. Spiegel, Blake R. Peterson, and Bruno G. De Geest. Synthetic Rhamnose Glycopolymer Cell-Surface Receptor for Endogenous Antibody Recruitment. *Biomacromolecules 21* (2), 793-802 (**2020**)

Maria Arista-Romero, Silvia Pujals, and Lorenzo Albertazzi. Towards a quantitative single-particle characterization by super-resolution microscopy: from virus structures to antivirals design. *Submitted and accepted*. Frontiers in Bioengineering and biotechnology.

Maria Arista-Romero, Pietro Delcanale, Lorenzo Albertazzi, and Silvia Pujals. Nanostructural characterization of recombinant viral proteins with super-resolution microscopy: from cells to virus-like particles. *Submitted*.

Congresses presentations

-17th CRG symposium: trends in biology: cutting edge techniques from genomes to organisms.
September 2018.
Maria Arista-Romero, Annasaheb Kolpe, Bert Schepens, Xavier Salens and Lorenzo Albertazzi**.** Super-resolution microscopy reveals significant impact of M2especific monoclonal antibodies on influenza A filamentous virion formation"
This talk was awarded by the best talk prize.

-XVIII SCB Virology meeting.
October 2019.
Maria Arista-Romero, Annasaheb Kolpe, Bert Schepens, Xavier Salens and Lorenzo Albertazzi. Super-resolution microscopy reveals significant impact of M2especific monoclonal antibodies on influenza A filamentous virion formation.

-PhD Discussions IBEC.
December 2019.
Maria Arista-Romero, Annasaheb Kolpe, Bert Schepens, Xavier Salens and Lorenzo Albertazzi**.** Super-resolution microscopy reveals significant impact of M2especific monoclonal antibodies on influenza A filamentous virion formation.

-IBEC 13th symposium: Bioengineering for future and precision medicine. Flash presentation.
October 2020.
Maria Arista-Romero, Pietro delCanale, Silvia Pujals and Lorenzo Albertazzi.
Nanostructural characterization of influenza virus-like particles with super-resolution microscopy.

-XIX SCB Virology meeting.
October 2020.
Maria Arista-Romero, Pietro delCanale, Silvia Pujals and Lorenzo Albertazzi.
Nanostructural characterization of influenza virus-like particles with super-resolution microscopy.
This talk was awarded by the second best talk prize.

Posters presentations

-IBEC 11th symposium: Bioengineering for regenerative therapies.
October 2018.
Pietro Delcanale, **Maria Arista-Romero**, Silvia Pujals, Lorenzo Albertazzi. Mapping Biomolecules at Sub-Diffraction Resolution with PAINT Microscopy.

-IBEC 12th Symposium: Bioengineering for active ageing.
July 2019.
Maria Arista-Romero, Annasaheb Kolpe, Bert Schepens, Xavier Salens and Lorenzo Albertazzi. Super-resolution microscopy reveals significant impact of M2especific monoclonal antibodies on influenza A filamentous virion formation.

-TU/e IBEC symposium.
July 2019.
Maria Arista-Romero, Annasaheb Kolpe, Bert Schepens, Xavier Salens and Lorenzo Albertazzi. Super-resolution microscopy reveals significant impact of M2especific monoclonal antibodies on influenza A filamentous virion formation.

-XVIII SCB Virology meeting.
October 2019.
Maria Arista-Romero, Annasaheb Kolpe, Bert Schepens, Xavier Salens and Lorenzo Albertazzi. Super-resolution microscopy reveals significant impact of M2especific monoclonal antibodies on influenza A filamentous virion formation.
This poster was awarded by the best poster presentation prize.

-IBEC 13th symposium: Bioengineering for future and precision medicine.
October 2020.
Maria Arista-Romero, Pietro delCanale, Silvia Pujals and Lorenzo Albertazzi.
Nanostructural characterization of influenza virus-like particles with super-resolution microscopy.

List of acronyms and abbreviations

6SL: 6'-Sialyllactose

Ab: antibody

BSA: bovine serum albumin

DCs: dendritic cells

DLS: dynamic light scattering

DMEM: Duldecco's Modified Eagle medium

DNA-PAINT: DNA points accumulation for imaging in nanoscale topography

dSTORM: direct stochastic optical reconstruction microscopy

EM: electron microscopy

FBS: fetal bovine serum

FFPE formaldehyde fixed paraffin tissues

GC-CNPs: glycoconjugate chitosan nanoparticles

GC: glycoconjugate

H_2Omq: miliq water

HA: hemagglutinin

HBV: hepatitis B virus

HBsAg: surface antigen from hepatitis B virus

HDAg: antigen from hepatitis D virus

HDV: hepatitis D virus

HPI: hours post infection

IAV: influenza A virus

LB: Luria-Bertani medium

M1: Matrix protein 1

M2: Ion channel matrix protein 2

M2e: external portion of M2

MAb: monoclonal antibody

MALDI-TOF: matrix-assisted laser desorption/ionization – time-of-flight

MDCK: Madin-Darby canine kidney cells

MEA: cysteamine (mercaptoethylamine)

MoDCs: monocyte-derived dendritic cells

NA: Neuraminidase

NP: Nucleoprotein

NPs: nanoparticles

OC: oseltamivir

PAMAM: Poly(amidoamine)

PB1: Polymerase basic protein 1

PB2: Polymerase basic protein 2

PBS: phosphate-buffered saline

PFA: paraformaldehyde

PFU: plaque forming units

qPAINT: quantitative-PAINT

SA: sialic acid

SIM: structured illumination microscopy

SMLM: single molecule localization microscopy

STED: stimulated emission depletion

TIRF: total internal reflection fluorescence microscopy

VLP: virus-like particles

vRNA: viral RNA

vRNP: viral ribonucleoproteins

WGA: wheat germ aggutinin

Acknowledgments

When Charles Dickens wrote, “It was the best of times, it was the worst of times” I am 90% sure that he was talking about the journey of a PhD candidate, basically because I could summarize my 4 years of PhD with that sentence. This rollercoaster has been the best thing that happened to me and at the same time, the hardest. Fortunately, I have been granted with great persons around me to make that trip easier and to whom I must acknowledge.

First I have to thank my director, Lorenzo. Thanks for have trusted me from that day in December of 2015 when I entered in your office, still under construction. From that moment we started a journey that began in 2017 and I hope we are not going to finish. The project was engaging and the STORM microscopy made me fell in love with the small-big world of the nanoscopy. I will always cherish those long hours in the dark microscope room when you passed by to chat, to check how was my sample or just to check how I was doing, with great empathy and expert-eye to teach me how to properly distinguish a good sample. Thanks a lot for giving me this amazing project, teach me everything about super-ress and left me be myself.

To the second person that made this thesis possible, my other director Silvia. Has sido un apoyo indispensable y único estos últimos años. Tu ayuda y dedicación semanal han sido en ocasiones el motor que me ha ayudado y permitido avanzar, sobre todo cuando todo estaba oscuro y no salía nada. No exagero si te digo que sin tu ayuda y apoyo constante mi tesis sería mucho peor, y es que saber que siempre estabas ahí para escucharme, apoyarme, darme ideas y ayudar a buscar otro punto de vista me ha ayudado no solo a progresar sino a sobrellevar la tesis. Eres una gran científica y persona y siempre podrás contar conmigo.

To all the N4N group, starting with Natalia, the founder of the lab protocols and STORM microscope. You have been an inspiration and role model during all these years, where I always asked myself: “What would Natalia do?”. Secondly, to my office team. Thanks Pietro, for all those long hours working together and creating the project DNA-PAINT, for hearing me complaining about the imagers or helping me with Matlab. Your company and support have been essential for my PhD. Thanks Edgar for being always so chatty, so helpful and such a great peer; seeing you growing from a master student to a scientist have been great and I am sure that your future will be bright and full of success. Thanks Madhu for being yourself in the office, your shine and happy spirit was very helpful, especially in those days when the experiments were not working and it was hard to find a reason to smile, I will miss your recipes and the

“Bacardi” that you always brought. Teo, you are an amazing person and scientist, you are always willing to chat, to help, to discuss science and become better scientist. Thanks a lot for all your help and company during these years (and the amazing coffee!). Thanks, Alis, for your kindness and serenity even in the worst times; keep drawing and bringing us your art. Adrianna, you were always my PhD companion, from the start to the end of our PhDs. You are so sweet, so intelligent and so patience that talking with you is always a pleasure, either to discuss about science or about our life and future. I am sure that your future is bright, and I hope I will be around to see it.

To the Eindhoven N4N team. Roger, Manos, Laura, Bea and Cristina, it was so nice to visit you and spend time in your city sharing great no-science related moments. I hope that post-pandemic times will bright us more funny and happy moments. To the other members of the team: Ana, Marrit and Yuyang. I wish we could have shared more moments together, but thanks a lot for your support and I am hopping to share more time with you in the future!

During these years I had the opportunity to collaborate with great researchers that made my PhD possible. Thanks to Dr. Xavier Saelens and all the members of his group: Annasaheb Kolpe, Bert Schepens, Eline Soetens, Koen Sedeyn, Dorien DE Vlieger and Anouk Smet. Thanks for welcoming me in Ghent and helping me during my journey at your lab. I had a great time there and it was all because of you. Also thanks for sharing samples, plasmids, experiments and experience with me; indeed without your help my PhD would not have been complete.
Thanks to Ester Garcia from IDIBAPS, for trusting me in testing your samples and trying to unveil the great mystery behind hepatitis delta, and also to Sofia Perez del Pulgar for welcoming me always at your lab and be one member of my PhD tribunal.
Thanks to all the IBEC team that made possible everything that I did at IBEC. Thanks to the core facilities team: Laura, Ramona, Tania, Sandra and Inma. Thanks also to Pilar Rodriguez and Clara from communications department, it was always great working with you.

I cannot forget about the other moral supporters of my PhD, Macià and Ariadna from XT. Gracias por las horas tomando café y charlando los días interminables de laboratorio. Os deseo lo mejor y ojalá poder estar a vuestro lado viéndolo.

Gracias a todos los que habéis hecho que los momentos malos de la tesis no fueran tan malos. A Estel y Marina, mis compis del IQS, por apoyarme y escucharme siempre a pesar de la distancia y las agendas apretadas. Nos debemos muchos cafés este año y seguro que los disfrutaremos en el futuro.

No puedo olvidarme de mi compañero de crimen durante toda la carrera y master, gracias Curro por escucharme siempre, por apoyarme, por aguantar mis mensajes y quitarme miedos. No evitaste que emprendiera el camino de la tesis doctoral pero si lo has hecho mucho más ameno y soportable. Ojalá seguir participando en los momentos de la vida del otro, como llevamos haciendo tantos años.

Gracias a mi gran amiga Cinta por apoyarme siempre, incondicionalmente. Tu amor y cariño ha sido un apoyo más que necesario, gracias por ser tan positiva y ser solo lo bueno que hay en mi en todo momento.

Y por último, pero no menos importante, porque han sido los más importantes en este camino. A mis padres, a quienes os dedico esta tesis. Por apoyarme SIEMPRE, por sentiros orgullosos de mi, por confiar en que podría hacerlo y nunca dudar de mis capacidades. Sin vuestro apoyo y amor no podría haber llegado a donde estoy, y os prometo que seguiré intentando que os sintáis orgullosos de mi.

A Genis, mi compañero de vida. El que me ha apoyado sin rechistar estos cuatro años, el que me ha celebrado conmigo los éxito y el que me ha abrazado cuando algo salía mal. La única persona que se que va a quererme siempre en lo bueno y en lo malo, porque ha visto muchos momentos malos. Por siempre, gracias.

Thanks you all,

Maria